technische universität
dortmund

Optically detected resonances induced by far infrared radiation in quantum wells and quantum dots

Dissertation

presented to the Institute of Physics of the Dortmund University of Technology, Germany in partial fulfilment of the requirements for the degree of

Doktor. rer. nat.

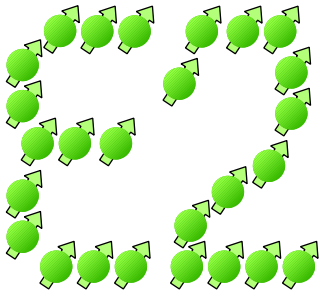

presented by Michael Gerbracht

Dortmund, April 2008

Accepted by the faculty of the Institute of Physics of the Technical University of Dortmund, Germany.

Day of the oral exam: 21st May 2008

Examination board:

Priv. Doz. Dr. Dmitri R. Yakovlev
Prof. Dr. Klaus Wille
Prof. Dr. Bernhard Spaan
Dr. Bärbel Siegmann

Contents

Chapter 1:

Introduction

1.1 Motivation

1.1.1 Motivation

Science related to nanostructures has become famous at the beginning of this decade. Today the word ’Nanotechnology‘ appears almost daily, even in newspapers and magazines not related to science. It is believed that nanotechnology is able to solve problems in many fields, from material science to biology and medicine. It is rated as technology of the future but it is widely unknown that nanostructures have been present in nature for very long time. The most common example is the ability of the Lotus (Nelumbo) plant to keep their leafs clean from dust. It has been found out, that the surface is not perfectly even as one might expect but shows a microscopic structure so that only 2-3% of the surface is thought by water droplets [Sol07]. Dust on the surface sticks to water and is washed of the leaf surface.

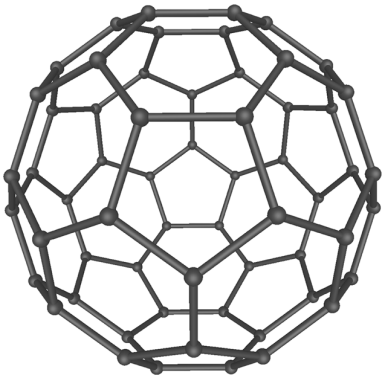

Fig. 1.1:
Structure of Carbon C-60 molecule.[1]

Another example are fullerene, carbon molecules consisting of 60 carbon atoms looking like a football[1] (Fig. 1.1) which have been discovered in 1985 [Kro85]. When people tried to produce these molecules they discovered that it can also be found in the smoke of a candle.

Humans have used nanoparticles already centuries ago without knowing so. The famous Damascus sabre which never tarnishes is based on nanostructures. Carbon and cementite nanotubes are sticking out at the edge of the blade acting like teeth of a saw [Rei06].

In recent years it became possible to fabricate nanostructures in a controlled manner. Many commercial products that make use of nanostuctures in the one or other way are available on the marked and the potential of these systems is not slowing down.

Also in the field of chip and computer technology, the shrinking of transistors and other fundamental structures found in every integrated circuit come along with faster processing power. First processors which are grown with structures sizes as small as 45 nm become available now and further minimization will stop when quantum effects come into play at even smaller structures. This will limit the development of faster processor which work in the conventional way. Other techniques such as massive parallel processing need to be used in order to enhance processing power further.

But quantum effects can also be used to create a new kind of computer: The quantum computer. It is not a digital device based on bits which can be either 0 or 1. In a quantum computer a bit can also represent all superpositions of 0 and 1, so its state can be somewhere in-between 0 and 1. Up to now only the basic principle was demonstrated with seven nuclei in a molecule that could be controlled by nuclear magnetic resonance [Van01]. For reasons of scaleability and incorporation into classical systems, efforts are made to realize a semiconductor quantum computer. A good system for the implementation are quantum dots (QD), zero dimensional structures which are sometimes compared to atoms. A possible candidate for the realization of a qu-bit is the spin in magnetic fields. This can either be the nuclear spins or electron spins, the latter is convenient to have in QDs. Critical for the creation of a semiconductor quantum computer are decoherence and dephasing times, which define how long information can be stored in a quantum bit before it gets lost. In our group it was demonstrated recently that spin states could be preserved for 3ms in a quantum dot ensemble [Gre06]. Due to the interaction of electrons with nuclei in the QD, information could be stored over several hours and read out optically [Gre07].
Besides the storing of information in a QD ensemble, it is also necessary to be able to manipulate the spin states. One possibility is the use of far infrared radiation which may couple to the electron spins and induce transitions between energy levels. While the influence of far infrared radiation was studied on two dimensional systems to some extend, only very few attempts have been made to investigate the impact on quantum dots.

1 See: http://en.wikipedia.org/wiki/Image:C60a.png

1.1.2 Outline

In this thesis experimental results of optically detected resonance on magnetic and nonmagnetic semiconductor quantum dots and quantum wells are presented. Also the photoluminescence of these structures was subject of investigation. The thesis is organized as follows:

Chapter 1 gives a short theoretical background of semiconductors and their optical properties at low temperatures and application of magnetic fields. The growth of low dimensional nanostructures will be covered as well in a short summary.

The experimental setup is described in Chapter 2 along with the software used for measurements and analysis of the results. The experimental technique is reviewed and an overview about the presentation of results is also given in this chapter.

Chapters 3 - 6 contain the experimental results on magnetic and nonmagnetic quantum wells and quantum dots and are organized as follows:

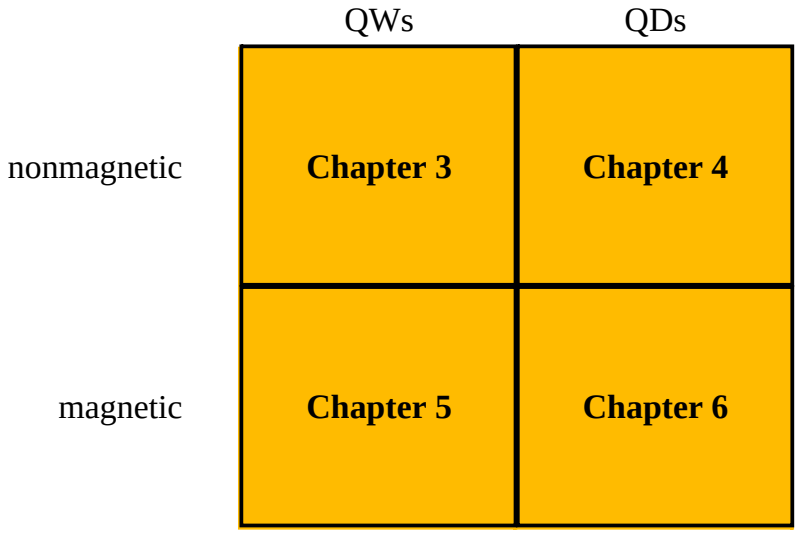

1.1.3 Technical notes

If you are reading the PDF version of this paper note that there are a number of internal and external links. All references to publications found in the text will open the website of the corresponding Jounal in a web browser. The same is true for links to websites as well as internal links to other sections which let you move to the page where the section starts.

The thesis was written with TechWriter 8.72 under RISC OS 6. Most graphs were created with OriginPro7 and reworked in ArtWorks 2.7.

1.2 From atoms to solid states

Many concepts and properties of solid state physics are deduced from atomic physics so it is worth to take a very brief look on atomic physics first. The nature of excitons and trions as well as donors and acceptors in a semiconductor is also often discussed in analogy with atomic-like energy spectra.

1.2.1 Hydrogen atom

The hydrogen atom is the lightest atom in the periodic system consisting of only one proton and one electron. The Bohr atomic model is a classic model which uses some additional assumptions to describe the hydrogen atom. A quantum mechanical model is required to describe all properties of the H-atom. But for a basic understanding, Bohrs model is sufficient enough.

The positively charged proton presents the atomic core which is circuit by the negatively charged electron on a trajectory where the coulomb attraction and the centrifugal force equalize. Only discrete radii are allowed since a de Broglie wavelength can be assigned to the electron on its orbit. The perimeter of the orbit has to coincide with a multiple of this wavelength. For all other radii the material wave vanishes due to destructive interference as shown in Fig. 1.2.

There is an infinite number of allowed orbits for the electron but the size of the radius is limited by the binding energy of the electron and proton. In case of the H-atom the binding energy is 13.6 eV. If no energy is transferred into the system the electron occupies the lowest orbit which is called the ground state.

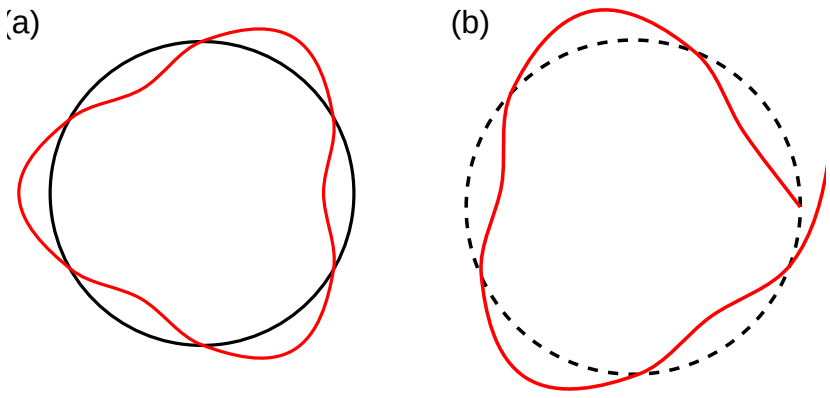

Fig. 1.2:
(a) Allowed orbit (black) if the perimeter coincides with a multiple of the de Broglie wavelength (red). (b) Other perimeters lead to destructive interference, the orbit is not stable.

If the atom is excited by light or e.g. by impacts with other atoms the electron can gain energy and therefore occupy a higher orbit. After a short time period it will re-

lax into the ground state. This process usually comes along with the emission of a photon that coincides in energy with the difference of the excited and the ground state. The energy or wavelength of the emitted radiation is typical for the element and allows identifying it if the radiation is analysed spectroscopically.

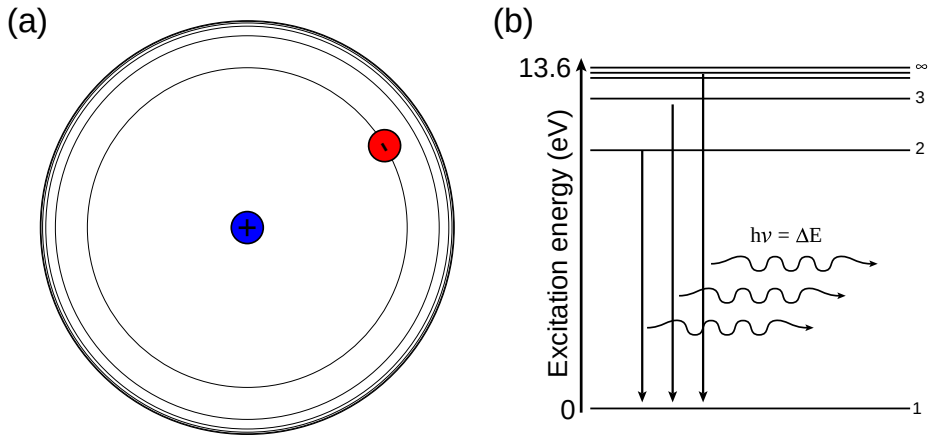

Fig. 1.3: *(a) Allowed orbits of the hydrogen atom. The electron occupies the ground state. (b) Energy levels of the H-atom. Arrows indicate energy relaxation processes and the emission of the corresponding photon.*

If the excitation energy exceeds the binding energy of the electron, in the case of hydrogen: 13.6 eV, the electron becomes a free particle and leaves behind the positively charged ion H^+. It is also possible that two electrons are bound to the proton. Such a negatively charged hydrogen atom is called H^-.

1.2.2 Pauli exclusion principle

As mentioned above a quantum mechanical model is required to fully understand the hydrogen atom. The three dimensional Schrödinger equation is used with the coulomb potential to derive the electron wave function and energy levels of the hydrogen atom. Taking into account the electron spin the solution contains four quantum numbers: *n* (principal quantum number), *l* (azimuthal quantum number), *m* (magnetic quantum number) and *s* (spin quantum number).

If more electrons are involved in the case of heavier atoms or solid states the Pauli exclusion principle has to be taken into account. It states that fermions (all particles with a half-integer spin) can not have an identical set of quantum numbers. This implies that not all electrons can occupy the ground state so that also higher energy levels are filled with electrons. The electrons of the highest (partially) filled level are called valence electrons. Their binding energy is lower than those of the other electrons so that a smaller amount of energy is necessary to set them free.

1.2.3 Molecules

Two or more atoms can form molecules by sharing their valence electrons in a way that the outer shell is completely filled (inert gas configuration).

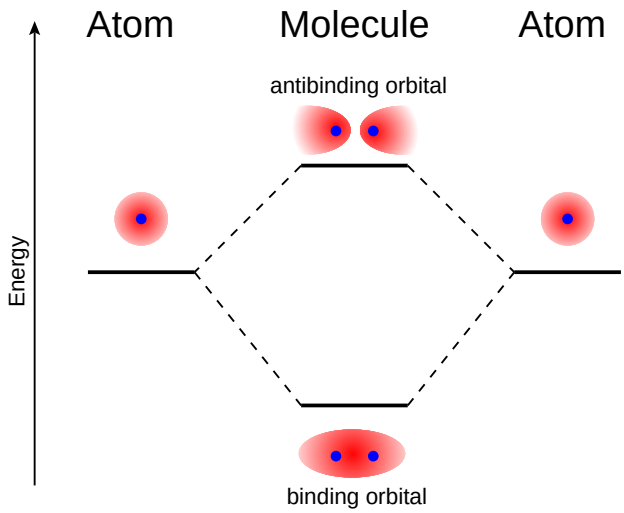

Fig. 1.4: *Binding and antibinding molecular orbitals are formed by the additive or subtractive overlap of the atomic wave functions.*

This process is combined with some gain in energy which can be explained by the formation of molecular orbits. The wave function of two atoms can be combined additive or subtractive leading to a (anti)binding orbital which is lower (higher) in energy than the atomic orbital as shown in Fig. 1.4.

1.2.4 Solid states

Atoms of the same or different elements can also be arranged in a lattice and form a crystal. These crystals are the basis for condensed matter physics. At the beginning of the last century crystals were analysed using X-rays which have been discovered by Wilhelm Conrad Röntgen in 1895. The inner structure of crystals, the lattice model and lattice constants, of different elements and materials was studied in this time. Later the focus changed to electrical and optical properties of solid states.

Like in atoms and molecules there are also energy levels in a solid state but due to the huge number of atoms interacting with each other, the energy levels expand into broader bands. They are often shown as a band structure plot. To understand the nature of metals, semiconductors and insulators it is important to have a look on the band structure of these materials (Fig. 1.5).

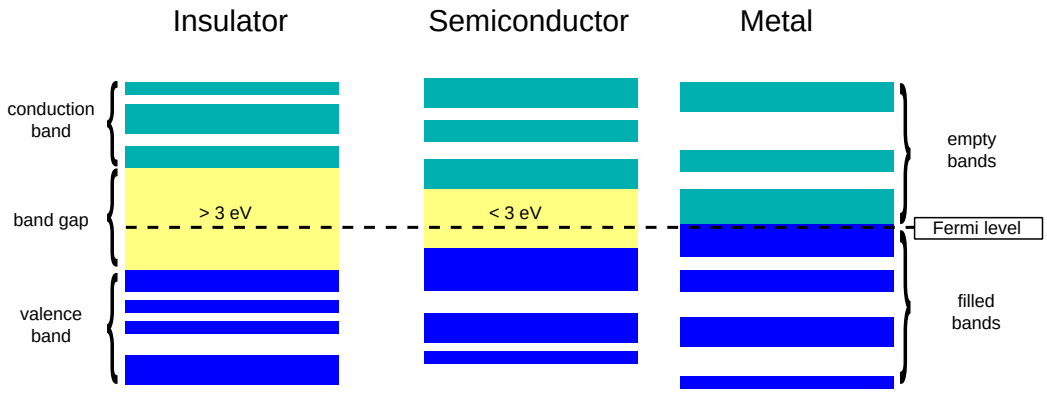

Fig. 1.5: *Band structure of insulators, semiconductors and metals.*

The valence band (VB) is the energetically highest band which is filled with electrons. These electrons are still bound to atoms in the lattice and are not free. The conduction band (CB) is an empty energy band where electrons can move freely if they reach it. It is called conduction band because only unbound electrons contribute to a current. So the number of free electrons in the conduction band determines the conductivity of the material. Free means that the electrons are not bound to atomic potentials and do not interact with each other. Therefore the state of the conduction band electrons is compared with an ideal gas and the expression "electron gas" has been coined for it. For metals, valance and conduction band overlap so that there are always enough free electrons available. In semiconductors and insulators there is a band gap between VB and CB where the probability density of electrons is zero. Electrons need to overcome the band gap to reach the conduction band and increase the conductivity. The difference between semiconductors and insulators is somehow arbitrary and depends on the size of the band gap and hence the probability of electrons to reach the CB. In general, materials with a band gab greater than 3 eV are considered insulators.

1.3 From bulk semiconductors to nanostructures

The energy gap of semiconductors can be overcome at certain conditions which makes it possible to tune the characteristics of the semiconductor by some kind of external stimulation. Due to this ability there are uncountable areas of applications. Semiconductors are used in many electronic components such as diodes and transistors and in more complex devices like chips and processors used in computers. Their optical properties allow their use as detectors and light sources or solar cells. Many semiconductors can be grown artificially at high purity. With the help of molecular beam epitaxy (MBE) it is possible to produce material films with the thickness of only one monolayer. Thin films of one material that are embedded in another bulk material are called quantum wells (QWs). These films are two dimensional nano structures. Also one and zero dimensional nano structures have been fabricated in the form of quantum wires and quantum dots.

1.3.1 Bulk semiconductors

As mentioned before the band gap is the characteristic attribute of a semiconductor. Electrons can reach the conduction band if they have enough energy to overcome the band gap. At room temperature semiconductors show some conductivity. The mean thermal energy of electrons at room temperature is about 25 meV which is not enough to pass the band gap, but due to the Boltzmann distribution there is a number of electrons whose energy reaches 1-2 eV. This also explains the increasing conductivity of semiconductors when the temperature is raised and more electrons reach the CB. However, temperature is usually not used to excite the semiconductor. Light in the visible region of 400 - 700 nm has an energy of 1.7 to 3.0 eV and is much more efficient in terms of increasing the conduction band population. The conductivity of a semiconductor will increase when it is exposed to light which makes it easy to build a simple detector to measure the light intensity by its conductivity. One problem that arises here is the thermal excitation of the semiconductor mentioned before, which influences the conductivity independent of the light intensity. This adds some random fluctuations, the so called noise, to the measured signal[2]. To avoid this effect it is necessary to cool the sample. Most experiments presented in this thesis have been performed at liquid helium temperature of 4.2 K or -267°C.

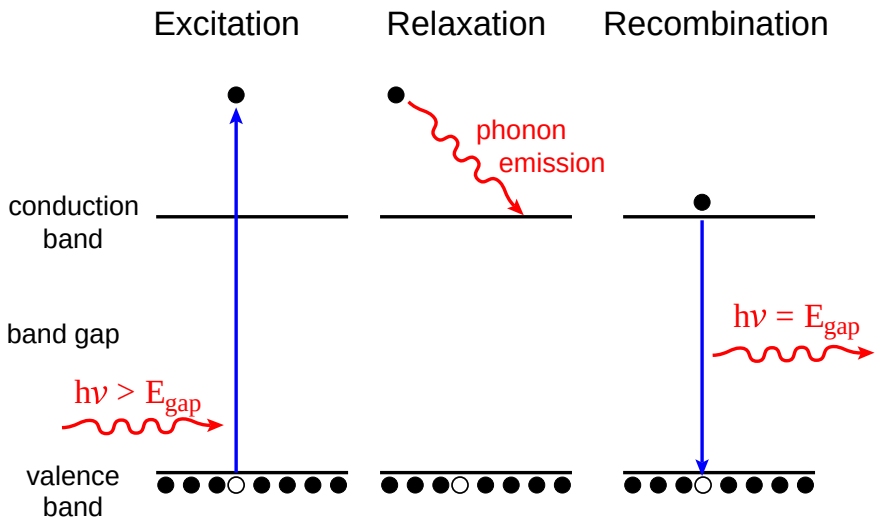

Fig. 1.6: *Creation of an electron-hole-pair by an excitation photon with energy exceeding the band gap. The electron relaxes to the conduction band edge by emitting phonons. The electron-hole-pair recombines and generates a photon with the energy of the band gap.*

2 This effect can also be observed with digital cameras which are also based on semiconductor light sensors. Pictures taken under low light conditions often appear noisy.

When electrons are transferred into the CB they leave behind an empty space in the VB which is called hole. Neighbor electrons of this hole can fill its empty space but also leave behind their space empty so that the hole can move. If there are enough holes in the VB they can also contribute to a current. Electrons in the conduction band can recombine with holes in the valence band by emitting a photon with the energy $h\nu = E_{gap}$ as shown in Fig. 1.6. This is called the photoluminescence of a semiconductor and comparable to the relaxation of atoms.

The band structure[3] of a semiconductor can be used to explain many electrical and optical properties. They show the wave function of electrons and holes as a function of the wave vector $\vec{k}$ in the reciprocal space[4].

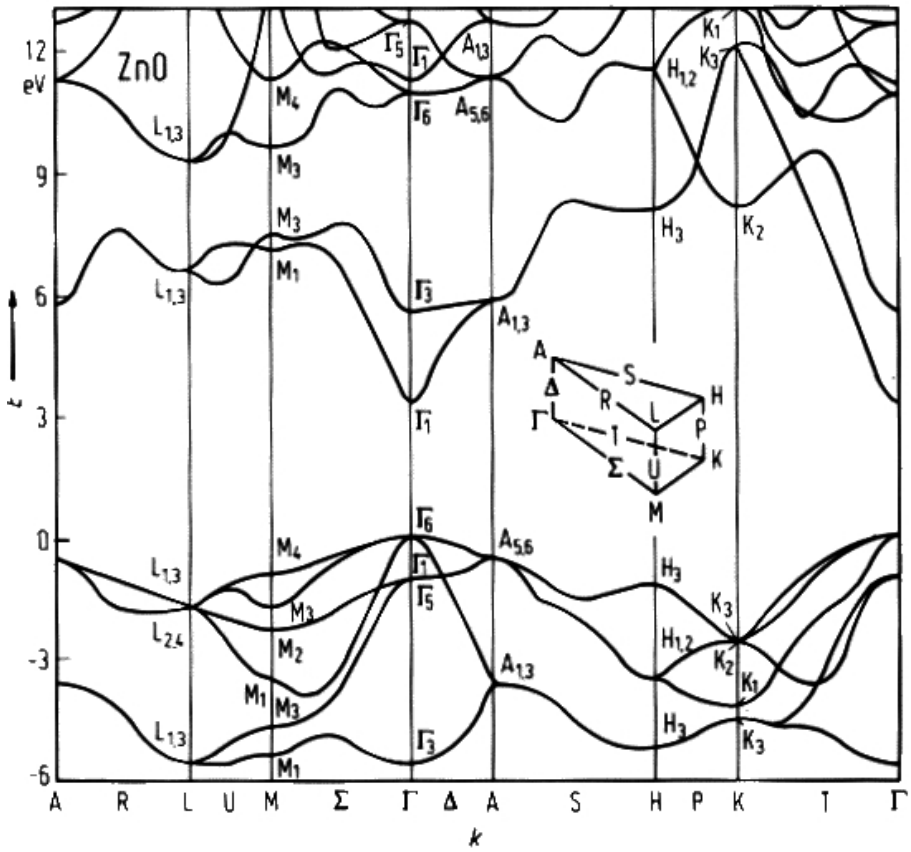

Fig. 1.7: *Band structure of GaAs. Letters on the k-axis indicate points in the reciprocal space where Γ is the centre of the Brillouin zone.*[3]

In Fig. 1.7 the band structure of GaAs is shown. The letters on the k-axis indicate points in the reciprocal space where Γ represents the centre of the Brillouin zone[5]. At this point the CB minimum and VB maximum coincide. Due to the tendency of electrons and holes to reduce their potential energy, the carrier density at this point

3 See: http://staff.bath.ac.uk/pysdw/band_structure.htm

4 See: http://en.wikipedia.org/wiki/Reciprocal_space

5 See: http://en.wikipedia.org/wiki/Brillouin_zone

is very high and recombinations of electron-hole-pairs are very likely to appear. Since the experiments in this thesis are based on the photoluminescence caused by this recombination, the consideration of the band structure can be reduced to the vicinity of the Γ-Point.

On a closer look the valence band splits into three subbands. To understand the origin of the splitting it is necessary to consider the angular momentums involved. An electron bound to an atom has an orbit angular momentum which is reflected in the Azimuthal quantum number and is symbolized by an l. It can have integer values. The other angular momentum important here is the spin of the electron symbolised by an s and a value of $\pm\frac{1}{2}$. The total angular momentum is given by: $j = l + s$. The coupling of l and s is known as spin-orbit interaction.

For the free electrons in the lowest conduction band niveau there is no orbit angular momentum: $l = 0$, so that $j_e = \pm\frac{1}{2}$. For the holes in the valence band there are six possible values with $l = 0, \pm 1$: Comparable to the $P_{\frac{1}{2}}$ state of the atom with $l = 0$ and $s = \pm\frac{1}{2}$ the possible values are $j_{soh} = \pm\frac{1}{2}$, and comparable to the $P_{\frac{3}{2}}$ state with $l = 1$ we get $j_{hh} = \pm\frac{3}{2}$ and $j_{lh} = \pm\frac{1}{2}$. The $j_{hh} = \pm\frac{3}{2}$ state corresponds to the heavy hole (hh) which has a smaller band curvature than the $j_{lh} = \pm\frac{1}{2}$ state which belongs to the so called light hole (lh). The names are derived from the fact that the effective mass is defined as the second derivative of the band curvature. A smaller curvature corresponds to a heavier effective mass. In low dimensional structures there is a small split between heavy and light hole bands at the Γ-Point caused by the confinement of carriers. The third, $j_{soh} = \pm\frac{1}{2}$ state builds the split off band which is much lower in energy due to the spin-orbit interaction.

Photons have very little momentum which allows only vertical transitions in k-space, but there are semiconductors where the conduction band minimum is shifted by a k-vektor relative to the valence band maximum (Fig. 1.8). Silicon and Germanium are examples for this type of semiconductors which are called indirect semiconductors. In this case transitions can only appear when the difference in momentum is compensated by a phonon. Since there is only a limited number of matching phonons available at a time, optical transitions in indirect semiconductors are unlikely and recombination times can be in the order of ms.

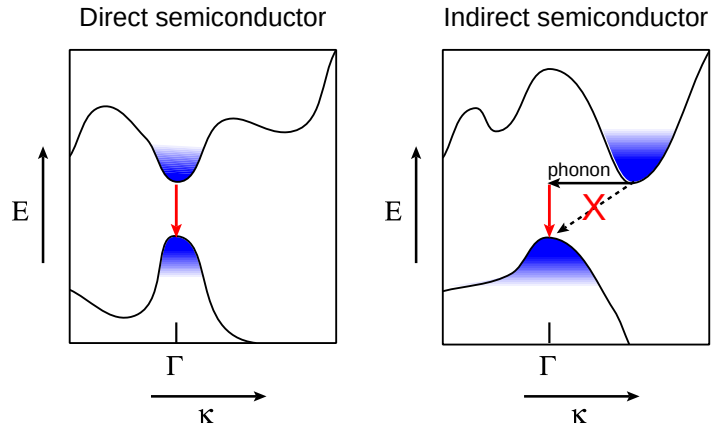

Fig. 1.8:
Band structure of direct and indirect semiconductors. Only transitions with $\Delta\kappa \approx 0$ are allowed. In indirect semiconductors a phonon with the right momentum is required to enable the transition.

The population density of VB and CB can be calculated from the density of states and the Fermi distribution of free electrons and holes. The density of states determines how many states exist in a given energy interval. Due to periodic boundary conditions there are only discrete states in the k-space.

A certain energy corresponds to a spherical shell with radius k and thickness dk containing a discrete number of allowed states. This number divided by the volume of the shell is the density of states which can be written as a function of energy:

$$D(E) = \frac{\sqrt{2m^3}}{\pi^2\hbar^3}\sqrt{E} \tag{1.1}$$

However not all states are occupied by carriers. The distribution of electrons and holes at a certain temperature is given by the Fermi distribution:

$$f(E) = \frac{1}{e^{\frac{(E-E_F)}{kT}} + 1} \tag{1.2}$$

The probability to find an electron with certain energy has to be multiplied with the density of states to derive the population density.

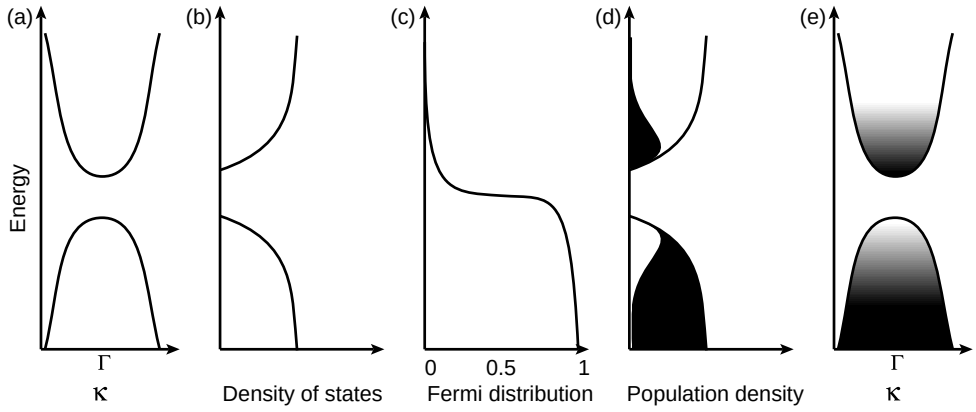

Fig. 1.9: *(a) Band structure of a direct semiconductor. (b) Density of states as a function of energy. (c) Fermi distribution: Probability to find electrons with certain energy. (d) Population density as a function of energy. (e) Band structure with population of energy states.*

Assuming that $E - E_F \gg 1$ and $E_F = \frac{1}{2}E_{gap}$ the electron population of the conduction band can be expressed as:

$$N(E) = \frac{8\sqrt{2}\pi m^{\frac{3}{2}}}{h^3} \cdot \sqrt{E - E_{gap}} \cdot exp\left(-\frac{E_{gap}}{2kT}\right) \tag{1.3}$$

Fig. 1.9 shows a schema of the band structure, the appropriate density of states together with the Fermi distribution and population density. Free electrons settle in the conduction band minimum, free holes in the valence band maximum.

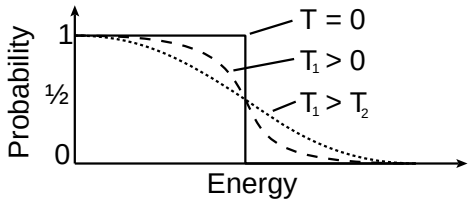

Fig. 1.10:
Fermi distribution for different temperatures. At T = 0 (solid line) the Fermi function is a step function. With rising temperature (dashed and dotted line) the Fermi edge is smeared out.

The Fermi distribution and consequently the population density strongly depend on the temperature (Fig. 1.10). At low temperatures the Fermi edge is quite sharp so that the density of the electron gas in the conduction band is rather low.

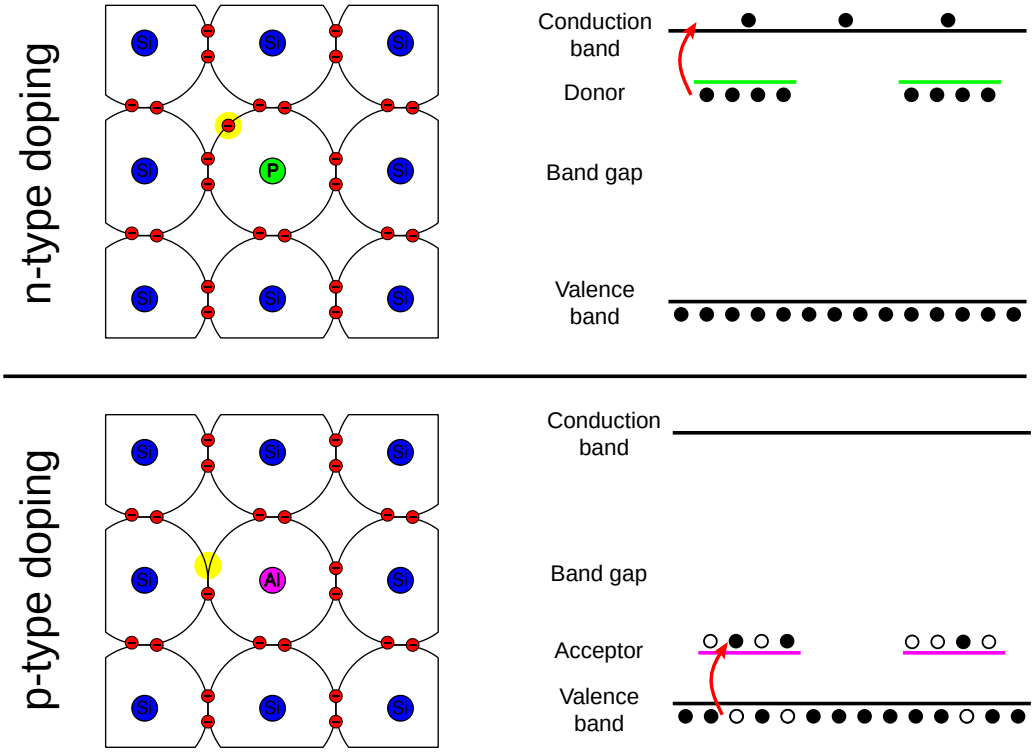

Fig. 1.11: *In n-type doped semiconductors some atoms are replaced by atoms with one more valence electron. The binding energy of this electron is close to the conduction band edge. In p-type doped semiconductors the replacement atom has one valence electron less. The gap can be filled by electrons from the valence band.*

It is possible to increase the electron or hole density by doping the semiconductor. In an undoped semiconductor neighbor atoms share their electrons in a way that the outer shell is completely filled.

To increase the electron density a small fraction of atoms in a semiconductor is replaced by atoms from the right neighbor column of the periodic system which has one more valence electron (donors). This electron is therefore only very weekly bound to the lattice and can easily contribute to the population of the conduction band, see Fig. 1.11. The term "n-type doping" describes this process. Replacing atoms with those of the left neighbor column (acceptors) will induce holes due to the

missing valence electron. This process is referred to as "p-type doping". Electrons can leave the VB and fill in these acceptor gaps by overcoming an energy gap which is much smaller than the band gap.

1.3.2 Quantum wells

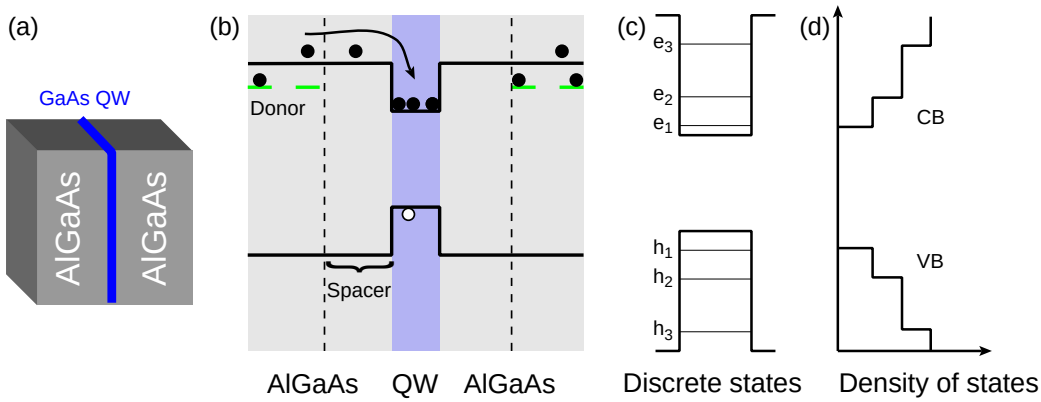

Fig. 1.12: *(a) GaAs quantum well in an AlGaAs semiconductor. (b) Electrons are trapped in the CB minimum of the QW and form a 2DEG. Donor atoms are spatially separated to improve the mobility of the 2DEG. (c) Confinement of the electrons leads to discrete energy levels. (d) Density of states for a QW.*

Quantum wells (QWs) are quasi two dimensional nanostructures. A quantum well is a thin film with a thickness of around 5-50 nm of one material system embedded in thick layers of another material. Usually a material is used for the QW which has a smaller band gap than the enclosing system. A typical example is a GaAs layer in a AlGaAs semiconductor (Fig. 1.12 (a)). The smaller band gap of GaAs represents an artificial conduction band minimum which confines the electrons in the QW. In a doped quantum well a two dimensional electron gas (2DEG) is formed. For many applications it is important that the electrons of the 2DEG have a high mobility. Impurity traps decrease the mobility so that it is more convenient to dope the bulk material and not the QW itself. Often a region around the quantum well, a spacer, is left undoped to increase the distance between impurities and the 2DEG (Fig. 1.12 (b)). Due to the electron confinement in a quantum well, which thickness is comparable to the de Broglie wavelength of electrons and holes, only discrete energy states are allowed (Fig. 1.12 (c)). To calculate the density of states the spherical shell used for the three dimensional system before has to be reduced to a ring with thickness dk in the k-space. The result for a L_x wide quantum well is a step function (Fig. 1.12 (d)):

$$D(E) = \frac{m}{\pi\hbar^2 L_x} \sum_l \Theta(E - E_l) \tag{1.4}$$

There are also samples grown with more that one QW. Multiple quantum wells (MQWs) have an increased efficiency as light detectors or emitters. It is necessary to differentiate between Type I and Type II MQWs. For Type II quantum wells the materials are chosen in a way that CB maximum and CB minimum are separated spatially. A comparison to indirect semiconductors seems obvious but it is important to keep in mind that in indirect semiconductors CB maximum and CB minimum are separated in momentum space whereas in Type II MQWs they are separated in real space.

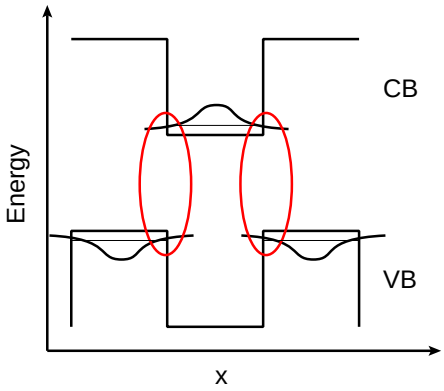

Fig 1.13: *Type II quantum well with spatially separate CB minimum and VB maximum. Transitions are only possible at the interface between both materials.*

Although there is no phonon required, the recombination time of the electron-hole-pair in Type II MQWs is larger than in Type I quantum wells. Recombinations can only appear at the interface between both materials where the overlap of the electron and hole wave function is small.

1.3.3 Quantum wires

Quantum wires are one dimensional quantum structures whose carriers are confined in two directions. However, it is very difficult to produce high quality quantum wires. One single defect or diameter fluctuations will trap the carriers and it becomes difficult to observe pure one-dimensional behaviour. A possible candidate are carbon nano tubes because they are self assembled. No measurements on quantum wires have been performed in the course of this thesis.

1.3.4 Quantum dots

Quantum dots are zero dimensional structures. There are different kinds of quantum dots like self-assembled, colloidal or etched quantum dots. Self assembled QDs are a congregation of some hundred thousand atoms of one semiconductor material embedded in a matrix of another. They are often shaped like a disc or pyramid with the size of a few nm in all directions — more details are given in the growth section. The QDs studied with ODR technique are all ensembles of self assembled QDs with a dot density of around $10^{10}\ cm^{-2}$ and a disc like shape (≈20x20x5 nm). The presents of carriers in the quantum dot depends on the doping of the buffer.

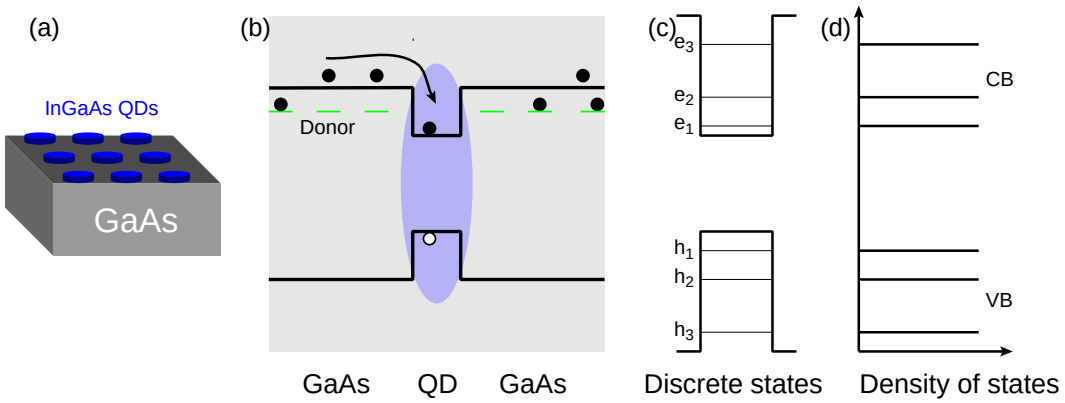

Fig. 1.14: *(a) InGaAs quantum dots on a GaAs substrate. (b) Electrons are confined in the CB minimum of the QD material (c) Confinement of the electrons leads to discrete energy levels. (d) Density of states for QDs.*

Electrons in QDs are confined in all directions so that they can not form a one or two dimensional electron gas like in quantum wires or quantum dots (Fig. 1.14 (b)). The density of states in a quantum dot is given by:

$$D(E) = \frac{2}{L_x L_y L_z} \sum_l \delta(E - E_l) \tag{1.5}$$

1.4 Growth of nanostructures

There are different technologies to grow semiconductor nanostructures. Liquid phase epitaxy (LPE) and vapor phase epitaxy (VPE) are used to grow semiconductor crystals. The growth rate is high but it is not possible to control the thickness of material depositions with monolayer precision. In order to grow sharp interfaces between two materials or to control the concentration of a dopant the molecular beam epitaxy (MBE) is used. This is important for the quality of the sample. A further advantage of this method is that the growth process occurs in ultra high vacuum (UHV) leading to a high purity of the deposit material.

An MBE system consists of a vacuum chamber and a sample holder that can be heated. A number of effusion cells containing the growth materials are placed around the sample. They can be heated to a temperature where the material starts to evaporate and forms a molecular beam pointing towards the sample. Shutters in front of the cells can start and stop the molecular beam immediately. The growth rate of this system is around one monolayer per second because the atoms at the surface need some time to arrange themselves in monolayers. The sample can be rotated to increase the uniformity of the sample. A schema of an MBE system is shown in Fig. 1.15.

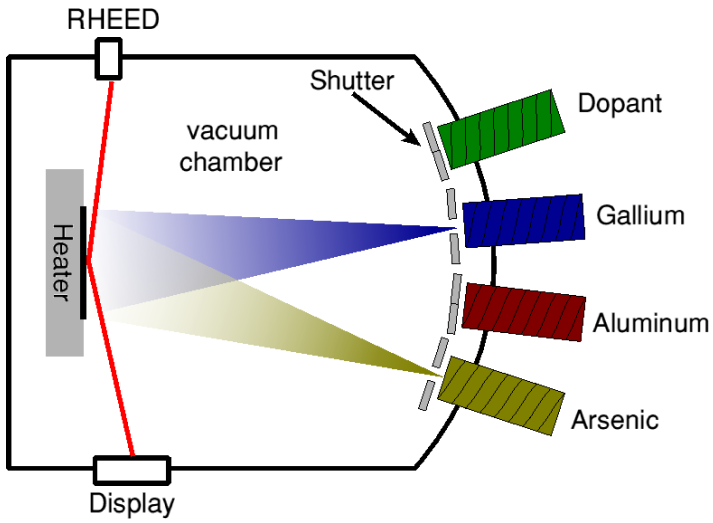

Fig. 1.15:
MBE system with heatable sample holder and effusion cells in a vacuum chamber. The molecular beam can be controlled by shutters to affect the material composition. RHEED allows the in situ control of the sample growth with monolayer resolution.

An electron beam is used to control the growth of the sample in situ with the so called RHEED (Reflection High Energy Electron Diffraction). The diffraction pattern of the sample surface is displayed on a phosphor screen for analysing the sample surface with monolayer resolution.

1.4.1 Quantum wells

As mentioned before a quantum well is a thin film of one material embedded in another material. It is important that the lattice constant of both materials matches to avoid strain in the quantum well. For the quality of the quantum well and the 2DEG mobility it is important to have a constant thickness of the QW film. This becomes more important for thin QW consisting of a few monolayers only where interfaces fluctuations change the QW width significantly. Fluctuations of the well width lead to a localization of electrons which increase the carrier scattering in the QW. The quality of a sample is reflected in the full width at half maximum (FWHM) of the photoluminescence signal which is small for high quality samples.

1.4.2 Self assembled quantum dots

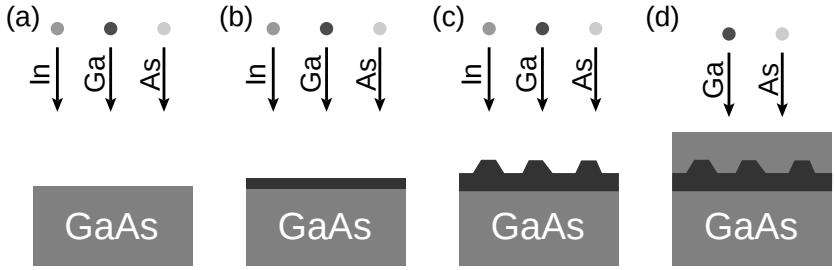

Fig. 1.16: *Growth process of InGaAs/GaAs quantum dots. (a) Deposition of InGaAs on a GaAs substrate. (b) Thin film of InGaAs on the GaAs substrate with a mismatch of the lattice constant leading to strain in the film. (c) If critical film thickness is reached, islands are formed as strain relieving process. (d) Capping of islands to create quantum dots.*

MBE systems can also be used to grow self assembled quantum dots. Using the Stranski-Krastanov growth method [Str39, Eag90] the first step is comparable to the growth process of quantum wells in the sense that a thin film of e.g. InGaAs is grown on top of a substrate, e.g. GaAs. For the formation of quantum dots there has to be a mismatch of the lattice constants of both materials in the order of a few percent. Due to this mismatch strain is introduced into the film and with it some additional energy. If some monolayers of the film are grown, the strain energy, interfacial energy and surface energy of the film can be minimised by the formation of islands as shown in Fig. 1.16. So the change of the surface morphology is caused by interplay between strain and surface energy which depend on various properties like substrate temperature and composition of the film. However, even for a strong mismatch of the lattice constant there always remains a small 2D film between sub-

strate and the islands which later form the QDs. This film is called the wetting layer and may play a role when it comes to optical properties of quantum dots. To complete the growth of the QDs they have to be capped with a material with a higher band gap.

Due to this capping process, the composition, shape and dimension of the quantum dots changes in a way that is not completely understood, yet. Another disadvantage of self assembled QDs is the size distribution among the dots which is in the order of 10% and the random distribution on the surface. The later has been tried to change by a pre patterned substrate surface. Steps in the surface influence the appearance of strain and control the spatial distribution of the dots which also leads to akin growth conditions and hence a smaller size distribution.

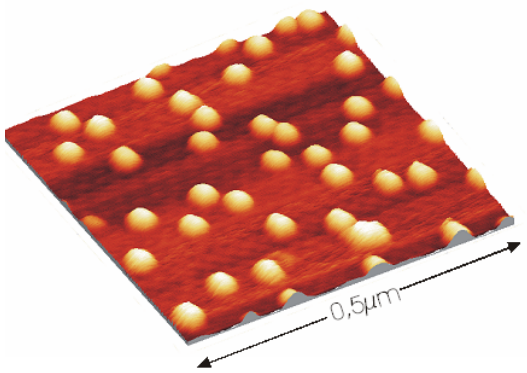

Fig. 1.17: *AFM-picture of an ensemble of self organized InGaAs/GaAs quantum dots.*[6]

1.5 Optical properties

Transitions between electronic levels in a semiconductor often involve the absorption or emission of photons. Therefore optical methods allow to study the internal properties of a semiconductor. All experiments described in this thesis are based on the photoluminescence of the samples. So it is important to take a look on the conditions under which optical transitions can occur.

To calculate the transition probability Γ_{if} of an electron from the initial state *i* to the final state *f*, Fermi's golden rule is used:

$$\Gamma_{if} = \frac{2\pi}{\hbar}\rho(\omega)\left|\langle f\left|\mathcal{H}'\right|i\rangle\right|^2 \tag{1.6}$$

where $\rho(\omega)$ is the density of final states and $\mathcal{H}'$ is the perturbation of the Hamiltonian for the electron in a potential $V(r)$:

$$\mathcal{H} = \frac{1}{2m^*}\left(\vec{p} + q\vec{A}(\vec{r})\right)^2 + V(r) + \mathcal{H}' \tag{1.7}$$

The perturbation is defined by the energy given by the product of the electric dipole operator $\vec{d}$ and the electric vacuum field $\vec{\varepsilon}(\vec{r})$:

$$\mathcal{H}' = \vec{d} \cdot \vec{\varepsilon}(\vec{r}) \tag{1.8}$$

These spontaneous emissions can be explained by fluctuations of the vacuum field caused by the appearance and disappearance of virtual photons which are allowed by Heisenbergs uncertainty principle when the following condition is satisfied:

$$\Delta t \Delta E \geqslant \frac{\hbar}{2} \tag{1.9}$$

So spontanious emissions can be explained as induced transitions triggered by virtual photons appearing randomly in time and space. Equation 1.9 also determines the width of the emission line which depends on the recombination time. In this case the width of the line is called natural line width. Fast recombination processes lead to lines which cover a broad energy interval.

Photons are bosons and therefore have an integer spin. If a photon is created the total angular momentum of the system has to be conserved. This means that transitions are only allowed if the angular momentum of initial and final state differs by 0 (linearly polarized photon) or ±1 (circularly polarized photon).

1.5.1 Exciton and trions

Due to the Coulomb interaction between electron and hole in a semiconductor the electron in the conduction band is not always a free particle. It can be bound to a hole and form a quasi-particle, which is called exciton. It is often compared to the hydrogen atom with a smaller binding energy of only a few meV and an orbit of up to 10 nm. In semiconductors with low electron density most electrons are bound to holes. Due to the high exciton population band-to-band transition between a free electron and hole can usually not be observed in PL spectra of cold samples. If two electrons are bound to one hole, or one electron is bound to two holes this complex is called trion (T). To distinguish between differently charged complexes the terms negatively (T^-) or positively (T^+) charged trion are introduced.

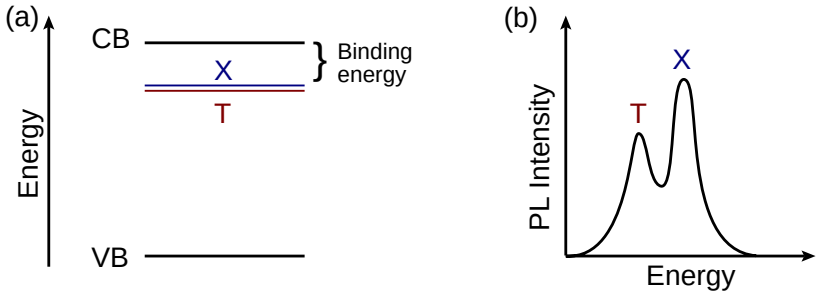

Fig. 1.18: *(a) Energy of the exciton (X) and trion (T) in a semiconductor. (b) Photoluminescence spectrum of an exciton and trion.*

The binding energy of the trion is usually 10%-20% of the exciton binding energy and is typically in the order of a few meV [Ast02]. In the photoluminescence a second peak arises at lower energy next to the exciton peak which belongs to the singlet trion state (Fig. 1.18 (b)). In order to analyse the peaks found in PL spectra it helps to draw the energy and spin structure of excitons and trions. See section 1.6.5 for details.

1.6 Effects of the magnetic field

1.6.1 Diamagnetic shift

If an external magnetic field *B* is applied to any material a diamagnetic effect can be observed. The magnetic field influences the motion of bound electrons and holes by the Lorenz force. Quantum mechanically this can be described as perturbation of the electron ground state which has an S-like envelope function. The admixture of the $n = 1,\ l = 0$ ground state with higher states $(l \neq 0)$ leads to an effective angular momentum which is proportional, but due to Lenz rule antiparallel to *B*. Since the energy of a magnetic dipole rises linearly with *B*, the diamagnetic shift can be expressed by:

$$\Delta E_{dia} = \alpha B^2 \tag{1.10}$$

where α is a material specific constant [Kli95]. The diamagnetic shift of a semiconductor can be observed in the photoluminescence which is shifted to higher energies with increasing magnetic field (see e.g. Fig. 3.14. for the shift of the exciton position).

1.6.2 Landau levels

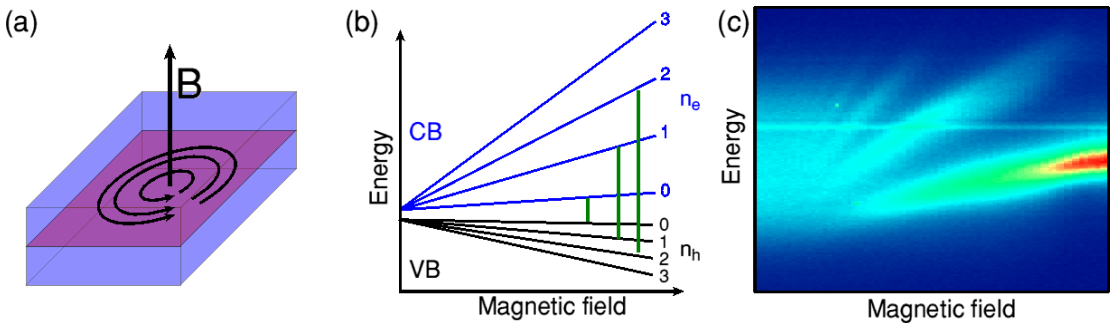

Fig. 1.19: *(a) Electron cyclotron motion in a magnetic field applied perpendicular to a 2DEG. (b) Electron and hole Landau levels, allowed transitions are marked in green. (c) Optical transitions between electron and hole Landau levels in the photoluminescence of a n-type GaAs/AlGaAs QW.*

If a magnetic field is applied perpendicular to the plane of a 2DEG, due to the Lorenz force the trajectories of free particles become circles around the lines of field (Fig. 1.19). For the emergence of Landau levels (LL) it is important that the electrons complete the cyclotron motion. Therefore following conditions need to be fulfilled:

The mean free path of the electrons needs to be large in order to be able to complete the cyclotron motion before they are scattered. Therefore high quality samples at low temperatures are required. Since the cyclotron radius decreases with the magnetic field but the scattering time is constant, complete cyclotron motion becomes more likely at high magnetic fields. The cyclotron frequency of the electrons is given by:

$$\omega_c = \frac{e\,B}{m^*} \tag{1.11}$$

which determines the quantization of the cyclotron radius:

$$r_c = \frac{m^* v}{e\,B} = \frac{v}{\omega_c} \tag{1.12}$$

Hence the cyclotron energy is:

$$E_n = \left(n + \frac{1}{2}\right) \hbar\omega_c \tag{1.13}$$

At low magnetic fields the electrons are bound to the holes and can not be handled as free carriers. This changes when the cyclotron energy rises with the magnetic field and eventually exceeds the exciton binding energy. Due to this increase of kinetic energy the importance of the exciton binding energy decreases and the nature of the electrons become comparable to free particles. The magnetic field can therefore not be handled as perturbation of a bound electron anymore like in the previous subsection. The energy shift of the photoluminescence is now determined by the first Landau level (Eq. 1.13 with $n = 0$). In highly doped QWs or at high excitation powers more that one LL may become visible in the photoluminescence (Fig. 1.19 (c)). Transitions between electron and hole LL are only allowed for $\Delta n = 0$.

The population of the Landau levels is described by the filling factor ν:

$$\nu = \frac{n_e}{e\,B/h} \tag{1.14}$$

It indicates the number of Landau levels filled with electrons. Occupancy of the first LL corresponds to filling factor 2. Filling factor 1 corresponds to a half filled Landau level. Each LL consists of two spin subbands which split in magnetic field.

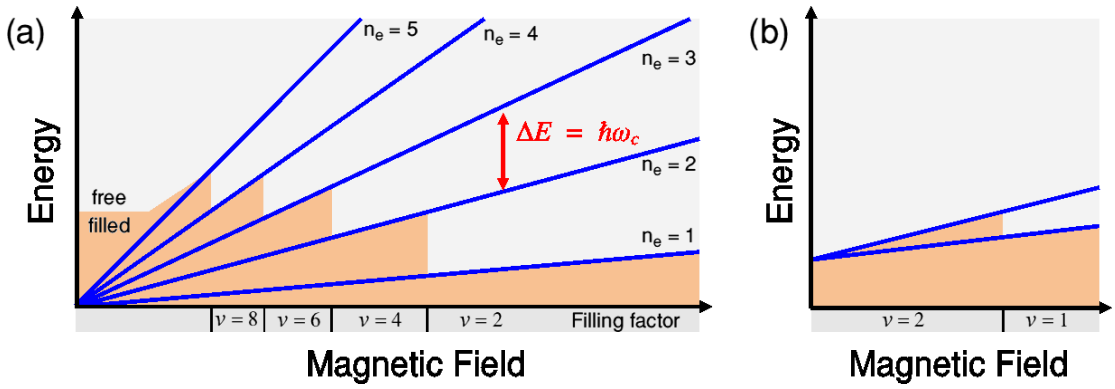

Fig. 1.20: *Population of Landau Level. (a) All LL below certain energy are filled. The filling factor indicates how many Landau levels are filled. It is shown here up o the fifth LL. (b) Odd filling factors can only be observed at high magnetic fields.*

So $\nu = 1$ corresponds to occupation of the lowest spin subband. A completely filled spin subband can only be reached at $T = 0$.

At final temperatures the existence of only one oppositely polarized electron means that the second subband starts to fill and the filling factor needs to be increased to $\nu = 2$. Therefore odd filling factors indicate maximum spin polarization, whereas even filling factors have an almost balanced number of oppositely polarized spins. Since the number of electrons that can occupy one LL rises with magnetic field but the total number of electrons is fixed, the filling factor decreases with B (Fig. 1.20 (a)). The filling factor decreases in steps of two because at finite temperatures one LL usually contains spins of both polarizations even if its total population is low. Only at high magnetic fields, when the splitting of the LL subbands is strong due to the Zeeman effect (See subsection 2.5.4), odd filling factors can be observed (Fig. 1.20 (b)).

1.6.3 Cyclotron resonance

The energy distance between two neighbor Landau levels is the cyclotron energy $\Delta E = \hbar\omega_c$ which is typically in the order of a few meV:

$$\hbar\omega_c\,[meV] = 0.116\,\frac{m_0}{m^*}\cdot B \qquad (1.15)$$

In ODCR measurements microwave or far infrared radiation is applied to induce transitions between Landau levels. The redistribution in the landau level population is reflected in the photoluminescence spectrum in the form of an intensity change. The amount of change depends on the magnetic field and shows a maximum at B_{res} where the LL splitting coincides with the MW or FIR energy E_{rad}. An example is shown in Fig. 3.2.

From the resonance position, the effective mass of carriers can be calculated as fraction of the free electron mass using Eq. 1.11 and 1.13 :

$$m^* = \frac{\hbar\, e\, B_{res}}{E_{rad}} \qquad (1.16\,a)$$

$$m^* = 0.116\, \frac{B_{res}\,[T]}{E_{rad}\,[meV]}\, m_0 \qquad (1.16\,b)$$

The full width at half maximum (FWHM) of the resonance indicates the mobility of carriers. High quality samples show a narrow resonance.

1.6.4 Zeeman splitting

The spin splitting of energy states in a magnetic field is called Zeeman splitting. The difference in energy is caused by the spin of the electrons. They can be orientated parallel or anti-parallel to the external magnetic field B_{ex}. Electrons with a spin parallel to B_{ex} are lower in energy than electrons with antiparallel spin. The energy shift at B_{ex} can be calculated by:

$$\Delta E = s\, g_e\, \mu_B\, B_{ex} \qquad (1.17)$$

Where s is the spin, g_e is the g-factor and μ_B is the Bohr magneton. The splitting of the two states of one electron level is therefore:

$$\Delta E_Z = g_e\, \mu_B\, B_{ex} \qquad (2.18\,a)$$

$$\Delta E_Z\,[meV] = 0.058\, g_e\, B_{ex} \qquad (2.18\,b)$$

The absolute value of the g-factor determines how strong the splitting is in the magnetic field, its sign defines which spin state is lower in energy. Classically a value of 1 would be expected. Quantum mechanical calculations show that the g-factor of free electrons in vacuum is 2. Similar calculations can be applied to the hole which also has a g-factor smaller than that of an electron. In a semiconductor the g-factor can be derived experimentally by photoluminescence measurements. In polarization resolved measurements the exciton g_x-factor, which is contributed by electron and hole g-factors, can be determined at high magnetic fields from the energy splitting of the exciton peaks in the photoluminescence. In semiconductors with magnetic ions the g-factor and hence the Zeeman splitting can be enhanced by two orders of magnitude. More details about magnetic semiconductors can be found in section 5.1.

1.6.5 Energy and spin structure of excitons and trions

In this sub-section an example is given for the exciton and trion energy spin structure, which is dependent on the value and sign of the electron and hole g-factors. For this example $g_e > 0$ is chosen. In a magnetic field this leads to a spitting of the electron states where the spin down state $(\downarrow)$ is lower in energy, as shown in Fig. 1.21. The given example was drawn for $g_h > 0$ so that also in case of the hole the spin down state $(\Downarrow)$ is lower in energy. In Fig. 1.21 the hole spins are represented by bold arrows. It is also assumed that $|g_e| < |g_h|$ and $|2g_e| > |g_h|$. These values have been chosen arbitrary for this example. Other configurations are possible and depend on material parameters. Different values will change the order of energy and spin levels, see the Appendix for more details (this examples corresponds to case A.2.a of the scheme presented in the appendix).

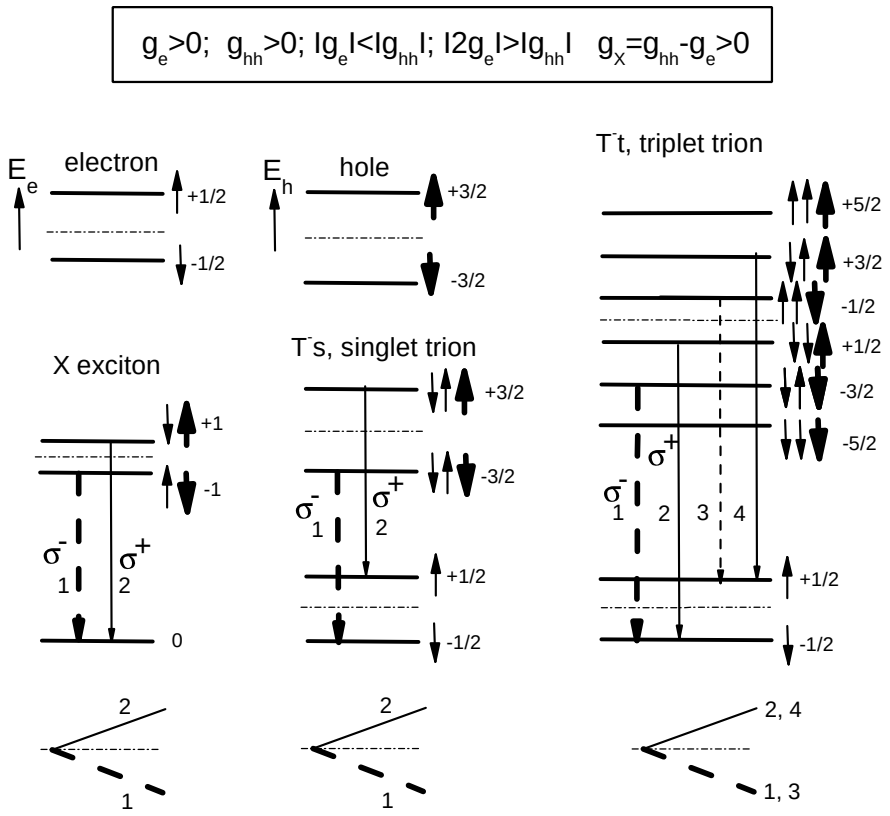

Fig. 1.21: Spin and energy scheme for electron, hole, exciton and trion states. See text for a detailed description.

Exciton and hole g-factors contribure to the exciton g-fator: $g_x = g_h - g_e$, leading to $g_x > 0$ in this case. The exciton states can be calculated in the following way:

$$\Delta E_x(\uparrow\Downarrow) = \frac{1}{2}\left(\frac{1}{2}g_e \cdot \mu_B \cdot B\right) + \frac{1}{2}\left(-\frac{3}{2}g_h \cdot \mu_B \cdot B\right) < 0 \qquad (1.19)$$

or short:

$$\Delta E_x(\uparrow\Downarrow) = \frac{1}{2}(\Delta E_e - \Delta E_h) < 0 \qquad (1.20)$$

and for $(\downarrow\Uparrow)$:

$$\Delta E_x(\downarrow\Uparrow) = \frac{1}{2}(-\Delta E_e + \Delta E_h) > 0 \qquad (1.21)$$

This means that the $(\uparrow\Downarrow)$ exciton state is lower in energy than the $(\downarrow\Uparrow)$ state, as shown in Fig. 1.21. The $(\uparrow\Downarrow)$ exciton has an electron spin of $s_e = +\frac{1}{2}$ and a hole spin of $s_h = -\frac{3}{2}$. When the exciton recombines, circularly polarized light is emitted. The polarization of the light can be determined from the spin difference: $+\frac{1}{2} - \frac{3}{2} = -1$, which corresponds to σ^--polarization (transition 1 in Fig. 1.21). Upon recombination the $(\downarrow\Uparrow)$ exciton emits σ^+-polarized light: $-\frac{1}{2} + \frac{3}{2} = +1$ (transition 2 in Fig. 1.21). In the photoluminescence spectrum with $B > 0$ the σ^--polarized line is expected lower in energy than the σ^+-polarized one, because it corresponds to the $(\uparrow\Downarrow)$ exciton state. Because this is the stronger populated ground state, also a higher peak intensity can be expected as compared to the σ^+-polarized line. This is also shown by the small diagram below the exciton energy and spin scheme in Fig. 1.21.

In this figure also the schemes for the singlet and triplet states of the negatively charged trion are shown. The singlet trion has an antisymmetric electron spin wavefunction, so the total spin of both electrons is $S = 0$. The $(\downarrow\uparrow\Uparrow)$ illustration of the singlet trion in Fig. 1.21 corresponds to the spin eigenstate $(\uparrow\downarrow - \downarrow\uparrow)$. The Zeeman splitting of the singlet trion state is identical to the splitting of the holes because the spin of the electrons is oriented oppositely and does therefore not contribute the the splitting:

$$\Delta E_t(\downarrow\uparrow\Uparrow) = \Delta E_h(\Uparrow) \qquad (1.22)$$

$$\Delta E_t(\downarrow\uparrow\Downarrow) = \Delta E_h(\Downarrow) \qquad (1.23)$$

When the hole recombines with the oppositely spin orientated electron, the second electron is left. To derive the polarization of the emitted light, the spins of the recombining electron and hole have to be taken into account. In case of the $(\downarrow\uparrow\Downarrow)$ trion, the $(\uparrow)$ electron recombines with the $(\Downarrow)$ hole, corresponding to $s_e = +\frac{1}{2}$ and $s_h = -\frac{3}{2}$. Therefore the emitted photon is σ^--polarized: $+\frac{1}{2} - \frac{3}{2} = -1$. The $(\downarrow)$ electron with spin $s_e = -\frac{1}{2}$ is left.

The triplet trion has a symmetric electron spin wavefunction, and the $(\downarrow\uparrow\Uparrow)$ illustration of the triplet trion in Fig. 1.21 corresponds to the spin eigenstate

$(\uparrow\downarrow + \downarrow\uparrow)$. It is called triplet state because there are three possible spin configurations with a total electron spin of $S = 1$ and a spin z-component of $S_z = -1,\ 0,\ +1$. Possible singlet and triplet states are summarized in Table 1.1.

	Spin wavefunction	S	S_z
Singlet	$\frac{1}{\sqrt{2}}(\uparrow\downarrow - \downarrow\uparrow)$	0	0
Triplet	$\uparrow\uparrow$	1	1
	$\frac{1}{\sqrt{2}}(\uparrow\downarrow + \downarrow\uparrow)$	1	0
	$\downarrow\downarrow$	1	-1

Table 1.1: *Electron spin configuration of singlet and triplet trions*

Here the electron spins can also be orientated parallel to each other as shown in Fig. 1.21. The Pauli exclusion principle states that the wavefunction of fermions must be antisymmetric. If the spin function is symmetric, this means that the spatial wavefunction must be antisymmetric. Therefore only one electron can occupy the lowest S_1 shell and the second electron occupies the higher S_2 shell. Also in case of the $(\downarrow\uparrow\Downarrow)$ configuration of the triplet trion, one of the electrons is situated on the S_2 shell, so its spatial wavefunction is antisymmetric. In this sense it differs from the singlet trion, which has an antisymmetric spin function, but a symmetric spatial wavefunction. Because of the second electron occupying a higher shell with a larger distance to the hole, a lower binding energy for the triplet trion can be expected as compared to the singlet one.

1.6.6 Fock-Darwin spectrum

Quantum dots are often formed like a disc with two almost identical extensions in x,y direction and only a limited thickness in z-direction. The rotational invariant potential of such a QD for a two dimensional harmonical oscillator is given by:

$$V(r) = \frac{1}{2} m \omega_0^2 r^2 \tag{1.24}$$

The Hamiltonian for a symmetric two dimensional potential can be written in the following way:

$$\mathcal{H} = \frac{p^2}{2m^*} + \frac{m^* \omega_0^2}{2}(x^2 + y^2) \tag{1.25}$$

leading to energy eigen-values of:

$$E = \hbar\omega_0 (n + 1) \tag{1.26 a}$$

$$= \hbar\omega_0 \left(n_1 + \frac{1}{2}\right) + \hbar\omega_0 \left(n_2 + \frac{1}{2}\right) \tag{1.26 b}$$

In the presents of a magnetic field it is necessary to modify the Hamiltonian with:

$$\vec{p} \rightarrow \vec{p} - \frac{q}{c}\vec{A} \tag{1.27}$$

where the vector potential $\vec{A}$ is defined as:

$$A = \frac{B_0}{2} \begin{pmatrix} y \\ -x \\ 0 \end{pmatrix} \tag{1.28}$$

The so called Fock-Darwin energy niveaus can be derived analytically:

$$E = \hbar\sqrt{\omega^2 + \frac{1}{4}\omega_c^2}\left(2n_r + |n_\varphi| + 1\right) + \frac{1}{2}\hbar\omega_c n_\varphi \tag{1.29}$$

with the cyclotron frequency ω_c:

$$\omega_c = \frac{eB}{m} \tag{1.30}$$

In Eq. 1.29 n_1 and n_2 have been transformed to n_φ and n_r:

$$n_r = \frac{1}{2}\left(n_2 + n_1 - |n_2 - n_1|\right) \tag{1.31}$$

$$n_\varphi = n_2 - n_1 \tag{1.32}$$

A plot of the Fock-Darwin spectrum can be found in Section 4.1 (Fig. 4.9).[Dar30]

Chapter 2:

Experiment and technique

2.1 Experimental setup

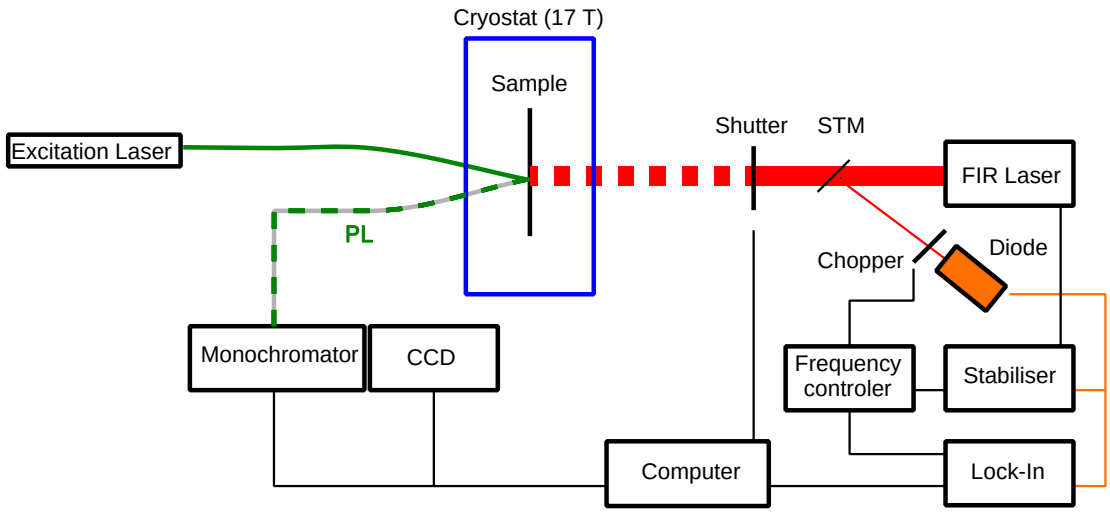

Fig. 2.1: *Schema of the experimental setup for ODR measurements. Sample is held inside a cryostat and illuminated by an excitation laser. The photoluminescence spectrum is recorded by a CCD connected to a monochromator. Additionally, far infrared radiation can be applied to the sample. STM: Semi transparent mirror.*

Central element of the experimental setup is the solenoid cryostat where the sample is held at a liquid helium temperature. Magnetic fields of up to 17 T can be applied. A variety of lasers in the visible and near infrared range are used to excite the sample. The laser light is guided to the sample by an optical fiber. A second fiber is used to collect the photoluminescence from the sample and transfer it to the entrance slit of the monochromator. A CCD records the photoluminescence spectra.

Additionally the sample can be illuminated by far infrared light which is guided into the cryostat by a wave guide. All main elements of the setup are controlled by a PC running LabView software.

2.1.1 Cryostat and inserts

The solenoid stainless steal cryostat from Cryogenic is used to keep the sample at cold temperatures and to apply magnetic fields. This cryostat is able to reach constant magnetic fields of 15 T at 4.2 K. This range can be extended to 17 T if the He surrounding the coils is cooled down to 2.2 K by pumping. There are no windows which would allow direct access to the sample. Instead optical fibers are used for excitation and detection. There are different inserts available intended for specific types of experiments.

For most results presented here the FIR insert was used. This insert offers a stainless steel oversized waveguide for the far infrared radiation which is focused onto the sample by a Teflon lens. The insert is usually filled with one atmosphere of gasoline He to enable thermal contact of the sample with the liquid He bath outside the insert. A resistor mounted close to the sample can be used as a heater in order to rise the temperature by up to 20 K.

For temperature dependent measurements a Variable Temperature Insert (VTI) can be used. It allows measurements in the range from 1.6 K to 400 K. Due to the small diameter of the insert it is not possible to install a FIR waveguide so that only PL measurements can be performed with the VTI.

The same is true for the He^3 insert. It is connected to an external reservoir of He^3 which allows lower temperatures when pumped than He^4. Temperatures as low as 0.25 K can be reached by this system. An extension for this insert allows microwave radiation to be applied to the sample through a cable which is much smaller in diameter than the FIR waveguide, enabling ODR measurements at very low temperatures.

All fibers used in the inserts destroy the polarization of the light. To obtain polarization resolved measurements, small pieces of linear and circular polarisers are mounted between the end of the fiber and the sample. The alignment of the polarisers can not be changed from outside. In order to change from the detection of σ^+ to σ^- polarization the direction of the magnetic field can be reversed. This is supported by the power supply so that no cables need to be exchanged manually.

2.1.2 Lasers

For excitation of the sample lasers in the optical and near infrared regime have been used. Typical excitation powers are in the order of 1 mW. Shown in Table 2.1 are

lasers which have been used to study the optical properties of quantum dots and quantum wells.

Laser type	Wavelength (nm)	Energy (eV)	Max. Power (mW)
Semiconductor	372	3.33	16
Semiconductor	405	3.06	50
Semiconductor	532	2.33	50
HeNe	632.8	1.97	7
Semiconductor	638	1.94	25
Semiconductor	660	1.88	60
Semiconductor	785	1.58	40
Titan-Saphire	780-885	1.40-1.59	500

Table 2.1: *Wavelength, energy and power of excitation lasers used in the experiments.*

2.1.3 Far infrared laser

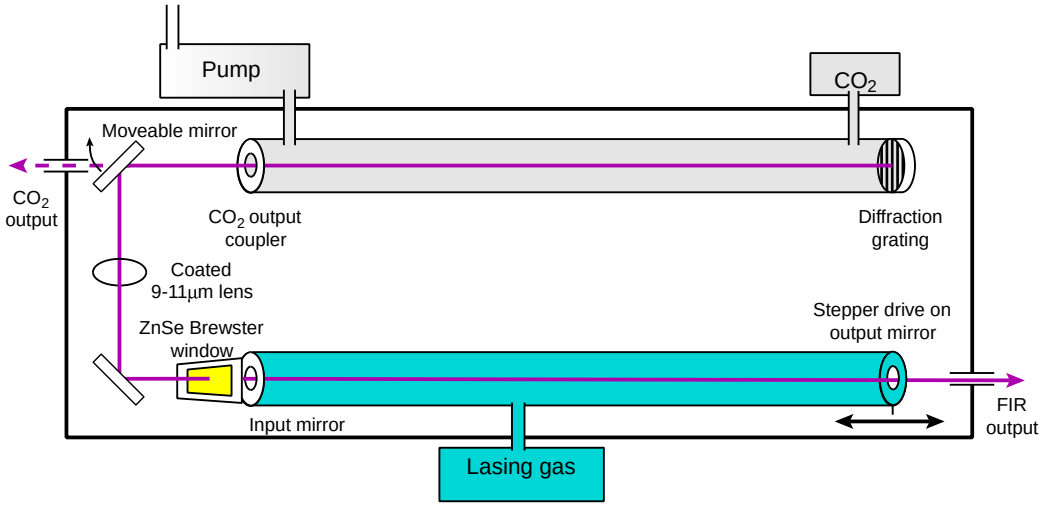

Fig. 2.2: *The FIR-Laser consists of a CO_2 cavity and a FIR cavity. The CO_2 part needs a constant flow of a special gas mixture and serves as pumping laser for the FIR part. The FIR cavity is filled with a lasing gas, converting the infrared radiation of the CO_2 laser into far infrared light.*

For the generation of far infrared radiation a combined CO2 and FIR laser is used. The “FIR L 100” from Edinburgh Instruments consists of two water cooled cavities

combined in one device (Fig. 2.2). The CO2 part of the laser generates IR light around 10 μm with a CW power of up to 100 W. The first cavity is filled with a gas mixture of 7% CO2, 18% N and 75% He. A constant gas flow through the cavity at a certain pressure is needed for operation. Two mirrors guide the IR light into the second cavity which is filled with a special lasing gas converting the IR light of the CO2 laser into far infrared radiation. Depending on the lasing gas used, there are many output laser lines in the range from 40 to 740 μm (Fig. 2.3).

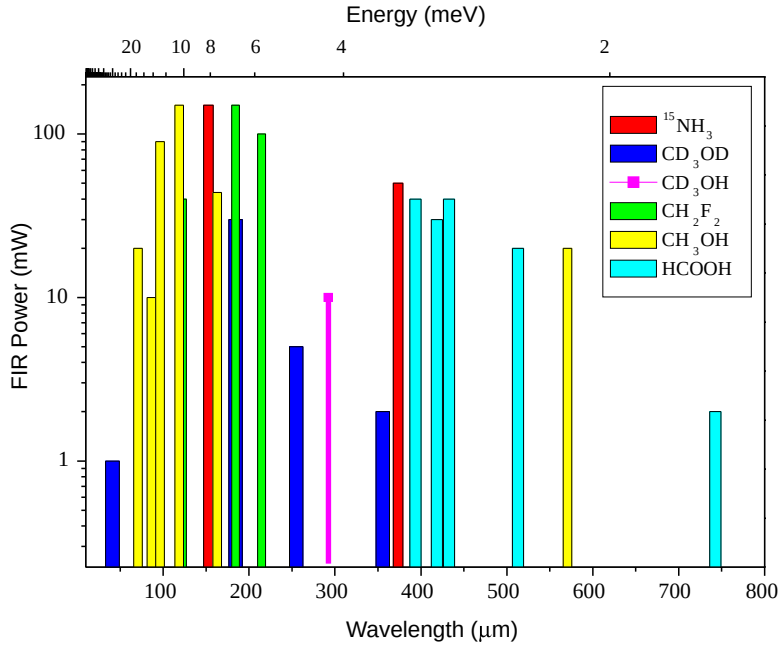

Fig. 2.3: *Available FIR laser lines and their output powers for the FIR L 100 laser system.*

However, only a small fraction of these laser lines can be used to drive the experiment since high output powers are required. For our experiments only ethanol (CH_3OH) was used as lasing gas because it offers lines with high output powers (Table 2.2).

Wavelength / μm	Energy / meV	Frequency / THz	Max.Output power / mW
163	7.6	1.84	60
118	10.5	2.54	200
96.5	12.8	3.11	90

Table 2.2: *Wavelength, energy, frequency and power of FIR laser lines used in the experiments.*

Radiation in the range of 100 μm or a few THz with suitable output powers is not easy to generate and there are not many light sources available in this range. In future, quantum cascade lasers are a candidate for THz generation when they become

commercially available. Also the handling of the radiation falls in-between light in the visible and infrared range, which freely propagate in air, and microwaves which require waveguides. In the experiment most of the pathway from the output coupler of the laser to the sample is equipped with oversized waveguides to minimise losses. The FIR light is focused onto the sample with a Teflon lens, a material which is 80% transparent for light in this range.

Due to long measurement series which usually last several hours, a stable FIR source is of high importance. Unfortunately the laser is sensitive for changes in the ambient temperature and humidity conditions and will not stay stable for more than 30 minutes without additional stabilization. This is provided by the ALS 1 Laser Stabiliser supplied with the system. It works by adjusting the cavity length of the CO2 part of the laser. A small fraction of the FIR laser light is coupled out by a semi-transparent mirror and its intensity is measured by a diode. Changes of the intensity are registered by an inbuilt Lock-In-Amplifier synchronised with the frequency of a chopper in front of the diode. A reference FIR intensity has to be set which will then be stabilised by the system. This reference intensity has to be chosen not on top of the peak but on the shoulder. A small detuning of the CO2 or FIR laser will lead to a change in intensity whereas the sign of the intensity change determines the direction for the correction issued by the stabiliser. Only the CO2 part of the laser can be automatically stabilised. The FIR cavity can only be controlled manually but still a stable system can be archived for several hours. A feedback of the laser intensity, measured by a separate Lock-in amplifier, to the software controlling the devices in the lab ensures that measurements are made under comparable conditions.

2.1.4 Monochromator and CCD

To resolve the photoluminescence spectrum a 0.3m Monochromator (Acton 300i) is used. Two gratings with 600 g/mm, blazed for 500 and 1000 nm offer enough resolution for most purposes. A high resolution grating with 1800g/mm, blazed for 500 nm, was also used in the experiments when necessary.

The light intensity over a certain spectral range is detected simultaneously by a liquid nitrogen cooled charge coupled device (CCD). This device is known from modern digital photo cameras that also make use of CCDs to record digital images. The device consists of a semiconductor (usually silicon) which is covered by a transparent insulator layer whose band gap does not differ too much from the semiconductor. On top of the insulating material, gates are grown by photolitography. By applying a voltage to the silicon layer a potential minimum is generated between semiconductor and insulator layer. Incoming photons generate electron-hole pairs. These electrons or holes are collected in the potential minimum forming a charge that is proportional to the incoming light intensity. Due to variation of the applied voltage the charge can be transferred to the gates on top of the insulating layer and read out. The CCD used in the setup consists of a matrix of 1340 x 400 light sensi-

tive pixels. In conjunction with the monochromator each of the 1340 row pixels represents another wavelength. It is possible to record 2 dimensional images but usually the 400 column pixels are summed up to increase the signal to noise ratio of the recorded spectrum. To increase the light sensitivity the size of each pixel is large (20μm x 20μm) in comparison to CCDs used in digital cameras.

2.2 LabView software

Typical ODR experiments consist of a series of very similar measurements. Often only one parameter like the magnetic field is changed whereas all other measurement parameters are fixed. A measurement series from 0 to 17 T with a small step size can easily require a few hundred measurements. To automate these measurement series a LabView program is used. LabView is a graphical programming language especially designed for the control of lab equipment that can be connected to a computer. Nowadays almost every commercial device comes with example LabView programs to control it via serial bus, GPIB, USB or a specific PCI card. However, what is missing is an interconnection between different devices. If a spectrum has to be taken at a certain magnetic field, then the software controlling the CCD must know about the status of the magnet and the current field position. This is not the case with the factory supplied software.

A LabView program called "Manager" written by Georgy Astakhov at the University of Würzburg was designed to overcome these problems. It offers a flexible environment in the sense that it can be extended to control many different devices and combine them in an intelligent way.

Improving and extending the LabView program to meet the demands of the ODR setup was an essential part of my research time. The initial version of the "Manager" program was lacking support for most of the devices that are part of the setup, they have been added in the mean time. Not only the implementation of devices is necessary. In case of the CCD it is important to filter out cosmic rays which lead to a strong enhancement of the intensity recorded by the CCD. This is done by a comparison of two spectra with the same exposure time. If a value in one of the two spectra is significantly larger it is replaced by the intensity of the control spectrum.

The FIR laser may fail after some operation time even if the external stabilizer is working. Therefore the output power of the laser is recorded by the LabView program. The user can set a lower and upper operation limit in percent of the reference intensity the laser had at the beginning. If the FIR intensity is beyond the limit, the measurement stops. Often the stabilizer can retrieve the initial value after a couple of seconds. In that case the last measurement is repeated and the series continues automatically. If the laser remains in an unstable state for more than two minutes the series is stopped and can only be reactivated manually after realignment of the laser. This tool made it very convenient to measure long series with some hundred data points without the need of intense supervision. The software is now also used

in other laboratories. At the current state the following devices are supported:

Device Class	Manufactor	Device
CCD	Roper Scientific Inc.	ST-133A
	Acton	PIXIS 256
Monochromator	Acton	SpectraPro 300i
	Acton	SpectraPro 2500i
	Jobin Yvon	HR460
Cryostats	Cryogenic	17T
	Cryogenic	10T
	Oxford	3T
	Oxford	7 T / 10 T
Temperature controller	Lakeshore	340
Photon counter	Stanford Research Systems	SR400
Lock-In amplifier	EG & G Instruments	Model 5110
	Signal Recovery	7225
Stepper motor	ThorLabs	apt-α
	Owis	SMC-1
Filer wheel	ThorLabs	FW102
Microwave genertor	Agilent Technologies	E8257D
Laser	Coherent	Cube
	InnoLas	Spitlight 600
OPO	GWU	PremiScan
	Spectra Physics	Quanta-Ray

Table 2.3: *Devices supported by the LabView program Manager*

It was also necessary to test optimal working conditions of the setup like exposure times, excitation powers or FIR wavelength and energies. Some of them are presented in Section 2.5.

2.2.1 Main program

The major part of the main window is governed by the graph display (Fig 2.4). It displays an x,y-Graph of the current measurement. This can be a PL spectrum as well as the time dependence of the sample temperature when cooling down. Up to three graphs can be shown at the same time to compare e.g. PL and ODR data as shown in Fig. 2.4 or spectra at different magnetic fields.

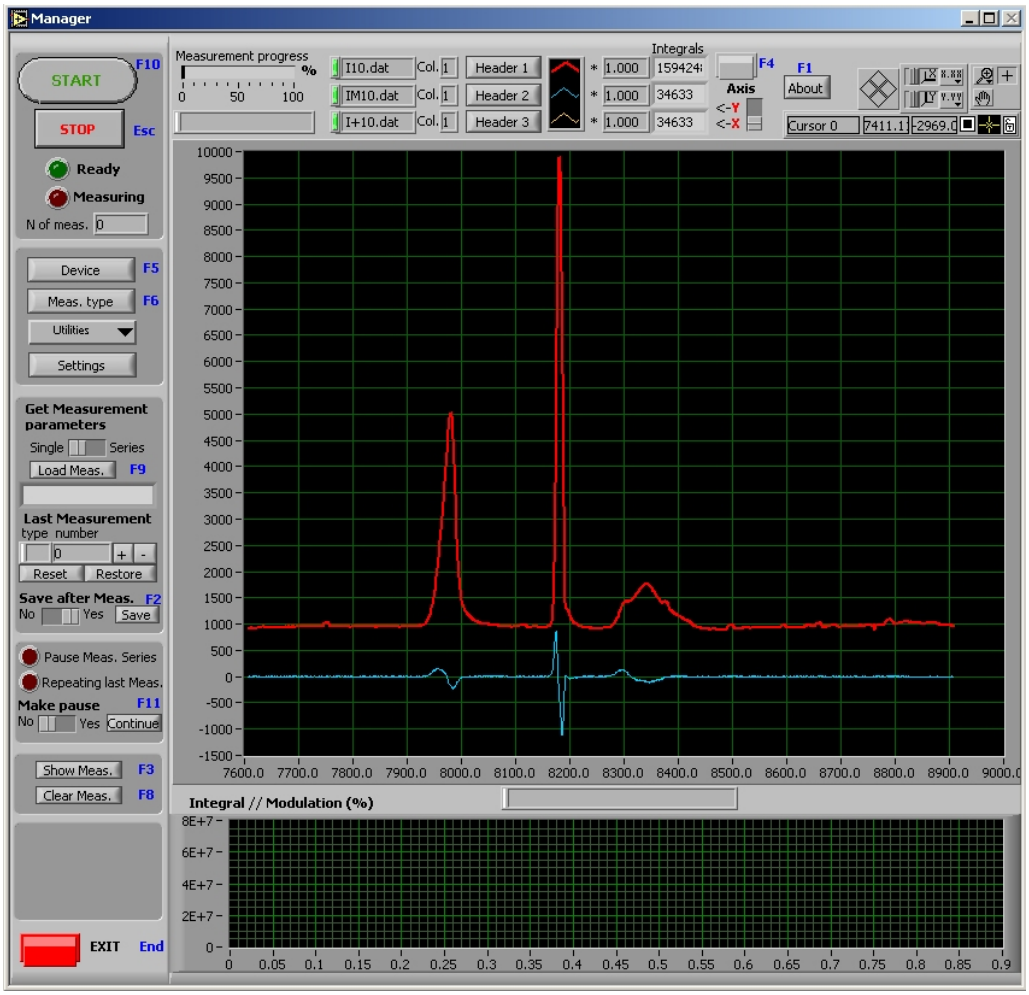

Fig. 2.4: *Main window of the LabView program "Manager" to control the ODR set-up.*

2.2.2 Devices

Before a measurement can be started all devices used in the laboratory need their virtual counterpart to be opened first. They allow direct control of the device. In the case of a monochromator one can select the wavelength and the grating to be used. Usually a set of devices needs to be opened. They can already be used in combination. Opening the CCD device window lets you take spectra at the position set by the monochromator. This can be used to improve the measurement conditions and initial settings such as exposure times, before actually starting a measurement.

Fig. 2.5: *Device control window for the monochromator which allows setting the wavelength.*

2.2.3 Measurement types

Measurement Types are some kind of prewired combination of devices. A single measurement will always produce one or more sets of x,y data. For example a measurement that combines monochromator and CCD will deliver a spectrum: Wavelength on the x-scale and intensity on the y-scale.

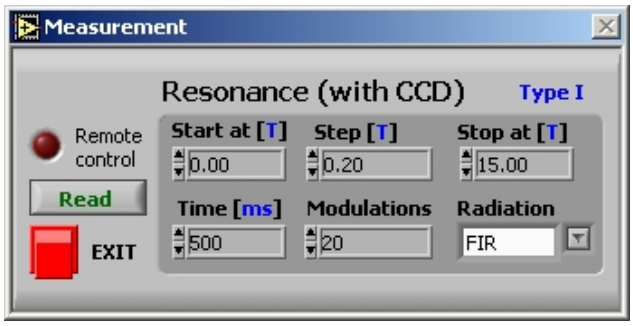

Fig. 2.6: *Control window for the ODR measurement type which allows to set the exposure time and number of modulations. For a measurement series the start and end magnetic field and the step size can be defined.*

A special measurement type is “Chart recorder” which just records a set of parameters with time. This can be used to record the stability of a laser with time or the sample temperature when cooling down to 2 K. It can also be used to measure dependencies which do not have a fixed measurement type.

2.2.4 Measurement series

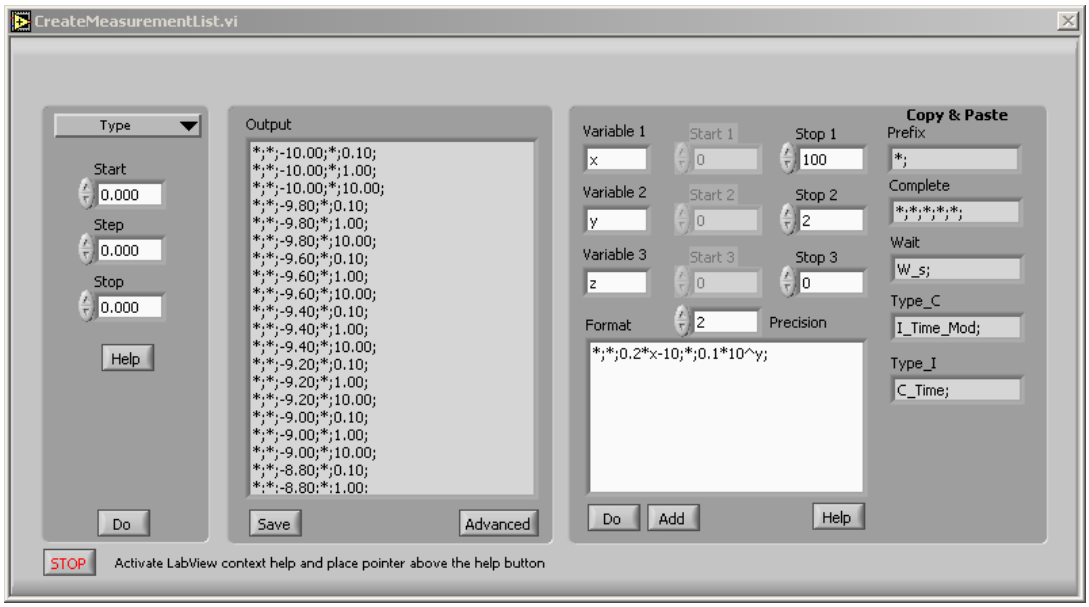

Fig. 2.7: *Utility to generate a measurement series. The left half of the panel allows the creation of simple series, where only one parameter is changed. The right half is only visible when the "Advanced" button is clicked. It can be used to build more complex series where several parameters are changed at once or in a certain order.*

The main benefit from the computer control of the devices is the ability to define measurement series. A simple measurement series is e.g. a number of PL spectra at different magnetic fields or different excitation laser powers. The parameters for the series are defined in a text file which can either be generated automatically by the program or manually. This text file is then executed consecutively, every line representing one single measurement. A utility is part of the program which assists by the generation of a measurement file as shown in Fig. 2.7. It allows defining measurement files with up to three dimensions. This means that for three given parameters (e.g. excitation power, temperature and magnetic field) measurements will be executed in a way that in the end all possible combinations have been measured.

2.3 Optically detected resonance technique

To observe the effect of radiation in the energy range of a few meV on semiconductor nano structures the optically detected resonance technique (ODR) is used. It is also often referred to as ODMR technique which either means "Optically Detected Magnetic Resonance" or "Optically Detected Microwave Resonance" or ODCR which stands for "Optically Detected Cyclotron Resonance".

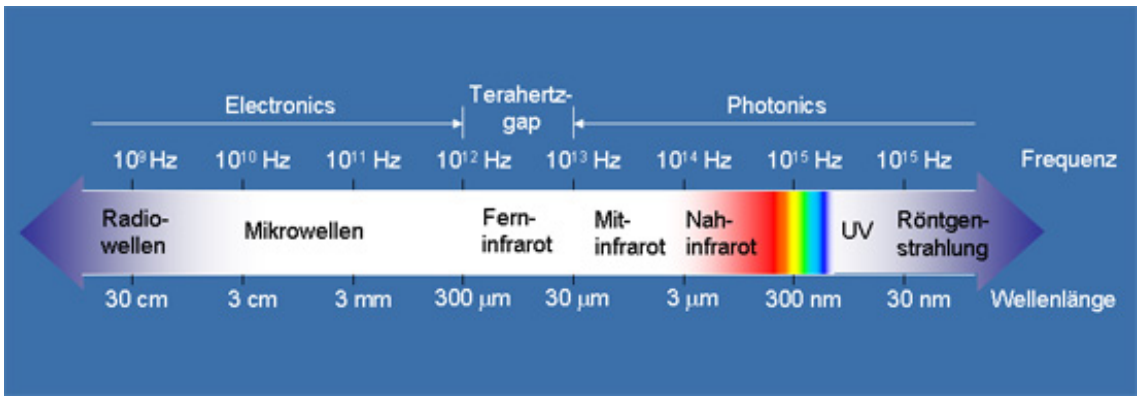

Fig 2.8: *Overview of frequency (Frequenz) and wavelength (Wellenlänge) of electromagnetic radiation. On the left hand side the frequency range is shown that can be generated by electronic devices whereas the right hand side shows radiation from sources based on optical effects. In-between there is a gap in the far infrared (Ferninfrarot) range, called the THz-Gap.*[7]

The internal energy structure of quantum dots and quantum wells often lies in the order of a few meV which corresponds to a frequency of some THz and belongs to the far infrared range. Sources and detectors for THz frequencies are of high interest not only in the field of science[8]. However, there are only few sources which offer high output powers in this range. Lower frequencies such as microwave radiation can be generated by electronic sources like Gunn-diodes.[9] Higher frequencies sources are devices based on optical or photonic effects such as lasers. It is also hard to find sensitive detectors for the same reasons. The term "THz gap" has been established to describe the situation (Fig. 2.8).

Due to the lack of sensitive detectors direct absorption measurements in the far infrared regime have proven to be difficult. This is especially true for experiments

7 Graph taken from:
http://www.iht.rwth-aachen.de/en/Forschung/opto/thztechno/thztechno.php

8 Many organic compounds such as explosives absorb THz radiation and good sources would allow contactless detection of these materials. Also the ability to penetrate non-organic materials is welcomed by security services offering the possibility to detect weapons worn under clothes.

9 http://en.wikipedia.org/wiki/Gunn_diode

with nanostructures with very small “active” volume. Another advantage of ODR is its spectral sensitivity, which allows separating the QW signal from substrate and also to study few QW’s of different thickness composed to the same structure.

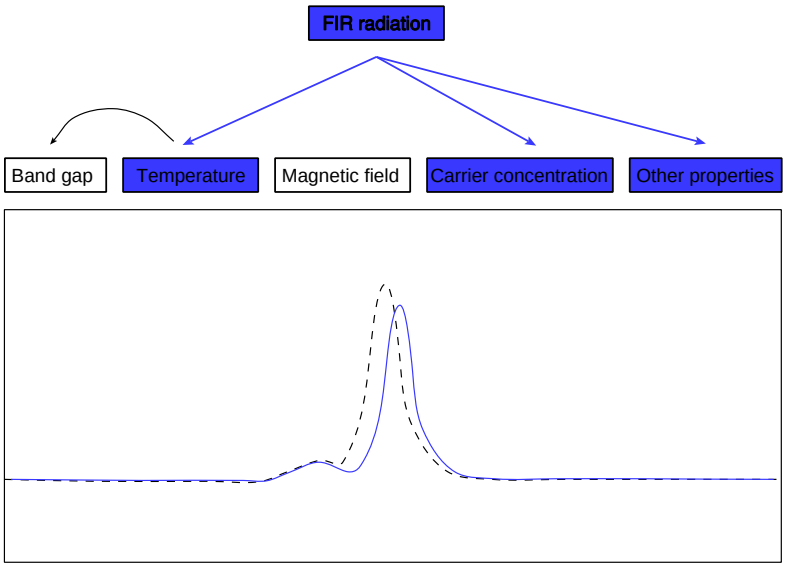

Fig. 2.9: *Photoluminescence without additional FIR radiation (black) and with FIR radiation (blue). Difference of the PL signals is caused by changes to the sample properties due to FIR radiation.*

The basic idea of the ODR technique is to study the photoluminescence of the semiconductor samples which often lies in the visible to near infrared range. The photoluminescence of these structures depends on properties such as temperature, magnetic field, electron density, population of energy levels etc. If some of these properties are changed by the FIR radiation, these changes will also be reflected in the photoluminescence signal (Fig. 2.9). A detailed description of the processes involved will be given in the next sub-section.

2.3.1 Effect of the FIR radiation

The far infrared radiation can have a variety of effects on the sample which depend very much on its nature. Before a measurement is started it is not initially predictable how the FIR radiation will affect the sample properties. Therefore it is important to take a closer look on how the PL is changed and hence draw conclusions from the experimental results.

Possible changes are summarised in Fig. 2.10. Pairs of PL spectra are shown in the upper row which demonstrates the FIR induced changes. Black curves show the photoluminescence spectrum without FIR radiation, blue curves with. In the bottom row the difference between both curves is shown in red as so called modulation spectrum. If the PL intensity at a certain energy rises with FIR radiation the modulation signal is positive, otherwise negative.

The position of the photoluminescence peak may be shifted by the FIR radiation. Other effects include a change of the PL intensity or its line shape.

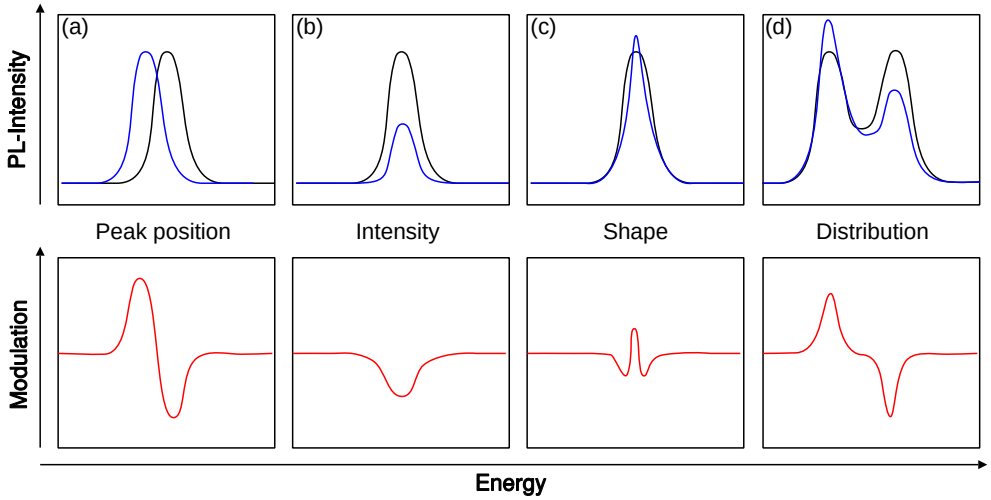

Fig. 2.10: *Effects of the FIR radiation of the PL with (blue curves) and without (black curves) and difference between both (red curves): (a) shift of the peak position, (b) change in PL intensity, (c) change of the line shape and (d) redistribution.*

A redistribution of carriers is also possible, e.g. between excitonic and trionic states. The strength of the modulation (the FIR effect) can be calculated from the area below the modulation spectrum as shown in Fig. 2.11 (a). The sign is ignored so that in this example the value for the modulation is a positive number, not zero. Usually not only one of these effects takes place but a combination of them which makes it harder to distinguish the processes in the sample. Therefore it can be important to separate the effects when analysing the experimental results. To study a shift of the line position both PL signals can be fitted with Lorenz functions to obtain their energy positions of the photoluminescence peak. If changes in the intensity are important the area below both PL spectra can be taken. If there are several peaks in the PL signal it is also possible to study them separately.

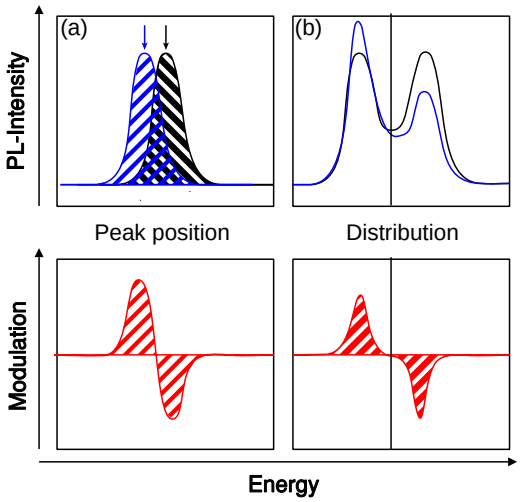

Fig. 2.11:
Different methods for analysing the change of the photoluminescence:
(a) The strength of the modulation signal can be expressed as area below the modulation curve (red). The intensity change can be calculated from the area below the PL signals (black and blue curve). The shift of the peak position can be derived from the shift of the peak maxima (black and blue arrows).
(b) Peaks of the PL spectrum can be handled separately.

If an external magnetic field is applied to the sample internal energy levels may change. One example is the splitting of the landau level discussed in Section 1.6.2. If the energy of the FIR radiation becomes comparable to the splitting of energy levels, transitions may be induced which change the population of energy level and hence the photoluminescence signal. If the strength of the modulation signal is calculated it will have a maximum at this position as shown in Fig. 2.12 (b). In the case of the landau level splitting these transitions are known as cyclotron resonance. They were the first application of the ODR technique.

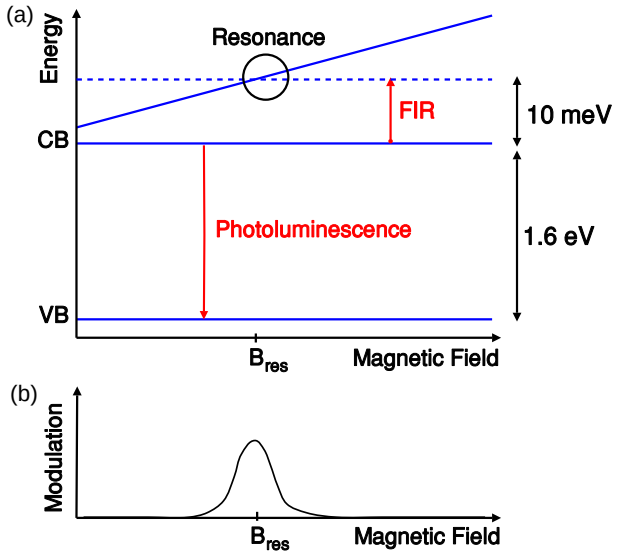

Fig. 2.12:
(a) Dependence of the internal energy structure on an external magnetic field. Energy levels may split and come into resonance with the FIR radiation leading to changes in the population of energy levels which lead to a change in the PL spectrum.
(b) Maximum of the modulation signal where energy of the FIR radiation and level splitting meet.

Not all maxima of the ODR signal are related to internal transitions, e.g. in case of the Diluted Magnetic Semiconductors (DMS) QDs introduced in Chapter 6.

2.3.2 Historic overview

The main focus of this thesis is the study of ODR on low dimensional semiconductor nanostructures. The basic technique, optical detection of cyclotron resonances in semiconductors, was first used in 1982 by Romestain and Weisbuch [Rom80]. Before, microwave induced CR was studied by detecting the absorption of microwave in a sample as a function of magnetic field. This technique was technically challenging in the 70th and 80th because MW detectors were not very sensitive and microwave absorption was small in semiconductor samples. Romestain and Weisbuch measured electron and hole CR to determine their effective masses in both bulk GaAs and CdTe. More detailed studies of CdTe samples were reported later that year [Dan82]. The technique has been used by Booth and Schwerdtfeger on other material systems, such as GaP, ZnTe and AgBr [Boo85] in 1985. First application of the ODR technique to quantum wells is reported by Cavenett and Paku-

lius in 1985 on GaAs/AlGaAs superlattices [Cav85]. They also observed the angular dependence of the CR. Especially for measurements on quantum wells with a 2DEG the high sensitivity of optically detected resonances compared to absorption measurements was a great advantage. A comparison of MW and FIR induced ODCR was reported on epitaxial InP and GaAs [Mol92] where effective masses and mobilities were measured. A study of effective masses in GaAs quantum wells of different width was presented by Warburton in 1992 showing that the effective mass increases when the well width is reduced. This was explained by monolayer-width fluctuations of the quantum well, localizing the carriers and hence leading to an additional binding energy to the cyclotron resonance transition [War92]. ODCR was also reported for undoped [Dre05] and Type I CdTe QWs [Hu98]. There are only very few publications of ODR applied to quantum dots [Jan03, Mei05]. Time resolved ODMR measurements have been reported by Ivanov in 2007 [Iva07].
In this thesis the photoluminescence of magnetic and nonmagnetic quantum wells and quantum dots is studied. The main luminescence features observed include singlet and triplet states of neutral, positively and negatively charged excitons and their behaviour at high magnetic fields. The existence of negatively charged excitons was first determined by K. Kheng in CdTe/CdZnTe quantum wells in 1993 [Khe93]. It was proposed already in 1958 by Lampert [Lam58] but could not be observed in bulk materials. Only when quantum wells of good quality became available at the beginning of the 90s charged excitons could be found in photoluminescence spectra. The triplet state of negatively charged excitons in GaAs quantum wells was first seen by Shields in 1995 [Shi95b]. Evidence for the positively charged exciton was also found by Shields in the same year in GaAs based quantum wells [Shi95a].

2.4 Analysing software

A series of PL or ODR measurements produce a high number of data files. Photoluminescence measurements save one data file for every magnetic field position. This file contains two rows, one with the wavelength and one with the corresponding light intensity. For ODR measurements three files are saved for every position. They contain the PL, PL under FIR radiation and the difference between both. Fortunately the structure of the data files is very similar for all measurements. In order to be able to handle the data in an automatic way, Gregor Bartsch wrote a couple of software tools which are embedded in Origin. They allow loading the data files in a simple way and offering a variety of features related to the analysis of the data. With a simple click on one button and setting of some parameters it is possible to perform complex analysis steps such as the determination of multiple peak positions for a magnetic field series. A detailed description of the software features can be found in Gregor Bartsch' Diploma thesis [Bar07].

Due to these tools the analysis of the data is the same for all samples. The following subsections discuss the most important tools used to present the results in this thesis.

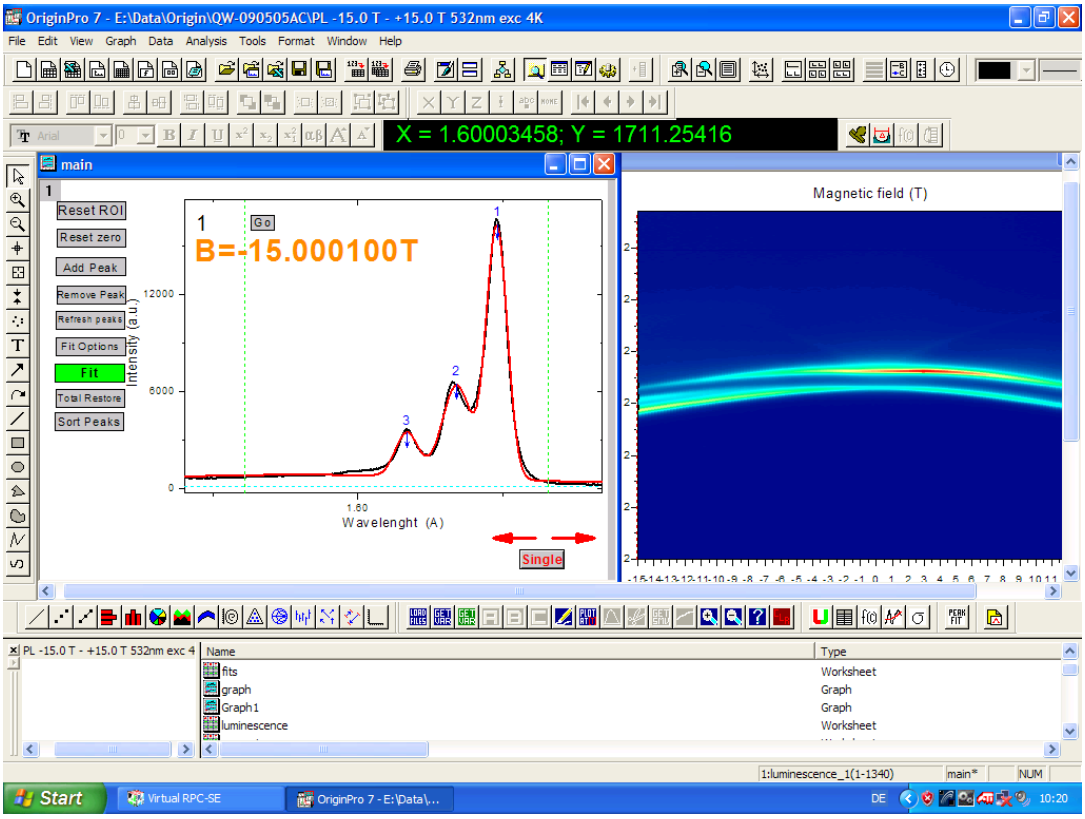

Fig. 2.13: *OriginPro 7 with additional tools for the data analysis. Here a tool for automatic and manual peak fitting is shown.*

2.4.1 False color maps

A complete magnetic field series for PL or ODR measurements in both circular polarizations consists of more than 150 spectra. A good way to present the results in a simple picture is to transform the intensity of a spectrum into a color scheme. Usually blue is used for low intensities and red for high intensities. So a PL spectrum can be converted into a single row of 1340 Pixels representing the light intensity of every CCD pixel at a certain magnetic field. A magnetic field series leads to a number of rows which can be combined to a two dimensional false color image. An example is shown on the right half of Fig. 2.13.

2.4.2 PL and modulation spectrum

In a PL spectrum the light intensity is shown as a function of energy or wavelength. In the figures presented here the spectrum without FIR radiation is a black line. If FIR radiation was applied to the sample two more spectra are shown: The PL spectrum with FIR radiation (blue line) and the difference between both, the so called modulation spectrum (red line), see Fig. 2.14 (a) as an example.

Data from the CCD is delivered in wavelength ($\mathring{A}$) and converted to energy (eV) by the following equation:

$$E\,(eV) \;=\; \frac{12398}{WL\,(\mathring{A})} \tag{2.1}$$

2.4.3 Modulation signal

To calculate the modulation, the PL with FIR, $L_{FIR}(E)$, and the one without FIR, $L(E)$, are taken. This difference, $m(E) = L_{FIR}(E) - L(E)$ is then integrated in an energy interval which is defined by the used in order to take into account only the relevant part of the spectrum. So, as an indicator for a FIR induced change of the PL at all (without getting insight into its nature) one can take M, the modulation, which is defined by:

$$M \;=\; \frac{\int |m\,(E)|\,dE}{\int L\,(E)\;dE}. \tag{2.2}$$

The modulation is given in percent because it compares the change of the integral PL intensity to the total integral PL intensity. If the modulation is shown as a function of magnetic field this is called the modulation signal.

2.4.4 Fitting peak positions

To analyse a spectrum with several peaks OriginPro allows the user to fit a number of Gauss or Lorentz curves to the data if the user sets the initial fitting parameters. Since the spectra do not deviate too much between two magnetic field values that are close to each other, it is a good idea to use the parameters from the previous magnetic field for the current one, once the initial parameters have been defined manually for the first data set. Three different tools have been written by G. Bartsch to enable the user to do that since Origin is lacking a feature like this. One of these tools is displayed in the left half of Fig. 2.13. After the fitting process the peak position, peak amplitude and peak width are available to the user for further analysis.

2.5 Experimental dependencies

In a complex experimental setup there are a number of parameters which can be - to a certain degree - set freely. This includes the sample temperature, power and wavelength of the excitation and FIR laser as well as methods for the noise reduction. In this part the correlation between experimental properties and the archived results are shown.

As test sample a high quality n-type doped GaAs/AlGaAs quantum well (Ash250) with 25 nm well width has been chosen. The cyclotron resonance of this sample has been observed at around 6.2 T for $\hbar\omega_{FIR} = 10.5\,meV$. As mentioned in section 1.6.3, from the cyclotron resonance basic parameters of the semiconductor such as effective masses and carrier mobility can be derived.

2.5.1 Exposure time

As difference between two photoluminescence spectra, which may be almost identical, the modulation spectrum is noise-prone. Therefore it is important to record high quality PL spectra with low noise. This can be achieved by long exposure times. On the other hand there is only limited time available at which the measurement conditions can be kept fixed. The optimal conditions also depend on the strength of the modulation signal that means the amount of change in the PL spectra

and the PL intensity of the sample. The noise dependence on the exposure time is shown in Fig. 2.14.

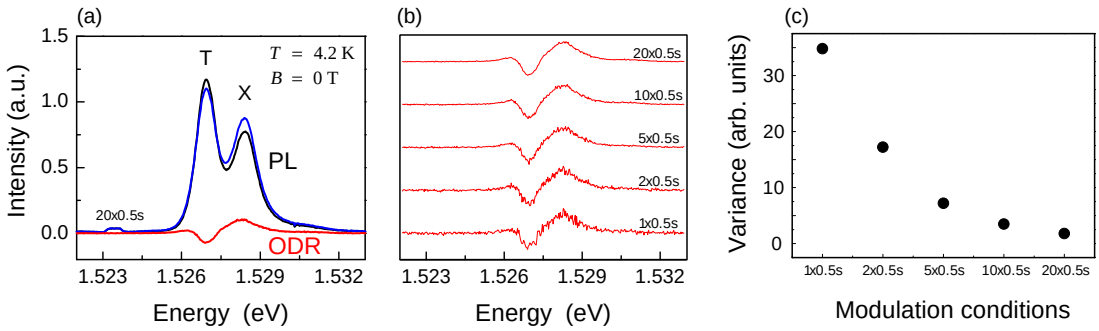

Fig. 2.14: *(a) PL and modulation spectrum of sample Ash250 at long exposure time. (b) Dependence of the noise level on the exposure time. (c) Noise of the modulation signal as function of exposure time calculated using the variance function.* $B = 0\,T$, $T = 4.2\,K$, $\lambda_{exc} = 632\,nm$, $P_{exc} = 35\,mW/cm^2$, $\hbar\omega_{FIR} = 10.5\,meV$, $P_{FIR} = 90\,mW/cm^2$.

The sample was excited by a HeNe-Laser with $\lambda_{exc} = 632$ nm and an output power of 7mW leading to a power density of $35\,mW/cm^2$. The photoluminescence without (black curve) and with (blue curve) FIR radiation is shown in Fig. 2.14 (a) together with the modulation signal (red curve) for a long exposure time. Redistribution between trion (T) and exciton (X) can be observed. PL spectra with an exposure time of 0.5 seconds with and without FIR radiation have been repeated 20 times in a row leading to a total exposure time of 10s. Too long exposure times lead to a heating of the sample and have to be avoided - more on this in the next subsection. In Fig. 2.14 (b) the number of repetitions and hence the total exposure time has been decreased from top to bottom coming along with an increase of the noise level. The noise level can be defined as the squared distance of measurement points from the mean value. The mean value was derived from smoothing the data with the adjacent averaging function of OriginPro set to 10 points. The corresponding statistical function is called variance and has been calculated from the modulation signal (Fig. 2.14 (c)). A strong decrease of the noise level can be observed if the exposure time is enhanced from 0.5 s to 10 s. It can also be observed that the variance starts to saturates at around 10s total exposure time. Therefore an exposure time of 20 x 0.5 s was used for most measurements. Due to the dependence of the noise on the strength of the modulation signal the exposure time could be reduced for a number of samples which showed strong ODR signal.

2.5.2 Repetition rates

When FIR radiation is applied to the sample the temperature of the sample and the electron system is increased. This heating effect which is independent of the mag-

netic field overlaps the resonant effect of the FIR radiation. In order to record spectra with long exposure times a sequence of alternating measurements with and without far infrared radiation are performed. During the measurements without FIR radiation the system can cool down. A series of measurements have been made where the total exposure time is left constant at 10s, but the exposure time during one cycle is increased from 20 x 0.5s to 2 x 5s.

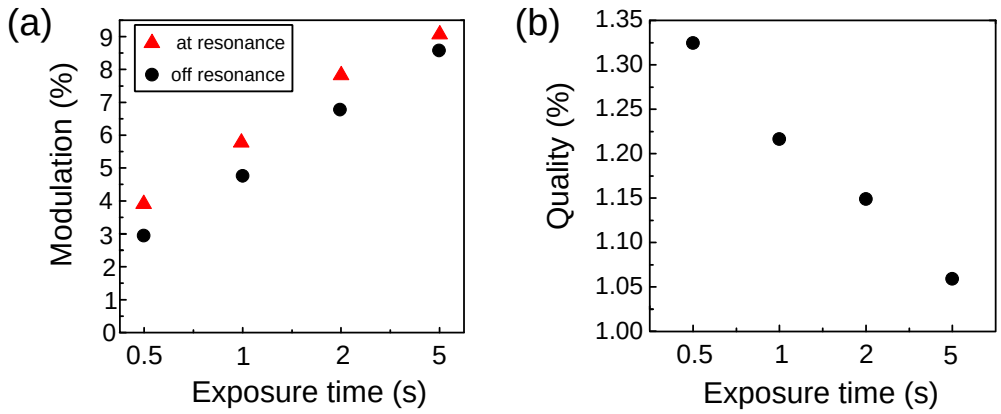

Fig. 2.15: *(a) Strength of the modulation signal at resonance (red triangle) and off resonance (black circle) depends on the exposure time. (b) The quality of the signal shows how the strength of the modulation signal changes between measurements at and off resonance. Sample: Ash250,* $B = 0\,T$, $T = 2.2\,K$, $\lambda_{exc} = 632\,nm$, $P_{exc} = 35\,mW/cm^2$, $\hbar\omega_{FIR} = 10.5\,meV$, $P_{FIR} = 100\,mW/cm^2$.

The modulation signal has been measured at the cyclotron resonance position ($B = 6.21$ T) and off resonance ($B = 6.10$ T) shown as red triangles and black circles in Fig. 2.15 (a). When the exposure time of individual measurements increased, the strength of the modulation signal rises. This seems to be good, but one has to keep in mind that also the background signal increases. Since only the resonant part of the modulation signal can be used to determine sample properties such as effective masses and mobility a high contrast is important between the ODR signal at and off resonance. So the quality of the modulation measurement can be defined as:

$$Quality\ (\%) = \frac{Modulation\ at\ resonance}{Modulation\ off\ resonance} \tag{2.3}$$

This relation has been plotted in Fig. 2.15 (b) and it is obvious that the quality of the modulation measurement decreases with longer exposure times. If the quality factor becomes one, no difference between a resonant and non-resonant field position can be found since the modulation signal would be the same at both positions. Due to the limitations of the experimental setup it is not possible to reduce the single exposure time below 0.5s. The limiting factors are the shutter opening and closing times and the processing time of the CCD images.

2.5.3 Temperature dependence

The cyclotron resonance has been measured for different sample temperatures (Fig. 2.17). The temperature T was set by current flowing though a resistor mounted close to the sample. From the position of the resonance the effective mass can be calculated. For the temperature range from 2.2 K to 10.0 K the magnetic field position of the cyclotron resonance seems to be constant. The average CR position has been determined as $B = 6.21$ T. According to Eq. 1.15 this corresponds to a effective mass $m^* = 0.067\, m_0$.

The strength of the modulation, which is defined by the modulation degree at the CR, strongly depends on the sample temperature (Fig. 2.16). For temperatures up to 8.0 K there is a linear decrease of the modulation signal with rising temperature. At $T = 10$ K a modulation signal of around 0.6 % can still be observed. However the increase at the CR position becomes hard to determine.

The FWHM of the cyclotron resonance increases with temperature up to $T = 6$ K. The mean free path length of the electrons in the 2DEG is decreased at higher temperatures due to interactions with phonons. For temperatures above 6 K the modulation signal becomes too small to retrieve valid values for the width of the resonance.

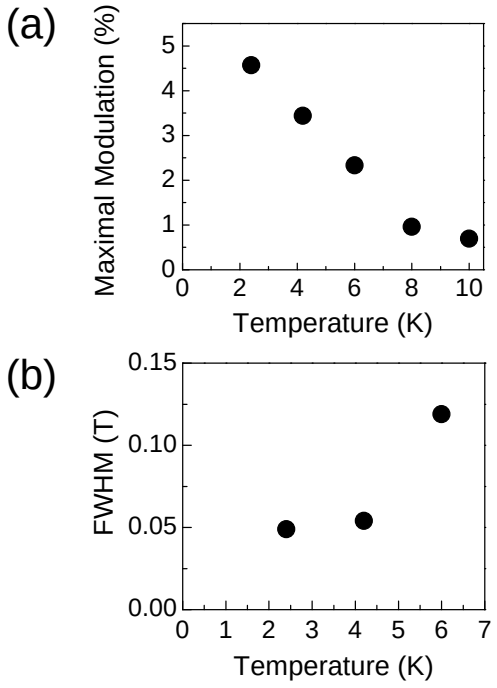

Fig. 2.16: *Temperature dependence of (a) the modulation signal at cyclotron resonance and (b) the full width at half maximum of the modulation signal. Sample: Ash250,* $B = 0\,T$, $\lambda_{exc} = 632\,nm$, $P_{exc} = 35\,mW/cm^2$, $\hbar\omega_{FIR} = 10.5\,meV$, $P_{FIR} = 100\,mW/cm^2$.

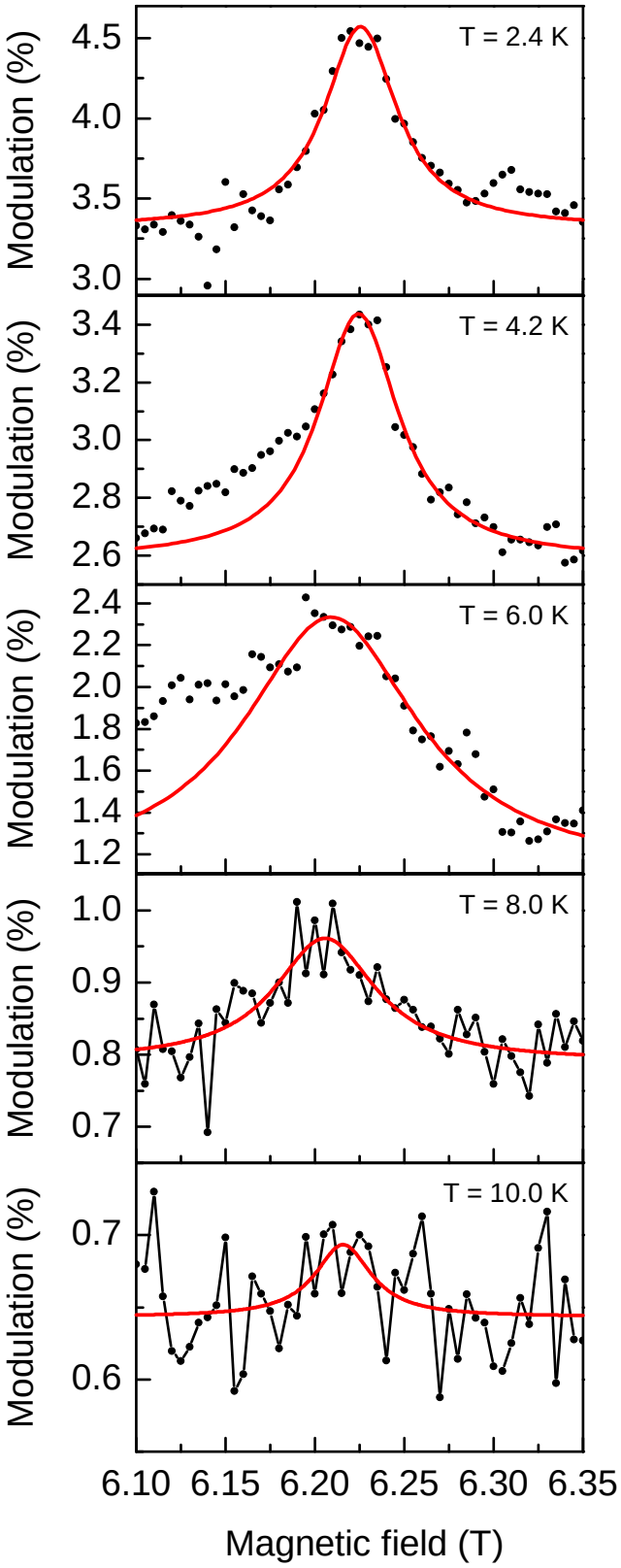

Fig. 2.17:
Temperature dependence of the cyclotron resonance. Data points have been fitted with the Lorenz function to obtain parameters of the resonance.
Sample: Ash250,
$B = 0\,T$,
$\lambda_{exc} = 632\,nm$,
$P_{exc} = 35\,mW/cm^2$,
$\hbar\omega_{FIR} = 10.5\,meV$,
$P_{FIR} = 100\,mW/cm^2$.

2.5.4 Dependence on excitation power and wavelength

The choice of the right excitation laser wavelength depends on the band gap of the quantum well material. Usually the sample is excited above the barrier (Fig. 2.18).

For the measurements with the GaAs/AlGaAs QW a HeNe laser with a wavelength of λ_{exc} = 628 nm and a maximum output power of 7mW was used as well as a solid state Coherent CUBE laser with λ_{exc} = 638 nm and up to 25 mW output power. With an energy of 1.97 and 1.94 eV illumination was well above the barrier. This leads to a higher density of the 2DEG as compared to the below barrier illumination. An increase of the excitation power will further enhance the electron density. This changes not only the PL intensity but also changes the probability of the trion formation as shown in Fig. 2.19. Due to the huge number of electrons the appearance of trions becomes much more likely. Sometime this effect can be used to turn nominally p-doped samples in n-doped ones by applying more power (See section 3.1.2 and section 3.2.1) or by using a second excitation laser with another wavelength to bring more electrons to the conduction band.

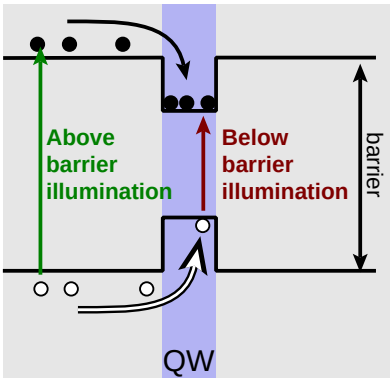

Fig. 2.18: *Above and below barrier illumination in a quantum well.*

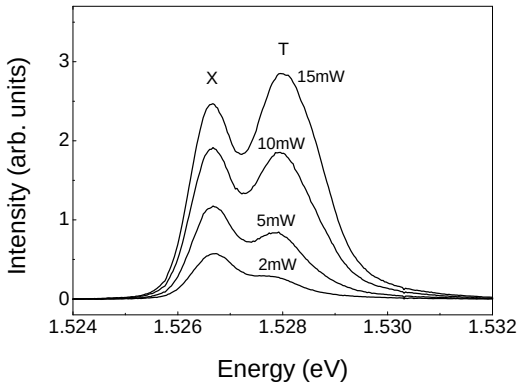

Fig. 2.19: *Photoluminescence in σ^--configuration of sample Ash250 at B = 6.21T, excited with a 638 nm laser at different output powers. T = 4.2 K.*

Also the ODR measurements are influenced by the excitation power. A higher electron density decreases the mean free path length. This reduces the ability of electrons to come into cyclotron resonance and will hence reduce the modulation signal as shown in Fig. 2.20 (a). Also the width of the CR is increases with excitation power (Fig. 2.20 (b)). This general tendency is therefore comparable to the heating of the sample temperature but the effect may be different in detail. The increase of the trions peak intensity as opposed to the electron peak intensity can not be observed at higher sample temperatures but might influence the ODR signal strongly.

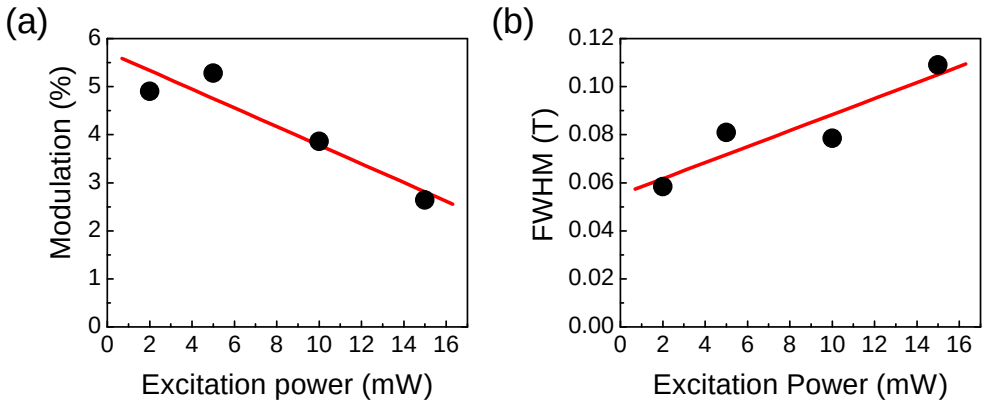

Fig. 2.20: *(a) Strength of the modulation signal depending on the excitation power of a 638 nm laser. (b) Increase of the width of the cyclotron resonance with increasing excitation power. Sample: Ash250,* $B = 0\,T$, $T = 4.2\,K$, $\lambda_{exc} = 638\,nm$, $\hbar\omega_{FIR} = 10.5\,meV$, $P_{FIR} = 90\,mW/cm^2$.

2.5.5 Dependence on FIR power and energy

In another experiment series the influence of the FIR power on the modulation signal has been investigated.

The FIR power has been reduced by one and two pieces of paper in the path of the FIR radiation behind the semi-transparent mirror so that the output power of the laser could be held constant at 100mW. As expected the modulation signal increases almost linearly with the FIR power (Fig. 2.21).

When the energy of the laser is increased to 12.8 meV the cyclotron resonance shifts to higher magnetic fields because the Landau level splitting needs to coincide with the higher energy.

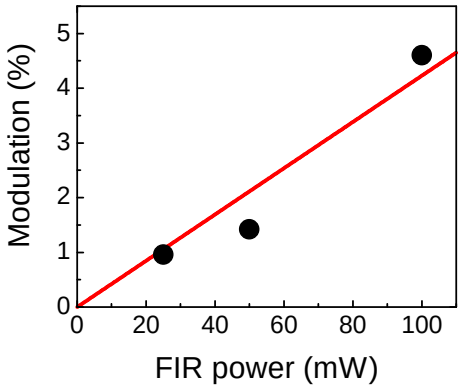

Fig. 2.21: *Strength of the modulation signal depending on the power of the far infrared laser line.*
Sample: Ash250, $B = 0\,T$, $T = 2.2\,K$, $\lambda_{exc} = 632\,nm$, $P_{exc} = 35\,mW/cm^2$, $\hbar\omega_{FIR} = 10.5\,meV$.

From the resonance of the 10.5 meV line at $B = 6.215$T the CR field can be estimated:

$$\frac{12.8\ [\mathrm{meV}]}{10.5\ [\mathrm{meV}]} \cdot 6.215\,[\mathrm{T}] = 7.576\,[\mathrm{T}] \tag{2.4}$$

The result of the measurement with the 12.8 meV line of the laser showing a resonance at $B = 7.592$T corresponds well to the expected CR position.

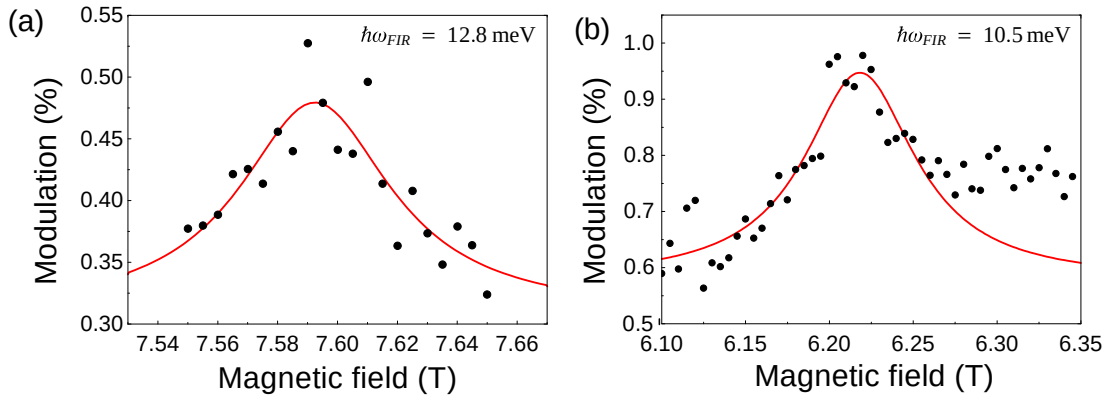

Fig. 2.22: *(a) Cyclotron resonance with FIR energy of 12.8 meV and 40 mW/cm^2 output power. (b) Cyclotron resonance with FIR energy of 10.5 meV and 25 mW / cm^2 output power. Sample: Ash250, $B = 0$ T, $T = 2.2$ K, $\lambda_{exc} = 632$ nm, $P_{exc} = 35$ mW / cm^2.*

2.5.6 Photomultiplier tube and FIR stability

As alternative for the CCD a photomultiplier tube (PMT) can be used to detect the PL and ODR signal. In fact the majority of published results from ODR measurements were archived using a single channel detector.

In order to improve the signal to noise ratio a Lock-in amplifier is used. For PL measurements a frequency stabilized chopper is placed between excitation laser and fiber input coupler. The reference frequency is fed into the LockIn amplifier to ensure that only signals which show a dependence of this frequency are amplified. For ODR measurements the chopper is placed behind the output coupler of the FIR laser to record signals caused by the FIR radiation. It is not possible to record PL and ODR data at the same time.

A comparison of CCD and PMT measurements on a nominally undoped CdTe/CdMnTe quantum well (040397C) of 8 nm width is shown in Fig. 2.23. The PMT signal is very noisy. A Gauss fit to the data shows a maximum at 9.2 T which corresponds to an electron mass of $m^* = 0.102\ m_0$.

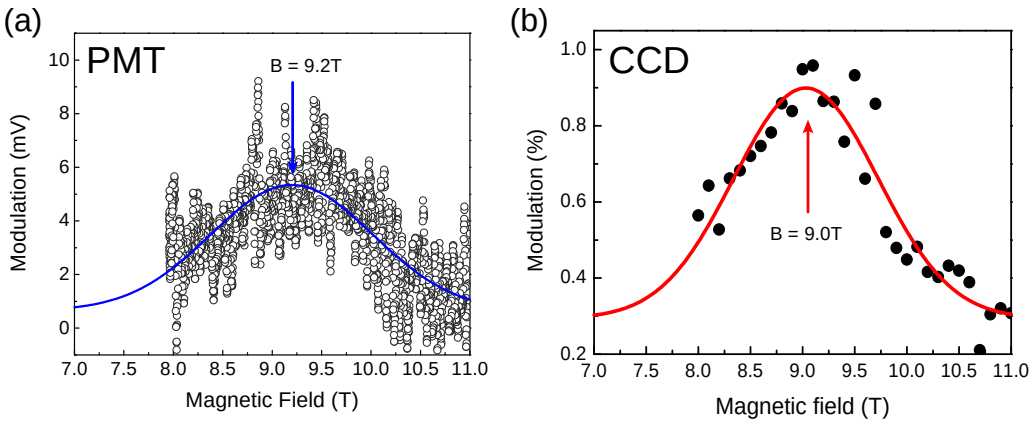

Fig. 2.23: *Modulation signal of a CdTe/CdMnTe QW sample 040397C measured between 8.0 and 11.0 T with (a) a PMT showing CR at 9.2 T and (b) a CCD showing CR at 9.0 T.* $T = 4.2\,K$, $\lambda_{exc} = 532\,nm$, $P_{exc} = 25\,mW/cm^2$, $\hbar\omega_{FIR} = 10.5\,meV$, $P_{FIR} = 80\,mW/cm^2$.

The data from the CCD slightly deviates showing a maximum at 9.0 T ($m^* = 0.099\,m_0$). The sample measured here has been subject of an ODR study showing the influence of the effective mass on the well width [Dre05].

A comparison of CCD and PMT measurements with the published data is given in Fig. 2.24. Both measurements do not coincide very well with the published data. In case of the photomultiplier tube this may be explained by the noise level. Different settings and chopper frequencies were tried but it was not possible to get a better signal using the PMT and LockIn amplifier. Further disadvantages of the PMT include the long measurement times for a spectrum which may take a couple of seconds instead of some hundred milliseconds in case of the CCD. For ODR measurements only one position in the spectrum can be studied, e.g. the exciton or trion peak position.

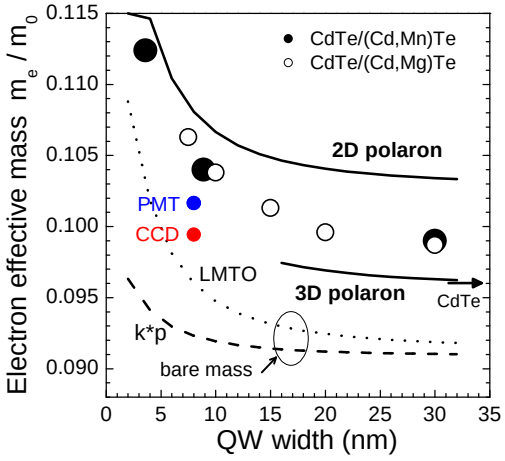

Fig. 2.24: *Comparison of CCD and PMT results with published results for comparable quantum wells [Dre05]*

When the magnetic field is ramped it is necessary to tune the monochromator in order to follow the line position. This requires to measure the PL first, fit the line positions and finally perform the ODR measurement. Due to the disadvantages of the single channel detector all measurements presented in this thesis were recorded with the CCD. The deviation between the CCD measurement and the published data may come from fluctuations of the FIR laser output power.

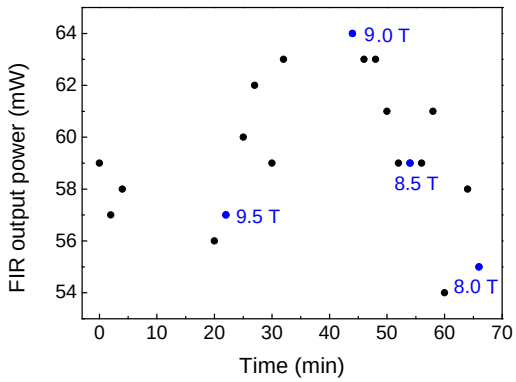

Fig. 2.25: *FIR laser output power as a function of time. Every point belongs to an ODR measurement at a certain magnetic field. Sample: 040397C,* $T = 4.2\,K$, $\lambda_{exc} = 532\,nm$, $P_{exc} = 25\,mW/cm^2$, $\hbar\omega_{FIR} = 10.5\,meV$.

In Fig. 2.25 the output power of the FIR laser is shown. It has been measured manually at every magnetic field position after the ODR measurement. The output power of the FIR laser seems to have a maximum at around 9.0 T, which is very close to the CR position determined from the ODR data. The evolution of the output power with time is arbitrary but the ODR measurement is strongly influenced by it. A high output power of the FIR laser leads to a strong ODR signal so that the curve shown in Fig. 2.23 (b) is a superposition of the real signal from the cyclotron resonance and the arbitrary contribution of the FIR laser power.

Because the maximum of the FIR output power is very close to the expected resonance position one can not trust the result of the ODR measurement. Therefore it is necessary to control the output power of the FIR laser and measure it as a reference.

A FIR laser stabilizer is delivered with the laser. All experimental results presented in this thesis have been measured with an actively stabilized system. Also the FIR laser power is continuously measured and can be used to normalize the ODR data.

Chapter 3:

PL and ODR study on nonmagnetic quantum wells

3.1 ODR in nonmagnetic quantum wells

3.1.1 Optically detected cyclotron resonance

Historically the ODR technique was first used to study cyclotron resonance in order to obtain basic parameters such as carrier masses and scattering times, hence the technique is also called optically detected cyclotron resonance (ODCR).

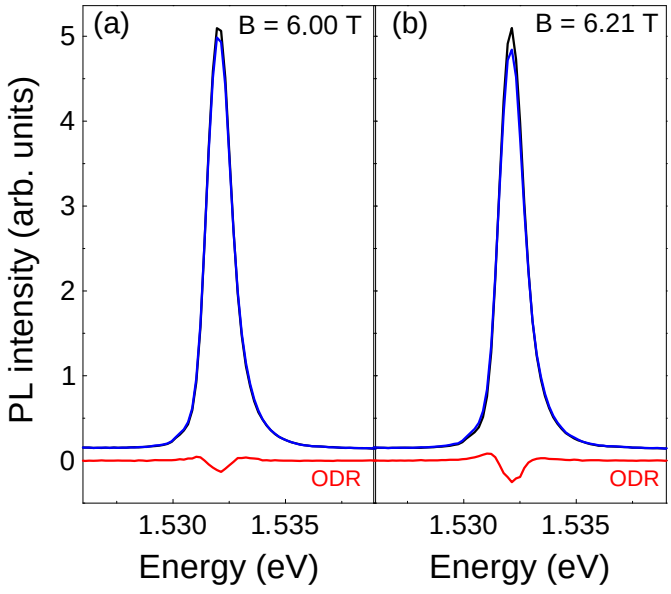

Fig. 3.1:
PL of sample Ash250 with (blue curve) and without (black curves) the influence of FIR radiation and their difference (red curve).
(a) Shows the influence off resonance and (b) at the cyclotron resonance position.
$T = 4.2\,K$, $\lambda_{exc} = 632\,nm$,
$P_{exc} = 35\,mW/cm^2$,
$\hbar\omega_{FIR} = 10.5\,meV$,
$P_{FIR} = 80\,mW/cm^2$.

The results shown here have been measured on the GaAs/AlGaAs QW (Ash250) sample that was introduced in Section 2.5. At a temperature of 4.2 K the sample was excited by a HeNe Laser (1.96 eV). For the FIR measurements the 118 μm (10.5 meV) line was used with an output power of 80 mW/cm^2. The effect of the FIR radiation can be seen in Fig. 3.1 (a): The black curve shows the photoluminescence which is dominated by the exciton signal at 1.532 eV. Under the influence of the FIR radiation the PL intensity is slightly reduced (blue curve). The modulation spectrum is shown in red and also shows a clear reduction of the PL intensity. The changes of the photoluminescence can be deduced to impact ionization of shallow donors and impurity bound excitons [Mol92]. Due to the FIR radiation the energy of free carriers is increased which leads to the ionization of excitons. It depends on the magnetic field as shown in Fig. 3.1 (b) where the reduction of PL is more pronounced. The modulation as function of the magnetic field is displayed in Fig. 3.2.

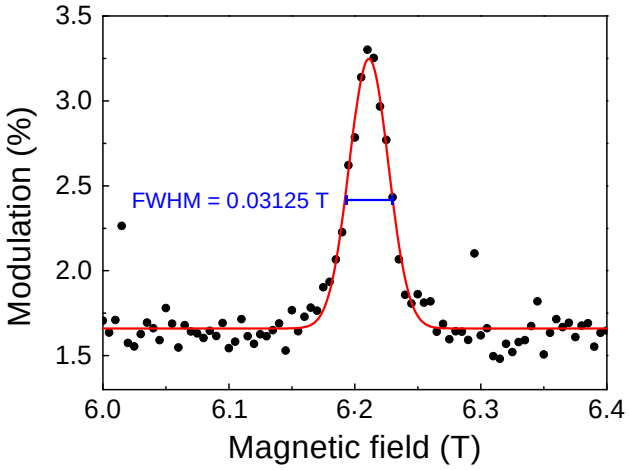

Fig. 3.2:
Modulation signal at $T = 4.2\,K$ showing cyclotron resonance with $B_{Res} = 6.21T$.
Sample: Ash250,
$T = 4.2\,K$,
$\lambda_{exc} = 632\,nm$,
$P_{exc} = 7\,mW/cm^2$,
$\hbar\omega_{FIR} = 10.5\,meV$,
$P_{FIR} = 80\,mW/cm^2$.

A clear resonance can be observed around $B = 6.21T$ which can be assigned to the cyclotron resonance because the effective mass, calculated from the FIR energy and the resonance position, according to Equation 1.15 is $m^* = 0.068\,m_0$ which is in good agreement with published values [Ryc02]. From the line width (FWHM) of 0.03125 T the mobility of the sample can be estimated according to:

$$\eta = \frac{1}{FWHM} = \frac{1}{0.0315\,T} = 317.460\ \mathrm{cm^2/(V \cdot s)} \qquad (3.1)$$

For comparison data of another quantum well (32A21M7) with lower mobility is shown in Fig. 3.3. The FWHM is about ten times larger indicating a mobility of around 76.000 $\mathrm{cm^2/(V \cdot s)}$. From the resonance position of 5.87 T an effective mass of $m^* = 0.065\,m_0$ is derived with is slightly below expectations for a GaAs/AlGaAs quantum well.

When the energy of the FIR quanta comes in resonance with the Landau level splitting, the absorption of the FIR radiation increases and induces more energy to the

carriers and hence increases the carrier temperature. This leads changes in the 2DEG emission which are reflected in an increase of the ODCR signal. The resonance position depends on the energy of the FIR or MW radiation. Fig. 3.4 shows the CR positions for different microwave frequencies between 13.5 and 60 GHz, recorded at the High Magnetic Field Laboratories, CNRS, in Grenoble (FR) and at the University of Dortmund.

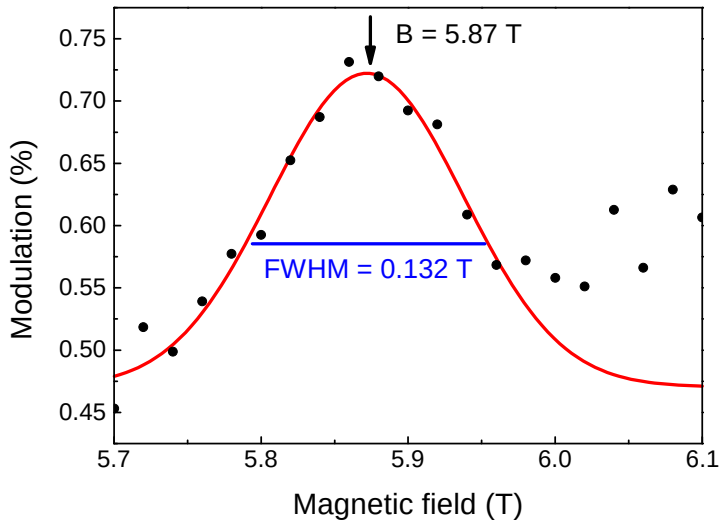

Fig. 3.3:
Modulation signal of a AlGaAs/AlAs quantum well (32A21M7) with a mobility of:
76.000 $cm^2/(V \cdot s)$.
$T = 4.2\ K$,
$\lambda_{exc} = 660\ nm$,
$P_{exc} = 7\ mW/cm^2$,
$\hbar\omega_{FIR} = 10.5\ meV$,
$P_{FIR} = 120\ mW/cm^2$.

The better signal quality of the 13.5 GHz measurement can be explained by the use of a cavity which lead to a much stronger MW power at the sample position. Also another MW generator with higher output power was used.

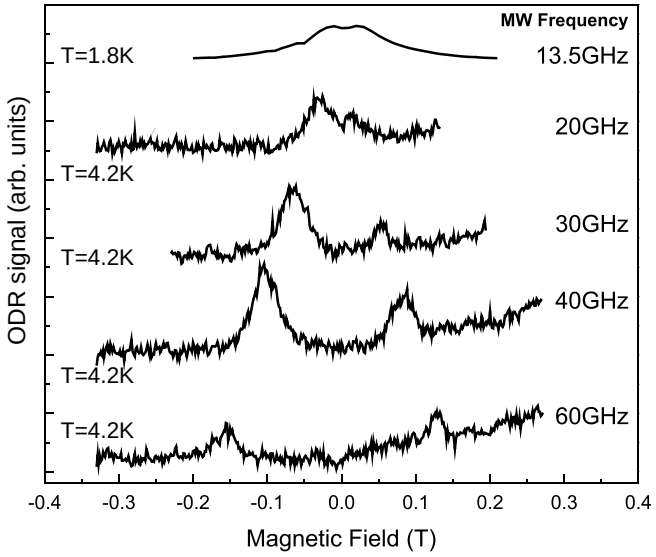

Fig. 3.4:
ODR signal for different microwave frequencies (Ash250). The signal for negative magnetic field values correspond to σ^--polarized, positive values for σ^+-polarized photoluminescence [Bar07].

A shift of the resonance positions towards higher magnetic fields can be observed for increasing microwave frequencies. Due to the linear splitting of the Landau levels a linear dependence is expected:

$$B_{res}[T] = 8.62 \frac{m^*}{m_0} E_{rad}[meV] \tag{3.2}$$

The CR positions for all MW and FIR measurements are plotted in Fig. 3.5 in a double logarithmic diagram also showing the corresponding effective masses. While the CR positions for frequencies above 40 GHz indeed show a linear behaviour there are deviations for the measurements at low frequencies. The discrepancy increases with decreasing frequency. Due to the appearance of this effect in two different laboratories a physical reason can be assumed whose origin has not been understood.

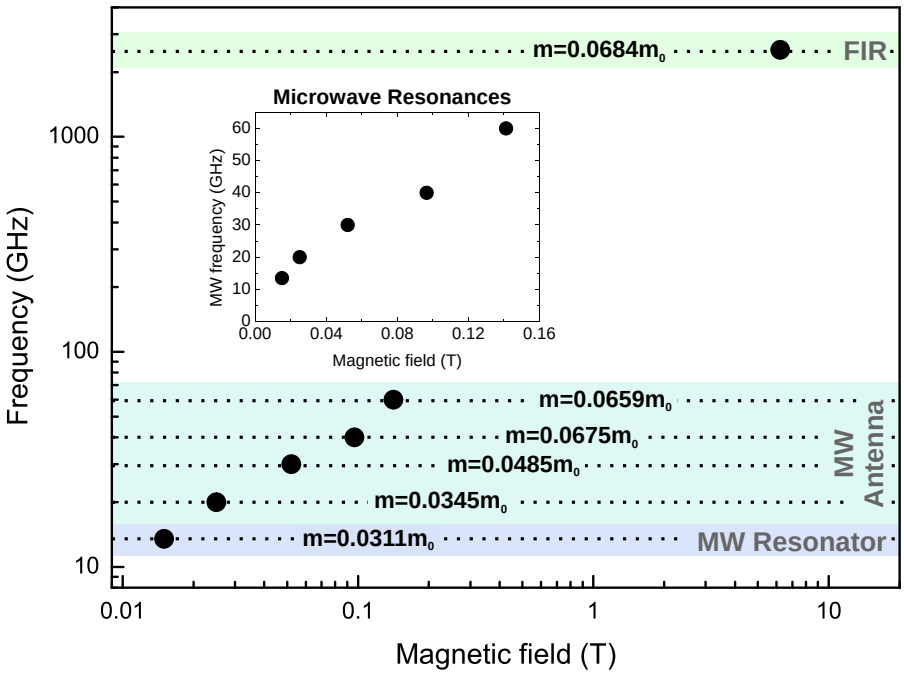

Fig. 3.5: *Magnetic field positions of the cyclotron resonances observed in ODR measurements for different Microwave and FIR wavelength. Data is shown in double logarithmic scales as well as linear ones in the inset [Bar07].*

3.1.2 Quantum well with optically tuneable carrier type

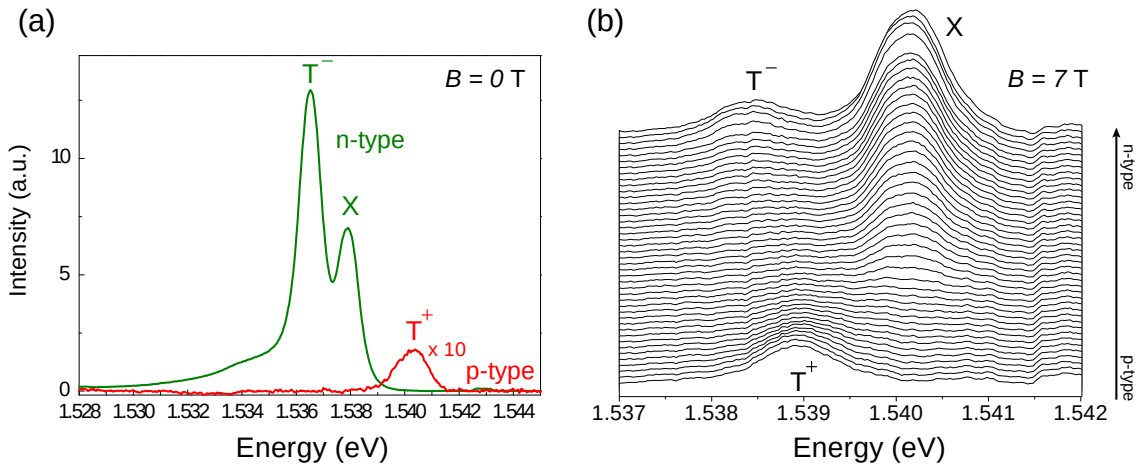

Fig. 3.6: *(a) Photoluminescence spectra ($B = 0\,T, T = 2.3\,K$) in p-type and n-type regime of a quantum well (12216) which carrier type depends on the excitation conditions. (b) Transition from p-type to n-type quantum well at $B = 7$ T by increasing above barrier illumination.*

The sample 12216 studied in this subsection is a nominally p-doped GaAs/ $Al_{0.34}Ga_{0.56}As$ quantum well of 15 nm width. By optical pumping above the barrier energy an increasing number of electrons is brought into the system. This allows to invert the carrier type in a way that the QW reaches the n-type regime.

Fig. 3.6 (a) shows the photoluminescence of the QW at $B = 0$T for both p-type and n-type conditions. A smooth transition from the p-type to the n-type quantum well is displayed in Fig. 3.6 (b) caused by additional illumination above the barrier by an Nd:YAG laser with a wavelength of 532 nm (2.33 eV). Note, that the excitation density is still much lower compared to (a) which explains the low trion intensity. Note, that due to the magnetic field the energy position of the exciton in the p-type regime has been shifted against the n-type exciton shown in (a).

For measurements in the n-type regime the quantum well has been excited by a Nd:YAG-Laser ($\lambda = 532$nm, $P = 6$ mW). The sample shows a strong influence of the FIR radiation on the photoluminescence spectrum which changes by more than 45% at resonance conditions. Fig. 3.7 shows the modulation signal up to $B = 17$ T for both circular polarizations. The strong peaks at around $B = 6.2$ T belong to the cyclotron resonance induced by the FIR radiation. From their position the effective mass of the electrons in the quantum well can be estimated according to Eq. 1.15. With the photon energy $\hbar\omega_{FIR} = 10.5$ meV we get $m^* = 0.0685\,m_0$ which is close to the value in bulk GaAs. The FWHM of around 0.5 T indicates a mobility in the order of 20.000 $cm^2/(V \cdot s)$.

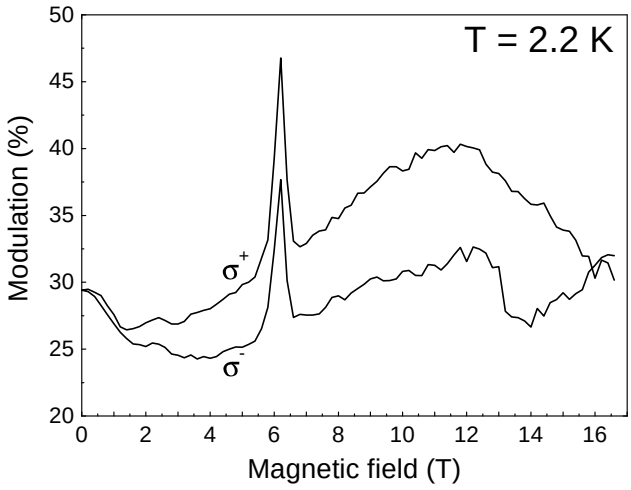

Fig. 3.7:
*Modulation signal of the quantum well (12216) in n-type regime for both circular polarizations. The peak at B = 6.2*T *belongs to the cyclotron resonance.*
$T = 2.2\,K$,
$\lambda_{exc} = 532\,nm$,
$P_{exc} = 21\,mW/cm^2$,
$\hbar\omega_{FIR} = 10.5\,meV$,
$P_{FIR} = 175\,mW/cm^2$.

A broad background can also be observed with a maximum at around $B = 12$T. Also at magnetic fields below 2 T there is an increase of the ODR signal. This is not fully understood but it might be related to the ratio of trions and excitons.

The spectral changes at and off resonance show (Fig. 3.8) that the number of trions is reduced by applied FIR radiation while the number of excitons increases strongly.

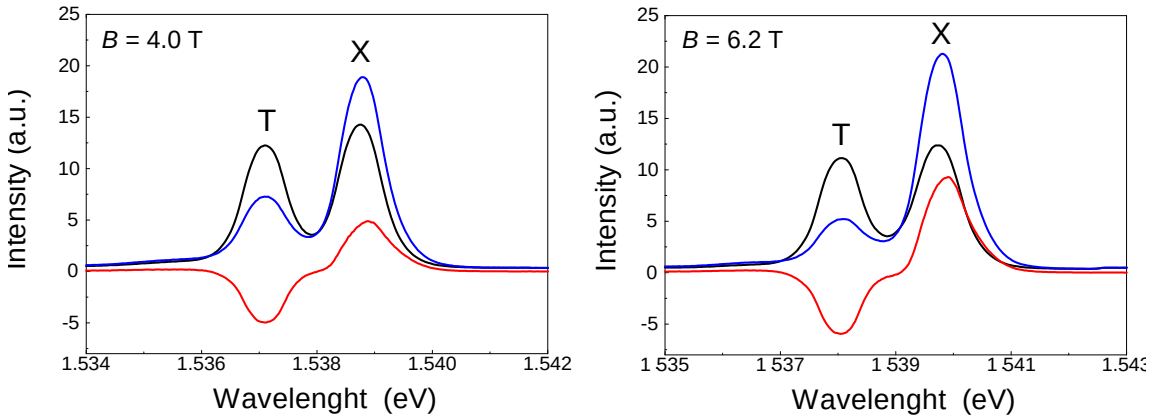

Fig. 3.8: *Modulation spectrum at B = 4.0* T *(off resonance) and B = 6.2* T *(at cyclotron resonance) for the n-type regime. Sample: 12216,* $T = 2.2\,K$, $\lambda_{exc} = 532\,nm$, $P_{exc} = 21\,mW/cm^2$, $\hbar\omega_{FIR} = 10.5\,meV$, $P_{FIR} = 175\,mW/cm^2$.

This can be attributed to FIR-induced heating of the carrier system. When the cyclotron resonance conditions are met, the kinetic energy of free carriers reaches a maximum and leads to a high carrier temperature that influences the ratio between excitons and trions. At high temperatures trion formation is suppressed. This can explain the sharp peak observed in the modulation signal.

Also off resonance the modulation signal is influenced by the ratio of trions and excitons. The ratio R is calculated by dividing the trion peak intensity I_T by the exciton peak intensity I_X:

$$R(B) = \frac{I_T(B)}{I_X(B)} \tag{3.3}$$

The ratio R is plotted as a function of magnetic field as blue symbols in Fig. 3.9 (a),(b) for both circular polarizations. For comparison the ratio under additional FIR radiation R_{FIR} is also shown by red symbols. At $B = 0\text{T}$ the trion PL intensity surmounts the one of the exciton by a factor of 2.4. The far infrared radiation strongly suppresses the trion formation so that the intensities of trion and exciton recombination becomes almost equal. At 6 T, the magnetic field of the cyclotron resonance, the ratio R_{FIR} drops further due to the more efficient heating of the carrier system.

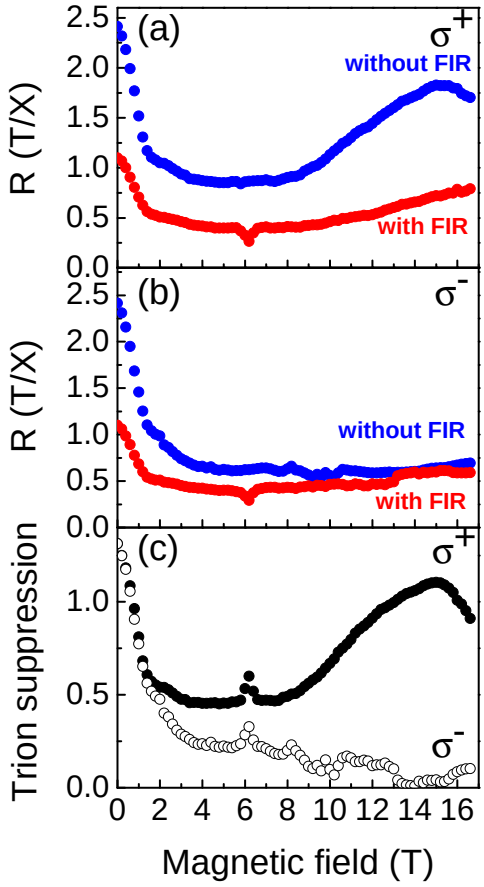

Fig. 3.9:
Ratio R between trion and exciton peak intensity in (a) σ^+-polarization and (b) σ^--polarization as a function of magnetic field. Blue symbols shows ratio R without additional FIR radiation, red symbols with. (c) Trion suppression ($R - R_{FIR}$) for both circular polarizations.
Sample: 12216,
$T = 2.2\,K$,
$\lambda_{exc} = 532\,nm$,
$P_{exc} = 21\,mW/cm^2$,
$\hbar\omega_{FIR} = 10.5\,meV$,
$P_{FIR} = 175\,mW/cm^2$.

The suppression of the trion formation under FIR radiation can be described by the difference $R - R_{FIR}$ which is shown in Fig. 3.9 (c) for both circular polarizations. The modulation signal shown in Fig. 3.7 can now be compared to the trion suppression. Four similarities can be found which indicate, that the modulation signal can be assigned to a suppression of the trion formation process by FIR induced temperature increase:

- In both cases the signal decreases between 0 - 2 T.
- At $B = 6$T a strong increase can be found in both signals.
- A broad maximum at high magnetic fields can be observed.
- Both signals are stronger in σ^+-polarization.

However, there are also some deviations, e.g. the broad maximum can be found at around 12 T in case of the modulation signal, whereas it is shifted to 15 T in the trion suppression data.

Measurements have also been performed in the p-type regime under illumination of a Ti:Sa Laser at $\lambda = 782$ nm (1.585 eV). As expected no cyclotron resonance signal can be observed since the hole mass is in the order of $m_h^* = 0.5\, m_0$ corresponding to a resonance position for the 10.5 meV FIR line at $B = 45$T. The origin of the strong double peak structure at high magnetic fields in σ^--Polarization is unknown. A phonon replica of the laser line was discussed but the energy difference between the occurrence of the enhanced PL signal at 1.544 eV and the TiSa laser line is 41 meV whereas the optical phonon energy is 36 meV in GaAs structures. A shift of the excitation laser line to $\lambda = 785$ nm (1.579 eV) did not influence the resonance position either. Additionally a similar enhancement of the signal in σ^+-Polarization would be expected.

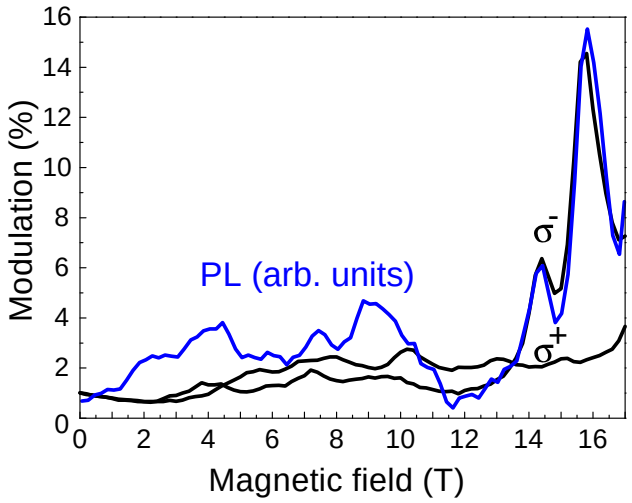

Fig. 3.10:
Modulation signal of the quantum well in p-type regime for both circular polarizations (black curves) and PL intensity in σ^--polarization (blue curve).
Sample: 12216,
$T = 2.2\,K$,
$\lambda_{exc} = 785\,nm$,
$P_{exc} = 80\,mW/cm^2$,
$\hbar\omega_{FIR} = 10.5\,meV$,
$P_{FIR} = 165\,mW/cm^2$.

A nonlinear amplification of the modulation signal with the PL intensity seems possible since the double peak structure can also be observed in the PL signal as shown in Fig. 3.10 (blue curve). However the weaker enhancement of the PL signal at 4.5 and 9.0 T does not lead to an increase of the modulation signal. Therefore it seems more likely that the rise in PL intensity and modulation signal is caused by the same, unknown effect.

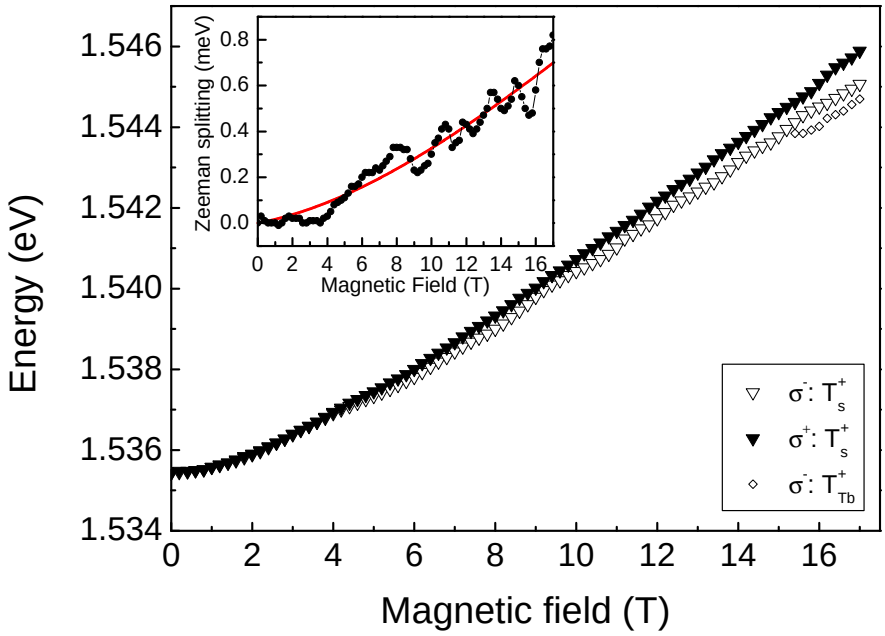

Fig. 3.11: *Energy position of the positive singlet trion for both polarizations in the p-type regime at* $T = 2.3$ K. *At high magnetic fields also the bright triplet state becomes visible. Inset shows the Zeeman splitting of the* X^+*-line, oscillations can be observed. Sample: 12216,* $T = 2.2\,K$, $\lambda_{exc} = 785\,nm$, $P_{exc} = 80\,mW/cm^2$,

At $B = 0$T only the positively charged trion T^+ can be observed in the p-type regime (Fig. 3.11). With increasing magnetic field the line splits into two lines which differ by their circular polarization due to the Zeeman effect. Starting from $B = 15$T also the bright triplet state of the trion becomes visible in σ^--polarization. A careful look at the spilling between the trion positions of different circular polarization reveals that it does not behave linearly. In the inset of Fig. 3.11 the Zeeman splitting is shown. Some oscillations of the splitting can be recognized. They may be due to a complicated valence band structure with (anti-)crossing Landau levels.

3.2 Photoluminescence in high magnetic fields

3.2.1 Spin and energy structure of positively and negatively charged excitons in CdTe/CdMgTe quantum wells

Optical studies of a modulation p-type doped 20 nm CdTe/CdMgTe quantum well (090505AC) have been performed at magnetic fields up to 15 T at the TU Dortmund and up to 33 T at the High Field Magnet Laboratory (HFML) in Nijmegen, the Netherlands. The type of resident carriers is inverted by above-barrier illumination to the electrons, which allows a comparative study of positively and negatively charged excitons in the same sample. Binding energy of the positively charged exciton decreases with growing field strength which is qualitatively different from known behavior for negatively charged excitons. Also the binding energy of triplet state is considerably smaller for positively charged excitons compared with the one of negatively charged excitons.

Introduction

Negatively charged trions have been studied in detail for QWs of different material systems: GaAs/AlGaAs, CdTe/CdMgTe and ZnSe/ZnMgSSe [Fin95, Khe93, Ast99]. Energy and spin structure have been analyzed in high magnetic fields up to 45 T and additionally to the ground singlet state few excited triplet states have been observed. Experimental picture is in good agreement with the model calculations performed [Ast05].

Experimental information on positively charged trions is rather limited. The positive singlet state was first observed in GaAs [Shi95a, Fin96a] and CdTe [Hau98]. Evidence for the triplet state of the positively charged trion was only reported for GaAs quantum wells by Glasberg [Gla99].

In ZnSe QWs [Ast99, Ast02] it was possible to distinguish T+ and T- by polarization of absorption. Different behaviour of the singlet state binding energy has been found. Contrary to the intuitive expectations T+ binding energy is smaller than the T- one. This fact has been confirmed by model calculations, which however are rather complicated due to complex structure of the valence band [Ess00].

Experimental

Sample for this study is a 20 nm CdTe/$Cd_{0.63}Mg_{0.37}Te$ single quantum well (QW) (090505AC). It was grown by molecular beam epitaxy on (100) oriented GaAs substrate. A top barrier separating the QW from the surface has a thickness of 135 nm. Sample is nominally undoped, but due to residual impurities the QW was slightly p-type doped. It contains a two-dimensional hole gas (2DHG) of a low density of a few 10^{10} cm^{-2}. Illumination with the light, which photon energy exceeds the band gap of $Cd_{0.63}Mg_{0.37}Te$ barriers (above 2.26 eV) increases the number of electrons in the QW and hence inverts the type of carriers (see Section 2.5.4). A two-dimensional electron gas (2DEG) of a density of a few 10^{9} cm^{-2} is achieved. We exploit this property to study positively and negatively charged excitons in the very same QW. This method has been used before to study T^- and T^+ ZnSe/(Zn,Mg)(S,Se) QWs, see Fig. 10 in Ref. [Ast02].

In this study we operate with 2D carrier gases of low densities. Their Fermi energies are smaller that the typical localizing potential for the carrier motion in QW plain. In the studied sample the localizing potential is about 0.5 meV which is evaluated from the broadening of exciton emission line.

Photoluminescence and reflection spectra

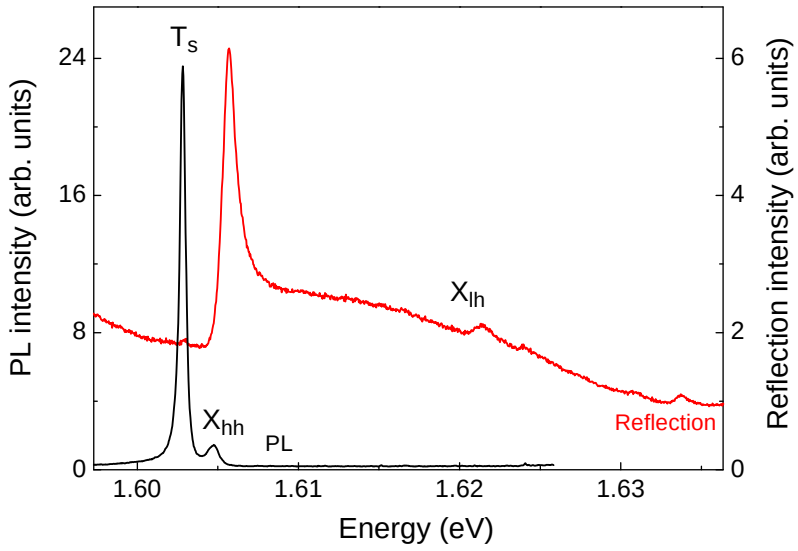

Fig. 3.12: *PL (black) and reflection (red) spectra of a 20nm CdTe/CdMgTe quantum well (090505AC) at B = 0 T and T = 0.35 K with excitation below the barrier of the sample, λ_{exc} = 745 nm, P_{exc} = 25 mW / cm^2. In the PL spectrum the neutral heavy hole exciton (X_{hh}) and the singlet state of the trion (T_s) are visible. In reflection spectrum also the neutral light hole exciton (X_{lh}) can be identified.*

Photoluminescence (PL) and reflectivity spectra were measured in high magnetic fields applied parallel to the structure growth axis (z-axis). Magnetic fields were generated either by superconducting solenoid (17 T) or resistive bitter magnet (33 T). Experiments were performed at low temperatures of 0.4 and 4 K. Light has been coupled to the sample via optical fibers, which ends with polarizers allowing analysis of circularly polarized light.

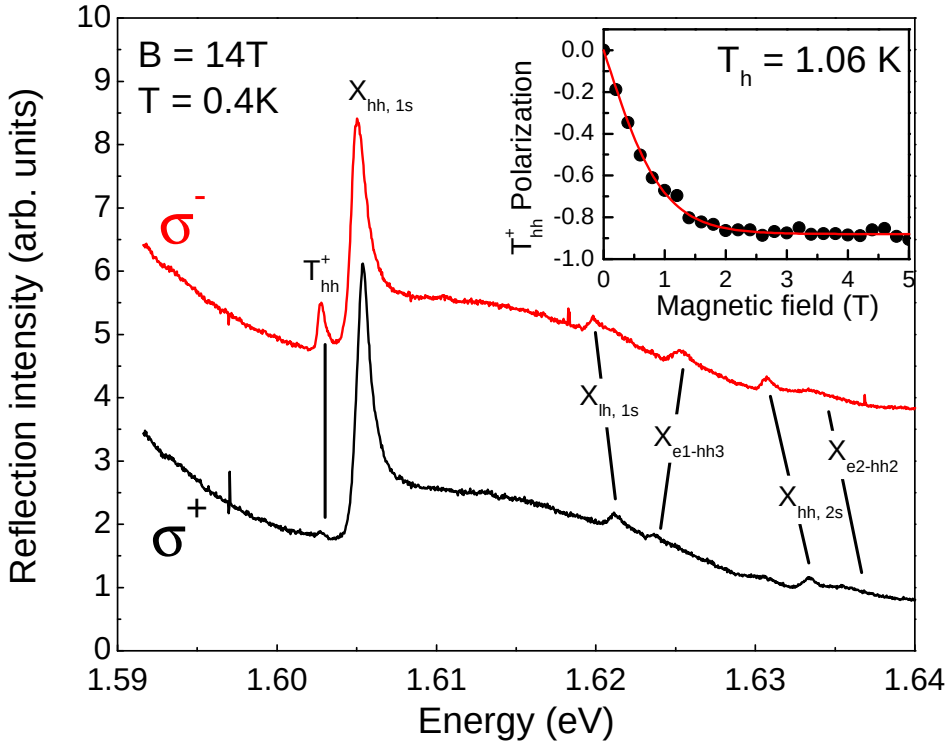

Fig. 3.13: *Reflectivity spectra at B = 14 T and T = 0.4 K for both circular polarizations. The sample was illuminated by a halogen lamp whose high energy part was cut by an RG 780 filter. The spectra are dominated by the 1s state of the heavy hole exciton. Signs for other exciton states are visible on the high energy side of X_{hh}, 1s which are labelled on the graph. A positively charged trion can be identified on the low energy side of the exciton which is fully polarized at 14 T. The polarization degree of the trion as a function of magnetic field is shown in the inset by solid circles. A fit (red line) to the polarization degree reveals a hole gas temperature of T_h = 1.06 K.*

The photoluminescence and reflection spectra of the sample at B = 0 T and T = 0.35 K are shown in Fig. 3.12. For the PL measurement the sample has been illuminated below the barrier by a TiSa-Laser with a wavelength of 745 nm (1.66 eV) in Dortmund and 710 nm (1.75 eV) in Nijmegen. For the reflection measurement, light of a halogen lamp has been used. The high energy part of the halogen spectrum was cut by a 3 mm RG780 filter so that for both measurements the sample was in the p-type regime were holes are the majority carrier type. Reflection measurements have also been done with additional illumination of an Nd:YAG laser

with a wavelength of 532 nm to bring the sample into n-type regime.

In the PL spectrum the neutral heavy hole exciton (X_{hh}) and the singlet state of the trion (T_s) are visible. The energy position of the exciton can be determined from the reflection spectrum. The reflection intensity is very sensitive to the oscillator strength which results in a pronounced exciton state in the reflection spectrum that allows identifying the energy position of the neutral exciton.

The reflection spectra at $B = 14\,\mathrm{T}$ also show additional peaks (Fig. 3.13) in both circular polarizations which are assigned to the neutral light hole exciton $(X_{lh,\,1s})$, 2S state of the exciton ($X_{hh,\,2s}$) and transitions between higher states of electron and heavy hole(X_{e1-hh3}, X_{e2-hh2}). The identification of lines has been done based on their behaviour with magnetic field (Fig. 3.18) but needs to be confirmed by calculations.

The inset of Fig. 3.13 shows the circular polarization degree of T_{hh}^{+} which is induced by magnetic field due to hole thermalization on spin sublevels and reaches almost 1 (i.e. 100%) for magnetic fields above 2 T. A fit (red line) to the polarization degree reveals a hole gas temperature of $T_h = 1.06\,\mathrm{K}$, which is above the bath temperature $T_{bath} = 0.4\,\mathrm{K}$, probably due to the power of the excitation laser. Exciton resonances are only weakly polarized, most probably due to X-hole exchange scattering [Ast00].

Excitons

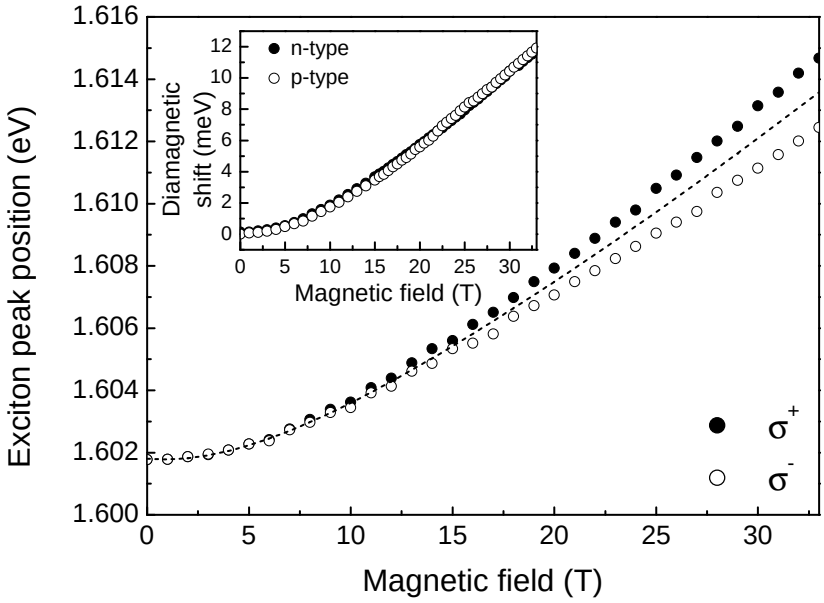

Fig. 3.14: *Exciton peak position from reflectivity measurement at T = 4.2 K. Closed symbols show σ^+-polarization, open symbols σ^--polarization. The dashed line shows the center of gravity, i.e. the exciton peak position without Zeeman splitting. Inset shows the diamagnetic shift for n- and p-type in comparison.* Sample: 090505AC.

Photoluminescence spectra have been recorded for both circular polarizations corresponding to two spin states of the exciton. In order to derive the diamagnetic shift of the exciton line the center of gravity of the exciton spin doublet has been evaluated and plotted as a function of magnetic field (dashed line in Fig. 3.14). The inset shows the diamagnetic shift in both, n- and p-type regime. It seems to be equal.

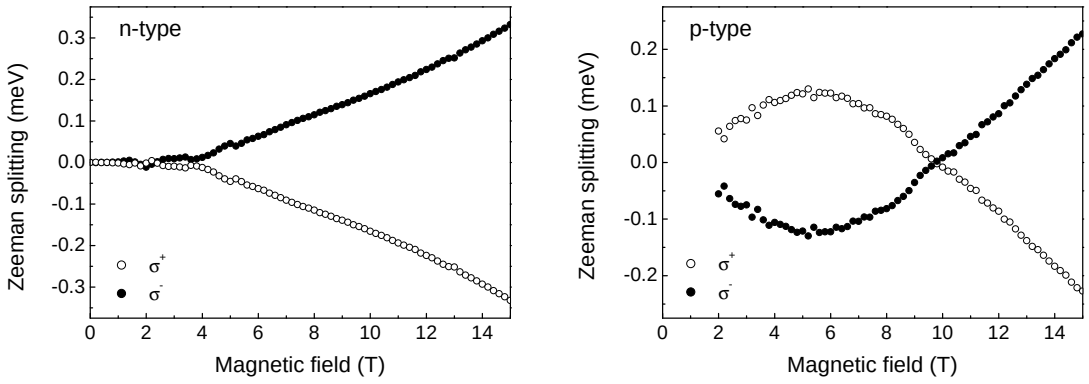

Fig. 3.15: *Zeeman splitting of the exciton in n- and p-type regime. Sample: 090505AC, T = 4.2 K, p-type excitation: λ_{exc} = 745 nm, P_{exc} = 25 mW / cm^2, n-type excitation: λ_{exc} = 532 nm, P_{exc} = 1 mW / cm^2.*

If the center of gravity is subtracted from the energy position of the exciton line values for the Zeeman splitting can be derived (Fig. 3.15).

For the n-type regime the Zeeman splitting increases linearly with the magnetic field strength up to around 12 T. Beyond this point a small deviation can be observed. The exciton spin splitting results from the splitting of conduction and valence band which are characterized by their gyromagnetic ratios g_e in case of the electron and g_{hh} in case of the heavy hole. The g factor for the exciton can be expressed as: $g_x = g_{hh} - g_e$. It is known that the electron g-factor increases linearly with the magnetic field up to very high fields.

So deviations from this behaviour can be ascribed to the heavy hole g-factor. Its changes are caused by an admixture of light hole states in high magnetic fields. The Zeeman splitting of the exciton behaves in an untypical way when the sample is illuminated below the barrier. Up to around 5.5 T the Zeeman splitting increases. At higher magnetic fields the splitting starts to decrease and becomes zero at around 10 T. Further above, a sign inverse of the splitting occurs which can be deduced to a change of the hole — and hence the exciton g-factor. Figure 3.16 shows the g-factors for electron, hole, exciton and trions which have been derived from photoluminescence and reflectivity measurements.

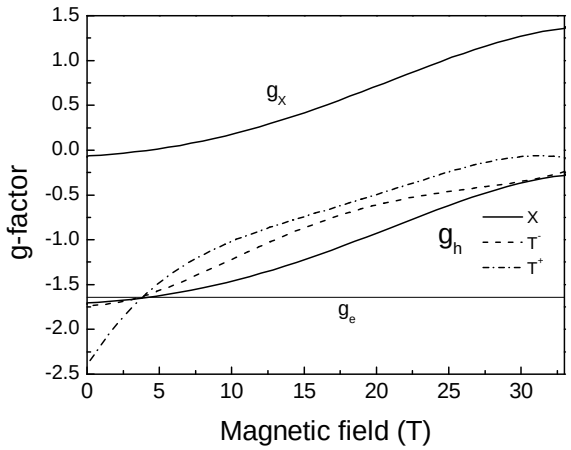

Fig. 3.16: *Shown are g-factors for electron, hole, and exciton which have been derived from PL and reflectivity measurements of sample 090505AC.*

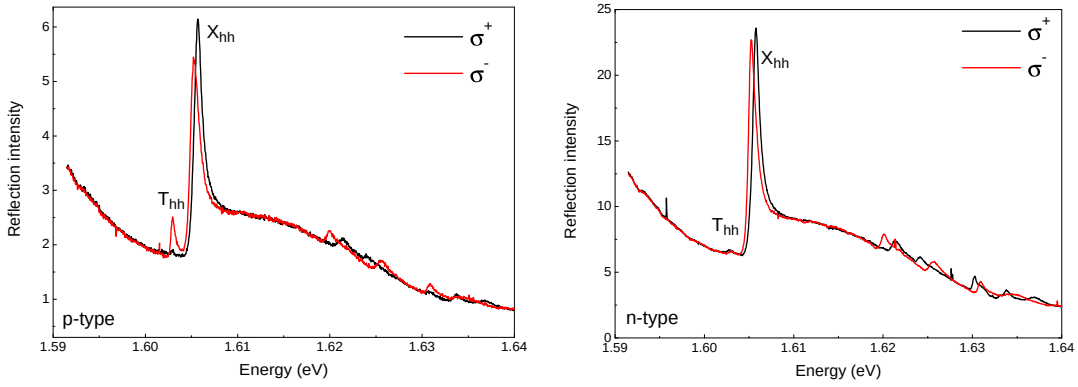

Fig. 3.17: *Reflection spectrum at B = 15 T. Left: halogen lamp with RG780 filter. Right: additional illumination by 532 nm laser light. Sample: 090505AC, T = 2.2 K.*

In Fig. 3.17 reflection spectra are shown in the p- and n-type regime at B = 15 T. Without additional illumination above the barrier there is a strong trion signal (T_{hh})

in σ^--polarization. It is suppressed in the n-type regime. Due to the sensitivity of reflection measurements to the oscillator strength of the energy states, the identification of the exciton signal is unambiguous.

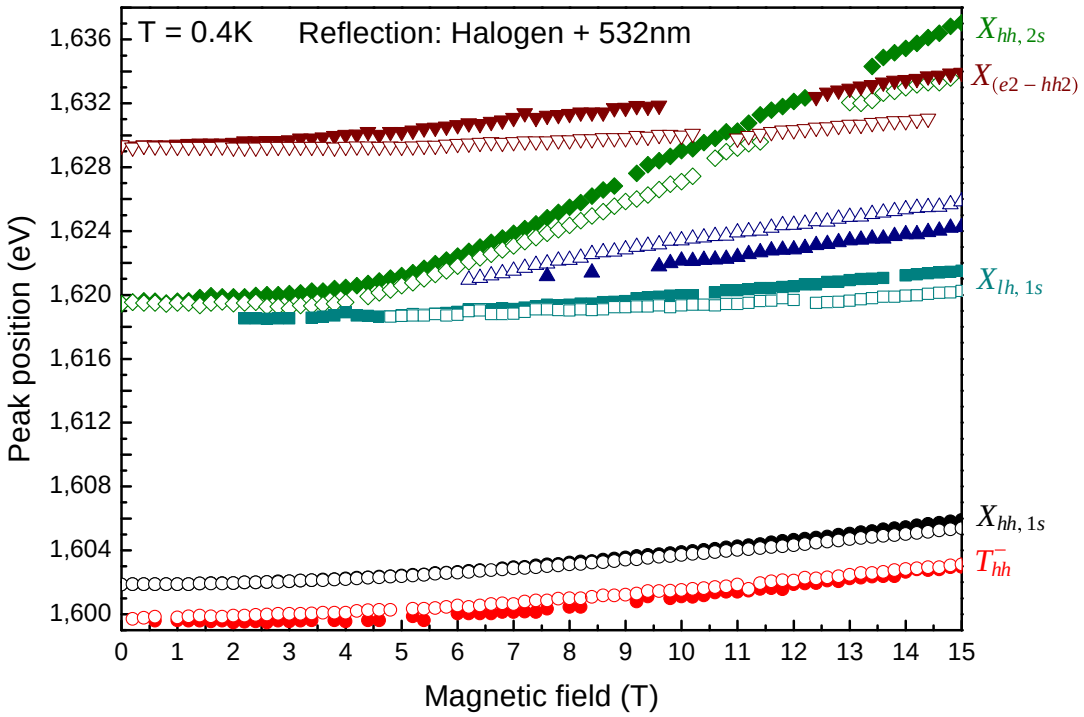

Fig. 3.18: *Energy positions of neutral and charged excitons taken from reflection measurement with additional above barrier illumination ($\lambda_{exc} = 532\,nm$, $P_{exc} = 0.3\,mW/cm^2$). Sample: 090505AC, $T = 0.35\,K$*

The oscillator strength of the neutral exciton exceeds the one of all other (quasi) particles so that it becomes the strongest signal in the reflection spectrum. Its energy position differs only slightly from the one in PL measurements which allows assigning the peaks found in the photoluminescence accordingly.

The evolution of the energy positions of neutral and charged excitons is shown in Fig. 3.18 up to 15 T. Despite the usual number of peaks found in photoluminescence more features can be identified in reflection spectra due to the contribution of unoccupied states. Apart from the 1S state of the heavy hole exciton $(X_{hh,\,1s})$ and singlet trion (T^-_{hh}) the 2S state of the exciton ($X_{hh,\,2s}$) can be identified as well as the light hole exciton ($X_{lh,\,1s}$).

Schematics for trion energy and spin structure in magnetic field

With the results from PL and reflection measurements it is possible to create a scheme for the singlet and triplet spin structure of exciton and trion as described in the Appendix.

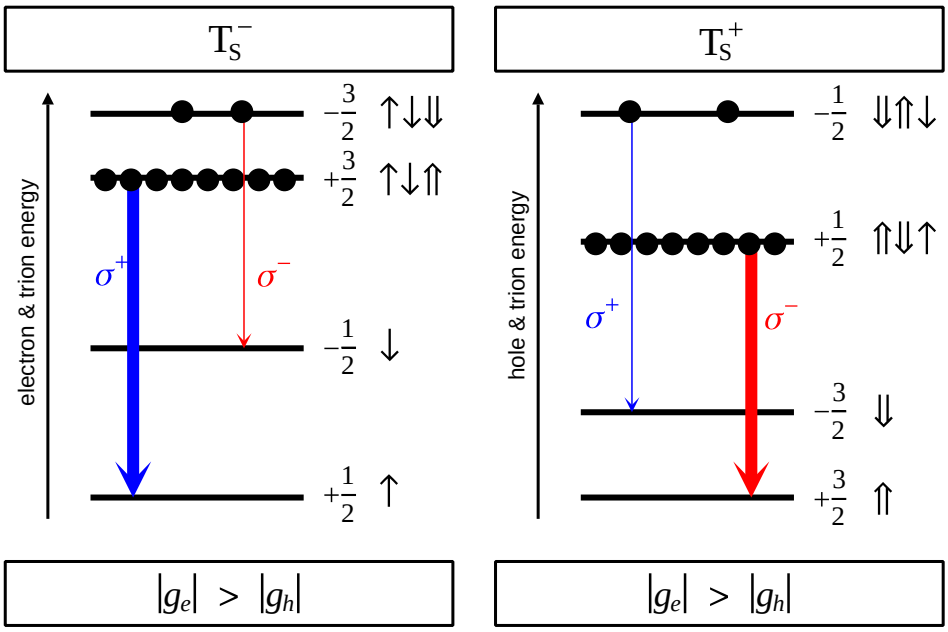

Fig. 3.19: *Illustration of the trion and electron (hole) energy levels and recombination energies. Electrons are represented by arrows (↑, ↓), holes by double-arrows (⇑, ⇓).*

Negatively and positively charged trion can be distinguished by their polarization. In Fig. 3.19 the spin structure of negatively (left) and positively (right) charged trions are shown. Electrons are represented by arrows (↑, ↓), holes by double-arrows (⇑, ⇓). The ground state emission is differently polarized, σ^+ for X^- and σ^- for X^+. The experimental results discussed in the next subsection coincide very well with this scheme. The spin structure for the triplet states of positively and negatively excitons is shown in Fig. 3.20 together with the polarization of spin allowed transitions.

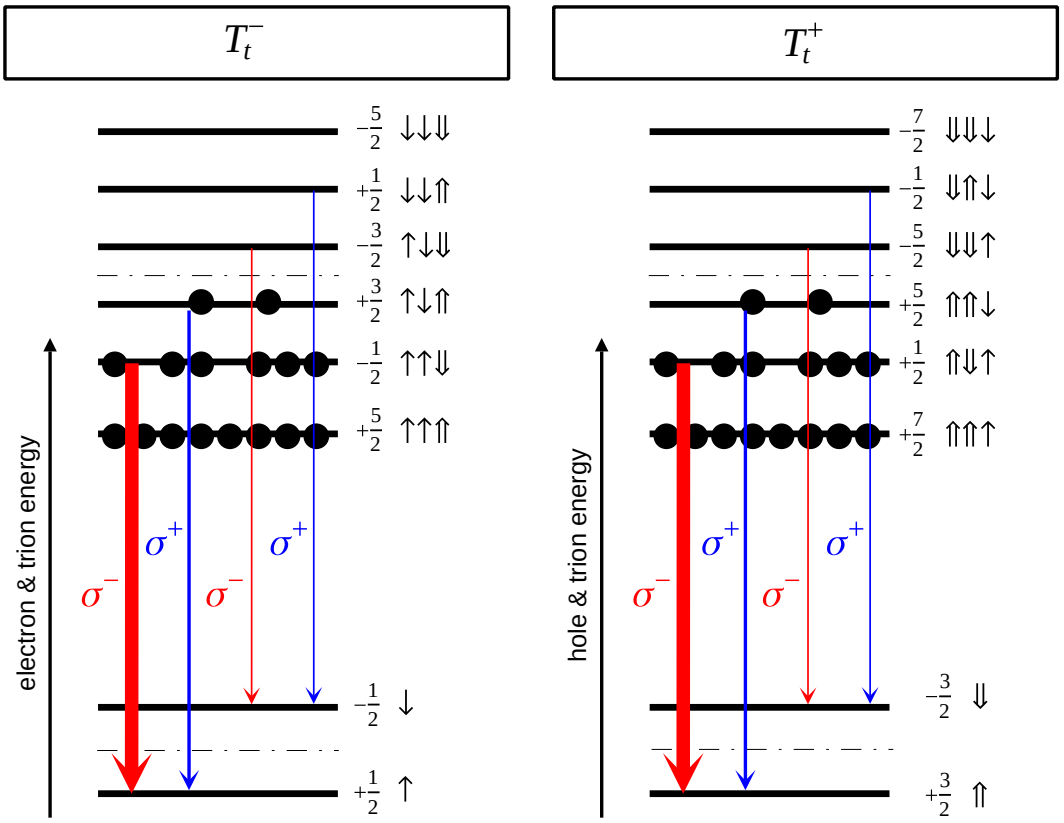

Fig. 3.20: *Scheme of the triplet trion and electron (hole) energy levels and recombination energies. Electrons are represented by arrows (↑, ↓), holes by double-arrows (⇑, ⇓).*

Identification of charged excitons in the p- and n-type regime

Figure 3.21 (a) shows two spectra at $B = 0$ T for illumination below and above the barrier. The exciton is more pronounced at the excitation wavelength of 532 nm. Also for the reflection measurements shown in Fig. 3.28 (b) difference between both regimes is indicated by the suppression of the trion peak in σ^--polarization when the sample is illuminated by the low energy part of an halogen lamp and light of a 532 nm laser.

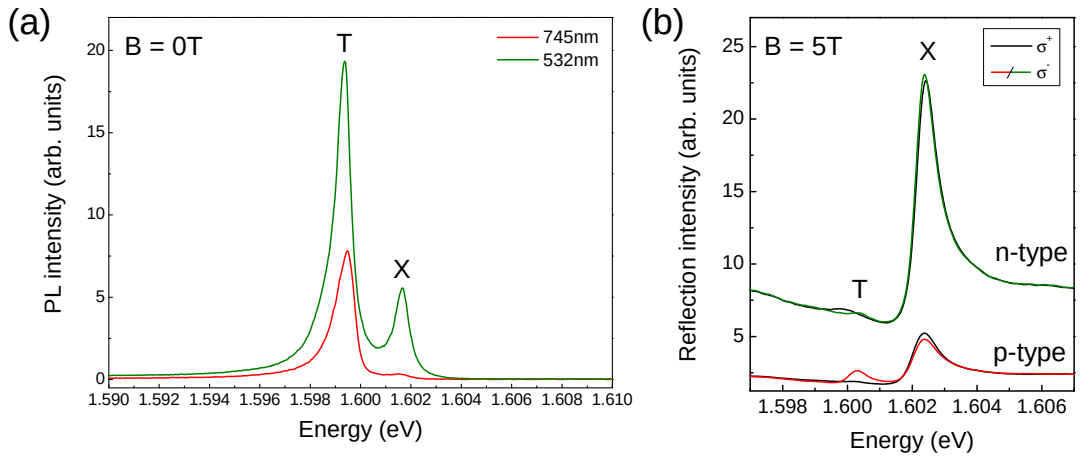

Fig. 3.21: *(a) PL at $B = 0T$ and $T = 0.35K$ for two different excitation wavelength: 1. below the barrier at 745 nm ($P_{exc} = 25\,mW/cm^2$) which leaves the sample in the p-type regime (red line) and 2. above the barrier ($\lambda_{exc} = 532\,nm$, $P_{exc} = 0.3\,mW/cm^2$) which activates more electrons and leads to an n-type regime of the sample (green line). (b) Reflectivity spectra at $B = 5T$ for both circular polarizations in n- and p-type regime.*

The magnetic field dependence of peak positions for the neutral and charged excitons is shown in Fig. 3.22 for comparison of below (a) and above (b) barrier illumination. Fundamental differences can be observed. The behaviour of the exciton spin splitting in the p-type regime has been discussed before. The singlet trion state can be observed in both regimes as a high intense peak below the exciton. A comparison between both regimes shows a population inversion of the high and low trion spin state in the photoluminescence. To understand these phenomena it is important to keep in mind that the energy of the observed photoluminescence transitions depends on both conduction and valence band states. So also for the n-type regime a high population of the low energy electron spin state can be assumed. Depending on the configuration of the hole states the recombination energy of this state may still exceed the one of the higher electron state.

In the n-type regime a new line appears above 5 T which can be assigned to the triplet trion state. It can not be observed for illuminations below the barrier.

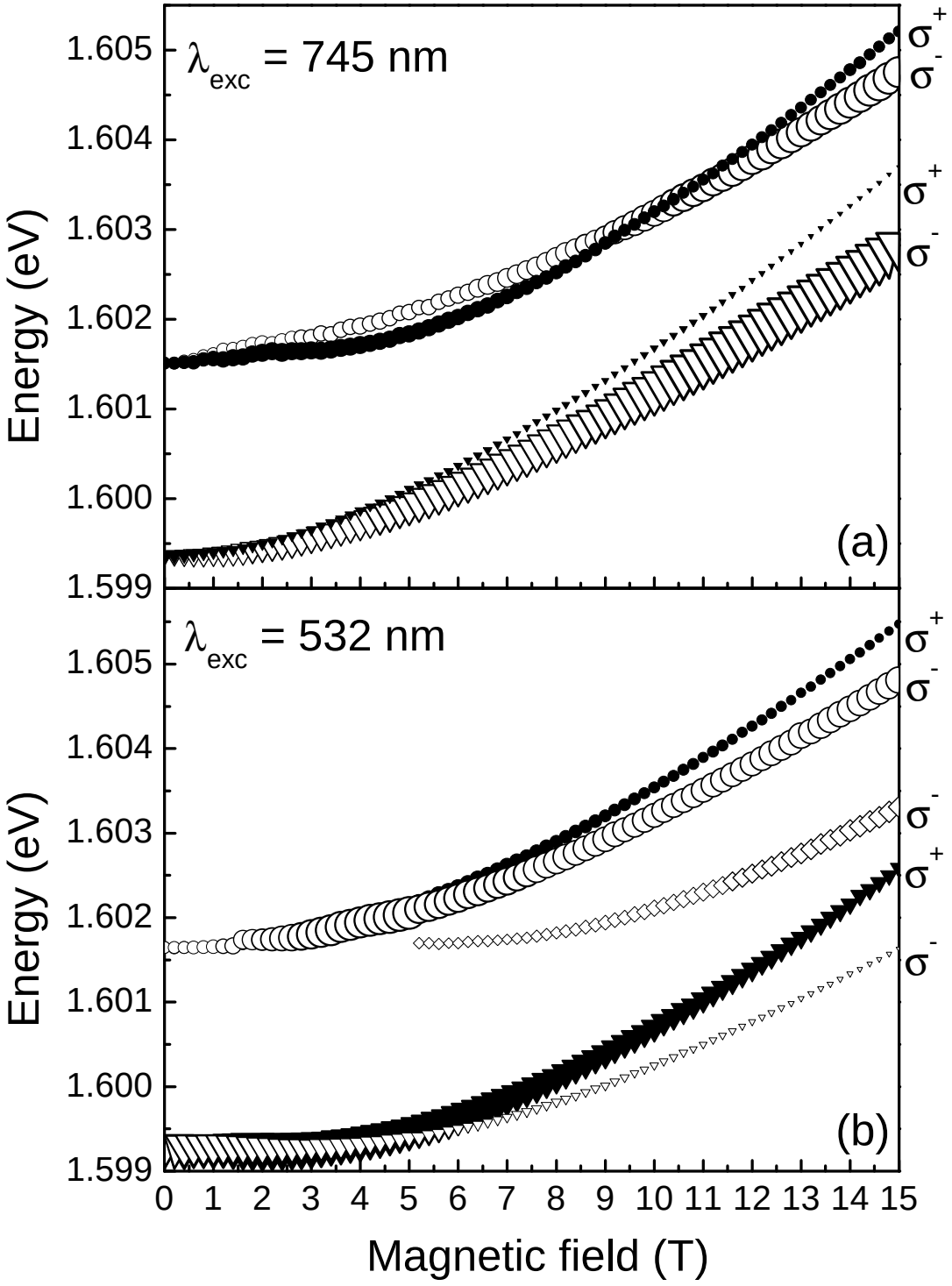

Fig. 3.22: *Energy positions of neutral excitons (X) and both singlet (T_s) and triplet (T_t) trions in σ^+-Polarization (closed symbols) and σ^--Polarization (open symbols) as a function of magnetic field at T = 0.35K. (a) PL in the p-type regime (b) PL of the sample in n-type regime. Sample: 090505AC, p-type excitation: λ_{exc} = 745 nm, P_{exc} = 25 mW / cm^2, n-type excitation: λ_{exc} = 532 nm, P_{exc} = 0.3 mW / cm^2.*

The strong dependence of the photoluminescence on the illumination wavelength can be understood if one assumes that in the p-type regime a positively charged trion is formed and a negatively charged one in the n-type regime. A scheme for the singlet state of the positively charged trion is shown in Fig. 3.19 (a). The trion spin $S_T = +1/2$ is lower in energy than the $S_T = -1/2$ state and therefore more densely populated. Upon recombination of the trion a hole is left in the $S_h = +3/2$ state. The emitted photon is σ^- polarized $(+1/2 - (+3/2) = -1)$. Together this explains the high intensity of the σ^- polarized trion line when compared to the σ^+ line. The absolute value of the electron g-factor exceeds the one of the hole and leads to a higher energy of the σ^+ polarized photons.

If the sample is illuminated by a Nd:Yag laser (532nm) above the barrier the behaviour changes. There is no crossing of the differently polarized exciton lines. The trion singlet lines (T_s^-) are remarkable because the higher state shows a stronger PL intensity than the lower state which may appear counter intuitive.

From the PL in Fig. 3.22 (b) evidence of the dark triplet trion (T_t^-) state can be found in σ^--polarization. The observation can be explained by the assumption that due to the changes in illumination negatively charged trions are formed in the system. A scheme is shown in Fig. 3.20 (b). The bright triplet state may appear at even higher magnetic fields. In some CdTe quantum wells the bright triplet state has only been observed above 35 T [And05].

The lower and highly populated singlet trion state $S_{T_s} = +3/2$ may recombine and leave the remaining electron in the $S_e = +1/2$ state. The emitted light is σ^+ polarized $(+3/2 - (+1/2) = +1)$. From the higher $S_{T_s} = -3/2$ state an electron in the $S_e = -1/2$ state is left behind emitting a σ^--polarized photon $(-3/2 - (-1/2) = -1)$. Still the energy of this recombination is lower than the one emitting the σ^+-polarized photon. So the origin of the strong intense σ^+ line is the ground state of the singlet trion but due to the large splitting of the electron states, which exceeds the hole splitting, the energy of this recombination is higher than the one from the higher trion state. This can also be seen in Fig. 3.20 by comparing the length of the arrows in (a) and (b).

Binding Energy

The binding energy has been evaluated from the center of gravity of the exciton and trion spin doublet in order not to take into account the spin splitting. The trion binding calculated from the photoluminescence data for a temperature of 0.4 K and 4.2 K is shown in Fig. 3.23 (a). The behaviour for both temperatures is very similar. The evolution of the binding energy is fundamentally different between n- and p-type regimes. The binding energy of the negatively charged trion exceeds the one of the positively charged one. This has also been observed for ZnSe-based quantum wells by Astakhov [Ast02]. They deduce it to the Coulomb repulsion between holes which is stronger in the QW than the one between electrons. The negatively charged trion complex consists of two electrons and one hole. The localization of

the electron wave function increases with the magnetic field and brings the electrons closer to the center hole which leads to an increase of the binding energy.

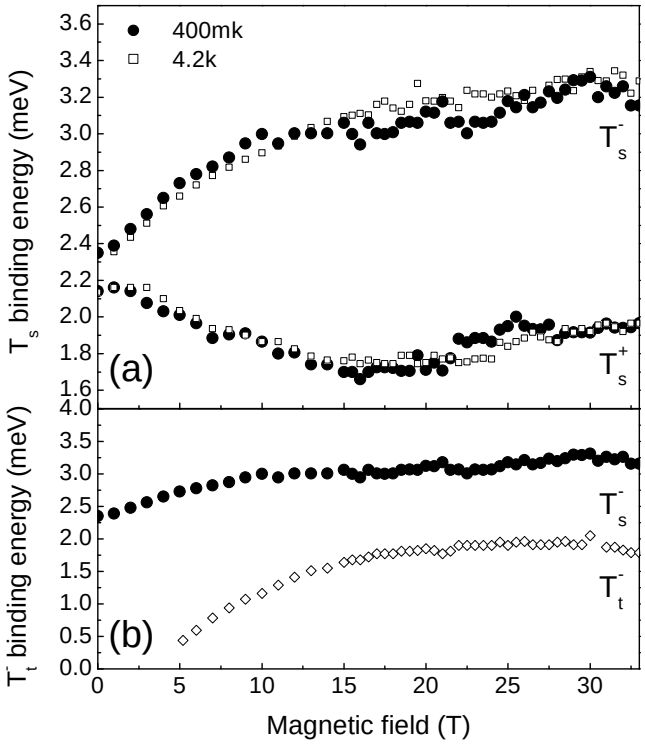

Fig. 3.23:
Trion binding energy calculated from the peak position of X and T in photoluminescence for both the n- and p-type regime.
Sample: 090505AC,
p-type excitation:
$\lambda_{exc} = 745\,nm$,
$P_{exc} = 25\,mW/cm^2$,
n-type excitation:
$\lambda_{exc} = 532\,nm$,
$P_{exc} = 0.3\,mW/cm^2$.

For the case of the positively charged exciton the situation is not so clear. The electron is shared between two holes and the reduction of the magnetic length with increasing B-field does not bring the electon closer to the holes. This behaviour may even lead to a decrease of the binding energy because the electron can not be bound to both holes equally well.

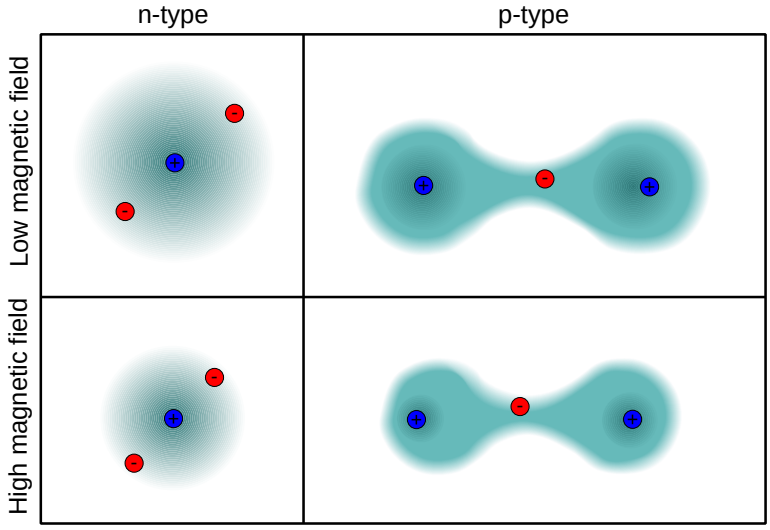

Fig 4.24:
Illustration of the trion binding energy at low and high magnetic fields.

A comparison between singlet and triplet state is given in Fig. 3.23 (b). As expected the binding energy of the triplet trion is lower than the singlet one. It seems to be unbound for $B < 3$T. For that reason the triplet state can only be observed at magnetic fields exceeding $B = 5$T.

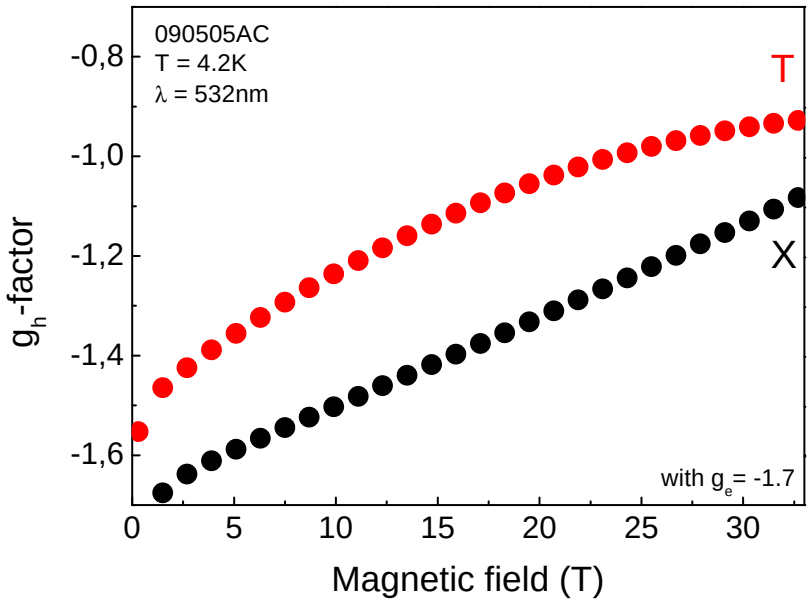

Fig. 3.25: *Hole g-factor for exciton (X) and Trion (T_s^-) derived from photoluminescence measurements in the n-type regime.*

Negatively charged triplet trion

Fig. 3.26 shows the energy position of peaks found in the photoluminescence. A spectrum at $B = 32$ T is shown in Fig. 3.27 for both circular polarizations. As already observed in PL measurements up to 15T (Fig. 3.22), the σ^+-polarized singlet trion state appears at a higher energy in the PL spectrum. It is stronger in intensity than the σ^--polarized line which indicates that its initial state is lower in energy, see also singlet trion scheme in Fig. 3.19. In the PL also the dark triplet state can be observed for $B > 5$ T. It crosses the σ^+-polarized singlet trion state at a magnetic field of around 22 T.

A similar result has been published for a 12 nm CdTe/CdMgTe QW, see Fig. 3 (a) in [Ast05]. There, a hidden crossing of singlet and triplet trion state was observed. While the σ^--polarized singlet trion state appeared at the lowest energy up to 44 T, its PL intensity strongly changed around $B = 24$ T. In the publication this was explained by a hidden crossing of singlet and triplet trion states, where the initial triplet state became the lowest energy state for magnetic fields above 24 T. The crossing could be made visible in Fig. 3 (b), [Ast05], which shows the initial energies of all trion states, measured with respect to the center of gravity of the neutral exciton

Zeeman doublet, which accounts for the overall diamagnetic shift.

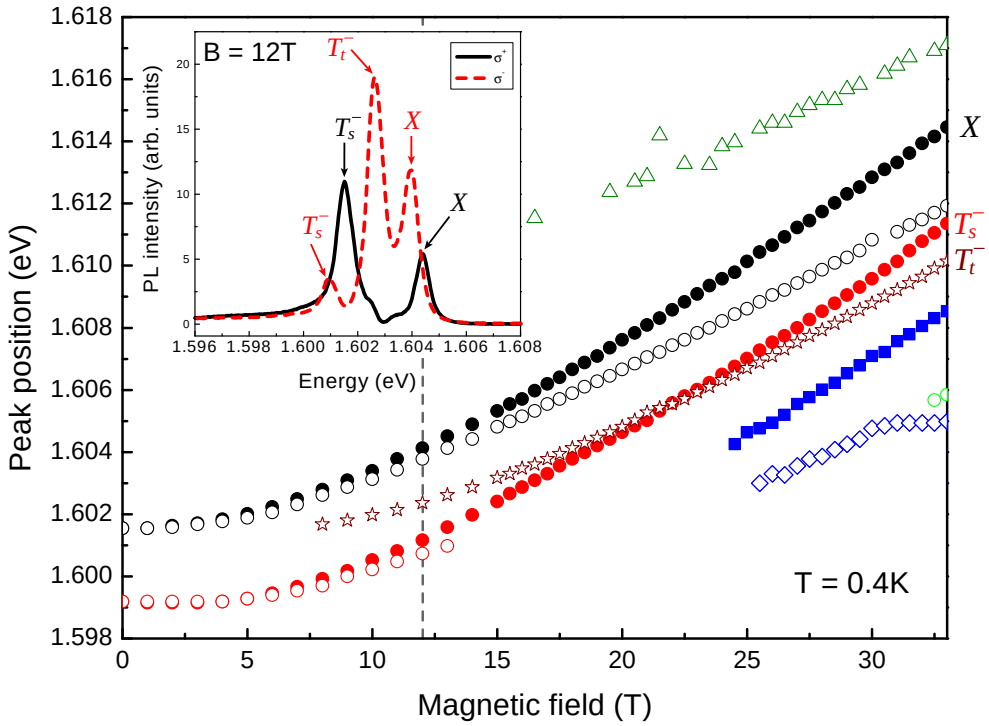

Fig. 3.26: *Energy positions up to 33 T in the n-type regime. Inset shows spectrum at B = 12T for both circular polarizations. Sample: 090505AC, T = 0.4 K, λ_{exc} = 532 nm, P_{exc} = 2 mW / cm^2.*

In Fig. 3.28 (a) the energy of the initial singlet and triplet trion states relative to the exciton are shown for sample 090505AC by subtracting the diamagnetic shift of the exciton in analogy to Fig. 3 (b), [Ast05]. It shows that the σ^+-polarized singlet trion state is indeed lower in energy than the σ^--polarized singlet trion. The crossing for the strongest spin allowed transitions $T_t\ (-1/2 \rightarrow +1/2)$, σ^- and $T_s\ (+3/2 \rightarrow +1/2)$, σ^+ can also be observed in the PL and is therefore "not hidden", i.e. crossing of optical transitions corresponds to energy coincidence of trion states. This can be explained by the final electron state which is the same for both transitions: $+1/2$.

At magnetic fields around 22 T, strong changes of the photoluminescence intensity can also be observed . The intensity of the trion line in σ^+-polarization has a distinct peak at around 22 T (Fig. 3.28 (b)). Up to this point the intensity increases with the magnetic field. At 22 T a crossing of the σ^+-polarized singlet and σ^--polarized triplet trion occurs and the triplet state becomes the lowest state. The crossing leads to a redistribution of the population density towards the triplet state. This is also reflected in the line intensity of singlet and triplet state at high magnetic fields, see Fig. 3.28 (b). It is not clear where the resonant increase of T_s intensity comes from.

In case of the 12 nm QW the situation was different, leading to a hidden S-T crossing which could only be observed in line intensities and not their PL positions [Ast05]. This can be explained by different g-factors. Section A.4 of the Appendix

summarises the conditions for visible or hidden S-T crossings.

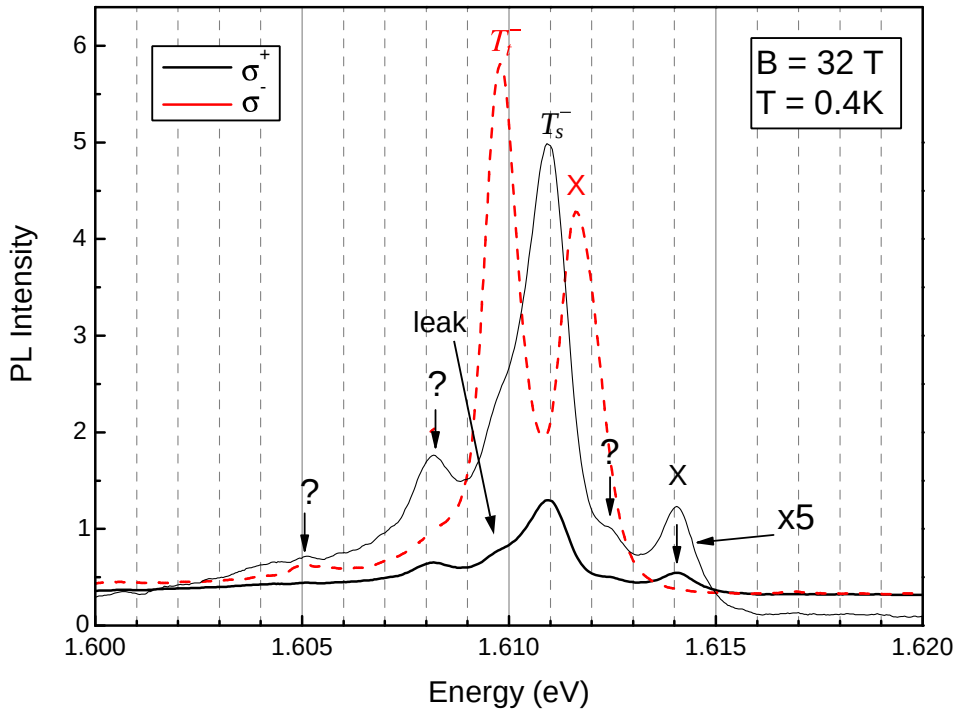

Fig. 3.27: *PL at B = 32* T*: In σ+-Polarization five peaks can be recognized at the low energy side of the exciton and of the trion. Sample: 090505AC, T = 0.4 K, λ_{exc} = 532 nm, P_{exc} = 2 mW / cm².*

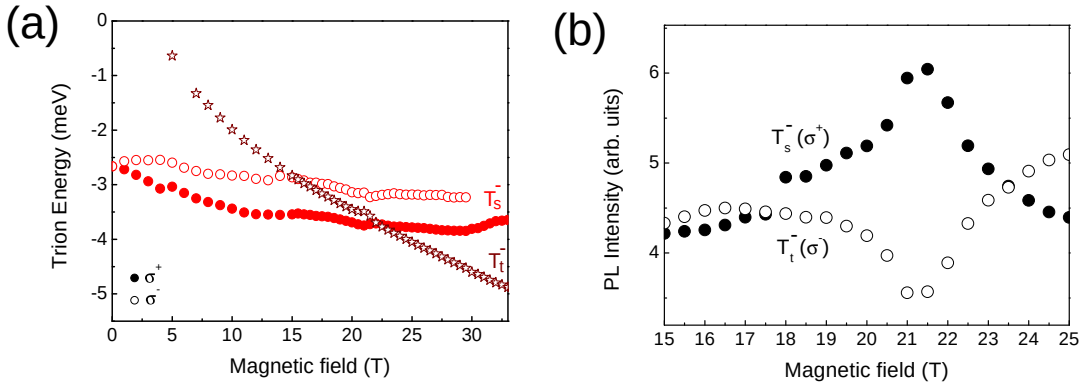

Fig. 3.28: (a) *Energy of the initial singlet and triplet trion states relative to the exciton in the n-type regime. Crossings can be identified at B = 16 and 22 T. (b) Dependence of peak amplitude for the singlet and triplet trion state. Sample: 090505AC, T = 0.4 K, λ_{exc} = 532 nm, P_{exc} = 2 mW / cm².*

Some additional lines appear at high magnetic fields in Fig. 3.26 and Fig. 3.27, where they have been marked by question marks because of their unknown origin.

Positively charged triplet trion

If higher magnetic fields are applied, the sample in the p-type regime shows two more peaks in σ^+-polarization than in magnetic fields up to 15 T (Fig. 3.22). One emerges from the exciton at fields above 24 T (blue squares in Fig. 3.29). The second peak is situated below the trion singlet state (red wine colored stars).

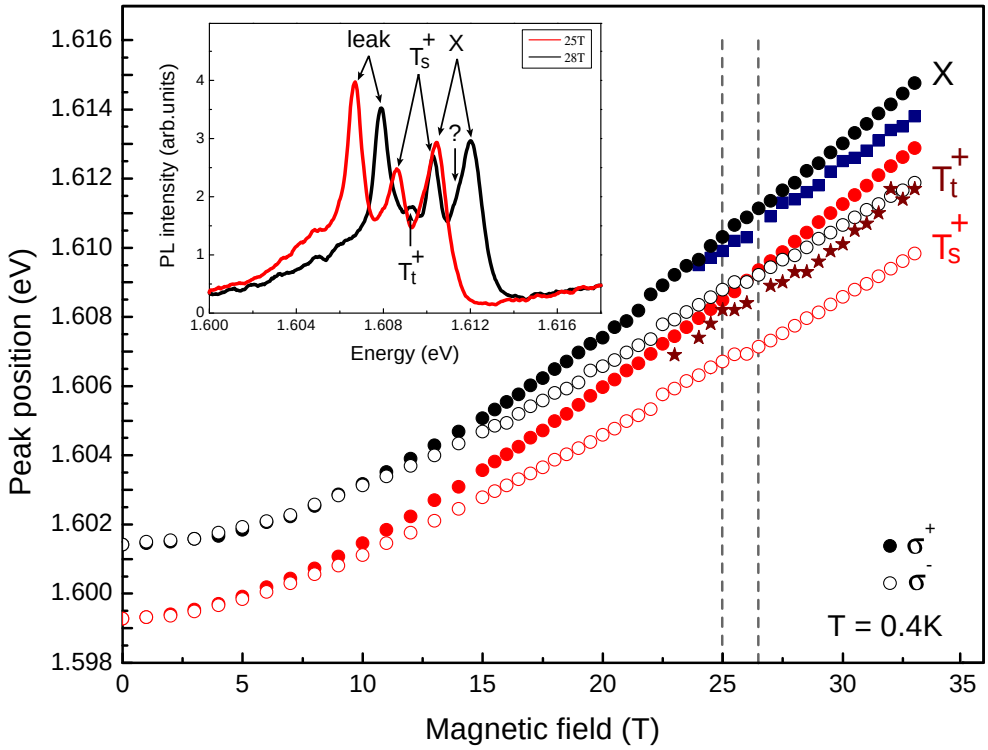

Fig. 3.29: *Energy positions up to 33 T in the p-type regime. Two additional peaks can be identified at high magnetic fields (blue squares and wine red stars). Inset shows PL spectra at 25 T and 28 T in σ^+-polarization. Sample: 090505AC, $T = 0.4\,K$, $\lambda_{exc} = 710\,nm$, $P_{exc} = 10\,mW/cm^2$.*

Spectra for both circular polarizations at $B = 32$ T are presented in Fig. 3.30. The σ^+-polarization (black curve) is lower in intensity and has been shown with a scaling factor of 8 for better comparability.

Five peaks can be recognised which have been marked by black arrows. However, the lowest energy peak has been rated as leakage since it follows exactly the position of the trion in σ^--polarization which is very strong in intensity. The peak at the low energy side of the singlet trion state may belong to the triplet state of the positively charged trion. An overview of the energy levels of triplet trion states for both polarizations is shown in Fig. 3.20.

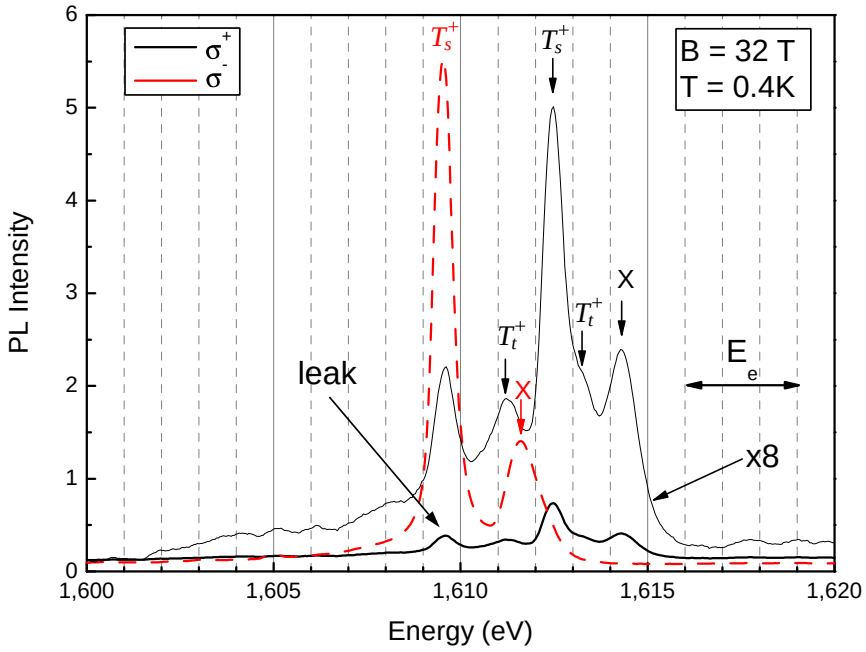

Fig. 3.30: *PL at $B = 32$ T: In σ^+-Polarization four peaks can be recognized at the low energy side of the exciton and of the trion. Sample: 090505AC, $T = 0.4\,K$, $\lambda_{exc} = 710\,nm$, $P_{exc} = 10\,mW/cm^2$.*

The $+7/2$ ground state of the positive triplet trion is spin forbidden. The lowest spin allowed state of T_t^+ is σ^--polarized and can not be observed because it falls on top of the exciton recombination which is higher in intensity. However, one line appears at an energy position corresponding to the T_t $(+7/2 \rightarrow +3/2)$, σ^+ transition. It has a +2 spin difference and is therefore not bound due to the Coulomb term, but can be bound due to Zeeman term. Also the polarization fits to the expectations. This will be discussed in more detail later. The second additional line that can be observed in σ^+-polarization coincides with the expectations for the spin allowed T_t $(+5/2 \rightarrow +3/2)$ transition.

The peaks found in the photoluminescence in the p-type regime were shown in Fig. 3.29. They have been plotted again in Fig. 3.31 subtracting the diamagnetic shift of the exciton gravity center. Wine red colored stars indicate the position of the additional line found in the PL spectra. Since the electron g-factor g_e is known and the hole g-factor g_h can be derived from experimental data, the splitting from the exciton center of gravity can be calculated for all triplet trion positions with the help of the triplet trion scheme shown in Fig. 3.20.

As an example the situation at $B = 30$ T will be discussed. The electron g-factor was determined as $g_e = -1.7$ leading to an electron Zeeman splitting of: $\Delta E_e = 0.058 \cdot (-1.7) \cdot 30\,T = 2.95\,meV$. The exciton Zeeman splitting of 2.36 meV is taken from experimental data shown in Fig. 3.35 at 30 T. With both values the hole splitting and g_h-factor can be derived:

$\Delta E_e = 2.95\,\text{meV}$	$g_e = -1.70$
$\Delta E_x = 2.36\,\text{meV}$	$g_x = +1.36$
$\Delta E_h = 0.59\,\text{meV}$	$g_h = -0.34$

The optical transition $(+7/2 \rightarrow +3/2)$ should be shifted from exciton gravity center by $\frac{1}{2}(\Delta E_e + \Delta E_h) = 1.77\,\text{meV}$ (zero Coulomb binding energy was considered for triplet T^+). This value compares very well to the splitting of 1.73 meV which was observed experimentally for the unidentified line at 30 T.

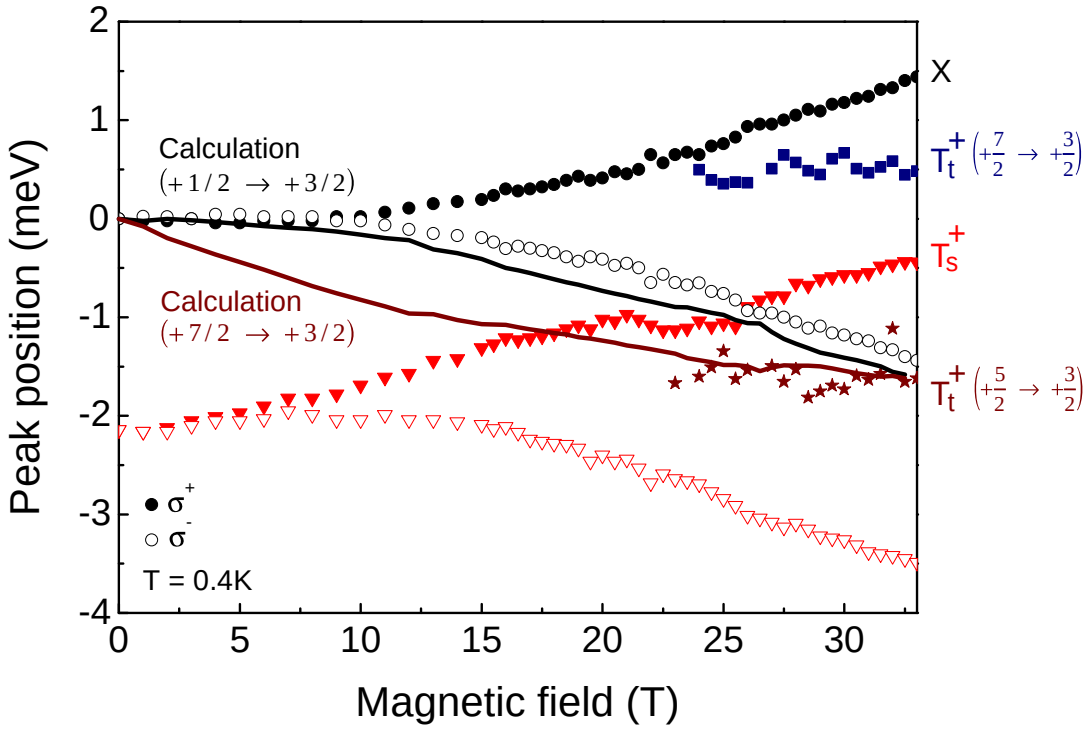

Fig. 3.31: *Symbols represent peak positions of exciton and trion complexes in p-type regime where the diamagnetic shift of the exciton has been subtracted from all peak positions. Solid lines show calculations for the $(+7/2 \rightarrow +3/2)$ transition (wine red colored line) and $(+1/2 \rightarrow +3/2)$ transition (black line).*

However, a value for the hole g-factor can also be derived from the splitting of the positively charged singlet trion. Experimental splitting of singlet T^+ is found to be $\Delta E_{T^+}(30\,\text{T}) = 2.7\,\text{meV}$, resulting in a hole g-factor of $g_h(30\,\text{T}) = -0.09$ and $\Delta E_h(30\,\text{T}) = 0.15\,\text{meV}$. The optical transition $(+7/2 \rightarrow +3/2)$ should than be shifted by 1.55 meV from exciton gravity center. For this case the expected position of the $(+7/2 \rightarrow +3/2)$ recombination is shown as red wine colored solid line in Fig. 3.35. It coincides very well with the observed peak positions. Therefore we may conclude that the line is the spin forbidden state of th T^+ triplet. Its optical transition $(+7/2 \rightarrow +3/2)$ goes from the lowest spin level $+7/2$ of T^+, i.e. is ther-

mally favourably occupied. However, an additional scattering process is necessary for the +2 spin transition to occur.

The calculated for the lowest allowed transition $(+1/2 \rightarrow +3/2)$ is plotted as black line. It is very close to the σ^--polarized exciton recombination and equally polarized. This makes it hard to distinguish the $(+1/2 \rightarrow +3/2)$ recombination in the PL spectrum. An additional line (blue squares in Fig. 3.35) is observed emerging from the σ^+-polarized exciton line. Its origin may be related to the $(+5/2 \rightarrow +3/2)$ transition of the triplet trion which is also σ^+-polarized.

Polarization degree of trion emission

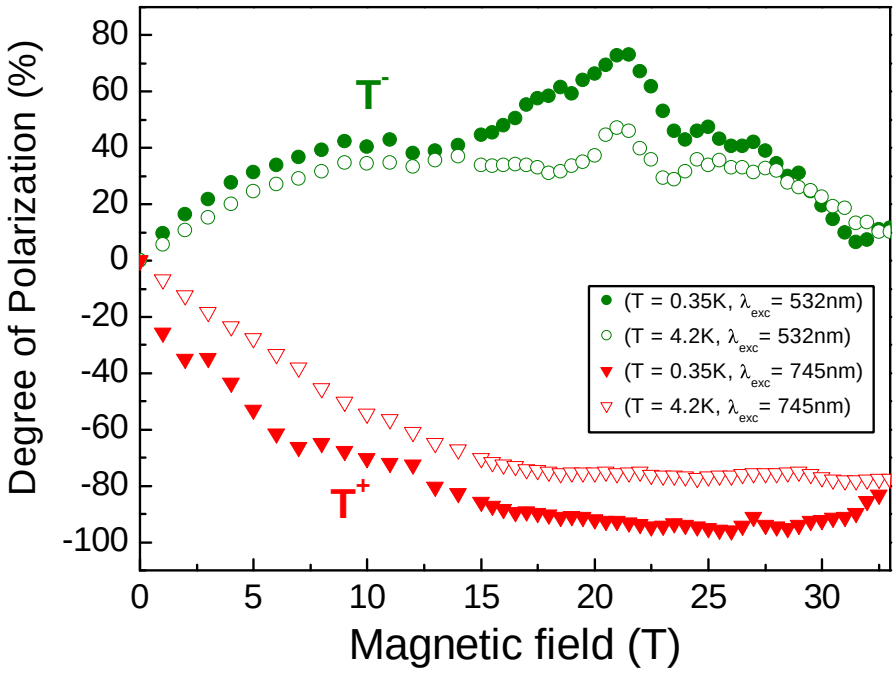

Fig. 3.32: *Polarization for the negatively (green symbols) and positively (red symbols) charged trion at T = 0.35K (closed symbols) and T = 4.2K (open symbols). Sample: 090505AC, p-type excitation:* $\lambda_{exc} = 710\,nm$, $P_{exc} = 10\,mW/cm^2$, *n-type excitation:* $\lambda_{exc} = 532\,nm$, $P_{exc} = 2\,mW/cm^2$.

Circular polarization degree due to trion thermalization on the spin levels in magnetic field are shown in Fig. 3.32. The polarization dependence of the positively and negatively charged trion has been measured as a function of magnetic field at two temperatures of 0.35 K and 4.2 K. The polarization has been calculated according to the following expression:

$$P = \frac{I(\sigma^+) - I(\sigma^-)}{I(\sigma^+) + I(\sigma^-)} \tag{4.8}$$

where $I(\sigma^+)$, $I(\sigma^-)$ are the peak intensities of the trion PL line in the indicated polarization. The polarization degree does not saturate at high magnetic field as one would expect. This indicates that the Zeeman splitting does not increase linearly with magnetic field. Since the electron Zeeman splitting is linear up to very high fields it can be assumed that the hole Zeeman splitting and hence the g_h-factor is developing nonlinearly. Because the electron g-factor is known the hole g-factor can be derived from the exciton and trion. Fig. 3.32 shows the exciton and hole Zeeman splitting. The hole Zeeman splitting derived from exciton (X) and trion (T^-, T^+) data deviates slightly but shows a general trend: The splitting saturates between 12 T and 17 T and starts to decrease afterwards. This is in good agreement with the polarization trend observed at high magnetic fields.

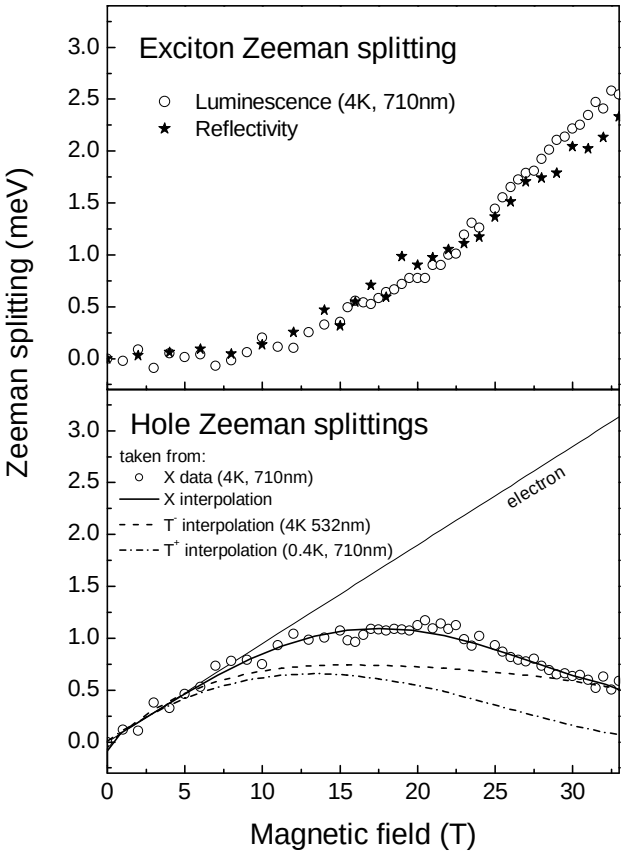

Fig. 3.33:
Hole Zeeman splitting derived from exciton (X) and trion (T^-, T^+) data. For comparison the electron Zeeman splitting is plotted in the same graph. Sample: 090505AC.

However, the polarization of the trion can not just be explained by a thermal distribution between two trion spin states. One has to take into account the formation process of trions which can be interpreted as chemical equilibrium between excitons and free electrons on the one side and trions on the other side [Jeu02]:

$$X + e \rightleftharpoons X^-$$

The polarization of trions that are formed strongly depends on the spin configuration of excitons and free electrons in the system. The polarization of the 2DEG in the sample can be determined from the trion resonance in reflection spectra (Inset of Fig. 3.13). When the free carriers are completely polarized in a high magnetic field formation of trions by optical excitation is limited to one polarization. In the p-type regime the trion is more pronounced in σ^--polarization. Therefore it can be assumed that the $S_{T_s} = -\frac{3}{2}$ ground state of the 2DHG is fully occupied and the formation probability for more electron hole pairs in this configuration is low. This explains the observed signal in σ^- excitation for which $S_{T_s} = +3/2$ is the initial state (Fig. 3.19). An example scheme of the trion formation process is displayed in Fig. 3.34.

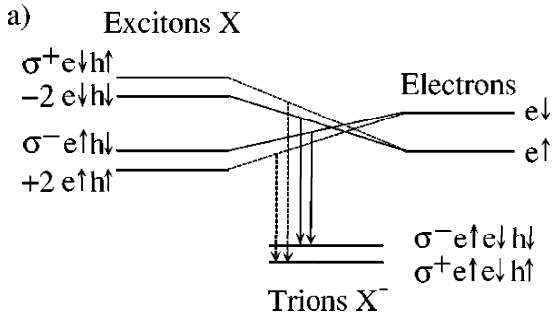

Fig. 3.34: *Example scheme of electron, exciton and trion spin splitting in a quantum well at low magnetic fields. [Jeu02]*

The illustration also includes optically non active levels which can therefore not be observed in photoluminescence spectra but may still influence the trion formation process. In the example case the spin-down electron state becomes less occupied with increasing magnetic field. Since the spin-down electron is necessary to form a trion with the excitons from the lower spin states, the probability for the trion formation is decreased. This may be visible in an intensity shift from the trion towards the exciton when the magnetic fields strength is increased. Other configurations may lead to a situation where the formation of a trion in the upper spin state is much more likely than for the lower spin state. In this case it depends on the timescale of the spin flip process and the trion recombination time whether a thermically non-equilibrium state is formed where the higher spin state is more densely populated.

In the following consideration it has been assumed that the exciton lifetime is rather short so that no thermal equilibrium of the exciton state is established and the excitons are unpolarized. In this case the degree of trion polarization can be calculated by the following equation:

$$P_c^T = \left[P_0^e \frac{\tau_0^e}{\tau_s^e + \tau_0^e} tanh\left(\frac{\Delta E_z^e}{kT}\right)\right] tanh\left(\frac{\Delta E_z^T}{kT}\right) \tag{3.4}$$

The inner part in square brackets describes the polarization of the 2DEG where τ_0^e is the electron live time τ_s^e is the spin relaxation time. The trion polarization depends

on the electron polarization, the temperature and the trion Zeeman splitting which is equal to the splitting of the heavy hole states due to its two complementary electron spins. In case of the trion the spin relaxation time can be neglected against the live time so that the fraction becomes 1.

Also in the polarization a strong difference can be observed between n- and p-type regime. Only T^+ is positively polarized at high magnetic fields (Fig. 3.34).

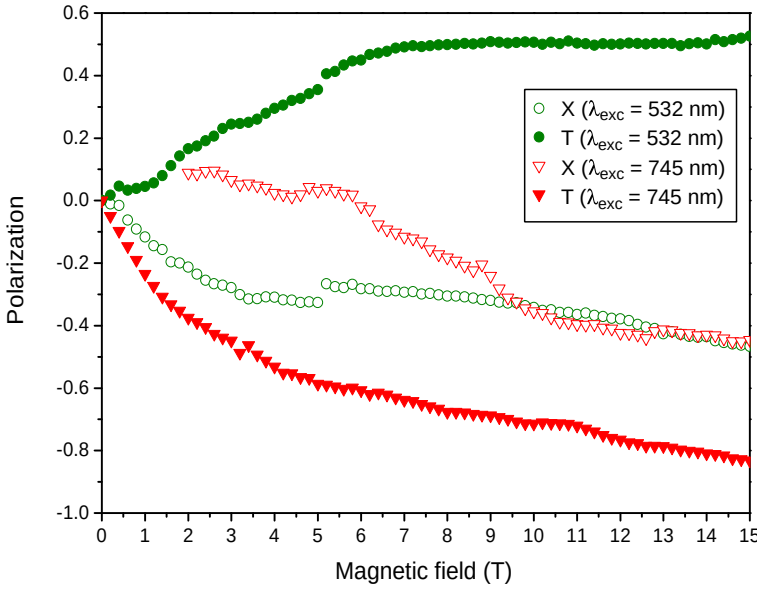

Fig. 3.35: *Polarization of the exciton (open symbols) and trion (closed symbols) for two different excitation wavelength: 532 nm (green symbols) and 745 nm (red symbols).*

Conclusion

Fundamental differences between photoluminescence and reflectivity spectra could be observed depending on the excitation energy which was chosen above and below the barrier. Due to the increase of electrons in the quantum well by above barrier illumination the type of carrier changes from hole to electron. Making use of different excitation energies both T^- and T^+ have been observed in the same sample. The difference could be observed in reflectivity measurements where T^+ is fully polarized at high magnetic fields but T^- is not. In PL measurements the T^+ line was strongly σ^--polarized, whereas the T^- line showed σ^+-polarization. These polarization properties fit to the spin level scheme drawn from data of the Zeeman splittings of this sample. Differences could also be found in the trion binding energy. The binding energy of T^- increases with magnetic field because it consists of two light electrons and one heavy hole. This complex has one center and magnetic field will localize the electron wave functions around the hole, thus inducing an increase of the binding energy [Ast02]. In case of the T^+ complex one electron is shared by two holes whose spatial distance does not change in magnetic field so that the localization of the electron is not influenced strongly. This has been observed experimentally where the binding energy of the positively charged trion is slightly decreasing up

to 17 T where it starts to increase again without reaching its initial value in magnetic fields up to 33 T.

At high magnetic fields additional peaks have been observed in the photoluminescence which may be assigned to triplet states. Negatively charged triplet states have been observed in samples of different material systems before. The additional peaks in the p-type regime coincide energetically with expectations for a nominally spin forbidden transition of two T_t^+ states.

3.3 High density 2DEG

3.3.1 Quantum hall regime in a modulation n-type doped AlGaAs/AlAs quantum well with high electron density

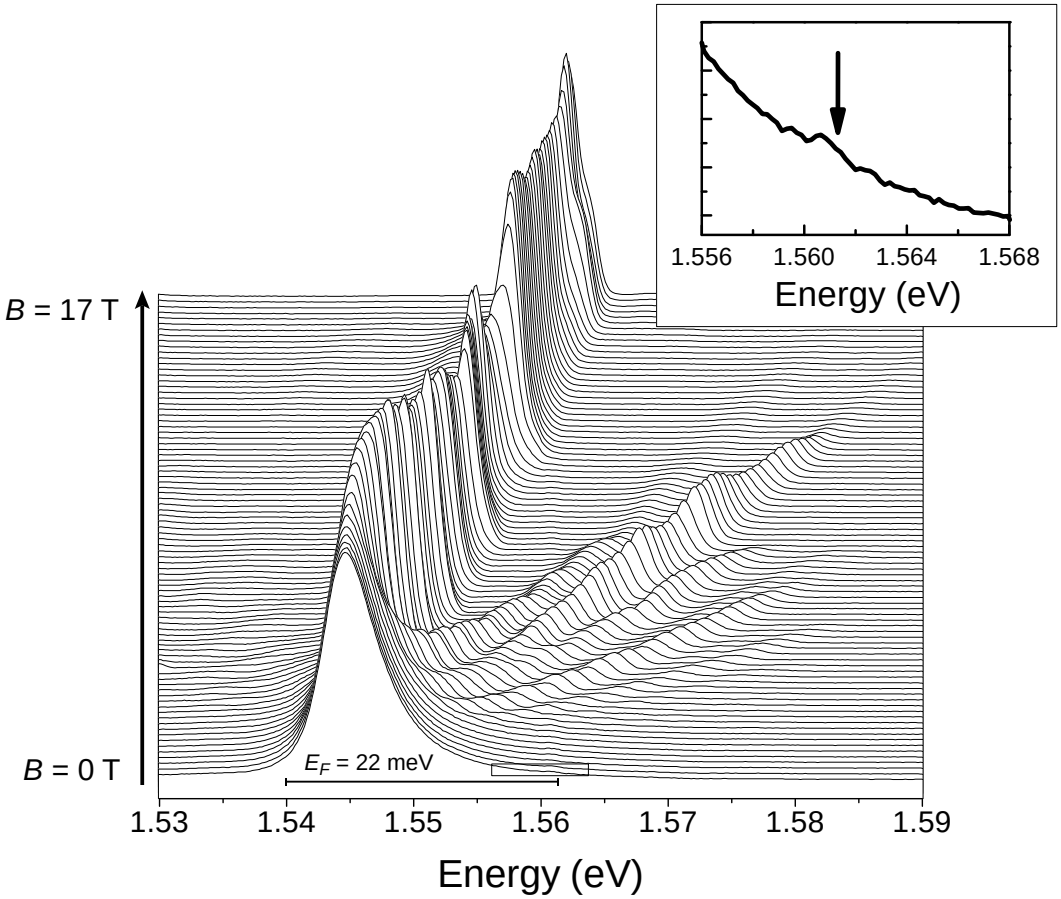

Fig. 3.36: *Photoluminescence of a highly n-type doped AlGaAs/AlAs QW (11309) in the magnetic field region between 0 and 17 T in σ^+-polarization. The Fermi energy E_F has been estimated to be 22 meV. $T = 2.2\,K$, $\lambda_{exc} = 632.8\,nm$, $P_{exc} = 3.5\,mW/cm^2$.*

Photoluminescence and ODR techniques have been used to investigate a highly doped AlGaAs/AlAs quantum well (11309). The samples consists of a single, 100Å wide AlGaAs QW embedded into a AlAs barrier. It is n-type doped by Silicon. In the PL three recombination peaks are found (not shown). To calculate the carrier density the following equation was used:

$$n_e = \frac{E_F\,[meV] \cdot m^*}{2.3 \cdot 10^{-12}} \tag{3.5}$$

The Fermi energy E_F can be estimated from the highest recombination peak found at an energy of 1.5446 eV at $B = 0$ T as shown in Fig. 3.36. A small step in the PL signal can be observed slightly above 1.56 eV. States at higher energies are empty and do not contribute to the photoluminescence. The width of the lowest recombination peak from the onset at 1.54 eV to the small step is in good approximation 22 meV. This value can be used as Fermi energy. With the well known effective mass of GaAs $(m^* = 0.067\,m_0)$ an electron density of about $n_e = 6.4 \cdot 10^{11}$ cm^{-2} can be derived.

A series of PL spectra have been taken at $T = 2.2$ K for magnetic fields between 0 T and 17 T for both circular polarizations. Results for the σ^+-polarization are plotted in Fig. 3.36. Up to five Landau levels can be identified from this graph. A strong variation of the line intensity can be observed for both the main peak and its Landau level multiples. Also a nonmonotonic shift of the peaks with increasing magnetic field can be seen. Both effects are related to changes of the filling factor.

The energy of the peak position as a function of magnetic field is shown in Fig. 3.38 (a) for σ^--polarization (red dots and lines) and σ^+-polarization (black dots and lines). A number of steps can be identified where the peak position does not increase smoothly with the magnetic fields but shows a strong, nonmonotonic shift. For both polarizations the sudden shift occurs at the same magnetic field positions. Ossau et.al. [Oss02] observe a similar behaviour for ZnSe quantum wells. They could assign the effect to changes in the filling factor (FF). For a known electron density n_e the magnetic field positions for a certain filling factor ν can be calculated according to:

$$B[\mathrm{T}] = \frac{n_e\,[cm^{-2}]}{\nu}\Phi_0 \tag{3.6}$$

where $\Phi_0 = hc/e$ is the flux quantum. At small magnetic fields a finite number of Landau levels is filled with electrons - the number of filled levels is given by the filling factor (see also Fig. 1.20 (a)). The electrons are separated from each other by the magnetic length which decreases with magnetic field. Thus more electrons can be stored on every LL and electrons from higher energy levels can decrease their potential energy by transitions to lower LL. Whenever the magnetic field reaches a value were the highest Landau level gets completely depopulated the filling factor decreases by two. This also means that the energy of the highest electron decreases by the energy splitting of the LLs and hence also the Fermi energy decreases accordingly. Therefore changes of electronic and optical properties can be expected for integer filling factors. To assign the experimental features with a certain number of the filling factor and to determine the electron density, the experimental data are evaluated in the following way: A linear fit is applied to the line position of the lowest recombination and subtracted from it to work out the deviations from a linear behaviour. The result is shown in Fig. 3.38 (b). The maxima of this curve define

the magnetic field positions of integer filling factors. The inverse magnetic field position of these positions plotted against the filling factor in Fig. 3.37.

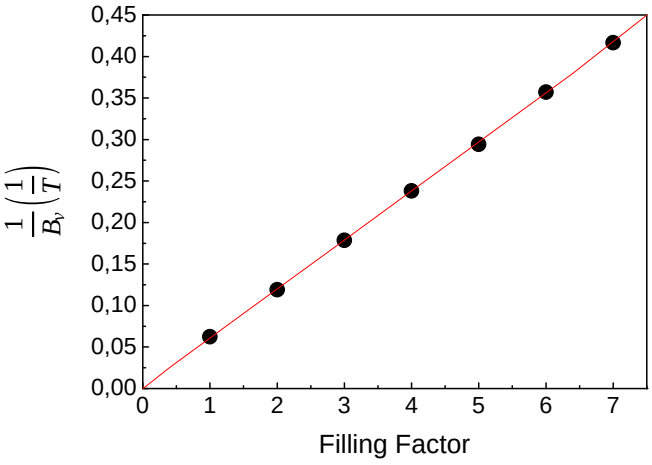

Fig. 3.37:
Inverse magnetic field position of the steps in the energy position of the main PL peak. The red line shows a fit through this points which is used to determine the electron density n_e. Sample: 11309, $T = 2.2\,K$, $\lambda_{exc} = 632.8\,nm$, $P_{exc} = 3.5\,mW/cm^2$.

The experimental data has to be assigned to the filling factors such that the fit through the points goes through zero. From the slope γ of the fit the electron density can be calculated:

$$n_e = \frac{e}{\gamma\, h} \tag{3.7}$$

With the slope $\gamma = 0.0591$ the electron density is $4.09 \cdot 10^{11}$ cm^{-2}, a value which slightly deviates from the estimation based on the line width at $B = 0$ T. Indeed the steps in the peak positions can be matched with integer filling factors if this electron density is used. The calculated position of integer filling factors is marked by black triangles in Fig. 3.38 (b).

Filling factor 1 is assigned to a magnetic field of 16.9 T which deviates from the shift of the peak position which seems to be closer to 16.0 T. For the other maxima the calculation coincides very well with the experimental findings.

At integer filling factors also vertical dashed lines have been drawn to compare features of different sample properties namely peak position and intensity, degree of polarization and the ODR signal. In all those properties changes of the FF are reflected. The PL peak intensities and degree of polarization are shown in Fig. 3.38 (c). At even filling factors a minimum in polarization is expected since both spin levels are equally filled, i.e. there is an equal number of electrons with opposite spin orientation. This has been observed by Ossau in ZnSe quantum wells [Oss02], but it can not be seen here. Also the ODR signal can just be related to integer FFs where it shows minima. A microscopic model can not be given since the high electron density makes it necessary to use many-body calculations. While most features correspond to an integer filling factor, there are also some additional peaks in-between them around $\nu = 1.5$ and $\nu = 2.5$ — these have been marked by arrows in all plots.

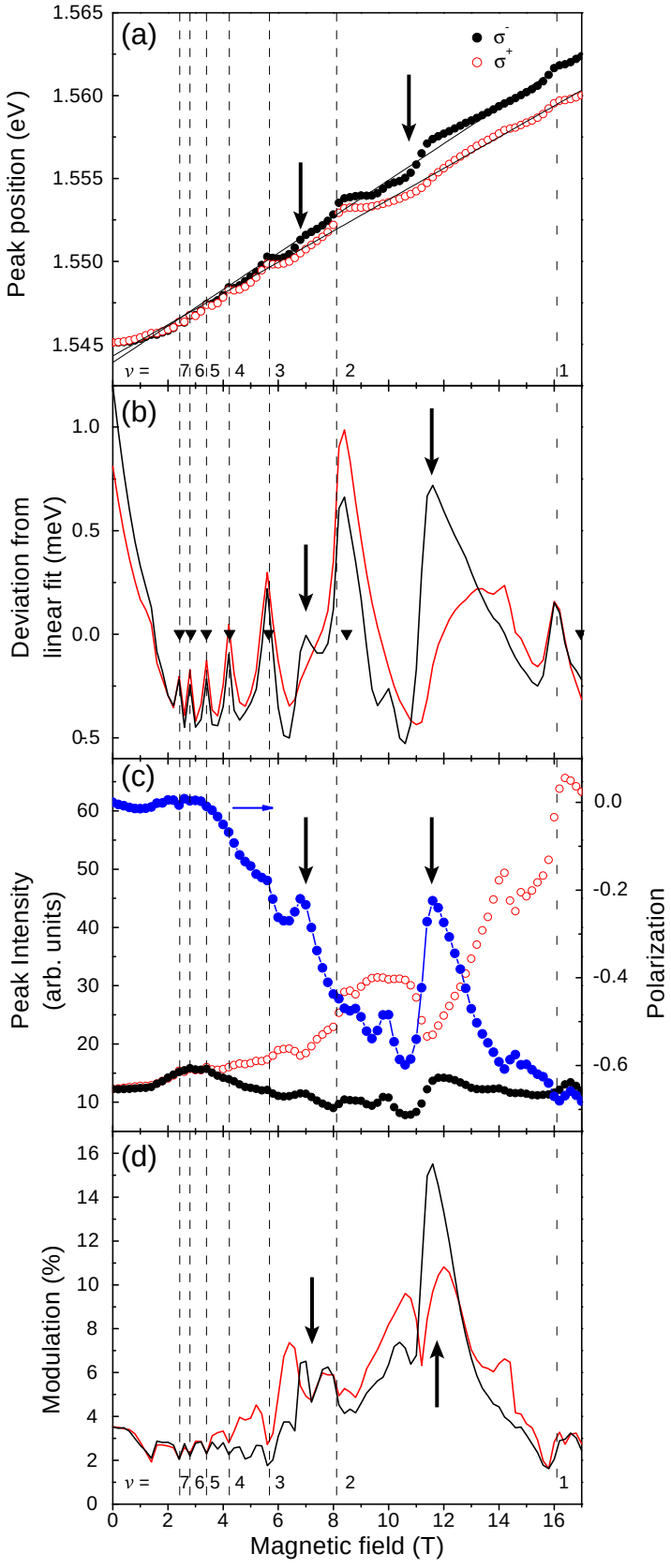

Fig. 3.38:
(a) Peak position of the lowest recombination peak as a function of the magnetic field for σ^- (○) and σ^+(•) polarization. Strong, nonmonotonic changes of the peak position occur at integer filling factors (▾ and dashed lines) calculated for an electron density of:
$n_e = 7.8 \cdot 10^{11}\,cm^{-2}$
(b) Derivation of the peak position from linear behaviour for better visibility of sudden changes. Red line indicates σ^- polarization, the black σ^+ polarization.
(c) Changes of the peak intensity as a function of magnetic field for both polarizations. The blue lines shows the degree of polarization.
(d) ODR signal as a function of the magnetic field. Features coincide with integer filling factors for both polarizations.
Arrows have been placed at features observed at positions between integer filling factors.

Sample: 11309,
$T = 2.2\,K$,
$\lambda_{exc} = 632.8\,nm$,
$P_{exc} = 3.5\,mW/cm^2$.

In high quality samples, at temperatures in the order of mK, effects corresponding to fractional filling factors[10] have been observed in optical and transport measurements, e.g. by Takeyama [Tak98] in CdTe/CdMgTe quantum wells. Still it is very unlikely that the features found between the positions of integer filling factors can be deduced to fractional filling factors.

10 The phenomenon of fractional filling factors is not fully understood, yet. It has been assumed that it is related to many-particle complexes, so called *composite fermions*.

3.4 Shake-up processes

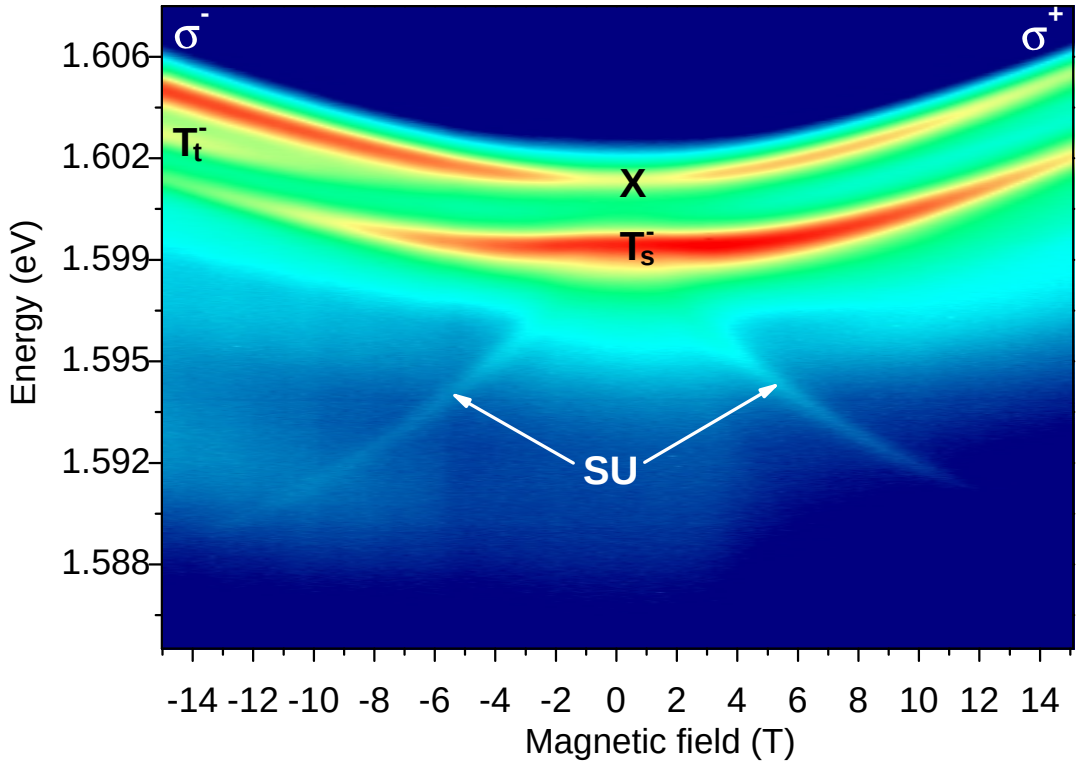

Fig. 3.39: *False color plot of the photoluminescence of a CdTe/CdMgTe QW (090505AC). Besides the neutral (X) and charged (T) excitons a line at the low energy side of the singlet trion can be seen. It can be assigned to a shake up (SU) process and splits up linearly from the trion with increasing magnetic field. Sample: 090505AC,* $T = 0.35\,K$, $\lambda_{exc} = 532\,nm$, $P_{exc} = 3\,mW/cm^2$

In the photoluminescence of quantum well samples, often satellite peaks can be observed that are lower in energy than the exiton or trion lines. Moreover, with increasing magnetic field they shift to lower energies, which is rather anusual. The origin of these lines can be described by the shake-up process: Energy from an electron-hole pair recombination is partly transferred to another electron which is lifted to a higher Landau level while reducing the recombination energy by the same amount.

There are two quite different mechanisms which are both referred to as Shake-up process. One can be found in quantum wells with high dense electron gas at filling factors> 2. The other process can also be seen in nominally undoped samples and describes internal transitions of a trion.

3.4.1 Shake-up in a high dense 2DEG

The appearance of satellite peaks in the photoluminescence of highly doped quantum wells has been observed in the early 90's by Nash [Nas93] and Skolnick [Sko93]. In the presence of a dense electron gas the shake-up process is a many body process where the recombination of an electron-hole pair is combined with the excitation of magneto-plasmons, which is a collective excitation of the 2DEG. However, the energy of magneto-plasmons is exactly equal to $\hbar\omega_c$ of isolated electrons and therefore shake-up processes are shown as additional electron transitions in the schemes of this subsection.

The energy transferred into the 2DEG is subtracted from the emitted photon energy so that new emission peaks appear below the trion line. The energy difference between the trion line and the satellite peaks increases linearly with the magnetic field. It coincides well with the Landau level splitting so that one can assume that the shake-up process induces transitions between LL. The lowest order transition amplitude for this process has been calculated by Finkelstein [Fin97]:

The transition from an initial state $|i\rangle$ to the final state $|f\,(SU_n)\rangle$ of the SU_n recombination process is described by:

$$W_n \propto \langle f\,(SU_n)|\,R\,|i\rangle \tag{3.7}$$

where R is the electron-hole recombination operator:

$$R = \sum_m a_m b_m \tag{3.8}$$

with the annihilation operators for electron and hole, a_m and b_m and the landau level number m.

The Hamiltonian of the system can then be expressed as:

$$\mathcal{H} = \mathcal{H}_0 + \mathcal{H}_{int} = \sum_m \left[E_{gap} + \hbar\omega_c^e\left(m + \frac{1}{2}\right)\right] a_m^\dagger a_m$$

$$+ \sum_{m,} \hbar\omega_c^h\left(m + \frac{1}{2}\right) b_m^\dagger b_m$$

$$+ \frac{1}{2}\sum V_{i,j,k,l}^{e-e} a_i^\dagger a_j^\dagger a_k a_l$$

$$+\sum V^{e-h}_{i,j,k,l} a_i^\dagger b_j^\dagger b_k a_l$$

$$+\frac{1}{2}\sum V^{h-h}_{i,j,k,l} b_i^\dagger b_j^\dagger b_k b_l \qquad (3.9)$$

where the first two terms express the energy of the electron and hole system and the other term the e-e, e-h and h-h interaction.

The resulting transition amplitude [Fin97] can be written in the following way:

$$W_n = \sum_m \frac{\sum_{i,k,l} V^{e-e}_{i,m,k,l} \langle f(SU_n)|a_i^\dagger b_m a_k a_l|i\rangle}{E_{gap} + \left(m + \frac{1}{2}\right)\hbar\left(\omega_c^e + \omega_c^h\right) - E_{ph}}$$

$$+ \sum_m \frac{\sum_{i,k,l} V^{e-h}_{i,m,k,l} \langle f(SU_n)|a_i^\dagger b_k a_m a_l|i\rangle}{E_{gap} + \left(m + \frac{1}{2}\right)\hbar\left(\omega_c^e + \omega_c^h\right) - E_{ph}} \qquad (3.10)$$

where E_{ph} is the energy of the emitted photon. One possible shake-up scenario is shown in Fig. 3.40 where the recombination of an LL_0 electron-hole pair induces two electron transitions between landau levels. The space left by the LL_0-electron is filled from LL_1, exciting another electron from LL_0 to a higher landau level.

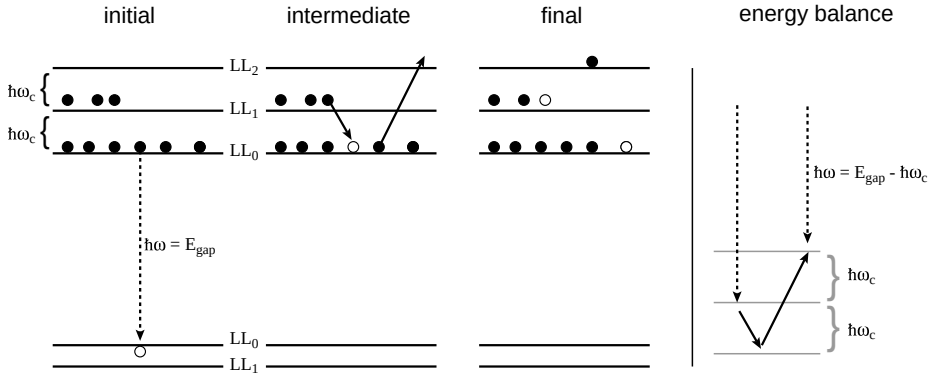

Fig. 3.40: *Shake-up process: Initial recombination of electron-hole pair leads to a intermediate redistribution of electrons in the Landau levels (leaving the final system in a state of higher energy) and a reduced photon energy. Exciton or trion binding energies have been neglected in this picture.*

The transition amplitude for the case can be written as:

$$W_n \propto \frac{\sum_x \langle f\,(SU_n)\,|\,R\,|\,x\rangle\,\langle x\,|\,\mathcal{H}_{int}^{e\text{-}e}\,|\,i\rangle}{E_i - E_x}$$

$$+ \frac{\sum_x \langle f\,(SU_n)\,|\,\mathcal{H}_{int}^{e\text{-}e}\,|\,x\rangle\langle x\,|\,R\,|\,i\rangle}{E_i - E_x - E_{ph}} \qquad (3.11)$$

The second term in Eq. 4.5 takes into account that the processes marked initial and intermediate in Fig. 3.40 may be exchanged in time.

Another shake-up process can take place when a hole is virtually excited to some higher landau level LL_m and shakes up an electron at the same time. This enables the recombination with a LL_m electron as shown in Fig. 3.41. In this case the final photon energy is also reduced by a multiple of $\hbar\omega_c$. In this case the transition amplitude is:

$$W_n \propto \frac{\sum_x \langle f\,(SU_n)\,|\,R\,|\,x\rangle\,\langle x\,|\,\mathcal{H}_{int}^{e\text{-}h}\,|\,i\rangle}{E_i - E_x} \qquad (3.12)$$

These shake-up processes strongly depend on the filling factor. At $\nu < 2$ the SU line is strongly suppressed. This can be explained by a hidden symmetry of the electron-hole system at the lowest landau level. Recombinations from LL_0 do not perturbate the charge distribution in the 2DEG. A breaking of this symmetry occurs at $\nu > 2$ when higher LL are filled. Recombinations from higher landau levels perturb the charge distribution and give rise to shake-up excitation processes [Fin98].

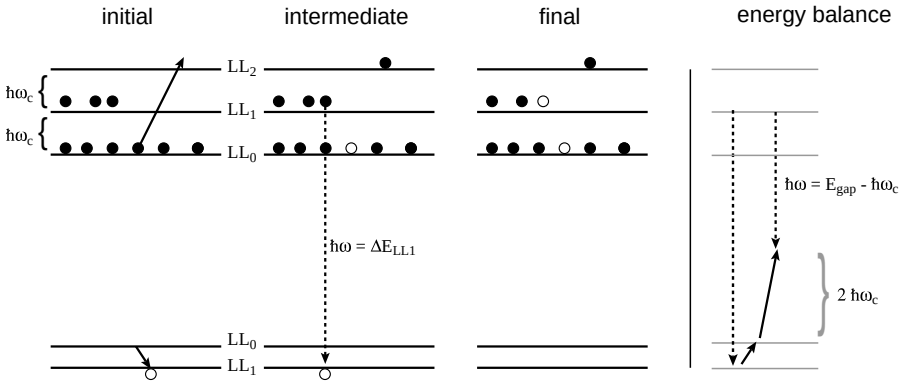

Fig. 3.41: *Example shake-up process: Transition of a virtual hole to a higher landau level LL_1 shakes up an electron to LL_2. The photon energy of the recombination of LL_1 electron and hole is reduced by the transition energies required for the shake-up electron and virtual hole.*

3.4.2 Shake-up in a low dense 2DEG

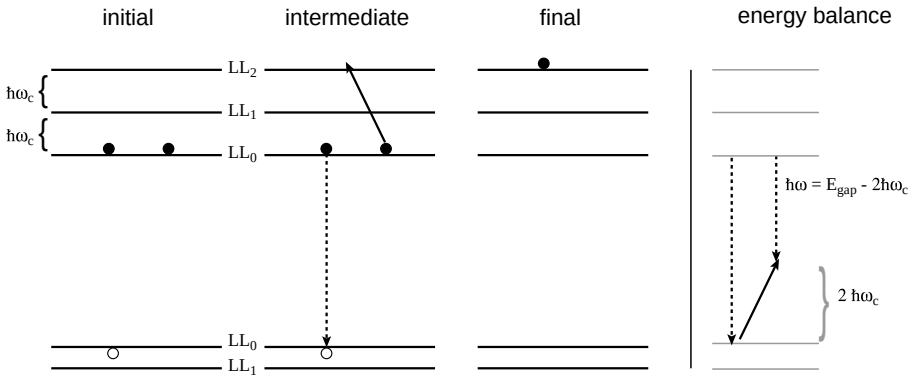

Fig. 3.42: *Shake-up process: Recombination of the electron-hole pair from the ground state of a single trion leads to a shake-up of the second electron to a higher LL. The photon energy is reduced by the energy required for the shake-up.*

Satellite peaks have also been observed [Fin96b] in the spectrum of quantum wells with a low dense electron gas and a filling factor lower than 2. This regime differs principially from dense 2DEG. In a low dense 2DEG no magneto-plasmons are involved but the shake-up process is a three-particle process where a single electron is excited. In a singlet trion both electrons occupy the ground state. The recombination of the electron-hole pair may come along with the shake up of the second electron to a higher Landau level reducing the photon energy by a multiple of $\hbar\omega_c$ as shown in Fig. 3.42.

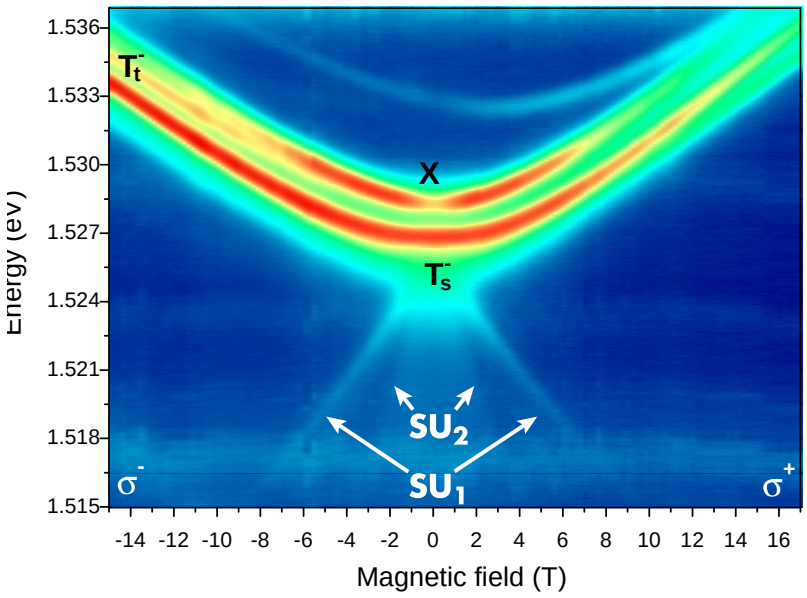

Fig. 3.43: *Photoluminescence of a AlGaAs/AlAs quantum well (32A21M7). Two shake up lines can be identified.* $T = 2.2\,K$, $\lambda_{exc} = 660\,nm$, $P_{exc} = 5\,mW/cm^2$.

In the photoluminescence of a AlGaAs/AlAs quantum well (32A21M7) two satellite peaks were observed. The shake-up process explains the additional lines shown in Fig. 3.43. The spectrum at $B = 2\,\mathrm{T}$ and $T = 2.2\,K$ in Fig. 3.44 shows the trion and exciton recombination of the quantum well together with two shake-up peaks on the low energy side. They have been multiplied with a factor of 10 for better visibility.

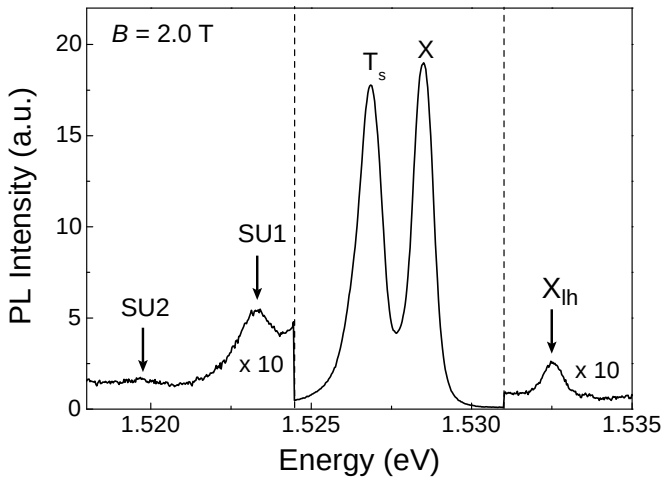

Fig. 3.44: *Photoluminescence spectrum of sample 32A21M7 at B = 2T. Two shake-up signatures (SU1, SU2) have been observed on the low energy side of the trion. Above the exciton line the light hole exciton peak (X_{lh}) can be found. $T = 2.2\,K$, $B = 2.0\,T$ $\lambda_{exc} = 660\,nm$, $P_{exc} = 5\,mW/cm^2$.*

The dependence of the energy position on the magnetic field is shown in Fig. 3.45. (a) for both circular polarizations. Due to a decline of the shake-up intensity with increasing magnetic field the energy position can be followed only to around 7 T for the SU1 line and 2.6 T for the SU2 line. The intensity decrease of the SU line with increasing magnetic field can be explained by the wave function overlap between LLs. At high magnetic fields the overlap becomes small and the probability for the occurrence of SU processes vanishes.

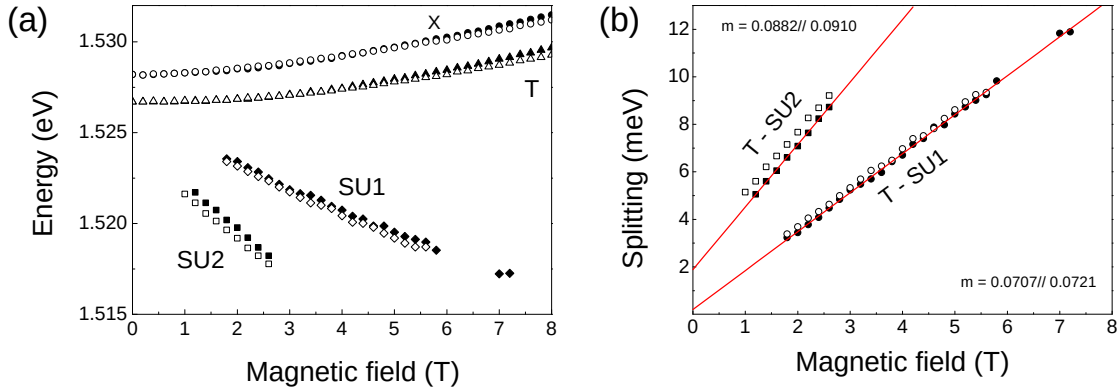

Fig. 3.45: *(a) Magnetic field dependence of the energy position of exciton (X), trion (T) and two shake-up (SU1, SU2) peaks of sample 32A21M7. Closed symbols show data for σ^+, open symbols for σ^- polarization. (b) Splitting between the trion and shake-up line. The effective mass of carriers can be determined from the slope of a linear fit to the data points. $T = 2.2\,K$, $\lambda_{exc} = 660\,nm$, $P_{exc} = 5\,mW/cm^2$.*

The splitting between the trion and SU1/SU2 as shown in Fig. 3.45 (b) corresponds to the splitting of Landau levels. A linear fit has been applied to the data points in σ^+ polarization. From the slope the effective mass of carriers can be calculated. For the SU1 line the effective mass is $m^* = 0.071\, m_0$, for the SU2 line $m^* = 0.088\, m_0$. Compared to the value of $m^* = 0.065\, m_0$ which was derived from the cyclotron resonance of this sample (see Fig. 3.3) the values for the effective mass increased. This behaviour has also been observed for other samples and may be due to the band nonparabolicity at $K \neq 0$. Finkelstein give another explanation for the deviation stating that it may be caused by the wave function penetrating the $Al_xGa_{1-x}AS$-Layer where the effective mass is around $0.1\, m_0$.
In one GaAs/AlGaAs sample (11302) (Fig. 3.46) it was even possible to observe two lines above the exciton which may be assigned to an inverse process, an Auger recombination within Landau levels [Pot91]. This can be described as combined exciton-cyclotron resonance (ExCR), where an incident photon creates not only an exciton, but, in addition, also excites a background electron from one Landau level to another [Yak97].

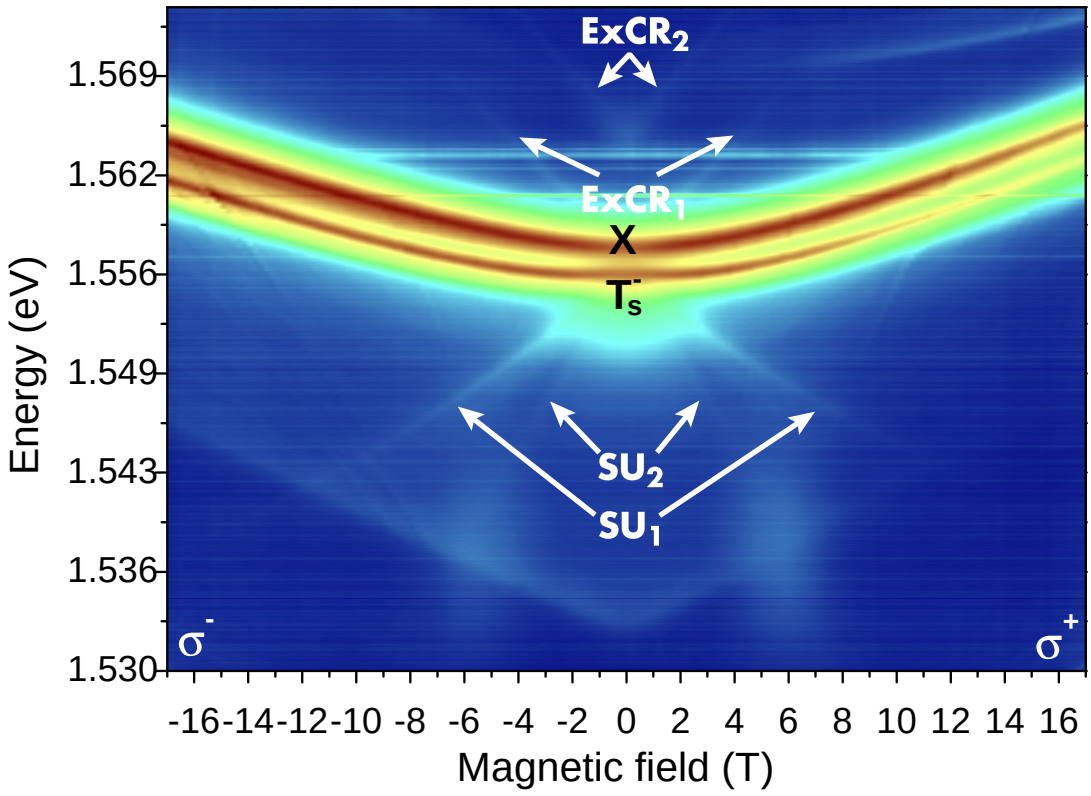

Fig. 3.46: *Photoluminescence of at GaAs/AlGaAs quantum well (11302) which shows two shake up lines (SU). On the high energy side of the exciton an opposite effect, the combined exciton-cyclotron resonance (ExCR), can be observed. Note, that the picture is shown with a logarithmic color scale in order to amplify small transitions.* $T = 2.2\,K$, $\lambda_{exc} = 632.8\,nm$, $P_{exc} = 35\,mW/cm^2$.

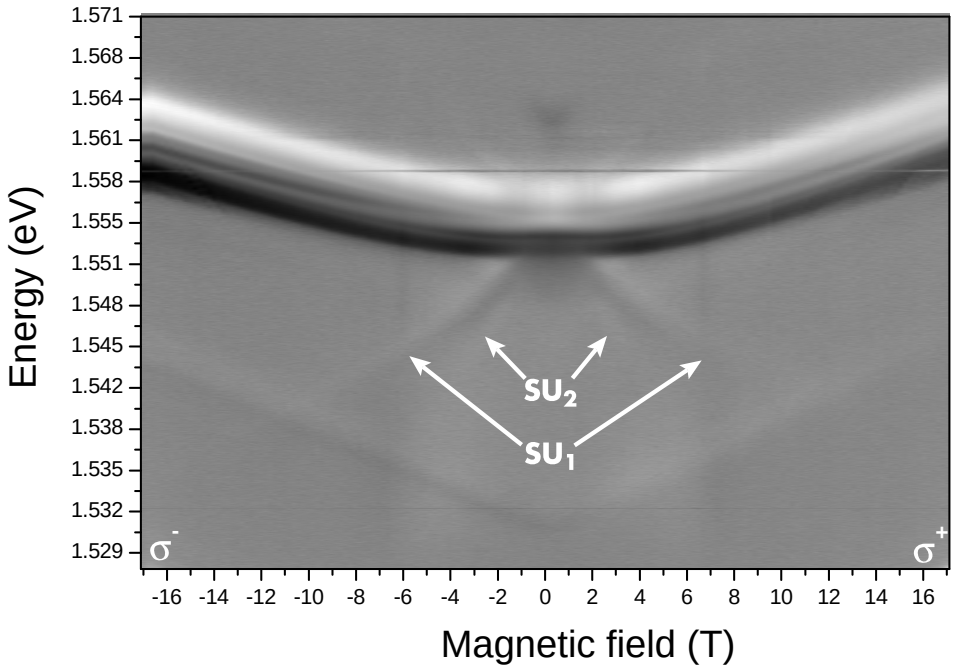

Fig. 3.47: *Evidence for the shake up signal can also be found in the modulation signal of sample 11302. Note that the modulation has been normalized on the PL intensity.* $T = 2.2\,K$, $\lambda_{exc} = 632.8\,nm$, $P_{exc} = 35\,mW/cm^2$, $E_{FIR} = 10.5\,meV$, $P_{exc} = 160\,mW/cm^2$.

Table 3.1 shows the line splittings between peak positions of excitons (X), trions (T), shake ups (SU) and combined exciton-cyclotron resonance (ExCR). The slope of the second shake up line (SU2) is exactly twice as large as the one of the first line (SU1). Both SU lines originate from the same point, the trion position at 0 T.
Due to the low contrast a fit to the ExCR line positions was not possible. The slope of the line was derived by hand from a plot of Fig. 3.46 and gives only approximate values for the effective mass. In comparison, the SU and ExCR lines look similar. However, the behaviour of the second ExCR line is different in two ways. First, it does not originate from the exciton line but shows an offset of 8.42 meV. Secondly the slope is not twice as large as the ExCR1 slope.

	Splitting / $\frac{meV}{T}$	Effective mass / m_0
T - SU1	1.40	0.0819
T - SU2	2.80	0.0819
SU1 - SU2	1.40	0.0819
X - ExCR1	1.3	0.089
X - ExCR2	1.6	0.073

Table 3.1: *Column 1 shows the splitting between peak positions of excitons (X), trions (T), shake ups (SU) and combined exciton-cyclotron resonance (ExCR). Column 2 lists the masses corresponding to these splittings.*

It seems that both, ExCR1 andExCR2 line are almost parallel. If this is true, the mean value for the effective mass from both ExCR lines can be calculated to be 0.081 m_0, which is quite similar to masses calculated from the SU lines. This comparison indicates that a similar process may be involved which includes an Auger like process between Landau levels.
Evidence of the shake up process can also be observed in the modulation signal, Fig. 3.47 shows the modulation signal which has been normalised on the PL intensity.

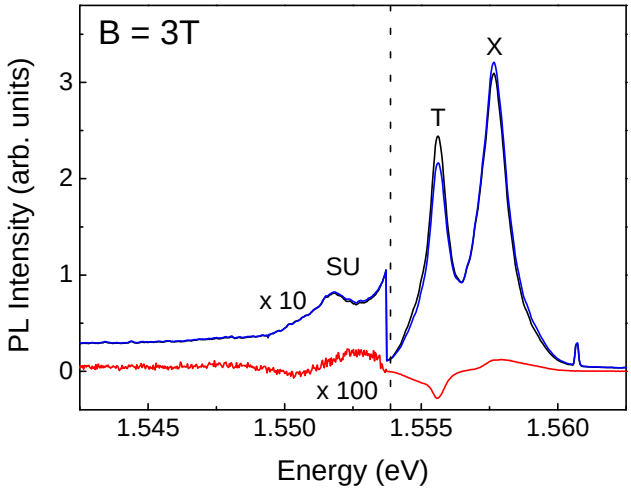

Fig. 3.48: *PL and ODR spectra of sample 11302 in σ^--polarization at B = 3 T and T = 2.2 K. The FIR radiation leads to a decrease of the trion (T) and an increase of the exciton (X) signal. At the low energy side of the trion a shake up (SU) signal can be observed that slightly shifts to higher energies under FIR illumination. $T = 2.2\,K$, $\lambda_{exc} = 632.8\,nm$, $P_{exc} = 35\,mW/cm^2$, $E_{FIR} = 10.5\,meV$, $P_{exc} = 160\,mW/cm^2$.*

The modulation spectrum at $B = 3$ T (Fig. 3.48) shows a redistribution from trions towards excitons under FIR illumination that, due to a temperature increase of the carriers, suppresses the formation of trion complexes. In case of the SU line a slight shift to higher energies can be identified from the derivative shape of the ODR signal.
Shake up lines have also been observed in two 8 nm wide ZnSe/ZnMgSSe QW samples with different electron concentrations. Sample zq1090 is nominally undoped with a small background electron concentration of less than $5 \cdot 10^9$ cm^{-2}. Sample zq1088 is n-type doped with an electron concentration of about 1.5 - 2.0 $\cdot 10^{11}$ cm^{-2}.
Fig. 3.49 (a) shows the photoluminescence of the undoped sample zq1090. Two shake up lines can be identified. Compared to the shake up lines in GaAs quantum wells the slope in case of ZnSe/ZnMgSSe QWs is not very steep and does not vanish in fields up to 17 T. In Fig. 3.49 (b) line positions of excitons, trions and SU line are shown. A linear fit through the positions of both SU lines reveals an effective mass of $m^* = 0.20\,m_0$ in both cases.

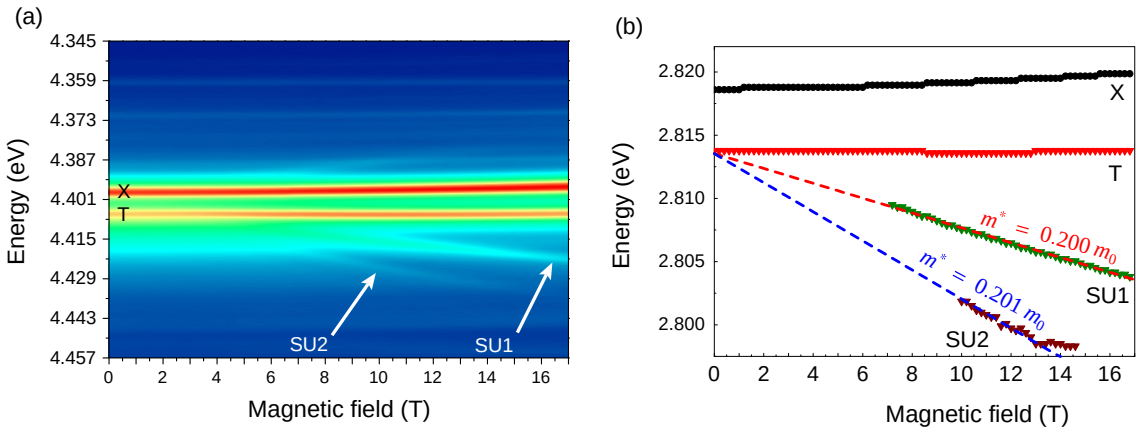

Fig. 3.49: *(a) False color representation of the photoluminescence of sample zq1090 at $T = 4.2K$. Two shake up lines can be identified at high magnetic fields. (b) Fit for energy positions of excitons, trions and shake up lines. Effective masses have been calculated from the slope of the SU lines. $\lambda_{exc} = 372\,nm$, $P_{exc} = 10\,mW/cm^2$.*

This value is much higher than expected for a ZnSe/ZnMgSSe quantum well. The effective mass is around $m^* = 0.14\,m_0$ in bulk ZnSe. Due to the n-type doping, the electron concentration in zq1088 is higher so that several Landau levels are filled at low magnetic fields (Fig. 3.50).

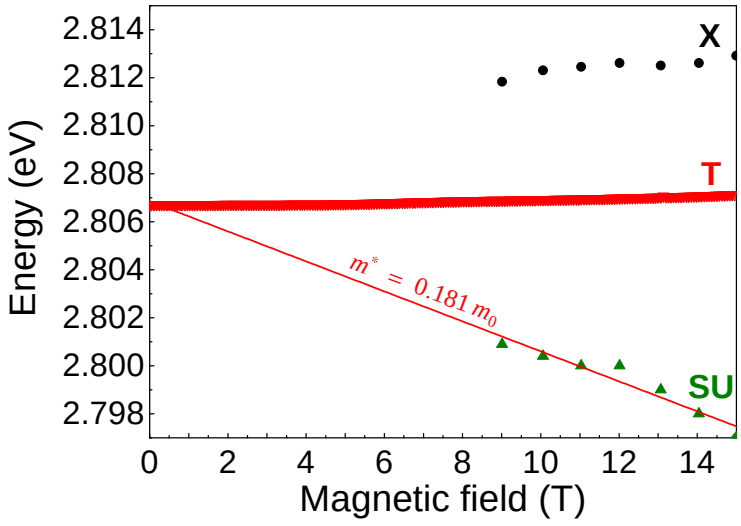

Fig. 3.50:
Energy positions of exciton, tron and shake up line for sample zq1088. From the slope of the fit to the SU positions an effective mass of $m^* = 0.181 m_0$ can be derived.
$T = 4.2\,K$,
$\lambda_{exc} = 372\,nm$,
$P_{exc} = 15\,mW/cm^2$.

At $B = 9\,T$ the exciton becomes visible in the spectrum which indicates that the filling factor reached one. In the n-type doped quantum well only one SU line can be resolved. A fit through the positions of the SU peaks reveals an effective electron mass of $m^* = 0.181\ m_0$. This value lies between the value for bulk ZnSe and the effective mass for sample zq1090. If the deviation can be explained by a non-parabolic band shape, one would expect that the effective mass in a n-type doped QW should be higher than in the undoped case. Fig. 3.51 shows that the deviation from the parabolic band shape increases for higher values of K because they be-

come mixed with heavy hole states. With increasing carrier density the Fermi level rises and higher energy states, reaching further into the K-space, become filled. Currently there is no explanation for the opposite behaviour observed in the PL study of both ZnSe/ZnMgSSe quantum wells. Most probably it is related to specifics of Auger-like processes for localized trion. It may also be possible that the electron concentration in sample zq1088 is high enough for magneto-plasmons to becoming involved. Then the regimes of both samples are very different and may result in a deviation of the SU line slope. However, a microscopic theory is necessary for further investigation of this effect. Also the shake up peaks appears at this magnetic field. Therefore the SU process observed in this sample also seems to be a trion internal three particle process.

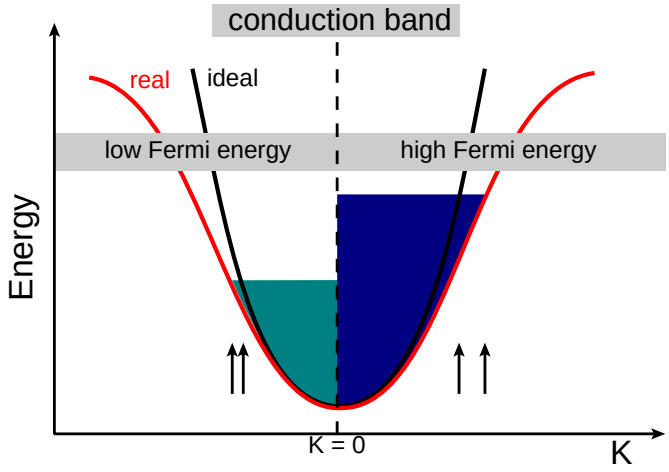

Fig. 3.51:
Scheme of the conduction band in an ideal, parabolic (black line) and real, nonparabolic (red line) case. The deviation from the ideal situation increases with the Fermi level as shown by arrows.

Conclusion

Shake up lines have been found in several nonmagnetic quantum wells of different material systems with low dense 2DEG. Most publications about shake up lines show results from highly doped quantum wells, were the excitation of magneto-plasmons is involved. Most samples presented here have a diluted 2DEG and observed shake up processes are likely to belong to internal trion transitions. The effective electron masses, derived from the slope of a line through the SU peaks observed here, is too high when compared to other, more direct methods. Further investigation and a microscopic theory are necessary to explain this deviation, but it is supported by results of two ZnSe/ZnMgSSe quantum wells. The effective mass derived from the SU slope of the sample with higher electron concentration is closer to the expected value for the effective mass of electrons in this QW.

Chapter 4:

ODR Study on nonmagnetic quantum dots

The ODR technique has been widely used to study properties of two dimensional structures. Some examples where shown in the previous chapter. However, up to now there have been only few experimental attempts to investigate QDs with ODR [Mei05, Jan03]. Theoretically, very recently the far-infrared absorption of a negatively charged exciton in a quantum dot has been calculated [Kor06]. There have been a few direct FIR studies, mostly done on n-doped QDs. One of the questions addressed was that of the phonon relaxation bottleneck. By ramping the magnetic field, dot level spacings were brought into resonance with the LO phonon. The FIR absorption showed then pronounced anticrossings which indicate the formation of polarons, facilitating carrier relaxation [Ham99, Ham02]. Also time-resolved studies have been performed, addressing the times of intra-subband carrier relaxation [Zib05]. In this article we present the results of ODR measurements on n-doped InGaAs/GaAs quantum dots. Besides FIR-induced transitions related to the wetting layer we also find transitions between confined QD levels which can be reasonably well described in a single particle picture. The different resonances can be separated by their distinct spectroscopic signatures in the modulation spectrum.

4.1 Experimental results

For our studies we used three samples of self-assembled InGaAs/GaAs QDs. Sample 11955-945°C contained 20 layers of QDs separated by 60 nm wide barriers, and was n-modulation doped by placing a δ-doping sheet 20 nm below each layer containing Si as dopant. The dopant density was roughly equal to the dot density for an average occupation by a single electron per dot, respectively. It was annealed at a temperature of 945°C. The second sample has been annealed at 850°C after the growth process but is otherwise identical. Sample 11376-940°C was nominally undoped and consisted of 11 dot layers separated by 100 nm wide barriers. The samples were fabricated by molecular beam epitaxy on a (001)-oriented GaAs substrate.

The layer dot density is about 10^{10} cm^{-2}. Their ground state emissions occurs around 1.401 eV (11955-945°C), 1.261 eV (11955-850°C) and 1.388 eV (11376-940°C).

The QDs were excited by a HeNe laser ($E = 1.96\,eV$, $\lambda_{exc} = 632.8\,nm$) through an optical fiber, the PL emission was collected by another fiber optics. Additionally the sample could be illuminated by FIR radiation with wavelengths of 96.5, 118, or 163 μm, corresponding to photon energies of 12.8, 10.5, and 7.6 meV, respectively. This radiation was taken from a FIR laser head pumped by a CO_2 laser and could reach power densities up to 20 $\frac{mW}{cm^2}$ for the 10.5 meV line, 7 $\frac{mW}{cm^2}$ for the 12.8 meV line and 6 $\frac{mW}{cm^2}$ for the 7.6 meV line. It was modulated by a shutter, then directed toward the sample by an oversized wave guide and focused by a Teflon lens. The separation between the carrier energy levels could be tuned by the magnetic field. In case of a resonance with one of the three FIR lines, absorption of the radiation can occur, potentially leading to a change of the PL signal. In our case PL changes as small as 0.01% could be detected. The magnetic field was mostly orientated parallel to the structure growth axis (Faraday geometry), but the sample could be also tilted relative to the solenoid axis. i.e. against the magnetic field with angles up to $\theta = 60°$.

For otherwise fixed experimental conditions we have recorded differential PL spectra, for which the difference between the spectrum with FIR, $L_{FIR}(E)$, and the one without FIR, $L(E)$, was taken. This difference, $m(E) = L_{FIR}(E) - L(E)$, will be termed the modulation spectrum in the following. To improve the signal-to-noise ratio, the measurement was repeated 20-times with an integration time of 0.5 seconds for each spectrum. The FIR radiation can affect the modulation spectrum differently. A shift of the peak position, for example, leads to a derivative shape with a positive and a negative part of equal areas (see sub-section 3.3.1). The intensity of the PL signal may also change, leading to a positive modulation spectrum in case of an increase. These situations can occur simultaneously or even more complex situations may happen which need to be analyzed individually.

To find out whether application of FIR leads only to a shift of a particular spectral line without intensity change one has to take the integral of the modulation spectrum over this line $I = \int m(E)\,dE$. This integral vanishes for a pure line shift. Otherwise an intensity change has occurred. As an indicator for a FIR induced change of the PL at all (without getting insight into its nature) one can take M, the modulation, which is defined by:

$$M = \frac{\int |m(E)|\,dE}{\int L(E)\,dE}, \tag{4.1}$$

where the integral is again taken over the emission line.

Fig. 4.1 shows the photoluminescence spectrum from sample 11955-945°C without and with FIR radiation at $B = 16.4$T. The FIR energy was 10.5 meV. The difference between the two spectra is quite small. To facilitate its visibility, the inset of Fig. 4.1 shows a close-up of the two traces around their maximum intensities. The resulting modulation spectrum multiplied by a factor of 10 is also shown in Fig. 4.1.

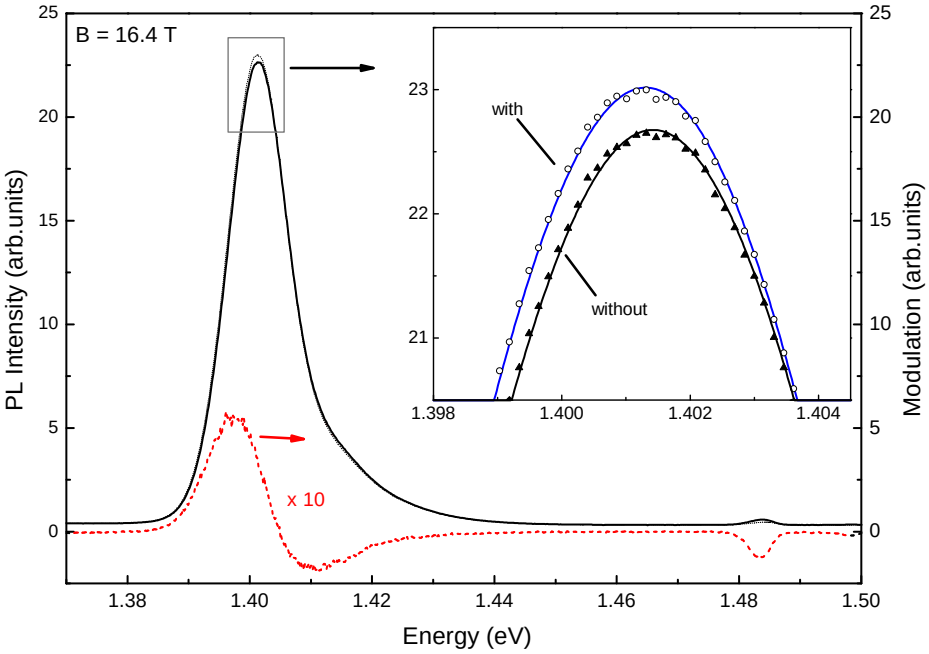

Fig. 4.1: *PL emission of the sample 11955-945°C at B = 16.4 T without (solid line) and with FIR radiation (dotted line). The FIR wavelength was 118μm (10.5 meV). The resulting modulation spectrum is shown by the dashed line. For clarity it has been multiplied by a factor 10. Inset: To make the difference between the two PL spectra better visible, a close-up around the maxima of the two lines is shown.* $T = 2.2\,K$, $\lambda_{exc} = 532\,nm$, $P_{exc} = 1\,mW/cm^2$, $P_{FIR} = 200\,mW/cm^2$

The PL spectra consist of the dominant emission from the quantum dot ground state and a weak feature at 1.482 eV related to wetting layer emission. From the modulation spectrum one sees that the FIR light reduces the wetting layer emission, while the derivative shape indicates that for the QD emission mostly a low energy shift occurs. However, taking the integral over the spectral line, leads to a positive, non-vanishing contribution, so that the PL intensity of the QDs increases as well.

More insight can be taken from looking at the magnetic field dependence of the integrated intensity I of the two features, shown in Fig. 4.2 (a). For the wetting layer (WL) it shows a smooth decrease with increasing magnetic field (dashed line) while for the QD emission a smooth increase is observed (dotted line) which is much stronger than the drop for the wetting layer as shown in the sum of both signals (solid line). The FIR can thermally activate carriers in the GaAs barriers which have been trapped by defects etc, so that they can reach the QD confinement. This heating in GaAs apparently prevents also trapping in the wetting layer. The orientation of the magnetic field along the heterostructure hinders carrier diffusion normal to it, while diffusion along B is still possible. This facilitates carrier transport towards the quantum dots. The smooth increase can be well described by a B^2 dependence and will be subtracted in the following, to work out features related to resonant absorption of the FIR radiation (Fig. 4.2 (b)).

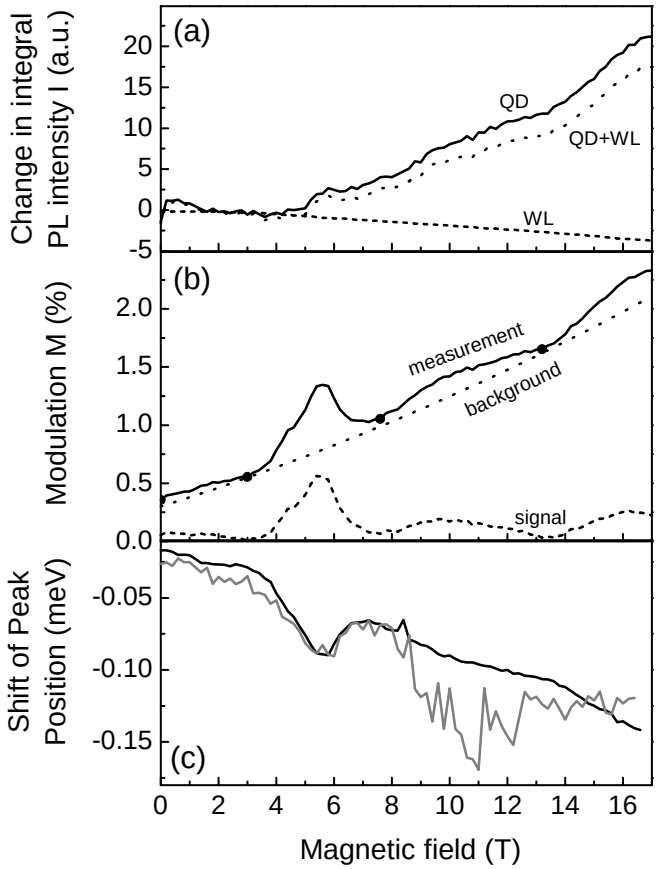

Fig. 4.2: *(a) Shown are the changes of integrated intensity I of the QD emission (dotted line) and the wetting layer emission (dashed line) from sample 11955-945°C as well as the sum of both intensities (solid line) as functions of magnetic field. (b) Modulation M of sample 11955-945°C QD emission (solid line) as function of magnetic field. The background (dotted line) is fitted through the minima of the modulation signal and subtracted from it to obtain only the resonant part of the signal (dashed line). (c) Shows the energy shift of the emission peak. PL excitation with the HeNe-Laser (black line) and the TiSa-Laser (grey line).* $T = 2.2\,K$, $\lambda_{exc} = 532\,nm$, $P_{exc} = 1\,mW/cm^2$, $\hbar\omega_{FIR} = 10.5\,meV$, $P_{FIR} = 200\,mW/cm^2$.

Now let us turn to the behavior of the QD ground state emission. Fig. 4.2 (b) gives the modulation *M* of this line as a function of magnetic field. Again the FIR energy was 10.5 meV. Clear resonances appear in the field dependence, a dominant one at 5.4 T (with potentially a weak shoulder on the low field side, see below), and two further rather broad resonances having their maxima at 10.2 T and 16.4 T. The modulation spectrum for the latter resonance was shown already in Fig. 4.1.

We have also determined the energy shift between the two spectra for which we have fitted the emission lines with Gaussian functions and calculated the energy difference between their centers. Resonances can be also seen in the energy shift on top of a smooth shift to lower energies (black curve in Fig. 4.2 (c)). The magnetic field positions of the resonances coincide with the ones found in the modulation.

Two of them can be also seen when the sample is excited not above the barrier in the GaAs but below the WL using a Ti:sapphire laser (grey curve in Fig. 4.2 (c)). The first one at 5.4 T is pronounced while the higher lying one is quite noisy due to the weak laser absorption.

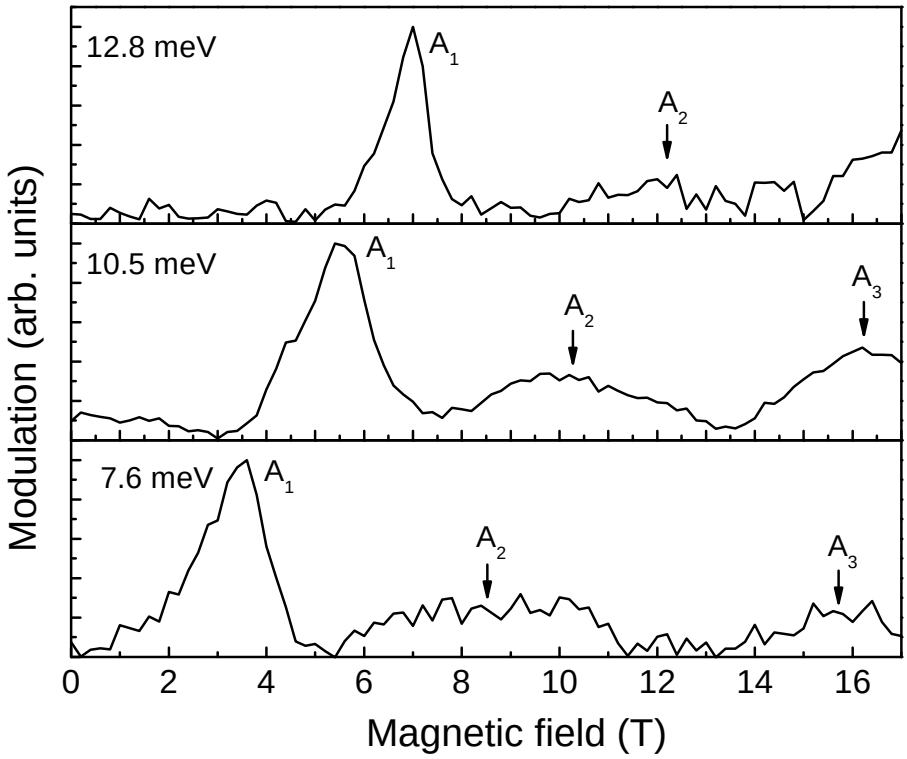

Fig. 4.3: *Modulation of sample 11955-945°C for three different FIR photon energies of 12.8, 10.5, 7.6 meV, respectively. Note that the signal is least noisy for the 10.5 meV FIR irradiation not only because of its strongest intensity. This indicates that the radiation is absorbed by more QDs within the inhomogeneous distribution.* $T = 2.2\,K$, $\lambda_{exc} = 532\,nm$, $P_{exc} = 1\,mW/cm^2$.

Modulations have been measured as a function of magnetic field for the three different FIR photon energies and are shown in Fig. 4.3. In all cases modulations of the PL emission similar to those described before can be observed, however, the magnetic fields have to be adjusted. For all three FIR lines a strong resonance appears which shifts to higher magnetic field with increasing FIR photon energy. Also a couple of other, significantly weaker and also significantly broader resonances appear. The magnetic field dependence of the broader resonances is summarized in Fig. 4.9 (b).

Extrapolation to zero magnetic field shows that the energy of the strongest resonance tends to zero. This behavior is very similar to that of a cyclotron resonance, for which FIR quanta are absorbed when their energy is equal to the cyclotron energy, $\hbar\omega_{FIR} = \hbar\omega_c = \hbar eB/m$. From a corresponding fit to the data we obtain a mass of 0.067 in units of the free electron mass, which is similar to the electron mass in

GaAs based systems as it is often used to model the electron level in QDs [Dio06].

The modulation signal of the sample 11955-850°C is significantly weaker and the change of the integral PL intensity reaches only 0.05%. However, still three resonances can be observed. Due to the low signal quality the shape of the modulation signal has been fitted with three Gauss curves as shown in Fig. 4.4 (a). Also here the first resonance is significantly stronger and its line width narrower than those of the other two resonances. The lower panel (b) contains the modulation signal of the wetting layer which shows only one distinct maximum which coincides in shape and position very well with the first resonance in the quantum dots. This supports the idea that the first resonance is caused by cyclotron resonance in the wetting layer. It is not clear why such a resonance is not observed for sample 11955-945°C.

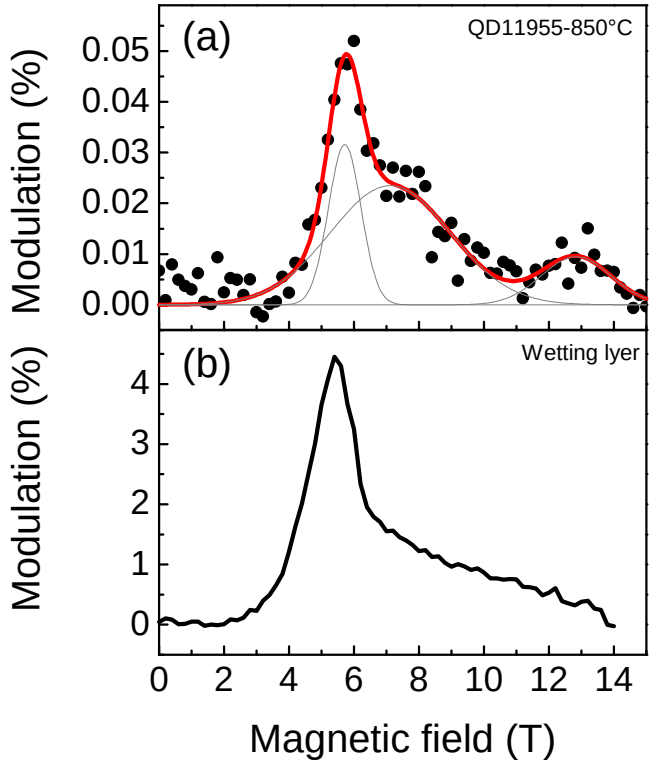

Fig. 4.4:
(a) Modulation signal of sample 11955-850°C (black dots). Three Gauss fits (grey lines) have been used to fit the data points (red line).
(b) Modulation signal of the wetting layer.
$T = 4.2\,K$,
$\lambda_{exc} = 532\,nm$,
$P_{exc} = 3\,mW/cm^2$
$\hbar\omega_{FIR} = 10.5\,meV$,
$P_{FIR} = 150\,mW/cm^2$.

To obtain further insight, we have tilted the magnetic field relative to the heterostructure growth direction. In case of bulk GaAs, the resonance, at which the field occurs, would not depend on the tilt angle. In case of a resonance in the quasi-two-dimensional wetting layer there would be a strong angle dependence as only the field component normal to the wetting layer is important. This component is given by $B_\perp = B\cos\theta$ with the angle θ between normal and field.

As the FIR energy is fixed in each case, the magnetic field B at which the resonance occurs would be shifted to higher fields. The resulting dependence of the resonance on magnetic field is proportional to $1/\cos\theta$ [Cav85].

The same is, to a good approximation, expected for a resonance in the QDs: Due to

the small dot height as compared to the cyclotron radius that can be obtained for the available field strengths, a magnetic field component normal to the QD plane has basically no impact on the carrier motion.

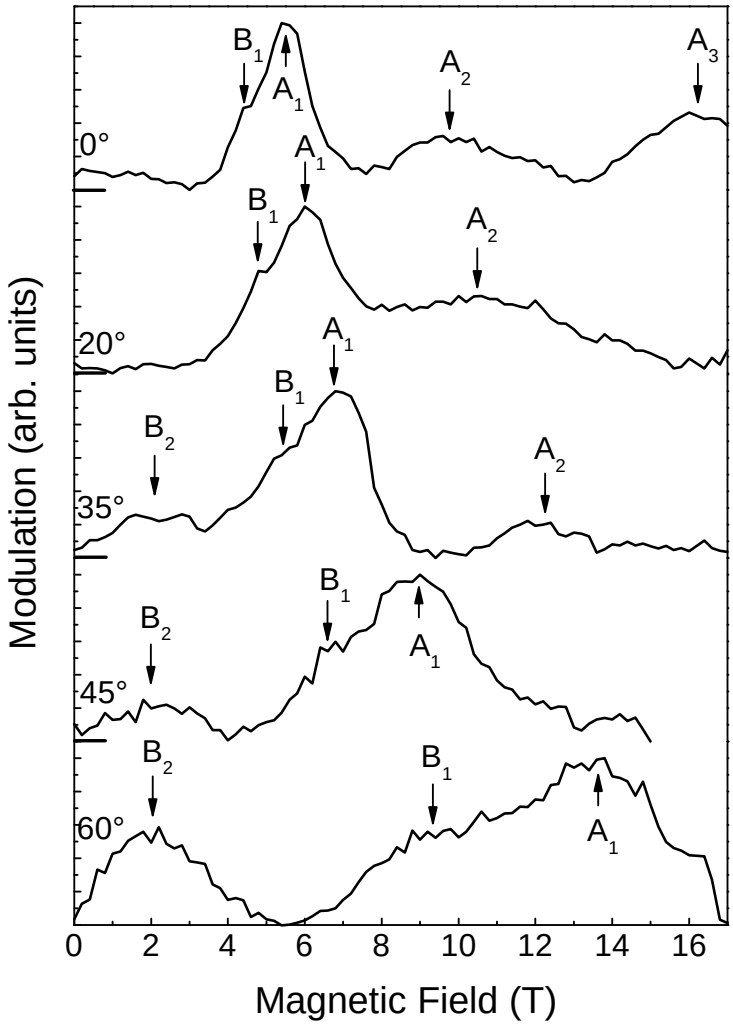

Fig. 4.5: *Sample 11955-945°C: Modulation signal measured at different angles between the growth axis of the sample and the direction of the magnetic field.* $T = 2.2\,K$, $\lambda_{exc} = 632.8\,nm$, $P_{exc} = 0.7\,mW/cm^2$, $E_{exc} = 10.5\,meV$, $P_{FIR} = 150 - 180\,mW/cm^2$.

Fig. 4.5 shows the corresponding spectra for tilt angles up to 60°. The FIR photon energy was 10.5 meV. One clearly sees that the main resonance shifts to higher fields for increasing tilt angle. Another resonance B_1 seems to emerge from the left side of the main resonance with θ. At very low magnetic fields a further resonance B_2 appears. The tilt angle dependence of the observed resonances is summarized for this fixed FIR energy in Fig. 4.6. Most resonances seem to fall indeed on a $\frac{1}{\cos\theta}$ dependence, showing that the resonance occurs in the wetting layer or the QDs, but not in the GaAs barriers, where carrier properties should be isotropic and show no dependence on the field orientation.

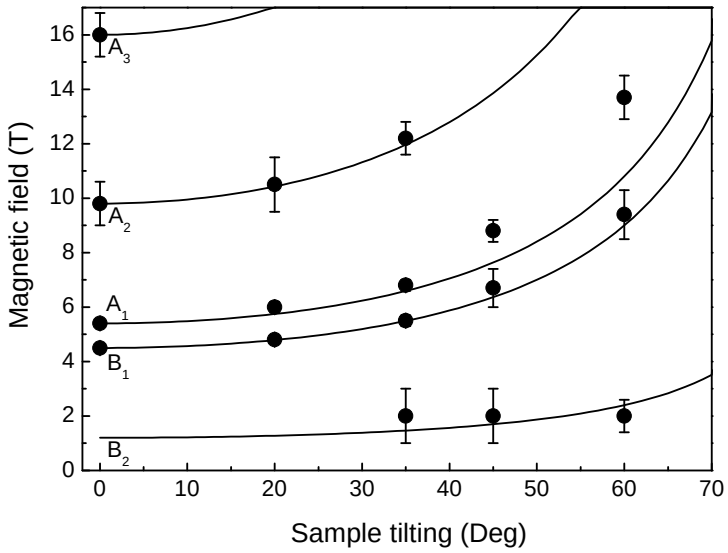

Fig. 4.6: *Magnetic field positions of the modulation resonances from Fig. 4.4 versus tilt angle. Lines show expected positions for a $1/\cos\theta$ dependence. Sample: 11955-945°C, $T = 2.2\,K$, $\lambda_{exc} = 632.8\,nm$, $P_{exc} = 0.7\,mW/cm^2$, $E_{exc} = 10.5\,meV$, $P_{FIR} = 150 - 180\,mW/cm^2$.*

To identify the origin of the observed resonances, we discuss first the selection rules for FIR radiation which apply for the carrier envelope wave functions. As described before, sample 11955-945°C was n-doped such that on average each QD contains a single electron. Optical excitation at the low powers used in experiment leads to formation of a charged exciton. Formation of a charged biexciton or even higher multi exciton complexes is unlikely. For simplicity of discussion we neglect Coulomb interactions and discuss the FIR induced transitions in terms of single particle excitations. Further, we describe the single particle spectrum by a Fock-Darwin model, which has been shown to give a reasonable description for self-assembled QDs [Foc28, Dar30, Che04]. The lateral confined levels are characterized by a radial quantum number n_r and an azimuthal quantum number n_φ which gives the angular momentum of the carriers. The FIR radiation is unpolarized at the sample so that the selection rules for this angular momentum are: $\Delta n_\varphi = -1, 0, +1$

In the Fock-Darwin spectrum there are indeed transitions which show a *B*-linear splitting corresponding to cyclotron-like resonances, namely those between states with positive and negative momentum and with the same n_r as well as the same modulus $|n_\varphi|$. But such transitions do not fulfil the selection rule. Therefore the strongest resonance cannot be attributed to any QD related transition, but has to be attributed to a resonance in the wetting layer, which is subject to Landau quantization. Since it leads to a low energy shift of the ground state QD emission, we attribute it to redistribution of electrons trapped in the disorder relief of the wetting layer to the quantum dots where they form together with the optically excited electron-hole pairs charged excitons. The low energy shift is due to the trion binding energy.

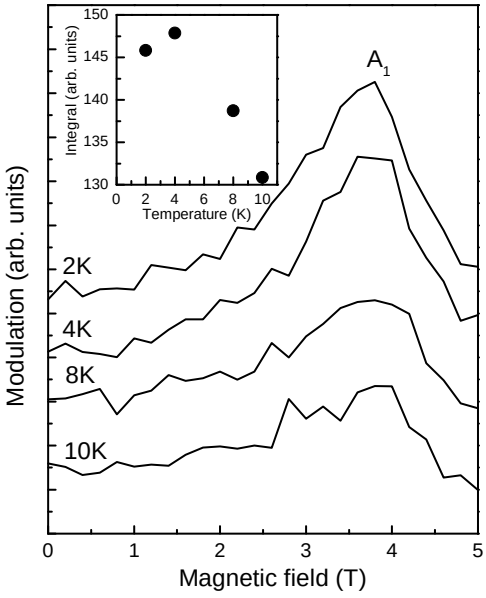

Fig. 4.7:
Magnetic field dependence of the most pronounced modulation resonance of sample 11955-945°C at different temperatures. Insert shows the temperature dependence of the integrated area of the resonance. $\lambda_{exc} = 632.8\,nm$, $P_{exc} = 0.7\,mW/cm^2$, $E_{exc} = 7.6\,meV$, $P_{FIR} = 45\,mW/cm^2$.

If, however, the wetting layer is subject to localization corresponding to the occurrence of lateral confinement, it is not a priori clear that Landau level quantization can take place. To confirm this, we have to learn about the strength of this confinement, which can be estimated by looking at the temperature dependence of the resonance. Fig. 4.7 shows the FIR modulation as function of magnetic field for four different temperatures. The insert of this figure shows the intensity of this resonance versus temperature. It is about constant for very low temperatures, but above 6 K it drops sharply.

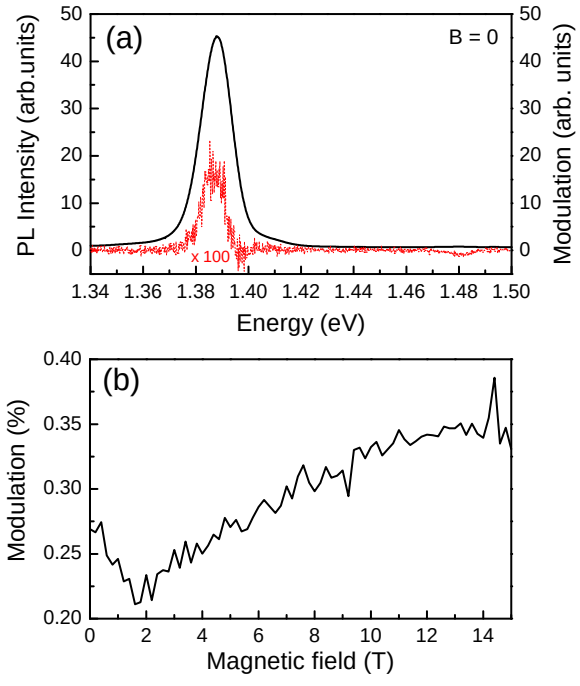

Fig. 4.8:
Photoluminescence and modulation spectrum of the undoped QDs (sample 11376-940°C) at zero magnetic field. The FIR energy was 10.5 meV.
$T = 4.2\,K$, $\lambda_{exc} = 632.8\,nm$, $P_{exc} = 0.4\,mW/cm^2$, $E_{exc} = 10.5\,meV$, $P_{FIR} = 150\,mW/cm^2$.

From this temperature dependence a thermal activation energy of not more than 1 meV can be estimated. Therefore the localization in the wetting layer is quite weak, and already for magnetic fields of one tesla the cyclotron energy is larger than the localization, so that Landau levels can be formed.

This conclusion is underlined by corresponding measurements on an undoped reference sample (11376) which are shown in Fig. 4.8. Given is the photoluminescence as well as the modulation spectrum at zero magnetic field. The FIR energy was 10.5 meV. The modulation spectrum, which was multiplied by a factor 100, shows a drop of the emission intensity from the wetting layer and an increase of the emission from the QD ground state. No pronounced derivative shape can be seen as was the case for the n-doped QDs, except of some drop of intensity on the high energy flank of the dot emission which might be associated with carrier heating, opening channels for a carrier redistribution from QDs with ground state energy at high energy to those with lower energy, leading to a redistribution of carriers among different dots. When ramping the magnetic field, no resonances appear in the modulation, except for the smoothly increasing background observed already for the n-doped QDs.

Now let us come to the dot-related features, whose magnetic field dispersion deviates from a *B*-linear behavior. Fig. 4.9 (b) shows the magnetic field dependence of these features as dots. The first resonances, which most likely appear due to the CR in the WL, are shown by squares. Data from sample 11955-945°C is shown by black symbols, data from 11955-850°C by open, white symbols. In general, the resonances may arise from the resident QD electron due to the doping, or from optically generated carriers. However, the lifetime of such carriers is rather short (about 500ps as determined from time-resolved photoluminescence), so that the efficiency of an excitation of these carriers by the FIR radiation most likely is small and can be hardly observed for the weak PL excitation used in experiment by which no quasi permanent population is maintained. Therefore we assume that the resonances are related to excitation of the resident electron.

From high excitation PL we know that the splitting between p- and s-shell emission is about 20 meV, which is dominated by the electron. For identifying the FIR transitions, we assume that 15 meV are contributed by the electron, while the rest 5 meV are given by the hole, neglecting Coulomb interactions. These values are taken as input for describing the level spectrum by a Hartree-Fock model [Foc28, Dar30, Che04]. The resulting field dispersion of the electron levels is shown in Fig. 4.9 (a) by the solid lines.

The arrows in this panel indicate possible electron transitions which are in accord with the selection rules above. The lower panel shows the magnetic field dependence of the transition energies, together with the observed resonances. The plot confirms again that the QD levels offer no allowed transition with dispersion linear with *B*. We also restrict to transitions which energetically are in the range of our FIR quanta energies.

The resident electron most likely occupies the s-shell. One can imagine also p-shell occupation in case of a phonon relaxation bottleneck. For example the optically excited hole may relax into its ground state, while the photoexcited electron remains

in the p-shell, either due to Pauli-blocking by an electron in the s-shell or due to a phonon relaxation bottleneck, as relaxation is for these QDs only possible by rather slow acoustic phonon emission. The latter situation may prevail also after radiative recombination of the electron-hole pair in the s-shell.

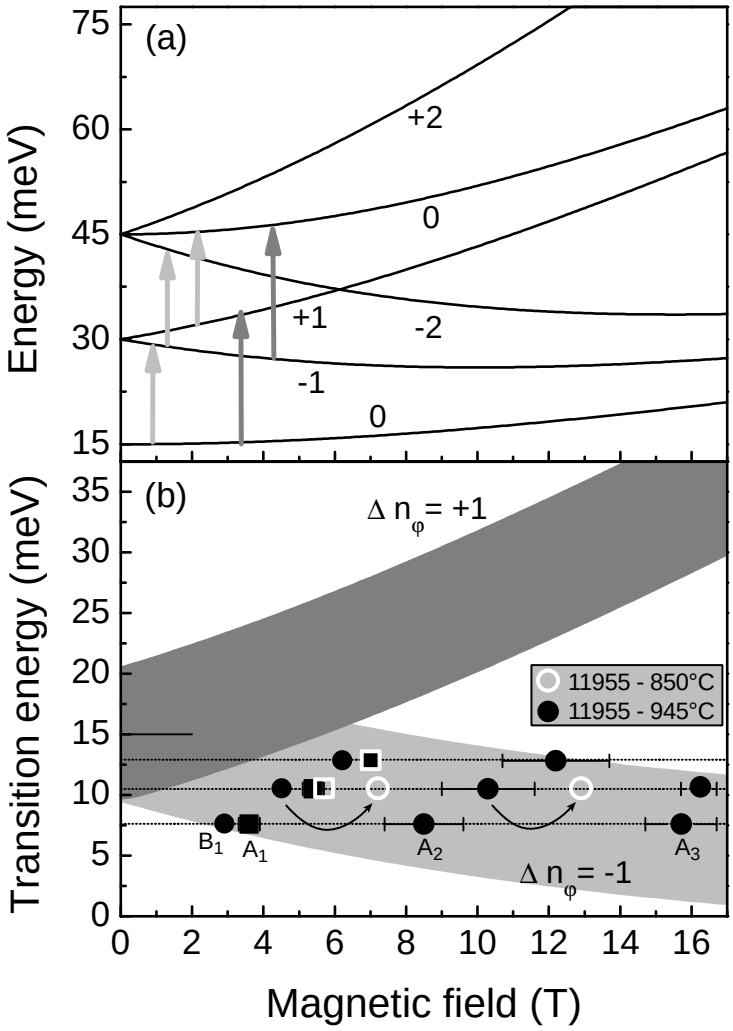

Fig. 4.9: *(a) The upper graph shows the magnetic field dependence of the Fock-Darwin-spectrum for electron states in quantum dots, assuming a confined level splitting of $\hbar\omega = 15meV$. The levels are labelled by the angular momentum quantum numbers. Allowed FIR transitions are indicated by arrows. (b) The lower graph summarizes the magnetic field dependence of the QD resonances (circles) and cyclotron resonances (squares) observed in the experiments together with the three FIR laser lines of 7.6, 10.5 and 12.8 meV (horizontal lines). Data from sample 11955-945°C is shown by black symbols, data from 11955-850°C by open, white symbols. The dark and light grey bars mark the energy range of the transitions between energy levels shown above, taking into account a total inhomogeneous broadening of 12 meV.*

Therefore we have considered all possible electron transitions from the electron s-shell and the electron p-shell, resulting in the lines in the lower panel (b). We note that several possible transition are degenerate, for example the transition from $n_\varphi = 0$ to $n_\varphi = -1$, and from $n_\varphi = -1$ to $n_\varphi = -2$. The comparison with the data shows that the resonances around 10 T most likely can be attributed exactly to such transitions. The appearance of resonances for the three different FIR quanta at first sight suggests that three different transitions may be involved. However, here one has to keep in mind that the transitions in a QD ensemble are strongly inhomogeneously broadened (see the PL in Fig. 4.1).

Also this broadening will be dominated by the electron, as due to its small mass the electron confinement energy will vary strongly because of fluctuations of size, composition etc of the dots. The PL broadening is about 12 meV, so that we can expect that the broadening of the electron transitions is of comparable magnitude. This value has to be compared to the range of energies covered by the FIR line which is only about 5 meV. Therefore the three resonances around medium field most likely do not correspond to different transitions but to the same inhomogeneously broadened one, for example $n_\varphi = 0$ to $n_\varphi = -1$. The splitting between these two states is reduced by the applied magnetic field, as the light grey area in Fig. 4.9 (b) shows.

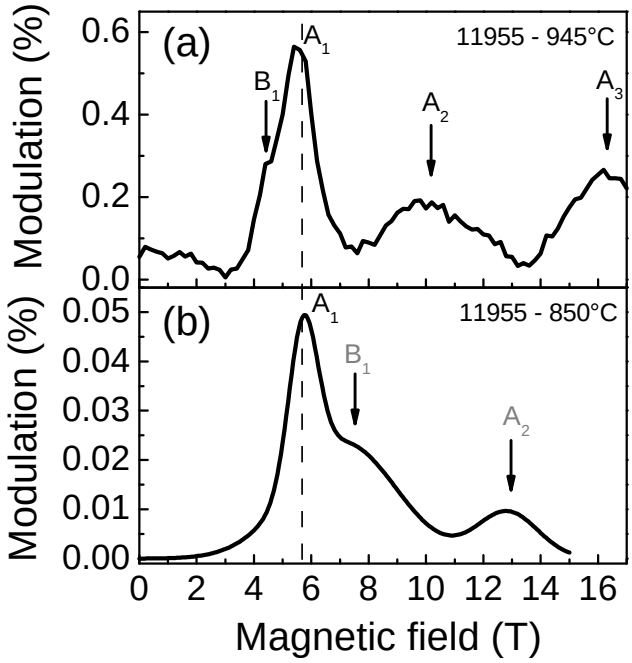

Fig. 4.10: *(a) Modulation signal of sample 11955-945°C compared to the fit of the modulation signal of sample 11955-850°C (b). A shift of the resonances (except of A_1) is observed. Labels in (b) are shown in grey because the assignment is only an assumption based on the Fock-Darwin energy spectrum (see text).*
$T = 2.2\,K$, $\lambda_{exc} = 532\,nm$, $P_{exc} = 3\,mW/cm^2$, $\hbar\omega_{FIR} = 10.5\,meV$, P_{FIR} (945°C) $= 200\,mW/cm^2$, P_{FIR} (850°C) $= 150\,mW/cm^2$.

The resonance positions are compared between samples 11955-945°C and 11955-850°C in Fig. 4.10. The main resonance A_1 can be found at almost the same position for both samples indicating that its origin lies in the wetting layer where a different annealing temperature has no distinct influence. The other resonances are shifted. A high annealing temperature leads to a broadening of the quantum dots which reduces the confinement of electrons. For the QDs with a temperature of only 850°C a greater splitting between the s- and p- shell can be expected. The s-p slitting in case of the 11955-850°C quantum dots is 27.6 meV, for the 11955-945°C: 18.7 meV. So for low annealing temperatures the s-p splitting is 8.9 meV larger. This means that a transition, in resonance with the FIR radiation of the same energy, shifts to higher magnetic fields because the splitting of $n_\varphi = 0$ and $n_\varphi = -1$ decreases with magnetic field. Therefore it can be assumed that the resonances observed in the modulation signal of 11955-850°C belong to the transitions labelled B_1 and A_2. However, just from the data of both samples it is not clear in which direction the resonances shift. ODR measurements on a series of quantum dots with different annealing temperatures make it easier to follow the movement and may give a strong indication about the shift direction.

If the sample is exposed to the 7.6 meV quantum, only rather large QDs absorb, for which the splitting between p- and s-shell is quite small. For the mid energy quantum also the medium sized QDs absorb, while for the quantum with 12.8 meV the smallest quantum dots are excited. The resonances appearing at the highest fields most likely can be attributed to the very same transition, but now the field has lowered the splitting between the involved levels such, that the lowest energy quantum can be absorbed by the medium sized dots, and the mid energy can be absorbed by the small dots. For the highest energy quantum there seems to be a resonance at the highest applied fields but its exact position cannot be determined anymore.

The inhomogeneity also explains the broadening of the resonance, as compared to the cyclotron-like feature. That the resonance follows the $1/\cos\theta$ behavior in the tilted magnetic field studies can be expected due to the rather flat shape of the dots, which prevents any significant change of the vertical motion of the carriers along the heterostructure by a field component normal to this direction, as discussed above. Only the in-plane motion can be changed considerably by a corresponding field component (see below).

Recently the FIR absorption of negatively charged excitons in a parabolic QD dot has been calculated [Kor06]. In contrast to dots charged with electrons only, for which the FIR radiation probes solely the center-of-mass motion and is insensitive to Coulomb interaction effects, the FIR spectra of trions depend on details of confinement and interaction. The trion states are described by the total angular momentum L, for which the selection rule $\Delta L = \pm 1$ holds under application of circularly polarized radiation. In the energy range of interest here, the absorption is dominated by a transition with $\Delta L = +1$ which shifts slightly to lower energies with increasing B, in accord with our observations. Besides this strong feature also a few other significantly weaker lines appear which arise from configuration mixing of single particle states by the Coulomb interactions.

For completeness, we note that for strong optical PL excitation no resonances can

be observed anymore. This may be related to the fact that the occupation of the QDs by multiple carriers leads to many possible transitions of the carriers among the dot levels, so that no resonances can be resolved anymore.

Finally, we need to discuss the resonances which appear at low magnetic fields when the field orientation is tilted, i.e. B_2 in Fig. 4.5. This field orientation breaks the rotational invariance of the QD structures, so that the angular momentum is no longer a good quantum number. As a consequence also the FIR selection rules are lifted. To obtain further insight, we treat the influence of the in-plane field component by perturbation theory. The magnetic field is assumed to have a *z*-component B_z and an in-plane component B_x along the x-direction. For this field choice the following gauge for the vector potential can be done:

$$A = A_1 + A_2 = \frac{1}{2}\begin{pmatrix} -B_z y \\ +B_z x \\ 0 \end{pmatrix} + \begin{pmatrix} 0 \\ 0 \\ B_x y \\ . \end{pmatrix} \tag{4.2}$$

When calculating the magnetic field, $\boldsymbol{B} = rot\,\boldsymbol{A}$, the contribution $\boldsymbol{A}_1$ of the vector potential, for which the symmetric gauge has been chosen, gives B_z. The second contribution for the *I*-component of the field leads to the perturbation in the Hamiltonian:

$$\mathcal{H}' = -\frac{e}{m}\boldsymbol{A}_2\boldsymbol{p} + \frac{e^2\boldsymbol{A}_2^2}{2m} \tag{4.3}$$

Neglecting it in lowest order gives the Fock-Darwin spectrum with the corresponding field component $B_z = B\cos\theta$.

Calculation of the influence of the perturbation on this spectrum gives no contribution in first order of the in-pane field B_x. The second order, however, does not vanish, and is proportional to $B_x^2 = B^2 sin^2\theta r^2\, sin^2\varphi$. Due to this proportionality, states which differ up to 3 angular momentum quanta can become mixed, so that for example the states with $n_\varphi = +1$ and $n_\varphi = -2$ which otherwise would cross around 6 T (see Fig. 4.8) become mixed and anticross. In the anticrossing range the electron eigenstates are given by $|E_{1,2}\rangle = \alpha^{1,2}|n_\varphi = +1\rangle + \beta^{1,2}|n_\varphi = -2\rangle$, where the coefficients depend on field strength. Due to this mixing two transitions, should appear from the $n_\varphi = -1$ state to E_1 and to E_2. These additional transitions which become possible through the in-plane field may explain the appearance of new resonances in the FIR spectra.

4.2 Conclusion and outlook

In summary, we have performed an ODR study of self-assembled QDs. For n-doped QDs we see a number of resonances. One of them can be related to a carrier redistribution from the wetting layer into the QDs, when the conditions for the cyclotron resonance are met. The other resonances show a dependence on the quantum dot size and are likely to be cause by transitions between confined electron levels. Here quantum dot samples with an annealing temperature of 850°C and 945°C have been studied, but more samples with the following annealing temperatures are available: 800°C, 820°C, 900°C and 980°C. Especially the sample with 900°C is interesting because it lies between the samples presented here. ODR resonances found in the 900°C sample may confirm the assumption that resonances shift to higher magnetic fields for smaller QDs.

Another interesting perspective for future measurements are doped colloidal quantum dots with a small size distribution. Unfortunately it is not a trivial task to incorporate doping material inside of colloidal dots. For conventional growth techniques the dopants often stick to the surface of the colloidal dots or remain in the fluid. Measurements of undoped colloidal CdTe quantum dots under the same experimental conditions are comparable to self-assebled undoped quantums dots presented in this chapter.

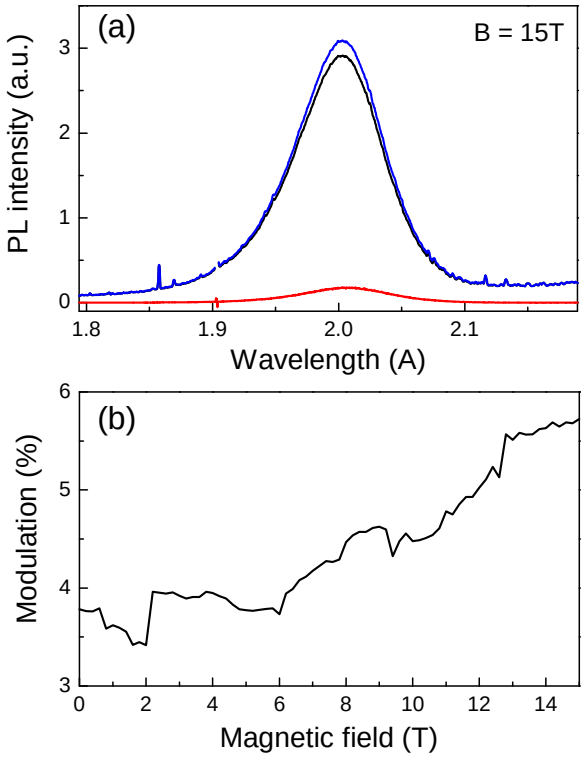

Fig. 4.11:
(a) PL (black line), PL+ FIR (blue line) and modulation spectrum (red line) at B = 15T and T = 4.2K of undoped colloidal CdTe quantum dots.
(b) Increase of the modulation signal with magnetic field. Sample: Colloidal CdTe-QDs,
$\lambda_{exc} = 532\,nm$,
$P_{exc} = 2\,mW/cm^2$,
$\hbar\omega_{FIR} = 10.5\,meV$,
$P_{FIR} = 140\,mW/cm^2$

Fig. 4.11 (a) shows the PL and modulation spectrum at $B = 15\,\mathrm{T}$ and $T = 4.2\,\mathrm{K}$. The photoluminescence is very broad due to the size distribution of the quantum dots. Under FIR radiation the PL increases but shows no shift of the line that was seen for n-type doped quantum dots. The modulation signal (Fig. 4.11 (b)) increases with magnetic field comparable to the behaviour of the self-assembled undoped QDs. No distinct resonance can be observed in the modulation signal.

Chapter 5:

PL and ODR study on magnetic quantum wells

In diluted magnetic semiconductors (DMS) the presence of additional magnetic ions (e.g Mn, Fe, Cr) with localized magnetic moments amplifies the effect of the external magnetic field. Typical examples of DMS based on II-IV semiconductors are $Cd_{x-1}Mn_xTe$ and $Zn_{x-1}Mn_xSe$ where x defines the concentration of Mn ions. In the photoluminescence of these materials cusps have been observed which can be related to interactions between Mn^{2+} ion pairs and single ions.

In ZnMnSe/ZnBeSe DMS quantum wells, electron spin resonance (ESR) of the Mn2+ ion was induced by 60 GHz MW radiation and detected optically [Iva07,Iva08].

A set of CdMnTe/CdMgTe DMS quantum well samples was studied in microwave induced ODR measurements showing nonmonotonic behaviour, which can be assigned to the electron paramagnetic resonance [Sad03].

5.1 Basic properties of diluted magnetic semiconductors

The presence of the magnetic ions strongly modifies magnetic and magneto-optical properties of DMS nanostructures. Even at low magnetic fields the material is magnetized very strongly at low temperatures. A small increase of the temperature influences the magnetization to a great extend. To study the temperature dependence of DMS quantum wells it is important to distinguish between three temperatures: The lattice temperature, the carrier temperature and the temperature of the Mn subsystem. Energy transfer between the systems is occurs by spin-lattice relaxation (SLR) and exchange scattering.

Sudden changes to the magnetization at high magnetic fields have been observed in

the early 1980s. They are caused by ion pairs or nearest neighbor interaction in Mn clusters, which only start to contribute to the magnetization at high B-Fields when their spins are not polarized in an antiparallel way. Experimental data presented in this chapter shows changes in the magnetization which can be deduced to next nearest neighbor interaction in Mn clusters.

5.1.1 Magnetization in DMS

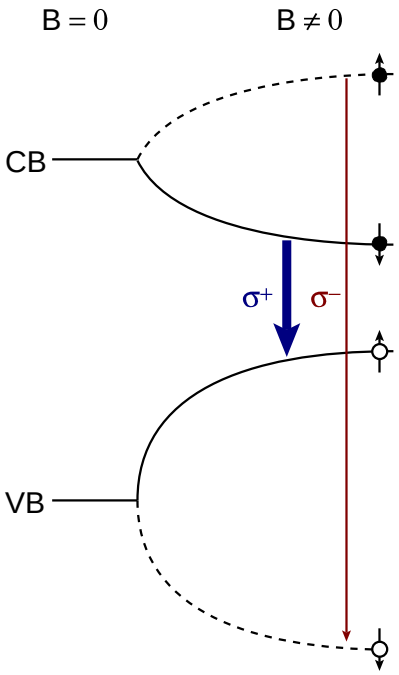

Fig. 5.1: *Giant Zeeman splitting of conduction and valence band. Recombinations with σ^--polarization are unlikely so that the PL is strongly polarized.*

The magnetization of the ions (e.g. Mn^{2+}) strongly depends on the external magnetic field and their temperature. At low lattice temperatures T_L a high percentage of single ions can be oriented parallel to B_{ex} at only moderate field strength. The presents of magnetic ions is reflected in the optical properties due to the $sp-d$ exchange interaction between delocalized s- and p-band electrons and localized d electrons of the magnetic ions. The spin orientation S depends on the spin temperature T_S which is equal to T_L in equilibrium conditions. The population of the spin sublevels $n_{\frac{1}{2}}$ and $n_{-\frac{1}{2}}$ at a temperature T_S can be expressed by:

$$\frac{n_{\frac{1}{2}}}{n_{-\frac{1}{2}}} = exp\left(-\frac{\mu_B\, g\, B}{k_B\, T_s}\right) \tag{5.1}$$

Carriers are very likely to be polarized due to a strong exchange interaction with the magnetic ions.

Flipping the spin from a parallel to an antiparallel orientation requires much more energy than in non-magnetic semi-conductors. This also means that the splitting has become stronger. It is therefore called giant Zeeman splitting (Fig. 5.1). The giant Zeeman splitting saturates when all single Mn ions are oriented parallel to B. The giant Zeeman splitting of optical transitions from CB to VB is described by:

$$\Delta E_{GZ} = (\alpha - \beta)\, N_0\, x\, \mu_B\, g_{Mn}\, S\, B_{\frac{5}{2}}\left(\frac{5\,\mu_B\, g_{Mn}\, B}{k_B\, T_S}\right) \tag{5.2}$$

Here, α, β are material specific exchange constants, N_0 is the number of cations in a unit cell volume, x is the mole fraction of the magnetic ion, e.g. the Mn concentra-

tion, g_{Mn} is the g-factor of the Mn ions and $B_{\frac{5}{2}}$ is the Brillouin function. Equation 5.2 is only true for the samples with low Mn content (x < 0.005). At higher concentrations the direct calculation of interacting magnetic ions distributed randomly in the cation sublattice is a nontrivial task because of the exchange interaction between Mn^{2+} ions. It can be avoided by a phenomenological approach, introducing effective spin and temperature [Gaj79]:

$$\Delta E_{GZ} = (\alpha - \beta)\, N_0\, x\, \mu_B\, g_{Mn}\, S_0\, B_{\frac{5}{2}}\left(\frac{5\,\mu_B\, g_{Mn}\, B}{k_B\,(T_S + T_0)}\right) \qquad (5.3)$$

where S_0 is the effective spin and T_0 the effective temperature [And]. At high Mn concentrations the probability for the formation of ion pairs (i.e. two Mn ions are situated close to each other) increases. Due to the antiferromagnetic orientation of the spin pairs they do not contribute to the magnetization. This means that for a high Mn content the magnetization is much lower than one would expect if all ions could be kept isolated from each other.

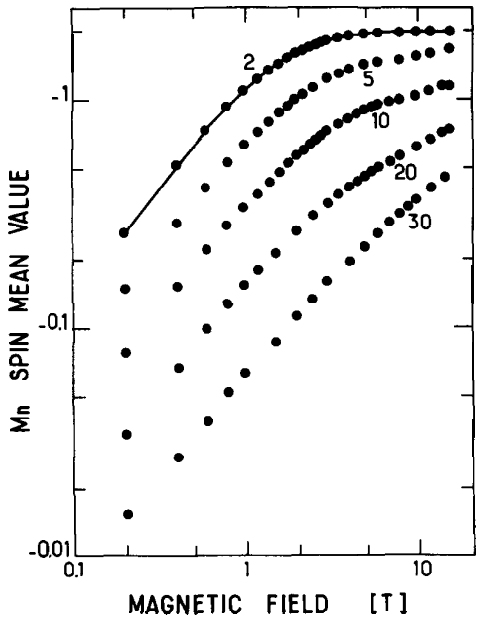

Fig. 5.2:
Mean value of the component of Mn^{2+} spin in $Cd_{x-1}Mn_xTe$ along the magnetic field, obtained from magnetization data at 1.5 K. Composition values indicated in %. Continuous line represents a Brillouin function [Gaj79].

This is reflected in two properties of the magnetization which are shown in Fig. 5.2: First the saturation level is lower. For single spins a mean value of $\frac{5}{2}$ for the Mn^{2+} spin component along the magnetic field would be expected. For a bulk $Cd_{1-x}Mn_xTe$ sample with x = 0.02 a value of 2.11 is reached. To account for this an effective spin S_0 has been introduced whose value is smaller than $\frac{5}{2}$ and depends on the Mn concentration as shown in Fig. 5.3. Secondly the slope of the magnetization curve when plotted versus magnetic field becomes less steep, similar to an increase of the temperature. Therefore an effective temperature T_0 is defined.

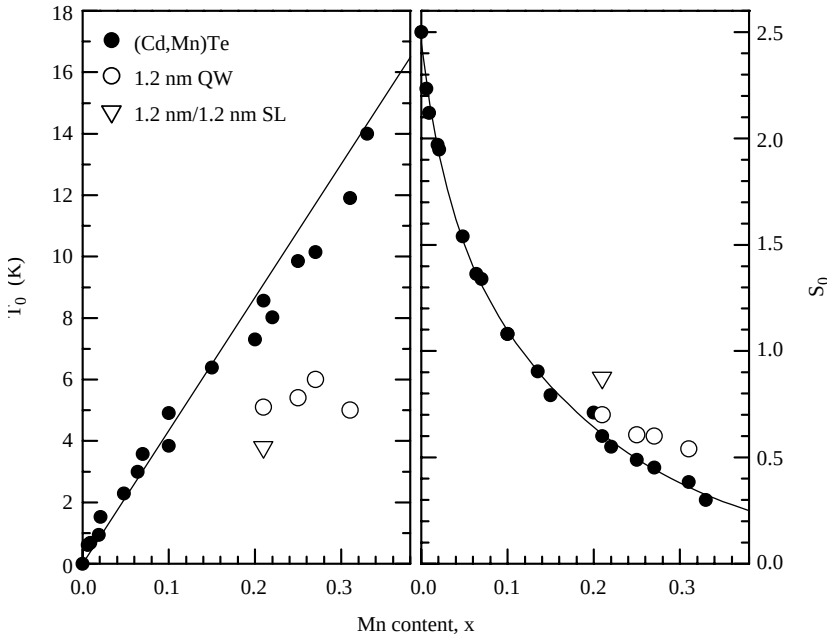

Fig. 5.3:
The dependencies of the phenomenological parameters T_0 and S_0 in the Mn content x for $Cd_{1-x}Mn_xTe$-based epilayers, QWs and superlattices [Oss93, Yak95].

At high magnetic fields a nonmonotonic increase of the magnetization can be observed (Fig. 5.4 (b)). This can be deduced to the nearest-neighbor exchange interaction which can be described by the following Hamiltonian [Nag80, Sän06, Fur88]:

$$\mathcal{H} = -2J_{NN}S_1 \cdot S_2 - g_{Mn}\mu_B(m_1 + m_2)B \tag{5.4}$$

where J_{NN} ($J_{NN} = -6.3K$ for $Cd_{1-x}Mn_xTe$) is the coupling constant of the $d-d$ exchange interaction between neighbor magnetic ions. The product of the spin operators S_1 and S_2 can be calculated by:

$$2S_1 \cdot S_2 = S^2 - S_1^2 - S_2^2 \tag{5.5}$$

The eigenvalues of the spin operators S_i^2 are $S_i(S_i + 1)$ with $S_1 = S_2 = \frac{5}{2}$. Then the eigenvalues of the Hamiltonian are given by:

$$E = -J_{NN}\left(S(S+1) - \frac{35}{2}\right) - g_{Mn}\mu_B m_s B \tag{5.6}$$

where $S = 0,1, \ldots,5$ is the total spin of the ion pair and $m_s = -S, -S+1, \ldots, S$ is the magnetic quantum number. A plot of the energy levels as a function of magnetic field is shown in Fig. 5.4 (a).

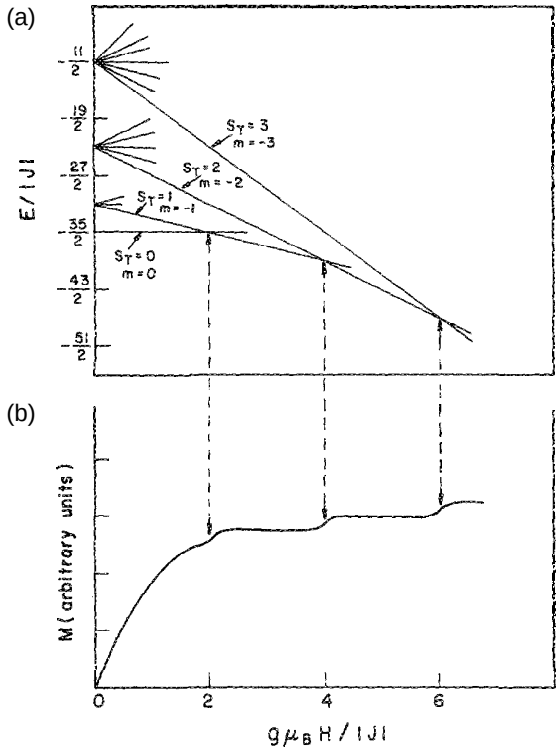

Fig. 5.4:
(a) Energy level scheme for a pair of Mn^{2+} ions, showing how steps occur in the magnetization at high fields (b). The relative size of the steps is exaggerated for clarity [Fur88].

Up to high magnetic fields the antiferromagnetic $S = 0$ state is the ground state. Beyond this point the $S = 1$, $m_s = -1$ state is lower in energy. Because this state has some magnetic moment, the ion pairs now start to contribute to the magnetization which can be observed as steps in the magnetization curve in Fig. 5.4 (b) [Agg85, Sha84, Sha86]. A second step can be observed when $S = 2$, $m_s = -2$ becomes the ground state at even higher fields. Maximum magnetization is reach when all Mn spins are orientated parallel to the direction of the magnetic field.

5.1.2 Energy and spin transfer in DMS semiconductors

Properties of magnetic semiconductors such as the magnetization are sensitive to changes of the temperature. While this is true in general, in case of diluted magnetic semiconductors it is necessary to distinguish between a number of temperatures: The temperature of the phonon system or lattice T_L, the temperature of the carriers T_c and the temperature of the manganese T_{Mn}. These temperatures are not completely isolated from each other, and in equilibrium conditions, without external excitation, they become equal to the lattice temperature which has the highest heat capacity and serves as a bath, so in general T_C, $T_{Mn} \geqslant T_L$ holds true. In this subsection the focus will be on changes to individual temperatures due to different kinds of excitation and on mechanisms for the energy exchange between them.

The carrier system consists of resident electrons (or holes) provided by n-type (p-type) doping of the sample and photo generated carriers under laser excitation. Depending on the excitation power the creation of photo created carriers heats the carrier temperature T_C (Fig. 5.5). It can relax to the lattice by efficient electron-phonon interaction on a timescale of ~100ps [Sha74].

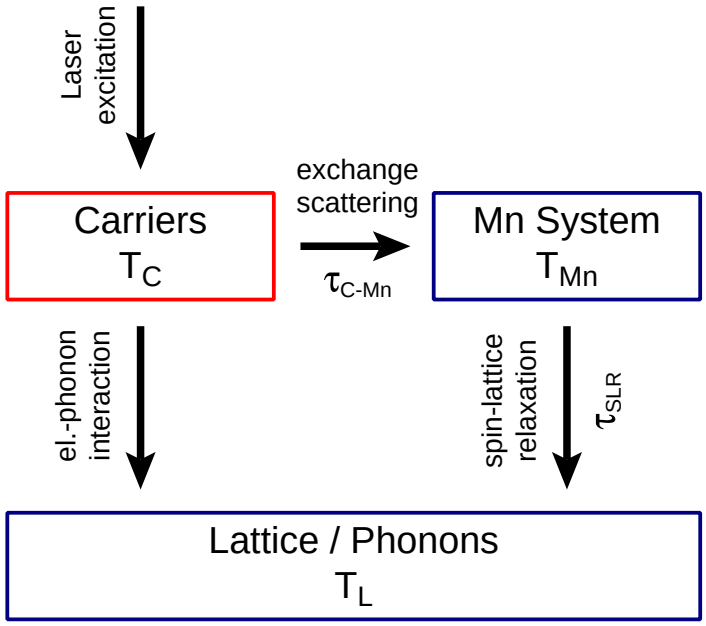

Fig. 5.5:
Energy system of a DMS QW consisting of carrier system, Mn System and lattice. Mechanisms of energy and spin transfer are shown by arrows for the case of a laser excited carrier system

Another indirect channel for the energy transfer to the lattice occurs via the Mn system. It is based on the very efficient exchange scattering between carriers and Mn ions which happens on a timescale in the order of 10ps [Die95]. However, the energy transfer from the Mn system to the lattice is based on spin-lattice relaxation whose typical timescale very much depends on Mn concentration [Kne06b] and can reach from milliseconds for samples with $x = 0.004$ down to nanoseconds for $x = 0.11$. Single Mn^{2+} ions have zero orbital moment and do not interact with the lattice. Energy transfer only occurs on Mn clusters which make the Mn content a critical value for the efficiency of the cooling process. The manganese temperature can be determined experimentally by direct observation of the magnetization degree, the corresponding giant Zeeman splitting or the polarization degree of the exciton photoluminescence.

Fig. 5.6 shows the photoluminescence of a $Zn_{0.988}Mn_{0.012}Se$ / $Zn_{0.94}Be_{0.06}Se$ QW of 100Å width under different excitation powers ranging from 16 mW to 13.2 W [Kel01]. Lines in Fig. 5.6 show a fit to the experimental data which is used to determine T_{Mn} from the Zeeman splitting. With increasing excitation power the temperature of the Mn system rises from 1.7 K, which is almost bath temperature (T_l = 1.6 K), to above 23 K where the Zeeman splitting is already strongly suppressed.

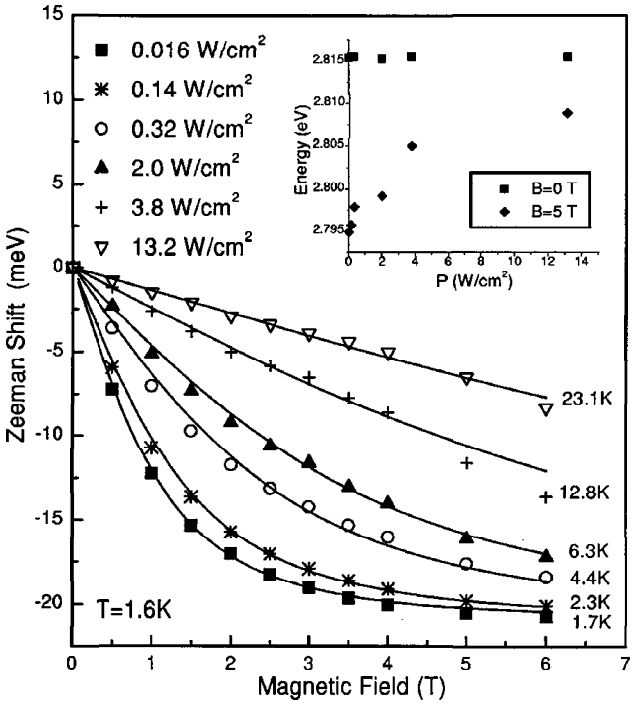

Fig. 5.6:
Giant Zeeman shift of the exciton line for a $Zn_{0.988}Mn_{0.012}Se$ QW. Lines represent a fit to the experimental data determining T_{Mn} values as indicated in the figure. Inset shows the dependence of the exciton energy on excitation density for two magnetic fields. [Kel01]

Energy can also be transferred to the DMS system by MW [Gis93, Yu07] or FIR radiation, heat pulses of nonequilibrium phonons [Sch99, Aki] or electric field heating. In this chapter experiments are presented that show the behaviour of DMS quantum wells under FIR radiation. The far infrared light can adress all three subsystems. Evidence for the directly influenced of FIR radiation to the kinetic energy of the carriers can be found by observation of cyclotron resonance in magnetic quantum wells (See Section 5.3).

5.2 Intrinsic resonance in spin system of DMS ZnMnSe/ZnBeSe QWs

Photoluminescence measurements have been performed on a series of $Zn_{1-x}Mn_xSe$ / ZnBeSe quantum wells which differ in Mn content, quantum well width and electron concentration. An overview of the samples is given in Table 5.1. The samples were excited by an semiconductor laser with a wavelength of 405 nm (3.061 eV) at various power densities.

Sample	Mn content, x	Electron concentration / 10^{10} cm^{-2}	QW width / Å
CB1541	0.012	undoped	100
CB1542	0.004	undoped	100
CB1651	0.012	undoped	150
CB2422	0.02	undoped	100
CB2033	0.004	3	100
CB2034	0.004	32	100
CB2037	0.004	55	100

Table 5.1: *Properties of $Zn_{1-x}Mn_xSe$ quantum wells*

The photoluminescence of sample CB2422 is shown in Fig. 5.7 at $T = 2.2$ K and a power density of 75 $\frac{mW}{cm^2}$. At around $B = 9.1$ T a step in the Zeeman splitting can be observed, marked by a black arrow in Fig. 5.7 (a). It looks similar to the magnetization steps observed by Shapira and Aggarwal (cp. Fig. 5.4). However, in $Zn_{1-x}Mn_xSe$ material systems the crossing of the lowest spin states occurs at higher magnetic fields in the region of 18-20 T. Here the step is observed at lower magnetic fields.

The magnetization step at 18 T is based on the interaction of nearest neighbor (NN) Mn^{2+} ions. At high manganese concentrations Mn clusters are formed and also next nearest neighbor (NNN) interactions between Mn pairs and a single Mn ion have to be taken into account. The exchange constant for NNN is sigificantly smaller due to the longer distance between paired and single ions. Larson calculated the exchange constant J_{dd} for both NN and NNN interactions for $Cd_{1-x}Mn_xTe$ and found that the NN exchange constant is about five times larger than the NNN one.

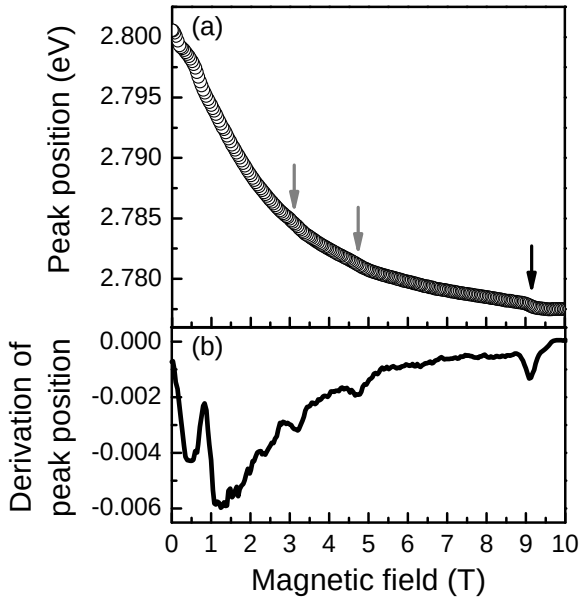

Fig. 5.7:
(a) Exciton position of sample CB2422. The black arrow indicates a step in the giant Zeeman splitting. The gray arrows show small irregularities in the shift of the exciton position.
(b) Derivation of exciton peak position.
$T = 2.2\,K$,
$\lambda_{exc} = 409\,nm$,
$P_{exc} = 0.3\,mW/cm^2$.

The calculation of the energy levels for NNN interaction is the same as for NN interaction (Equation 5.6) with a exchange constant J_{DD}. In $Zn_{1-x}Mn_xSe$ the values for the exchange constants are: $J_{DD}(NN) = 12.2K$ and $J_{DD}(NNN) = 3.2K$. The NN exchange constant has been determined from measurements in Los Alamos.[11] For the NNN constant it was assumed that it is about 20% of the NN constant

11

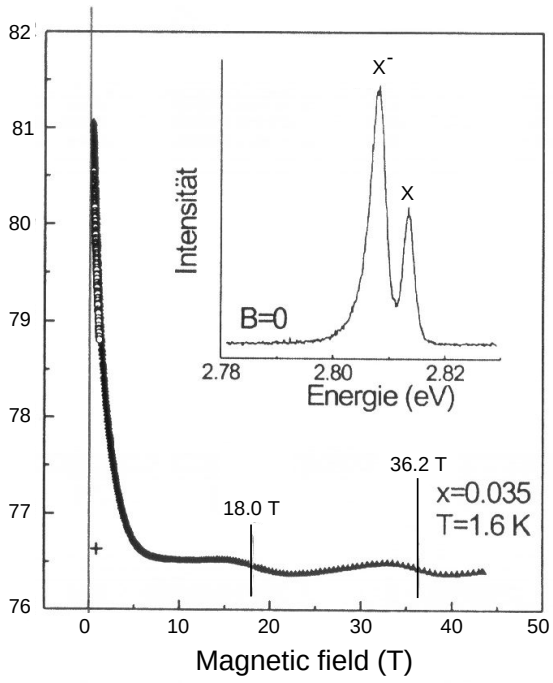

Energy of exciton (triangles) and singlet trion (circles) in σ^+-polarized PL spectra of a $Zn_{0.965}Mn_{0.035}Se/ZnBeSe$ QW as a function of magnetic field up to 44 T. Spectra have been taken at $T = 1.6K$. Inset shows PL spectrum at $B = 0$ T.
Measurements have been done by D. R. Yakovlev and S. Crooker in Los Alamos.

[Lar85]. The value was then adjusted to fit the cusp positions (see below). The energy level scheme (Fig. 5.8) shows that the $S = 1$ state (red line) becomes the ground state above $B = 9$ T. An increase of the total magnetization observed in the position of the exciton line follows in analogy to the interaction of Mn^{2+} ion pairs discussed in Section 5.1.

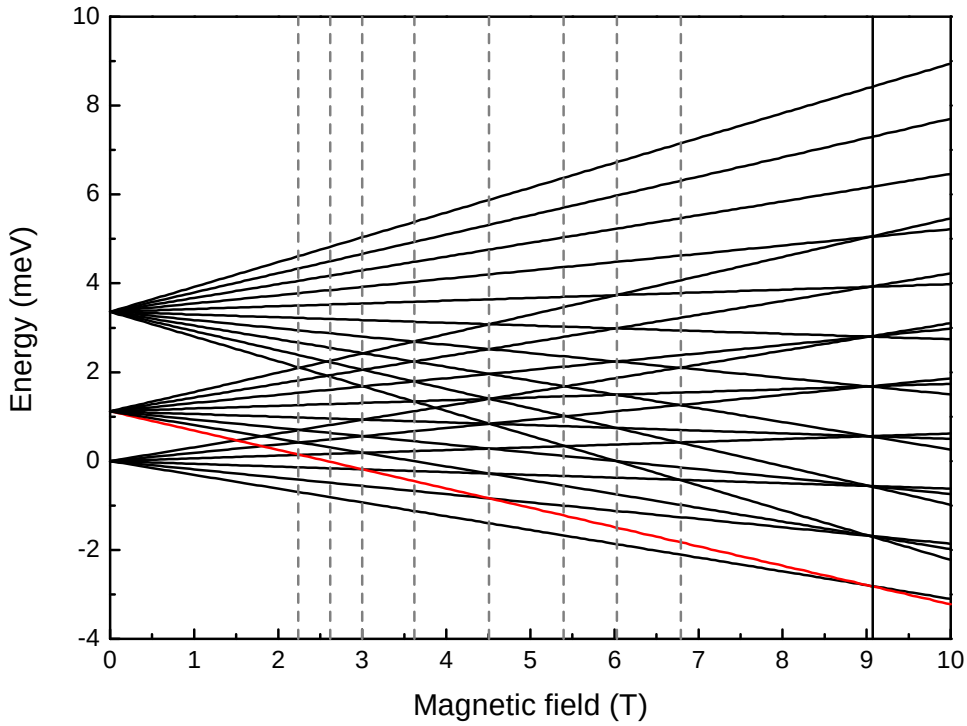

Fig. 5.8: *Energy levels for interaction of single ion with NN pair. At 9.1 T the $S = 1$ states (red line) becomes the ground state. At specific magnetic fields, indicated by vertical lines, a number of electron levels crosses.*

There are some more, but less pronounced irregularities in the shift of the exciton line marked by grey arrows in Fig. 5.7 (a) at $B = 3.1$ T and 4.6 T. They can be identified more clearly in the derivation of the line position (Fig. 5.7 (b)). A comparison of these line positions with the energy level scheme (Fig. 5.8) reveals that a high number of energy levels cross at these positions. All magnetic fields which show multiple energy level crossings have been marked by vertical lines.

Similar cusps have also been found in other DMS quantum wells. A false color image of the photoluminescence of sample CB1541 at $T = 2.2$ K and a power density of 12.5 $\frac{mW}{cm^2}$ is shown in Fig. 5.9. The positions of nonmonotonic line shift are shown by white arrows. The exciton position of the same measurement has been plotted in Fig. 5.10 (a) together with a magnification of a cusp at $B = 3.2$ T in the inset. A derivation of the exciton position is shown in Fig. 5.10 (b). From the magnification a shift of the exciton position towards lower energies can be recognized at $B = 3.3$ T. It can not be assigned to a change of the ground state. Also the deviation from the expected line position occurs only at a certain field. Before and beyond the exciton follows the expected line shift. This is different from the behavi-

our seen at 9 T where the exciton position does not relax back to higher energies when the magnetic field is increased further. But the magnetization and hence the position of the exciton line does not only depend on the energy structure but also on T_{Mn}. If the manganese temperature is increased the exciton line is shifted to higher energies. Since we see the opposite effect, the cusps may be caused by a cooling process which is more efficient at certain magnetic fields.

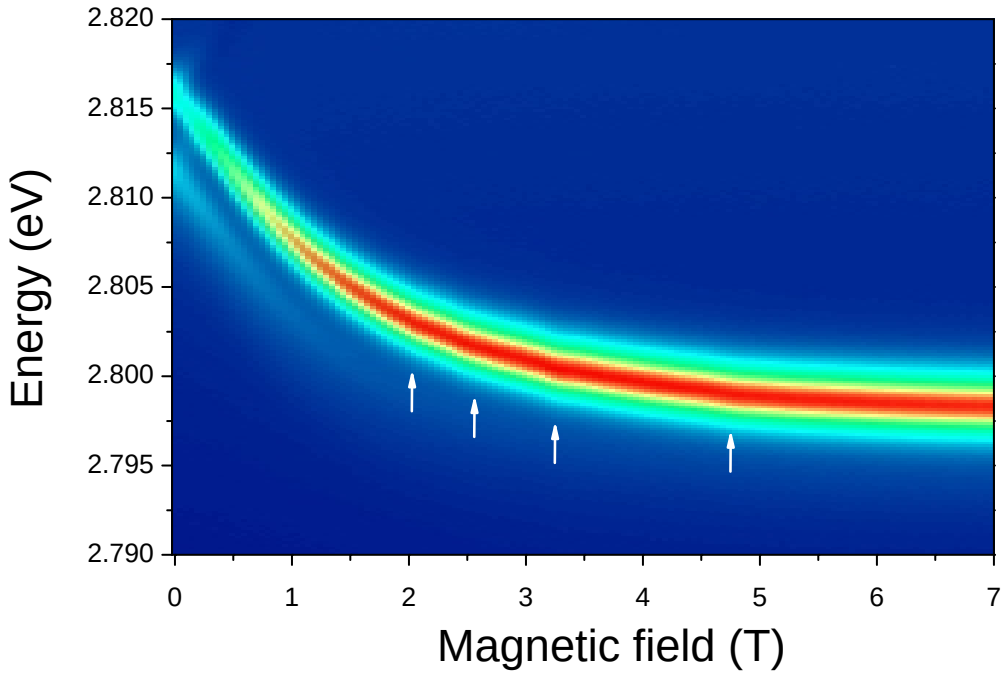

Fig. 5.9: *PL of sample CB1541 at 2.2 K showing the giant Zeeman splitting. White arrows indicate positions of nonmonotonic line shift.* $T = 2.2\,K$, $\lambda_{exc} = 405\,nm$, $P_{exc} = 1.5\,mW/cm^2$.

As discussed in Section 5.1 there are two possible ways for the energy transfer from the Mn system to the carrier system or the lattice: Carrier exchange scattering and spin lattice relaxation. Energy transfer to the carrier system can only be established if $T_C < T_{Mn}$. Since the sample is illuminated continuously T_C is high and it is more likely that energy is transferred from the carrier system to the Mn system than vice versa. A comparison between the magnetic field positions of the cusps and the energy scheme shows that at these positions there is a strong degeneracy of energy levels.

This allows energy to be transferred between single Mn ions and ion pairs. Since single ions do not couple to the lattice, they can transfer the energy to the lattice only at the crossing positions, without the need of additional phonons to bridge the energy gap. Processes are slowed down when a phonon of certain energy is required which is not always available immediately.

Due to the independence from the phonons the energy transfer from single ions to pairs is more efficient at the crossing points. An influence of the energy scheme to the SLR times has been shown before for nearest neighbor interaction [Str92].

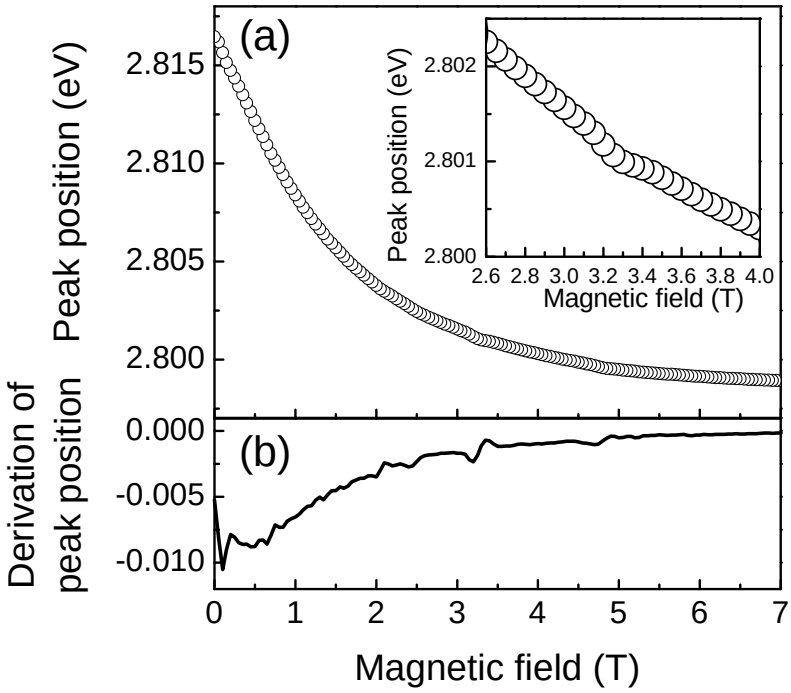

Fig. 5.10: *(a) Exciton position of sample CB1541 as a function of magnetic field. Inset shows magnification of one irregularity around 3.3 T. (b) Deviation of exciton position.* $T = 2.2\,K$, $\lambda_{exc} = 405\,nm$, $P_{exc} = 1.5\,mW/cm^2$.

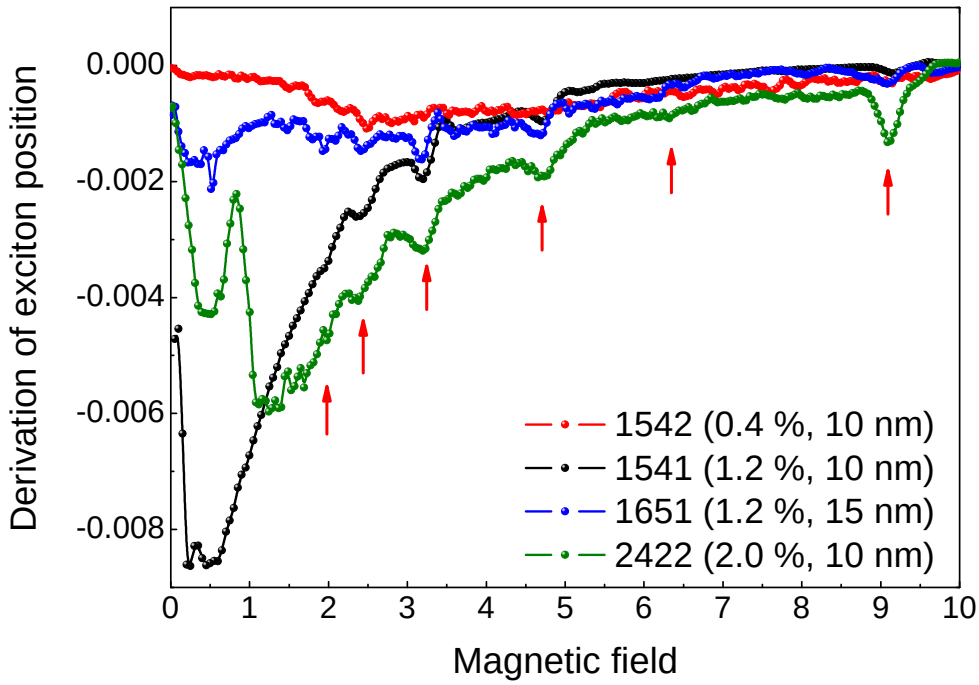

Fig. 5.11: *Derivation of exciton peak position for* $Zn_{1-x}Mn_xSe/ZnBeSe$ *samples with different Mn content and QW width, details are given in the figure. Arrows indicate cusp positions which coincide for all samples.* $T = 2.2\,K$, $\lambda_{exc} = 405\,nm$.

A comparison between samples with different Mn content and quantum well width shows that the cusp positions are independent of these parameters. All four samples compared in Fig. 5.11 show the same cusp positions at:

$B = 2.15T,\ 2.60T,\ 3.35T,\ 4.85T,\ 6.35T,\ 9.15T.$

However, no cusps could be found in doped DMS QWs samples. This is due to acceleration of SLR via free electrons from 2DEG which are efficiently coupled with both Mn-ions and lattice.

5.3 ODR on DMS quantum wells

The photoluminescence of DMS quantum wells has also been studied under far infrared radiation. Fig. 5.12 shows the PL of sample CB1541 at $B = 0$ T and 3 T. At low magnetic fields two lines can be identified, the exciton and the trion recombination signal. The trion vanished for higher magnetic fields. Due to the giant Zeeman splitting the exciton line is shifted by 14.6 meV already at moderate magnetic fields of 3 T. Application of FIR radiation shifts the exciton resonance to higher energies (blue line). This shift is caused by an increase of T_{Mn}. The FIR radiation couples to the carriers and leads to an increase of their kinetic energy which is transferred to the Mn system by exchange scattering. Also a direct coupling of the FIR quanta to the spins of the Mn ions is possible.

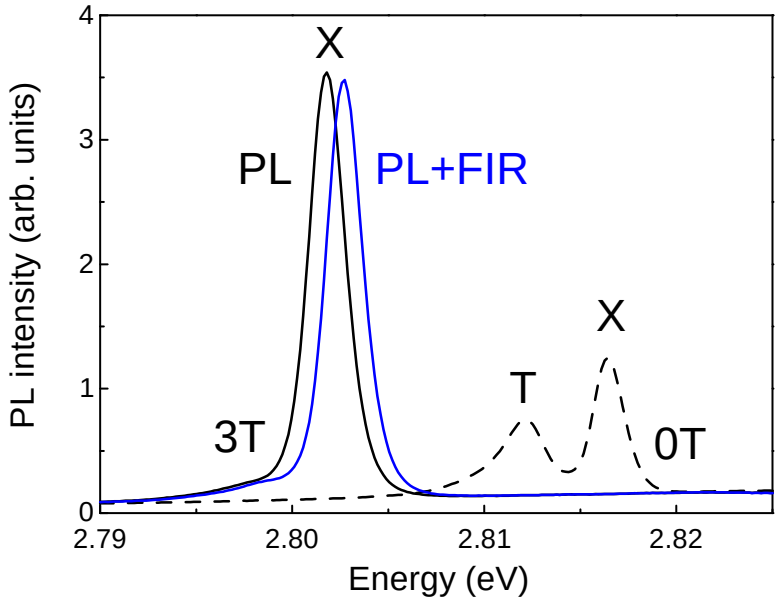

Fig. 5.12: *PL of sample CB1541 at 0 T (dashed line) and 3 T (solid lines). At 3 T illumination of the sample with FIR radiation leads to a shift towards higher energies.* $T = 2.2K$, $\lambda_{exc} = 405\,nm$, $P_{exc} = 1.5\,mW/cm^2$.

Fig. 5.13 shows the line positions of the exciton as a function of magnetic field for both PL with and without additional FIR illumination. The shift of the line due to the temperature increase of T_{Mn} is strong up to $B = 7\,\mathrm{T}$ where the giant Zeeman splitting saturates and is not very sensitive to temperature variations anymore. The inset of Fig. 5.13 shows a false color image of the modulation signal. Blue area corresponds to a decrease of photoluminescence intensity at the low energy side, red to an increase at higher energies.

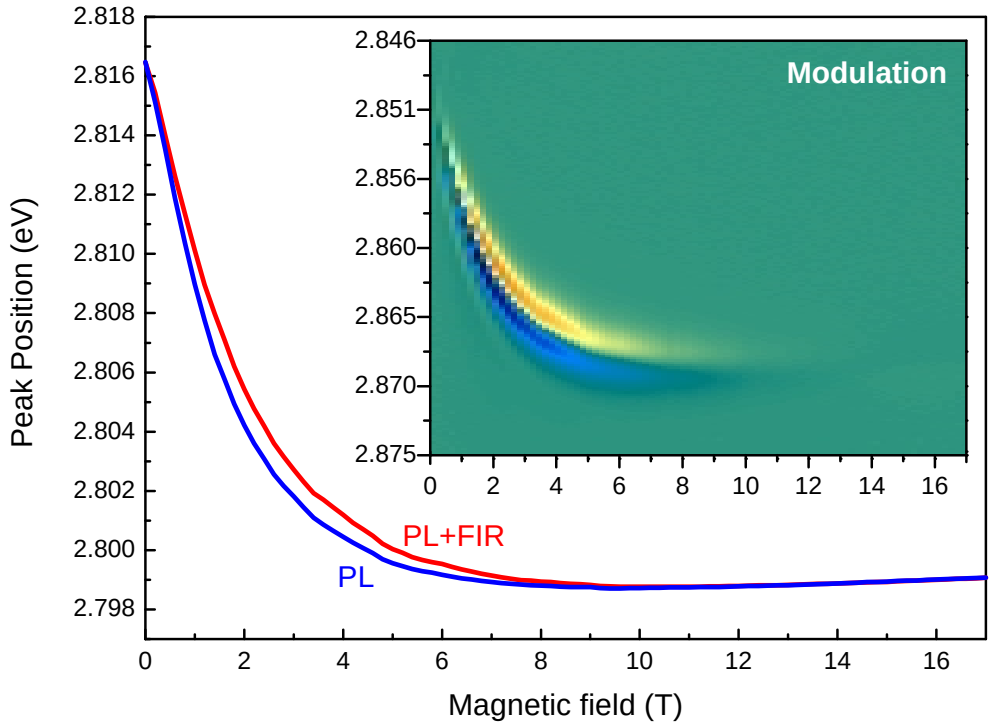

Fig. 5.13: *Exciton peak position of CB1541 at $T = 2.2K$ as a function of magnetic field. Blue line shows the exciton of the PL at low T_{Mn}. Red line shows the position under FIR radiation at increased values of T_{Mn}. Inset shows false color image of the modulation signal. Blue area corresponds to a decrease of photoluminescence intensity at the low energy side, red to an increase at higher energies. $\lambda_{exc} = 405\,nm$, $P_{exc} = 2\,mW/cm^2$, $\hbar\omega_{FIR} = 10.5\,meV$, $P_{FIR} = 155\,mW/cm^2$.*

5.3.1 Cyclotron resonance

In the modulation signal of the doped DMS quantum well CB2034 two contributions can be identified in Fig. 5.14: a broad signal with a maximum of 9% at around 3 T, and a smaller one (2.5%) at 12.5 T. The broad signal at 3 T can be assigned to the shift of the line position due to the increase of T_{Mn}. The shift of the exciton peak position also has a maximum at 3 T as can be seen in the inset of Fig. 5.15. The second peak of the modulation signal is due to cyclotron resonance in the

$Zn_{1-x}Mn_xSe$ / ZnBeSe QW. Its position of 12.5 T needs to be corrected to around 12.8 T because of the tail from the first signal which leads to background which decreases from 2% at 10 T to slightly below 1% at 16 T.

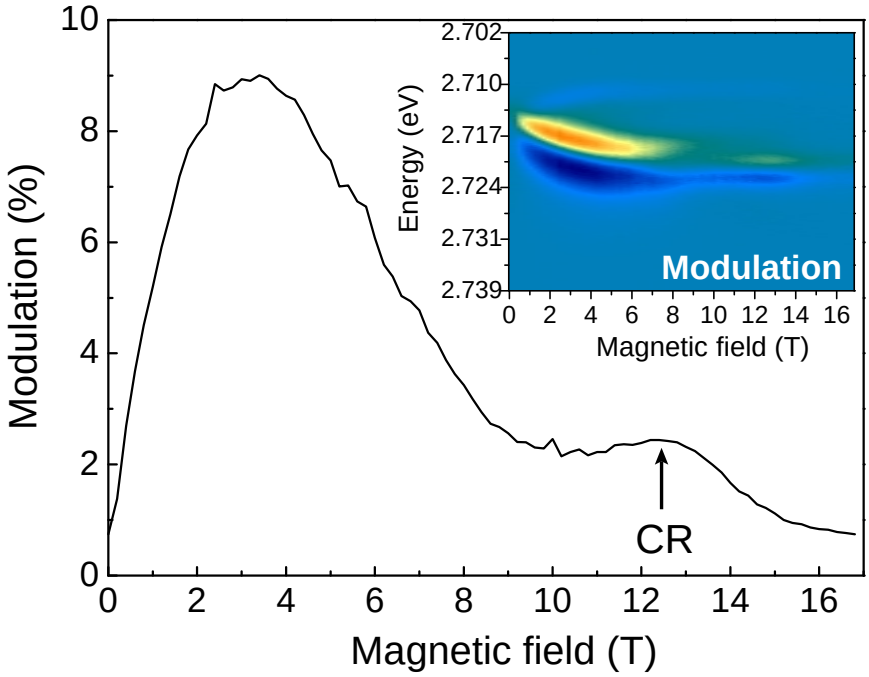

Fig. 5.14: *Modulation signal of sample CB2034 at $T = 2.2K$ showing two peaks at 3 T and 12.5 T. Inset shows false color image of the modulation. $\lambda_{exc} = 409\,nm$, $P_{exc} = 1\,mW/cm^2$, $\hbar\omega_{FIR} = 10.5\,meV$, $P_{FIR} = 145\,mW/cm^2$.*

For a resonance position of 12.8 T an effective mass of $m^* = 0141\,m_0$ can be derived which is close to the effective mass reported fot ZnSe [Oss93]. An effect of the CR can also be observed in the exciton peak position shown in Fig. 5.15. At $B = 10$T the shift caused by FIR radiation decreases to almost zero until it starts to rise again slightly above 12 T and reaches a local maximum at 13.5 T. When the cyclotron resonance conditions are met, energy is transferred from the FIR radiation to the carriers very efficiently, increasing their kinetic energy and hence their temperature. This can also be observed by an increase of the manganese temperature which leads to a smaller giant Zeeman splitting as observed from the excitonic peak position. In the inset the line shift is shown and a strong resonance can be observed at around 13.5 T, which is slightly higher than the value obtained from the modulation signal. From this position an effective mass of $m_e = 0.149\,m_0$ can be calculated which is very close to the value of pure ZnSe.

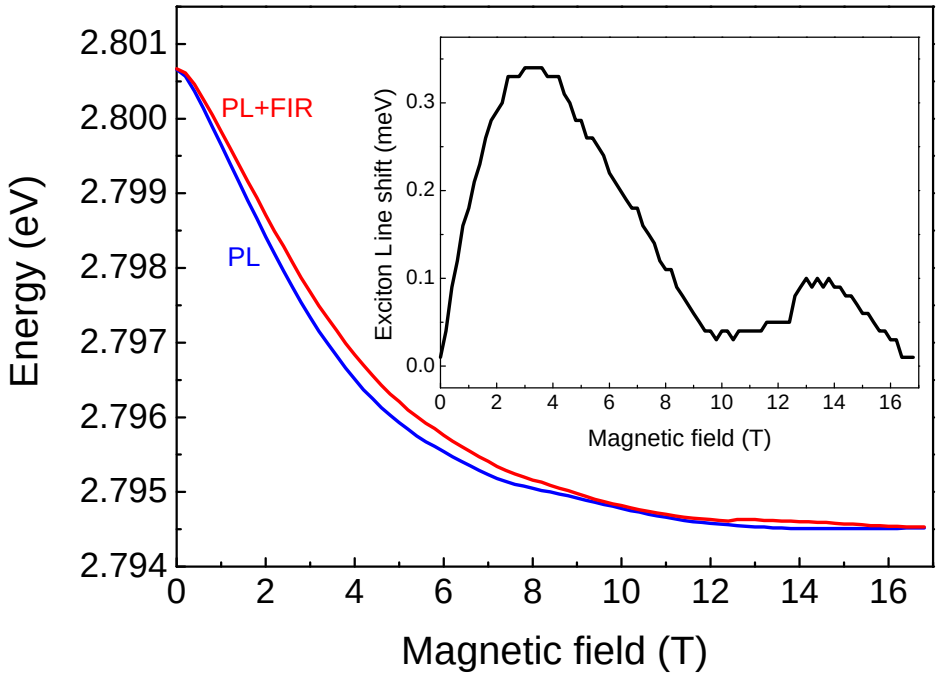

Fig. 5.15: *Exciton peak position of sample CB2034 as a function of magnetic field. Blue line shows the exciton of the PL at low T_{Mn}. Red line shows the position under FIR radiation at increased values of T_{Mn}. Inset shows the difference between both curves, the shift of the position.* $\lambda_{exc} = 409\,nm$, $P_{exc} = 1\,mW/cm^2$, $\hbar\omega_{FIR} = 10.5\,meV$, $P_{FIR} = 145\,mW/cm^2$.

Also in the modulation of sample CB2033 a narrow peak can be found at 13.6 T that may be assigned to the cyclotron resonance. However a similar signal of unknown origin can also be seen at 3.6 T. Still the modulation peak is very close to the resonance found in sample CB2034 which makes it reasonable to assume that it is also caused by cyclotron resonance. An effective mass of $m_e = 0.150\,m_0$ can be calculated for this sample.

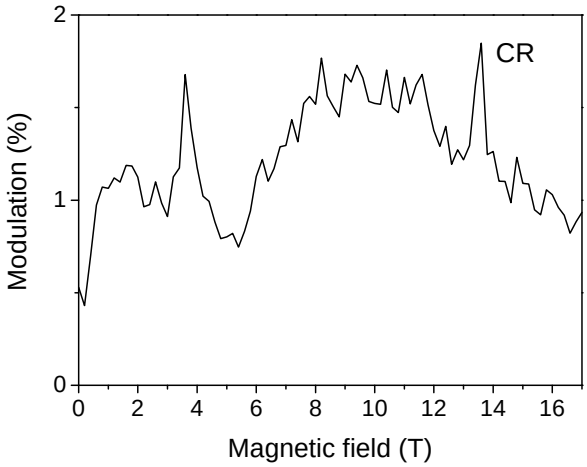

Fig. 5.16:
Modulation signal for sample CB2033 at T = 2.2K showing two narrow resonances at 3.6 T and 13.6 T.
$\lambda_{exc} = 405\,nm$,
$P_{exc} = 0.6\,mW/cm^2$,
$\hbar\omega_{FIR} = 10.5\,meV$,
$P_{FIR} = 145\,mW/cm^2$.

5.3.2 Nonmonotonic behaviour of the ODR signal

The modulation signal of sample CB1541 looks similar to CB2034, exept that no cyclotron resonance can be observed. Also in this case a broad signal, which has a peak at low magnetic fields, can be observed (Fig. 5.17). In case of CB1541 a number of steps in the modulation signal can be seen which are marked by arrows in the graph. These steps can also be observed in the shift of the exciton position due to the FIR radiation (not shown). The position of the steps does not coincide with the cusps observed in the photoluminescence of the DMS quantum wells. Between the maximum of the modulation at 1.5 T and the saturation at a low level at around 14 T the modulation signal decreases monotonically. At the positions of the steps the descent of the modulation signal is delayed and shifted to higher magnetic fields.

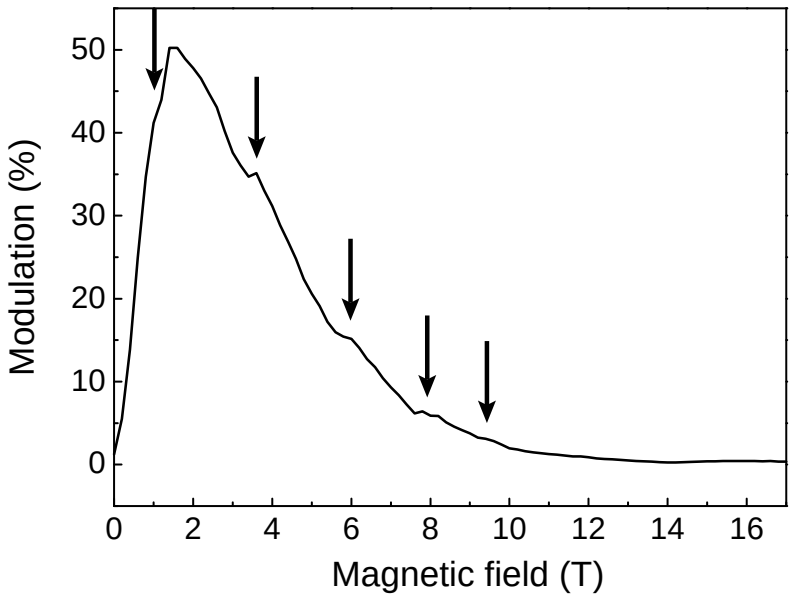

Fig. 5.17: Modulation signal of sample CB1541 at $T = 2.2$ K. A number of steps in the modulation signal, marked by arrows, occur between 3 T and 10 T. $\lambda_{exc} = 405$ nm, $P_{exc} = 2\,\mathrm{mW}/cm^2$, $\hbar\omega_{FIR} = 10.5\,meV$, $P_{FIR} = 155\,\mathrm{mW}/cm^2$.

Since the steps could not be observed in measurements without FIR radiation it is more likely that they are caused by additional heating of the Mn system. A possible scenario is that internal trion transitions are induced by FIR radiation if the splitting of the trion states coincides with the FIR quanta of 10.5 meV at the step positions. This may lead to an additional heat transfer to the Mn system which can be observed in ODR measurements. However, additional measurements are necessary to confirm this scenario. Weak steps can also be seen in the modulation signal of sample CB2034 (Fig. 5.14) and in the shift of the exciton position (Inset of Fig. 5.15).

5.4 Conclusion

Nonmonotonic behaviour of the magnetization curve in DMS quantum wells could be assigned to crossings of between energy states of single ions and pairs which allow energy transfer from single Mn ions to the lattice via SLR processes. Under FIR radiation cyclotron resonances where found in n-type doped samples. Also steps in the modulation signal of an undoped sample have been found which do not coincide with the crossing points responsible for the steps in the magnetization. It is necessary to study a series of undoped DMS quantum wells under FIR excitation to study the dependence on Mn concentration and QW width.

Chapter 6:

ODR study on magnetic quantum dots

Diluted magnetic semiconductor CdMnTe/ZnCdTe quantum dots grown by molecular-beam epitaxy have been studied by optically detected resonance (ODR) technique in magnetic fields up to 15 T. The photoluminescence (PL) of samples has been measured with and without additional illumination of far infrared (FIR) radiation with photon energies of 7.6, 10.5 and 12.8 meV. Strong changes of the excitonic photoluminescence induced by FIR radiation have been found at magnetic fields below 1 T. Measurements performed for various temperatures and for samples with different Mn contents varied from 0% up to 4% allow us to conclude that the ODR signal is caused by heating of the spin system of magnetic Mn ions. Also the competition of intrinsic and exchange contributions to the Zeeman splitting of excitonic states have been recognized as a decrease of the Zeeman splitting at high magnetic fields.

Magnetic quantum dots are an interesting material for spintronic devices. Optical properties of quantum dots under FIR radiation have not been studied by many groups (See Chapter 5 for ODR experiments on nonmagnetic quantum dots). The author is not aware on any publication of ODR on diluted magnetic semiconductor (DMS) quantum dots.

6.1 Competition between intrinsic and exchange Zeeman splitting

In general the optical properties of DMS structures are strongly sensitive to the Mn^{2+} spin temperature T_{Mn} and qualify therefore for ODR measurements. The temperature T_{Mn} can be elevated considerably above the bath temperature of the lattice by means of interaction with free carriers [Kne06a, Kne06b] or due to heating by MW or FIR radiation [Mal83, Str92]. In this chapter the effect of FIR radiation on

$Cd_{1-x}Mn_xTe$ QDs is investigated.

Four samples have been studied with Mn concentrations of 0% to 3%, see Table 6.1. The self-assembled quantum dots were grown in the group of J. Kossut.[12] As barrier material $Zn_{0.6}Cd_{0.4}Te$ was chosen to shift the excitonic emission below the Mn optical transition at around 2.0 eV in order to avoid effective transfer of the excitation to the Mn subsystem. The Mn ions are introduced directly into the QDs itself. The dots have a lens-like shape with a typical radius of the order of 10 nm and a height of about 2 nm [Woj07].

Sample	Mn content
032504A	0.03
602005B	0.0035
602005C	0.002
070306B	0

Table 6.1: *Sample name and Mn content of $Cd_{1-x}Mn_xTe$ / ZnCdTe quantum dots*

A microluminescence study [Woj07] of sample 602005B ($x = 0.0035$) allowed to estimate the number of Mn ions in individual dots. For large dots around 25 Mn ions per dot were found, 13 for medium size dots and 5 for small dots. Results obtained from FIR measurements presented in this chapter will be compared with the results of this publication.

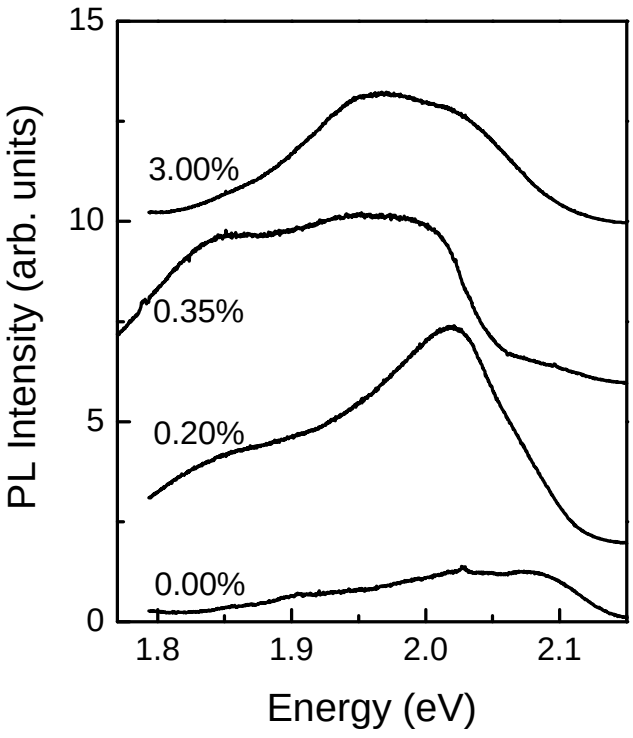

Fig. 6.1: *Photoluminescence of $Cd_{1-x}Mn_xTe$/ZnCdTe QDs with different Mn contents varied between at 0.00% and 3.00% at $T = 4.2K$ under illumination of $\hbar\omega_{exc} = 2.33eV$ with a power density of $5 \cdot 10^{-7} \frac{W}{cm^2}$.*

12 Institute of Physics, Polish Academy of Sciences, and ERATO Semicoductor Spintronics Project, Al. Lotnikow 32/46, 02-688 Warsaw, Poland

The quantum dot samples were excited by a solid state laser operating at a wavelength of 405 nm (3.06 eV). Three wavelengths: 96.5, 118 and 163 μm, corresponding to photon energies 12.8, 10.5, 7.6 meV, respectively offer output powers between 40mW and 150mW, which was suitable for the measurements of this study. For PL measurements the photoexcitation density$P_{exc} = 5 \cdot 10^{-7} \frac{\mathrm{W}}{\mathrm{cm}^2}$ has been chosen carefully to avoid heating of the Mn spin system by the incident laser light. We choose the regime where the polarization of the photoluminescence P_c was not sensitive to variation of P_{exc}.

The circular polarization degree P_c of the photoluminescence is defined as:

$$P_c = \frac{I^+ - I^-}{I^+ + I^-} \tag{6.1}$$

where I^+ (I^-) is the PL intensity for σ^+ (σ^-) polarization respectively.

Fig. 6.1 shows the PL spectra of all four samples at B = 0T. The photoluminescence of the $Cd_{1-x}Mn_xTe$ quantum dots appears very broad due to the inhomogeneous broadening of the quantum dot size. The low energy part of the spectrum represents large QDs whereas small QDs can be found at the high energy side towards 2.1 eV. At magnetic fields above zero Tesla the PL becomes strongly polarized because of the (giant) Zeeman splitting in DMS as can be seen in Fig. 6.2.

In order to understand the polarization of the four samples, especially at high magnetic fields, we have to take into account that the spin splitting in DMS can be separated into two contributions. The intrinsic Zeeman splitting, also found in non-magnetic semiconductors and the exchange contribution or giant Zeeman splitting typical for diluted magnetic semiconductors. In the following we will consider the energy splitting of the conduction band only:

$$\Delta E_{CB} = E_Z(S) + E_{GZ}(S) \tag{6.2}$$

The first term describes the spin splitting due to the Zeeman effect,

$$E_Z(S) = g_e \mu_B B \tag{6.3}$$

where g_e is the g-factor of excitons and μ_B is the Bohr magneton.

The second term in Eq. 6.2 describes the giant Zeeman splitting in diluted magnetic semiconductors [Fur88]:

$$\Delta \mathrm{E}_{GZ} = (\alpha - \beta) N_0 x \mu_B g_{Mn} S_0 B_{\frac{5}{2}}\left(\frac{5 \mu_B g_{Mn} B}{k_B (T_S + T_0)}\right) \tag{6.4}$$

where x is the Mn content of the sample and $g_{Mn} = 2$ the manganese g-factor, k_B is the Boltzmann constant, and T_{Mn} is the temperature of the Mn-spin system. In our experiment it is equal to the lattice temperature, $T_{Mn} = T_L$, as long as we do not apply FIR radiation and hence increase T_{Mn}. S_0 and T_0 are phenomenological parame-

ters, which allow one to account for the Mn-Mn antiferromagnetic interaction within the magnetic ion system. $B_{\frac{5}{2}}$ is the modified Brillouin function. $N_0\alpha$ is the exchange integral for the conduction and valence band states, interacting with the localized magnetic moments of the Mn^{2+} ions. In $Cd_{1-x}Mn_xTe$ $N_0\alpha = 220meV$.

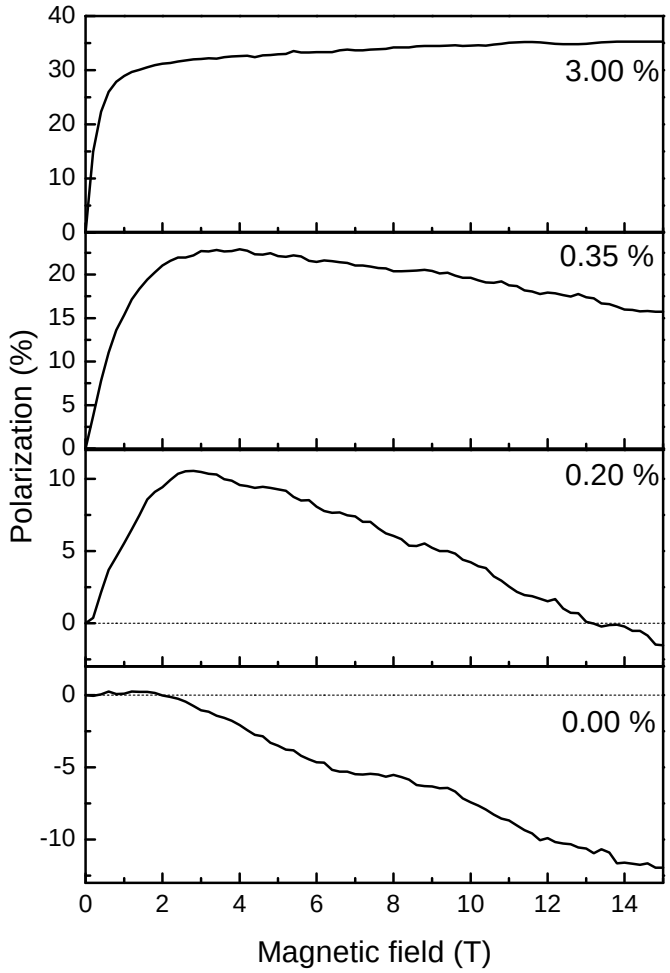

Fig. 6.2: *PL Polarization degree versus magnetic field for $CD_{1-x}Mn_xTe/ZnCdTe$ QDs with different Mn contents. $T = 4.2\ K$, $\lambda_{exc} = 532\ nm$, $P_{exc} = 5\ mW/cm^2$,*

In samples with Mn content of a few percent the intrinsic Zeeman splitting only plays a minor role and can be neglected for magnetic fields below some tens of Tesla. However for samples with low Mn content, the effect of the giant Zeeman splitting can become comparable to the intrinsic splitting as shown in Fig. 6.3.

Since the polarization $P_c(B)$ of the photoluminesence depends on the the Zeeman splitting in the following way:

$$P_c \propto tanh\left(\frac{\Delta E_Z(B,\ T_{Mn})}{2k_BT}\right) \tag{6.5}$$

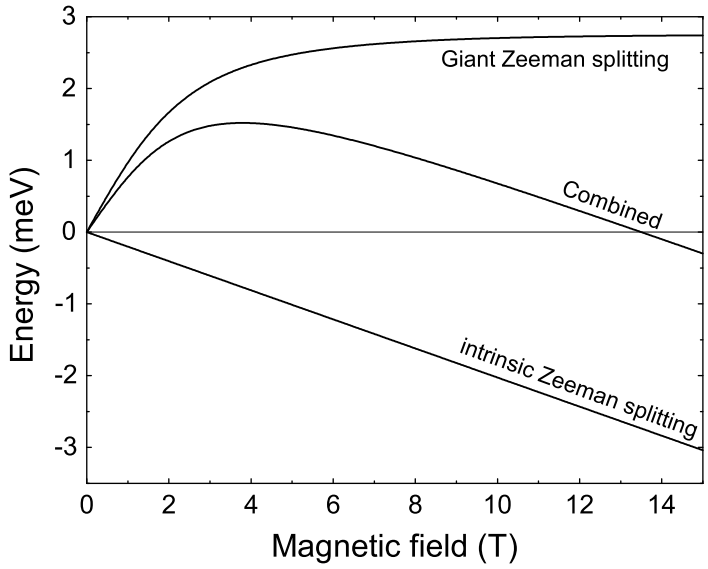

Fig. 6.3:
Model scheme of the intrinsic and exchange contribution to the conduction band Zeeman splitting in DMS with low Mn content.

the competition between intrinsic and exchange contribution can be observed experimentally as shown in Fig. 6.2. For the sample with a Mn concentration of 3% the giant Zeeman splitting dominates. For samples with lower Mn content the contribution of the intrinsic Zeeman effect decreases the total amount of polarization towards higher magnetic fields. For the sample with 0.2% Mn the PL becomes unpolarized at 13.2 T where both contributions cancel each other. For samples with low Mn content it can not be excluded that a small number of dots contains no Mn ions. For sample 602005B ($x = 0.0035$) the number of Mn ions in the smallest dots was estimated to be around five. So it can be assumed that also in case of sample 602005C ($x = 0.002$) even the small dots contain one or more Mn ions on average. This makes it generally possible to determine the Mn content in samples with small E_{GZ} where the direct observation of the shift is hindered by strongly broadened PL bands and can only be observed by microluminescence.

It can also be observed that even for the sample with 3% Mn content the polarization saturates at 35%. This stands in contrast to microluminescence observations where the polarization degree of sample 602005B ($x = 0.0035$) reaches 100% at $B = 5$T. The photoluminescence for both polarizations for sample 032504A ($x = 0.03$) at $B = 15$T is shown in Fig. 6.4 (a). The degree of polarization is shown in the lower panel and reaches up to 80% for certain recombination energies.

A strong dependence of the energy can be observed which agrees well with the microluminescence measurements. The Zeeman shift of larger dots (at the low energy site) was stronger than the shift of small dots (at high energies). This may be explained by a stronger interaction between carriers and Mn ions due to the close confinement in small dots. This makes the intrinsic magnetization less sensitive to external magnetic fields. In σ^--polarization the PL intensity becomes maximal at around 2.4 eV which is in the region of internal optical Mn transitions. These transitions may lead to an unpolarized background signal in the degree of polarization.

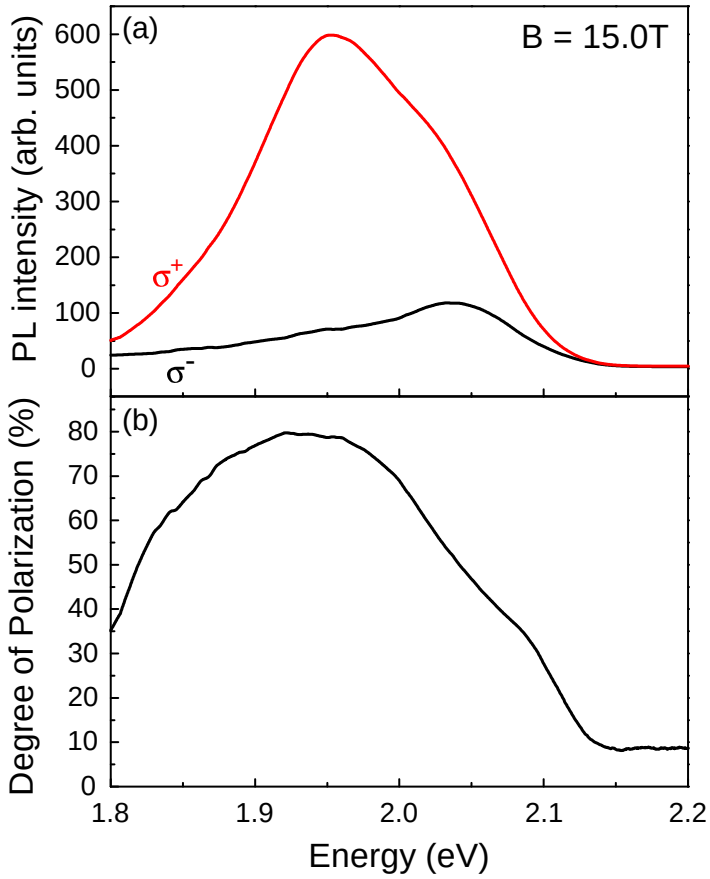

Fig. 6.4:
(a) PL of sample 032504A ($x = 0.03$) at $B = 15T$ and $T = 4.2K$ for both polarizations.
(b) Degree of polarization as function of the emission energy.
$\lambda_{exc} = 532\,nm$,
$P_{exc} = 5\,mW/cm^2$,

6.2 Heating of the Mn spin system by far infrared radiation

Lets have a look on the PL spectrum of sample 032504A (x = 0.03) again in Fig. 6.5 (a). A second PL spectrum of the same sample but with additional illumination of far infrared radiation is shown in Fig. 6.5 (a) for comparison. The modulation signal which is defined as difference between both PL spectra is also plotted in the same graph. It shows a decrease of the PL intensity in σ^+-polarization over the whole spectral range. At the same time an increase in the intensity in σ^--polarization of approximately the same amount can be observed in Fig. 6.5 (b).

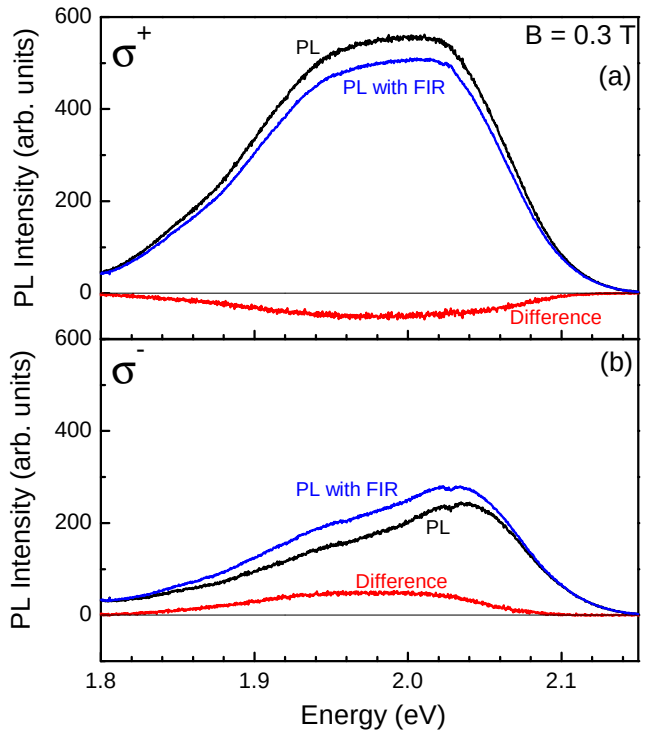

Fig. 6.5:
PL of sample 032504A (x = 0.03) at B = 0.3T and T = 4.2K in σ^+ – (a) and σ^- – polarization (b). A second PL spectrum of the sample with additional FIR illumination is shown for comparison. The difference between both PL signals (Modulation) is also shown as indication for the in- or decreasing effect of the FIR radiation. λ_{exc} = 532 nm, P_{exc} = 5 mW / cm^2, $\hbar\omega_{FIR}$ = 10.5 meV, P_{FIR} = 115 mW / cm^2.

To study the magnetic field dependence of the modulation the integral PL intensity of the spectrum with and without FIR illumination is calculate. The difference between these two values indicates how much the spectrum changes under FIR radiation. The change of the integrated PL intensity for both σ^+ (closed symbols) and σ^- (open symbols) polarization is shown as a function of magnetic field in Fig. 6.6 (a). A strong dependence on the magnetic field can be observed. It has a maximum of modulation (strongest change in the photoluminescence) at B = 0.3 T. The shape of both curves is very similar indicating a correlation between both polarizations.

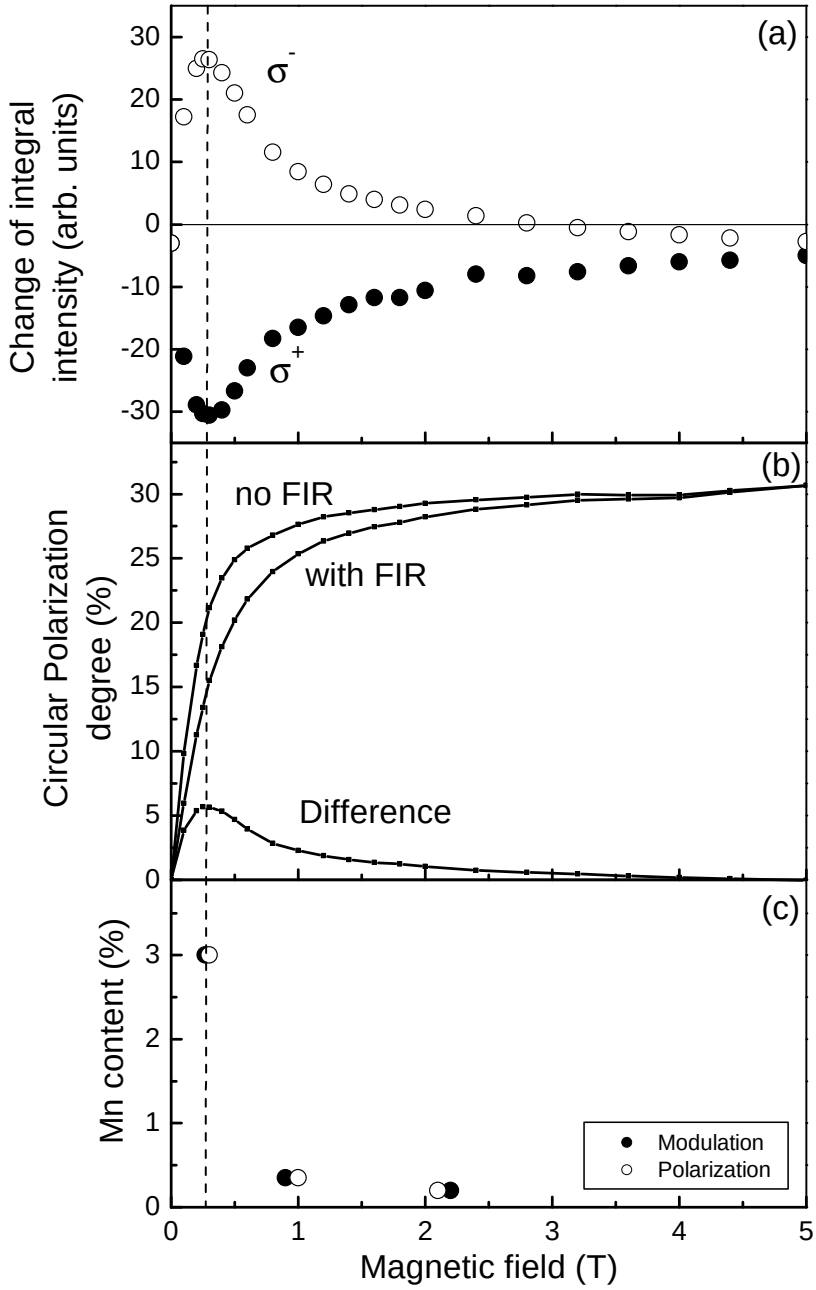

Fig. 6.6: *(a) Change of the integrated PL intensity of sample 032504A ($x = 0.03$) at $T = 4.2K$ induced by $\hbar\omega_{FIR} = 10.5\,meV$ ($P_{FIR} = 115\,mW/cm^2$) as a function of magnetic field. Changes of the σ^+-polarization (closed symbols) coincide with the σ^--polarization (open symbols).*
(b) Degree of polarization for the photoluminescence with and without additional FIR illumination of sample A under the same conditions. The maximal change in the polarization appears at $B = 0.3T$. (c) shows comparison between the maxima observed in the modulation (closed symbols) and in the polarization (open symbols) for samples with different Mn content. $\lambda_{exc} = 532\,nm$, $P_{exc} = 5\,mW/cm^2$.

This redistribution from the σ^+- to the σ^--channel in the PL signal can be explained by a redistribution of carriers between spin sublevels caused by the FIR radiation.

There are two mechanisms which can explain this behavior. If the giant Zeeman splitting lies in the same range as the photon energy of the FIR radiation, spin flip transitions between both spin states may be induced. The other possible mechanism is an increase of the temperature of the manganese system T_{Mn} due to the FIR radiation, which reduces the giant Zeeman splitting of carriers and respectively the total amount of PL polarization.

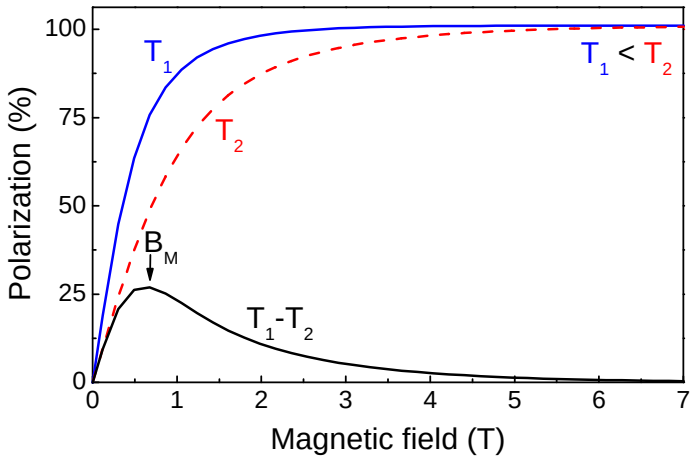

Fig. 6.7: *Model for the degree of polarization of the photoluminescence caused by giant Zeeman splitting at two different temperatures. The difference between two temperatures changes with magnetic field and has a maximum at low magnetic fields B_M.*

In Fig. 6.7 the polarization degree is shown as a function of magnetic field which can be described by a modified Brillouin function. The difference between two Brillouin functions described by different T has a maximum at a certain field B_M. This difference is absent at $B = 0$ T since the PL is unpolarized and therefore independent of the temperature. It is also reduced at high magnetic fields, when E_{GZ} saturates and looses its sensitivity to small changes in T_{Mn}.

In order to revise the idea of direct transitions between the spin states, different FIR photon energies have been used for the modulation measurements. Since the giant Zeeman splitting is increasing linearly at low magnetic fields, a shift of the magnetic field position B_M of the modulation maximum can be expected if the photon energy is changed. No clear sign for a shift is seen for the maxima of the modulation signal for three FIR energies (Symbols in Fig. 6.8). If the modulation signal is compared to the difference of the polarization degree, represented by lines in the same graph, a good agreement is found even when comparing absolute values. So the ODR origin does not seem to be caused by direct transitions. The exciton life time in the QDs is in the order of 200 - 500 ps. A short lifetime reduces the population of the conduction band and makes it unlikely for FIR photons to interact with the carriers and cause intraband transitions, which could be observed by the ODR technique.

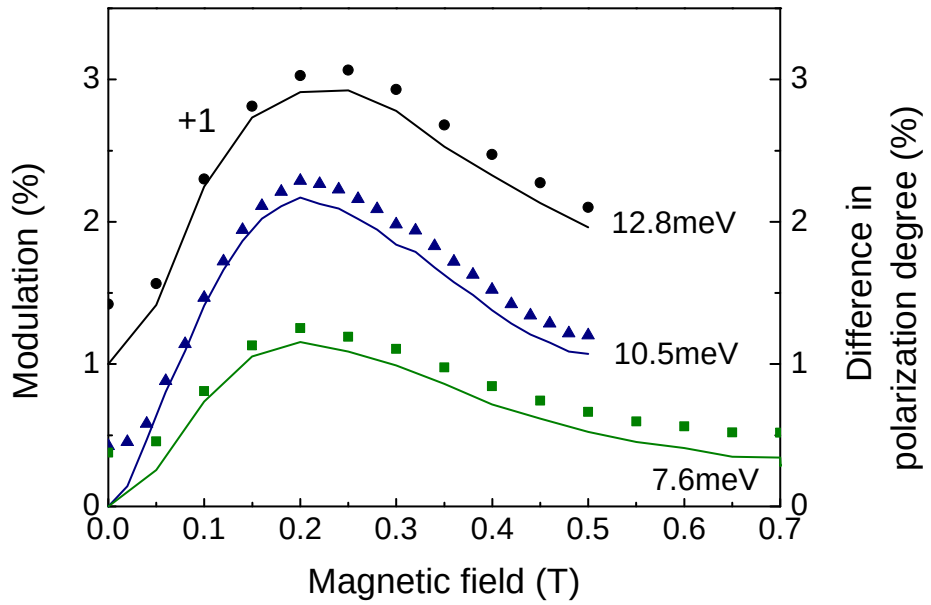

Fig. 6.8: *Symbols: Modulation of* sample 032504A *(x = 0.03) for three FIR laser lines. Lines: Difference in the polarization degree induced by FIR radiation. Results for 12.8 meV laser line have been shifted by +1 for better visibility.* $\lambda_{exc} = 532\,nm$, $P_{exc} = 5\,mW/cm^2$.

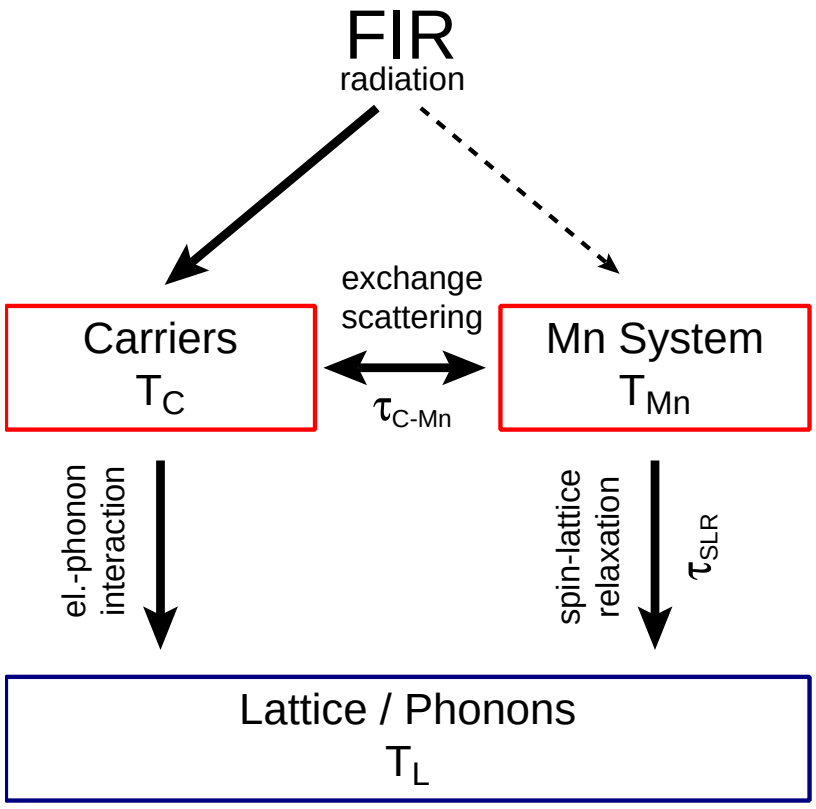

Fig. 6.9: *Energy transfer in DMS quantum dots. Carriers are heated by FIR radiation. The Mn spin system exchanges energy with the carriers by spin-flip scattering. It is cooled by energy transfer to the lattice via spin-lattice relaxation.*

If T_{Mn} is increased due to the FIR radiation, the degree of P_c is expected to decreases because it is controlled by the giant Zeeman splitting, which in term is proportional to magnetization of the Mn spin system:

$$E_{GZ} \propto M(T_{Mn}, B, x) \tag{6.6}$$

Fig. 6.6 (b) shows that this is the case and that the difference between both polarizations is maximal at $B = 0.3\,\mathrm{T}$ where P_c is reduced from 21% to 15%. This coincides with the magnetic field position of the modulation maximum shown in (a). A comparison between both, the maximum of the polarization difference and the modulation signal for the samples with different Mn contents is given in Fig. 6.6 (c). For all samples there seems to be a strong correlation between the observed modulation maxima and their change in polarization.

This can be explained by the energy and spin transfer in the sample which is comparable to the interaction in quantum wells [Kel01], see also Section 5 of this thesis. There are three energy reservoirs in DMS QDs: The carriers, the Mn spin system and the lattice (phonons) as shown in Fig. 6.9. Energy transfer between the reservoirs is enabled by scattering and relaxation processes indicated by arrows in the schema. Photo carriers with excess kinetic energy are generated by illumination with a laser.

A spin-flip scattering process enables the energy transfer into the Mn system which leads to a rise in spin temperature T_{Mn}. Due to great lattice heat capacity, the lattice temperature T_{Mn} is usually lower than T_{Mn}. So energy of the Mn system is passed to the lattice by spin-lattice relaxation, a cooling process which in terms of relaxation times and effectiveness strongly depends on the Mn concentration [Yak07].

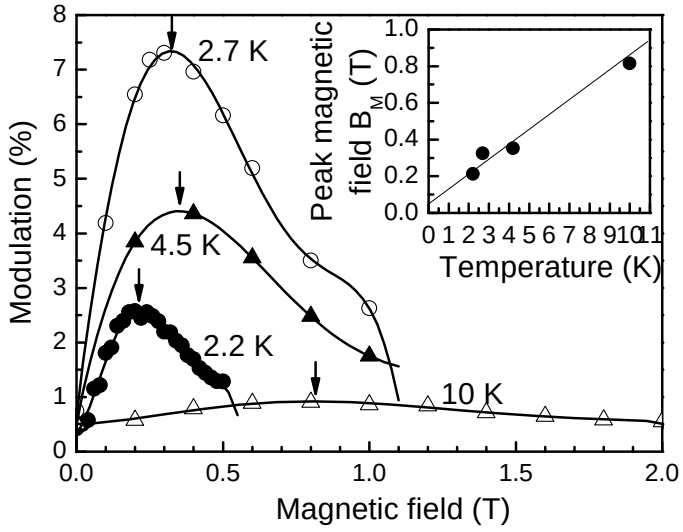

Fig. 6.10: *Temperature dependence of the modulation signal ($\hbar\omega_{FIR} = 10.5meV$, $P_{FIR} = 100\,mW/cm^2$) in σ^--polarization for sample 032504A ($x = 0.03$). Inset shows the resonant field position B_M which is shifted linearly to higher fields with increasing lattice temperature. $\lambda_{exc} = 532\,nm$, $P_{exc} = 5\,mW/cm^2$.*

The FIR radiation couples to the photo carriers. Unlike in a quantum well where the kinetic energy of carriers in a 2DEG can be increased by FIR photons there are limited possibilities for the FIR quantum to interact with the carriers. It is possible that additional spin flips of the excitons are induced by the FIR radiation which transfer their energy to the Mn spin System when they relax, elevating its spin temperature T_{Mn}. Also a direct influence of the FIR radiation on the Mn System, which does not depend on the magnetic field, can not be excluded.

When the temperature is increased by current through a resistor mounted close to the sample, T_{Mn} will also be increased. The temperature has been measured with a calibrated cernox sensor mounted close to the sample with good thermal contact. At higher temperatures E_{GZ} is decreased, shifting the modulation maximum to higher magnetic fields and leading to a broadening of the signal as shown in Fig. 6.10. The modulation signal for the measurement at $T = 2.2\text{K}$ is smaller because the FIR power was reduced from 120 mW to 40 mW in order to reach lower temperatures. The FIR radiation itself heats the sample so that the measured sample temperature can reach $T = 2.7\,\text{K}$, which is 0.5 K above the temperature of the pumped He reservoir. The modulation signal for these conditions is also shown in Fig. 6.10.

6.3 Conclusion

A linear decrease of the polarization degree at high magnetic fields for magnetic quantum dots with low Mn content was found. This makes it possible to determine the Mn content just from photoluminescence measurements. Spin flip processes induced by FIR radiation could not be observed, probably due to the short exciton life time. Maxima found in the modulation signal could be assigned to changes in the polarization degree which are caused by a rising temperature of the Mn system under FIR radiation.

Appendix

Optical transitions and spin selection rules for trions in QWs

In this appendix the rules for constructing spin structure of carriers, excitons and excitonic complexes (e.g. trions) in external magnetic fields are summarized. The appendix is based on a summary about optical transitions and spin selection rules for trions in QWs by D. R. Yakovlev [Yak08].

The problem is that in the literature different approaches to g-factor definitions and to labelling the spin levels are chosen. The differences are caused by used representations (electron or hole) and are related to hole levels in valence bands. Also one should be careful in using the single electron picture commonly used for band-band transitions and often for excitons. It is different from the energy scheme for excitonic complexes (excitons and trions) where the energy level can be occupied by few carriers (e.g. by two electrons and one hole in case of negatively charged trion). Also the spin selection rules are different for these schemes.

The results (spin splitting, values of g-factors, polarization of optical transitions, selection rules) are independent of the details of approaches chosen for description. This is what one can expect. But one needs to stay consistently in the frame of the very same approach! This makes problems for comparing published results of different teams, as different approaches might be taken, but not always they are fully described. We will note where one can meet stones under the water.

We do not pretend that our approach is the only correct. However, in our view it has few convenient points and offer only few simple rules to draw the spin diagrams of excitons and trions and handle them. Details of the Dortmund approach can be found in Ref. [Yug07], where all details are included being exemplified by excitons in InGaAs/GaAs QDs. Few examples for trions can be found in [Ast99, Ast02, Ast05].

A.1 How to handle exciton and trion schematics: simple rules

We are considering here simplified case of the heavy-hole exciton and external magnetic field applied along the structure growth axis (z-axis), i.e. the Faraday geometry. Therefore, the Hamiltonian will be analyzed only for z-direction. Consideration is for complexes in the electron representation (energies for all particles increase from bottom to top). Mixture of hh-lh states, which can be changed by magnetic field, can be accounted phenomenologically by field dependence of hole and exciton g-factors: $g_h(B)$, $g_x(B)$.

Exciton spin Hamiltonian consists of electron and hole parts:

$$\mathcal{H}_x = \mathcal{H}_e + \mathcal{H}_h = g_e S \mu_B B + \frac{g_h}{3} J \mu_B B = \left(g_e S + \frac{g_h}{3} J \right) \mu_B B \qquad (A.1)$$

Here $S \equiv S_z = \pm\frac{1}{2}$ is electron spin and $J \equiv J_z = \pm\frac{3}{2}$. The hole g-factor is divided by three in order to have an "universal form" for the hole Zeeman splitting $\Delta E_h = \mu_B g_h B$.

Our Hamiltonian differs by the sign for the hole term from the one used in some papers on fine structure of trions and excitons [Kes90, Sne92, Bla94, Mas97], being suggested by van Kesteren [Kes90]). It results in difference for g-factor signs for holes and excitons. Namely, If we would like to use for our classifications data on g-factors in GaAs QWs collected in Fig. 1 of [Sne92], for that signs for hole and exciton g-factors should be inverted.

There are some simples rules to construct fine structure scheme:

- All particles (electron, hole, exciton, trion) have the same energy axis, which increases from bottom to top.
- All g-factors correspond to "universal rule": for the positive g-factor value the spin with sign "+" has higher energy. (Actually it just follows from the form of Hamiltonian, e.g. $\mathcal{H}_e = g_e S \mu_B B$. Exciton g-factor for bright states with spin ±1 corresponds to $g_x = g_h - g_e$.
- The length of arrows connecting spin states and denoting optical transitions correspond with the photon energy. I.e. the length can be used to conclude which transition will be the lowest in energy.
- Spin allowed optical transitions should satisfy the selection rule $\Delta S = \pm 1$, where the moment ±1 is introduced (or removed) by a circular polarized photons. To calculate formally the polarization of transition (both for absorption and emission) one should subtract from the spin value of the higher energy state the spin value of low energy state. And difference +1 corresponds to σ^+-polarized photon, and -1 to

σ^--photon. Another reference point is that an exciton $\left(-\frac{1}{2}; +\frac{3}{2}\right) = +1$ recombine with emission σ^+-polarized photon, and exciton $\left(+\frac{1}{2}; -\frac{3}{2}\right) = -1$ give rise to σ^--photon.

- Spin scheme is constructed from the Hamiltonian (A.1) by substituting in it the respective values for carrier spins, which form exciton or trion states. It is very convenient to draw also separately levels for electrons and holes (both in electron representation) and to mark their centre-of-gravity. It helps to combine Zeeman contributions to the exciton and trion states constructed from these carriers. In Fig. A.1 an example is shown for $g_e > 0$, $g_h > 0$ and $g_e > g_h$, which gives us $g_x > 0$.

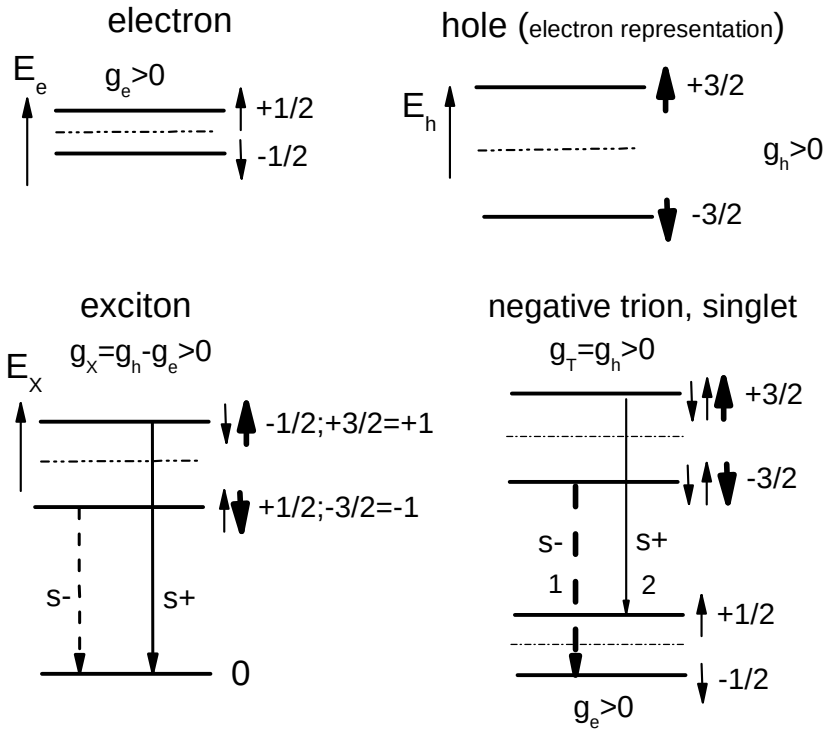

Fig. A.1: *Example of electron, hole, exciton and trion energy and spin scheme for $g_e > 0$, $g_h > 0$ and $g_e > g_h$.*

The Zeeman pattern of trion can be calculated as a shift of optical transition from the centre-of-gravity. One can see (dashed arrow) the decrease in energy for trion state reduces the photon energy, but the energy decrease for the resident electron increases the photon energy. Therefore, the photon energy for σ^--polarized transition 1 is varied in magnetic field by $\frac{1}{2}\left(-\Delta E_h + \Delta E_e\right) < 0$. Respectively, σ^+-polarized transition 2 is varied by $\frac{1}{2}\left(\Delta E_h - \Delta E_e\right) > 0$. And the total Zeeman splitting of trion singlet state is $\left(\Delta E_h - \Delta E_e\right)$. Note that it is equal to the Zeeman splitting of the exciton optical transitions.

A.2 Selection rules for trion singlet states

It is important to note that the polarization of trion optical transition may be different for emission and absorption. An example for that is given in Fig. A.2 for $g_e > 0$, $g_h < 0$ and $g_e < g_h$. The reason for this difference is that the polarization for absorption of T^- is controlled by polarization of background electrons and is determined by g_e. But in emission it is caused by polarization of trions itself, which is caused by g_h.

Polarization properties allow to receive a detailed information about the type of trion (T^+ and T^-) and the signs of electrons and holes participating in it formation having experimental information on absorption and emission polarization. Detailed analysis for singlet and triplet trion states of both T^+ and T^- is given below.

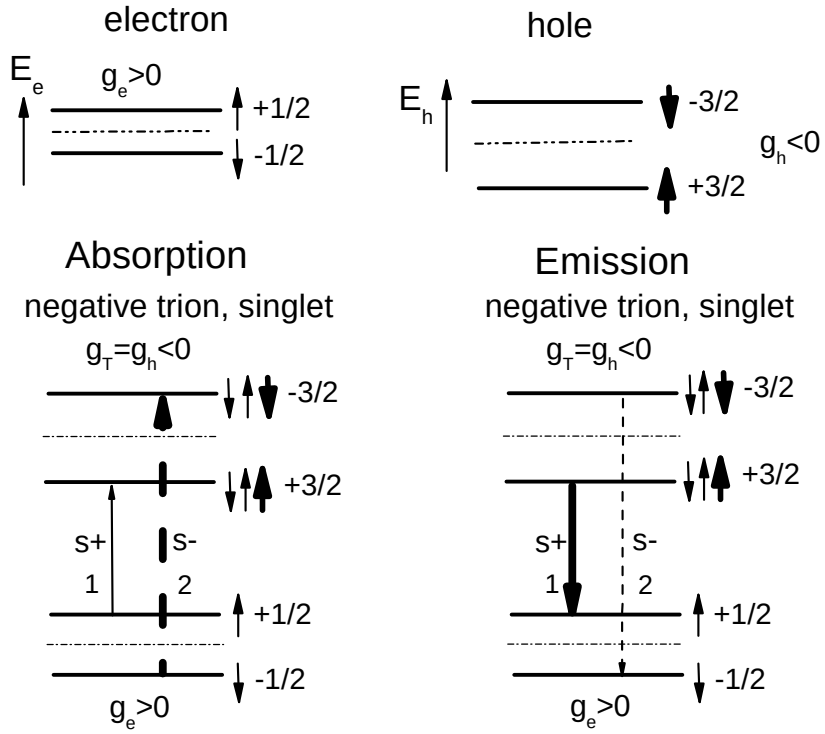

Fig A.2: *Example of electron, hole and trion energy and spin scheme for $g_e > 0$, $g_h < 0$ and $g_e < g_h$.*

A2.1 Heavy-hole trions

Table A.1 is to determine polarizations of strong optical transitions (absorption and emission) for singlet states of positive and negative trions. Polarizations may differ for absorption and emission, as they are controlled by different factors. For absorption it is controlled by polarization of resident carriers and for emission by polarization of trions. For trion state in "()" spins for electron and hole contributions are shown. Singlet state give "0", which e.g. corresponds to the singlet electron state $\left(-\frac{1}{2};+\frac{1}{2}\right)$, or heavy-hole state $\left(-\frac{3}{2};+\frac{3}{2}\right)$.

We note also energy of optical transitions for respective states as "low" and "high", which does not necessarily coincide with level ordering for the trion state, but include both splittings of trion and of resident carrier. As a result a variety of configurations are controlled by signs of electron and hole g-factors and relative ratio of their absolute values.

Scheme for the specific case has label "A.1.A", which means the case "A" for g-factors signs $g_e > 0$, $g_{hh} > 0$, condition "1" for values ratio $(|g_e| > |g_{hh}|)$, and "A" for absorption process. Then according table the singlet state for T^- is "σ^-, high".

	g-factor	Spin configuration	Absorption		Emission	
			(1) $\lvert g_e\rvert > \lvert g_{hh}\rvert$	(2) $\lvert g_e\rvert < \lvert g_{hh}\rvert$	(1) $\lvert g_e\rvert > \lvert g_{hh}\rvert$	(2) $\lvert g_e\rvert < \lvert g_{hh}\rvert$
A	$g_e > 0$	$T_s^- - \frac{3}{2}\left(0;-\frac{3}{2}\right)$	σ^-, high	σ^-, low	σ^-, high	σ^-, low
	$g_{hh} > 0$	$T_s^+ - \frac{1}{2}\left(-\frac{1}{2};0\right)$	σ^+, low	σ^+, high	σ^+, low	σ^+, high
B	$g_e < 0$	$T_s^- + \frac{3}{2}\left(0;+\frac{3}{2}\right)$	σ^+, high	σ^+, low	σ^+, high	σ^+, low
	$g_{hh} < 0$	$T_s^+ + \frac{1}{2}\left(+\frac{1}{2};0\right)$	σ^-, low	σ^-, high	σ^-, low	σ^-, high
C	$g_e > 0$	$T_s^- + \frac{3}{2}\left(0;+\frac{3}{2}\right)$	σ^-, high	σ^-, high	σ^+, low	σ^+, low
	$g_{hh} < 0$	$T_s^+ - \frac{1}{2}\left(-\frac{1}{2};0\right)$	σ^-, high	σ^-, high	σ^+, low	σ^+, low
D	$g_e < 0$	$T_s^- - \frac{3}{2}\left(0;-\frac{3}{2}\right)$	σ^+, high	σ^+, high	σ^-, low	σ^-, low
	$g_{hh} > 0$	$T_s^+ + \frac{1}{2}\left(+\frac{1}{2};0\right)$	σ^+, high	σ^+, high	σ^-, low	σ^-, low

Table A.1: *Singlet trion states formed from heavy-holes*

From Table A.1 a few conclusions can be drawn:

- *Absorption* and *Emission* coincide when electron and hole g-factors have the same sign, cases A and B
- Positive and negative trions coincide in *Absorption* and *Emission* if g_e and g_{hh} have opposite signs, cases C and D.
- "Inverted" polarization in *Emission* (i.e. when the higher energy com-

ponent of optical transitions is stronger polarized) is observed for T^- in A.1.E and B.1 and for T^+ in A.2 and B.2. For all other cases polarization is "normal".

- Positive and negative trions can be distinguished on base of spin selection rules for *Absorption* and *Emission* in A and B cases only.

A2.2 Light-hole trions

For the trions formed with participation of light-holes (instead of heavy-holes) the spin selection rules will have the form given in Table A.2. Spin states differ from the heavy-hole trions, but for selection rules the following coincidence can be established (lh trion groups are marked by "*"): $A^* \rightarrow D$, $B^* \rightarrow C$, $C^* \rightarrow B$, and $D^* \rightarrow A$.

	g-factor	Spin configuration	Absoption		Emission	
			(1) $\lvert g_e\rvert > \lvert g_{hh}\rvert$	(2) $\lvert g_e\rvert < \lvert g_{hh}\rvert$	(1) $\lvert g_e\rvert > \lvert g_{hh}\rvert$	(2) $\lvert g_e\rvert < \lvert g_{hh}\rvert$
A*	$g_e > 0$	$T_s^- - \frac{1}{2}\left(0; -\frac{1}{2}\right)$	σ^+, high	σ^+, high	σ^-, low	σ^-, low
(D)	$g_{hh} > 0$	$T_s^+ - \frac{1}{2}\left(-\frac{1}{2}; 0\right)$	σ^+, high	σ^+, high	σ^-, low	σ^-, low
B*	$g_e < 0$	$T_s^- + \frac{1}{2}\left(0; +\frac{1}{2}\right)$	σ^-, high	σ^-, high	σ^+, low	σ^+, low
(C)	$g_{hh} < 0$	$T_s^+ + \frac{1}{2}\left(+\frac{1}{2}; 0\right)$	σ^-, high	σ^-, high	σ^+, low	σ^+, low
C*	$g_e > 0$	$T_s^- + \frac{1}{2}\left(0; +\frac{1}{2}\right)$	σ^+, high	σ^+, low	σ^+, high	σ^+, low
(B)	$g_{hh} < 0$	$T_s^+ - \frac{1}{2}\left(-\frac{1}{2}; 0\right)$	σ^-, low	σ^-, high	σ^-, low	σ^-, high
D*	$g_e < 0$	$T_s^- - \frac{1}{2}\left(0; -\frac{1}{2}\right)$	σ^-, high	σ^-, low	σ^-, high	σ^-, low
(A)	$g_{hh} > 0$	$T_s^+ + \frac{1}{2}\left(+\frac{1}{2}; 0\right)$	σ^+, low	σ^+, high	σ^+, low	σ^+, high

Table A.2: *Singlet trion states formed from light-holes*

A.3 Selection rules for singlet and triplet states of T^-

Table A.3 summarizes an order of spin levels for triplet state of negative trions. (For singlet state we have only two states which split with g_h). Here additional criterions should be considered. Additional to the ratio of values of g_e and g_h, for some cases with $|g_e| < |g_{hh}|$ (*.2 cases) ratio of $2g_e$ and g_h will determine levels ordering. We label this criterion with: (a) $|2g_e| > |g_{hh}|$ and (b) $|2g_e| < |g_{hh}|$.

A.1	A.2.a	A.2.b	B.1	B.2.a	B.2.b	C.1	C.2.a	C.2.b	D.1	D.2.a	D.2.b
+5/2	+5/2	+5/2	-5/2	-5/2	-5/2	-1/2	-1/2	-1/2	+1/2	+1/2	+1/2
-1/2	+3/2	+3/2	+1/2	-3/2	-3/2	+5/2	-3/2	-3/2	-5/2	+3/2	+3/2
+3/2	-1/2	+1/2	-3/2	+1/2	-1/2	-3/2	+5/2	-5/2	+3/2	-5/2	+5/2
-3/2	+1/2	-1/2	+3/2	-1/2	+1/2	+3/2	-5/2	+5/2	-3/2	+5/2	-5/2
+1/2	-3/2	-3/2	-1/2	+3/2	+3/2	-5/2	+3/2	+3/2	+5/2	-3/2	-3/2
-5/2	-5/2	-5/2	+5/2	+5/2	+5/2	+1/2	+1/2	+1/2	-1/2	-1/2	-1/2

Table A.3: *Energy order of spin states for triplet negative trion. Energy increases from bottom to top.*

Few points to note by proceeding with optical transitions:

- The intensity may differ for emission and absorption (like for singlets)
- Triplet ground states for A and B have spins $\pm\frac{5}{2}$, i.e. are spin forbidden. Therefore, in optical transitions first excited states will be involved.

A.4 Crossing of triplet and singlet states (S-T crossing): Hidden or visible?

With increasing magnetic field binding energy of triplet increases faster that of singlet. One can also shown from general principles that in infinitely high B triplet configuration is energetically favourable (qualitative arguments are the following: for triplet state two electrons have parallel spins and therefore are located father from each other. This reduces Coulomb repulsion between them). Therefore, it is just a matter of the field strength applied whether one achieve S-T crossing or not. And we know that these fields should be rather strong (20-100 T).

However binding energy of trion states are contributed by two terms: the Coulom-

bic term and the Zeeman term. And the Zeeman term can reduce or increase the S-T crossing field. Also due to the Zeeman term, the S-T crossing of trion states may be hidden in optical spectra [Ast05]. I.e. the S-T crossing may take place, but it would not lead to crossing of optical transitions. Reason for that is difference in final state of electron, which is left after trion recombination, the electron Zeeman splitting will shift the optical transitions. A. Dzyubenko made a theoretical analysis of the situations when S-T crossings are hidden or not.

	A	B	C	D
singlet	-1/2	+1/2	+1/2	-1/2
triplet	-1/2, first excited	+1/2, first excited	-1/2,	+1/2,
ST crossing	visible	visible	hidden	hidden

Table A.4: *Conditions for hidden and visible S-T crossing for T-. In table spin of the final state resident electron after trion recombination is given.*

Table A.4 is received from comparison of Tables A.1 and A.3. Condition for this comparison is very simple. If the final electron states for T_s and T_t recombination coincide, i.e. have the same spin, than S-T crossing is “visible”, i.e. takes place in the same field where the optical transition shows crossing. If they are different, then S-T crossing is hidden. Here only main classes are important. For T_s final state is $-\frac{1}{2}$ for A and D, and $+\frac{1}{2}$ for B and C. For triplet situation is a bit more complicated as the lowest state may have spin $\pm\frac{5}{2}$ and results in spin forbidden transition. In this case the next excited, spin allowed transition is taken into consideration: (i) A $-\frac{1}{2}$, first excited state; (ii) B $+\frac{1}{2}$, first excited state; (iii) C $-\frac{1}{2}$, ground state and (iv) D $+\frac{1}{2}$, ground state.

Publications

Part of this work will be published as follows:

1 . *"Optically detected far infrared resonances in the photoluminescence of (In,Ga)As/GaAs self-assembled quantum dots"*

M. Gerbracht, G. Bartsch, A. A. Dremin, D. R. Yakovlev, D. Reuter, A. Wieck, and M. Bayer

Submitted to Phys. Rev. B, (2008)

2 . *"Optically detected resonance study of diluted magnetic semiconductor CdMnTe quantum dots"*

M. Gerbracht, G. Bartsch, P. Wojnar, D. R. Yakovlev, U. Woggon, J. Kossut, and M. Bayer

Submitted to Phys. Rev. B, (2008)

3 . *"High magnetic field study of positively charged excitons in CdTe/ CdMgTe quantum wells"*

G. Bartsch, **M. Gerbracht**, D. R. Yakovlev, J. Blokland, P. C. M. Christianen, E. A. Zhukov, A. B. Dzyubenko, N. A. Gippius, G. Karczewski, T. Wojtowicz, J. Kossut, J. C. Maan, and M. Bayer

In preparation.

Bibliography

[Aki06] A. V. Akimov, A. V. Scherbakov and D. R. Yakovlev,
›Spin lattice relaxation in magnetic semiconductor nanostructures“,
Chapter 2 in ›Handbook of Semiconductor Nanostructures and Nanodevices“
(American Scientific Publishers, Los Angeles, 2006, ISBN: 1-58883-076-4),
edited by A. A. Balandin and K. L. Wang. pp. 45-93.

[Aki] Andrey V.Akimo, Alexey V. Scherbakov, Dmitri R.Yakovlev,
"Handbook of Semiconductor Nanostructures and Nanodevices",
ISBN: 1-58883-076-4, edited by A. A. Balandin and K. L. Wang

[Agg85] R. L. Aggarwal, S. N. Jasperson, P. Becla, R. R. Galazka,
Phys. Rev. B 32, 5132 (1985)

[And05] D. Andronikov, V. Kochereshko, and A. Platonov, T. Barrick and S. A. Crooker,
G. Karczewski, Phys. Rev. B 72, 165339 (2005)

[Ast99] G. V. Astakhov, D. R. Yakovlev, V. P. Kochereshko, W. Ossau,
J. Nürnberger, W. Faschinger, and G. Landwehr, Phys. Rev. B 60, R8485 (1999)

[Ast00] G. V. Astakhov, V. P. Kochereshko, D. R. Yakovlev, W. Ossau, J. Nürnberger,
F. Faschinger, and G. Landwehr, Phys. Rev. B 62, 10345 (2000)

[Ast02] G. V. Astakhov and D. R. Yakovlev, V. P. Kochereshko, W. Ossau,
W. Faschinger, J. Puls, F. Henneberger, S. A. Croocker, Q. McCulloch,
D. Wolverson, N. A. Gippius, A. Waag, Phys, Rev. B 65, 165335 (2002)

[Ast05] G. V. Astakhov, D. R. Yakovlev, V. V. Rudenkov, P. C. M. Christianen,
T. Barrick, S. A. Crooker, A. B. Dzyubenko, W. Ossau,1 J. C. Maan,
G. Karczewski, and T. Wojtowicz, Phys. Rev. B 71, 201312 (2005)

[Bar07] Gregor Bartsch, Diploma thesis "Optisch detektierte Resonanzen in
Halbleiter-quantenstrukturen, University of Dortmund (2007)

[Bla94] E. Blackwood, M. J. Snelling, R. T. Harley, S. R. Andrews, and C. T. B. Foxon,
Phys. Rev. B 50, 14246 (1994)

[Boo85] I. J. Booth, and C. F. Schwerdtfeger, Phys. Stat. Sol. B 130, 749 (1985)

[Cav85] B. C. Cavenett, and E. J. Pakulius, Phys. Rev. B 32, 8449 (1985)

[Che04] S.J. Cheng , W. Sheng, P. Hawrylak, S. Raymond, S. Studenikin, A. Sachrajda,
Z. Wasilewski, A. Babinski, M. Potemski, G. Ortner, M. Bayer,
Physica E 21, 211 (2004)

[Dan82] L. S. Dang, G. Neu, R. Romestain, Sol. Stat. Commun. 44, 1187 (1982)

[Dar30] C.G. Darwin, Proc. Cambridge Philos. Soc. 27, 86 (1930)

[Die95] T. Dietl, P. Peyla, W. Grieshaber, and Y. Merle d'Aubigne,
Phys. Rev. Lett. 74, 474 (1995)

[Dio06] M. de Dios-Leyva, N. Porras-Montenegro, H. S. Brandi, L. E. Oliveira,
J. Appl. Phys. 99, 104303 (2006)

[Dre05] A. A. Dremin, D. R. Yakovlev, A. A. Sirenko, S. I. Gubarev, O. P. Shabelsky, A. Waag, M. Bayer, Phys. Rev. B 72, 195337 (2005)

[Eag90] D. Eaglesham and M. Cerullo, Phys. Rev. Lett. 64, 1943 (1990)

[Ess00] Axel Esser, Erich Runge, Roland Zimmermann, and Wolfgang Langbein, Phys. Rev. B 62, 8232 (2000)

[Fin95] G. Finkelstein, H. Shtrikman, and I. Bar-Joseph, Phys. Rev. Lett. 74, 976 (1995)

[Fin96a] G. Finkelstein, H. Shtrikman, and I. Bar-Joseph, Phys. Rev. B 53, R1709 (1996)

[Fin96b] G. Finkelstein, H. Shtrikman, and I. Bar-Joseph, Phys. Rev. B 53, 12593 (1996)

[Fin97] G. Finkelstein, H. Shtrikman, and I. Bar-Joseph, Phys. Rev. B 56, 10 326 (1997)

[Fin98] G. Finkelstein, H. Shtrikman, and I. Bar-Joseph, Physica B 249-251, 575 (1998)

[Foc28] V. Fock. Z. Phys. 47, 446 (1928)

[Fur98] J. K. Furdyna, J. Appl. Phys. 64, R29 (1988)

[Gaj79] J.A. Gaj, R. Planel and G. Fishman, Sol. Stat. Commun. 29, 435 (1979)

[Gis93] S. J. C. H. M. van Gisbergen, M. Godlewski, R. R. Galazka, T. Gregorkiewicz, C. A. J. Ammerlaan, and N. T. Khoi, Phys. Rev. B 48, 11767 (1993).

[Gla99] S. Glasberg, G. Finkelstein, H. Shtrikman, and I. Bar-Joseph, Phys. Rev. B 59, R10425 (1999)

[Gre06] A. Greilich, D. R. Yakovlev, A. Shabaev, Al. L. Efros, I. A. Yugova, R. Oulton, V. Stavarache, D. Reuter, A. Wieck, M. Bayer, Science 313, 341 (2006)

[Gre07] A. Greilich, A. Shabaev, D. R. Yakovlev, Al. L. Efros, I. A. Yugova, D. Reuter, A. Wieck, M. Bayer, Science 317, 1896 (2007)

[Ham99] S. Hameau, Y. Guldner, O. Verzelen, R. Ferreira, G. Bastard, J. Zeman, A. Lemaître, J.M. Gérard, Phys. Rev. Lett. 83, 4152 (1999)

[Ham02] S. Hameau, J.N. Isaia, Y. Guldner, E. Deleporte, O. Verzelen, R. Ferreira, G. Bastard, J. Zeman, J.M. Gérard, Phys. Rev. B 65, 085316 (2002)

[Hau98] A. Haury, A. Arnoult, V. A. Chitta, J. Cibert, Y. Merle d'Aubigne, S. Tatarenko, and A. Wasiela, Superlattices Microstruct. 23, 1097 (1998)

[Hu98] C. Y. Hu, W. Ossau, D. R. Yakovlev, G. Landwehr, T. Wojtowicz, G. Karczewsi, and J. Kossut, Phys. Rev. B 58, R1766 (1998)

[Iva07] V. Yu. Ivanov, M. Godlewski, D. R. Yakovlev, S. M. Ryabchenko, G. Karczewski, and A. Waag, Phys. Stat. Sol. (a) 204, 174 (2007)

[Iva08] V. Yu. Ivanov, M. Godlewski, D. R. Yakovlev, S. M. Ryabchenko, M. K. Kneip, M.Bayer, and A.Waag, about to be published

[Jan03] G. Janssen, E. Goovaerts, A. Bouwen, and B. Partoens, B. Van Daele, N. Žurauskien, P.M. Koenraad, and J.H. Wolter, Phys. Rev. B 68, 045329 (2003)

[Jeu02] C. R. L. P. N. Jeukens, P. C. M. Christianen, and J. C. Maan, D. R. Yakovlev and W. Ossau, V. P. Kochereshko, T. Wojtowicz, G. Karczewski, and J. Kossut, Phys. Rev. B 66, 235318 (2002)

[Kel01] D. Keller, D. R. Yakovlev, B. König, W. Ossau, Th. Gruber, A. Waag, and L. W. Molenkamp, A. V. Scherbakov, Phys. Rev. B 65, 035313 (2001)

[Kes90] H. W. van Kesteren, E. C. Cosman, W. A. J. A. Van der Poel, and C. T. Foxon. Phys. Rev. B 41, 5283 (1990)

[Khe93] K. Kheng, R. T. Cox, Y. Merle d'Aubigné, F. Bassani, K. Saminadayar, and S. Tatarenko, Phys. Rev. Lett. 71, 1752 (1993)

[Kli95] C.F. Klingshirn, "Seminconductor Optics", Springer-Verlag Berlin Heidelberg, (1995)

[Kne06a] M. K. Kneip, D. R. Yakovlev, M. Bayer, A. A. Maksimov, I. I. Tartakovskii, D. Keller, W. Ossau, L. W. Molenkamp, A. Waag, Phys. Rev. B 73, 035306 (2006)

[Kne06b] M. K. Kneip, D. R. Yakovlev, M. Bayer, A. A. Maksimov,I. I. Tartakovskii, D. Keller, W. Ossau, L. W. Molenkamp, A. Waag, Phys. Rev. B 73, 045305 (2006)

[Kor06] M. Korkusinski, Phys. Rev. B 74, 075317 (2006)

[Kro85] H. W. Kroto, J. R. Heath, S. C. O'Brien, R. F. Curl, and R. E. Smalley, Nature 318, 162 (1985)

[Lam58] M. A. Lampert, Phys. Rev. Lett. 1, 450 (1958)

[Lar85] B. E. Larson, K. C. Hass and E. Ehrenreich, Sol. Stat. Commun. 56, 347 (1985)

[Mal83] A. V. Malyavkin, Phys. Stat. Sol. (b) 115, 353 (1983)

[Mas97] I. V. Mashkov, C. Gourdon, P. Lavallard, and D. Yu. Rodichev, Phys. Rev. B 55, 13761 (1997)

[Mei05] C. J. Meining, V. R. Whiteside, A. Petrou, B. D. McCombe, A. B. Dzyubenko, J. G. Tischler, A. S. Bracker, and D. Gammon, Physica E 26, 158 (2005)

[Mol92] A. Moll. C. Wetzel, B. K. Meyer, P. Omling, and F. Scholz, Phys. Rev. B. 45, 1504, (1992)

[Nag80] S. Nagata, R. R. Galaka, D. P. Akbarzadeh, J. K. Furdyna, and P. H. Keesom, Phys. Rev. B 22, 3331 (1980)

[Nas93] K. J. Nash, M. S. Skolnick, M. K. Saker, and S. J. Bass, Phys. Rev. Lett. 70, 3115 (1993)

[Oss93] W. J. Ossau and B. Kuhn-Heinrich, Physica B 184, 422 (1993)

[Oss02] W. Ossau, D. R. Yakovlev, G. V. Astakhov, A. Waag, C. J. Meining, H. A. Nickel, B. D. McCombe and S. A. Crooker, Physica E 12, 512 (2002)

[Pot91] M. Potemski, R. Stepniewski, J. C. Maan, G. Martinez, P. Wyder, and B. Etienne, Phys. Rev. Lett. 66, 2239 (1991)

[Rei06] M. Reibold, P. Paufler, A. A. Levin, W. Kochmann, N. Pätzke, D. C. Meyer, Nature 444, 286 (2006)

[Rom80] R. Romestain, C. Wiesbuch, Phys. Rev. Lett. 45, 2067 (1980)

[Ryc02] K. Ryczko, G. Sek and J. Misiewicz, Sol. Stat. Comm. 122 (6), p. 323 (2002)

[Sad03] M. L. Sadowski, M. Byszewski, M. Potemski, A. Sachrajda, G. Karczewski, Appl. Phys. Lett. 82, 3719 (2003)

[Sän06] I. Sänger, "Magnetic-Field-Induced Second Harmonic Generation in Semiconductors and Isolators", ISBN: 3-8322-5180-4, Dissertation, Dortmund (2006)

[Sch99] A. V. Scherbakov, A. V. Akimov, D. R. Yakovlev, W. Ossau, G. Landwehr, T. Wojtowicz, G. Karczewski, and J. Kossut, Phys. Rev. B 60, 5609 (1999).

[Sne92] M. J. Snelling, E. Blackwood, C. J. McDonagh, R. T. Harley, and C. T. B. Foxon, Phys. Rev. B 45, 3922 (1992)

[Sha74] J. Shah, R. F. Leheny, and W. F. Brinkman, Phys. Rev. B 10, 659 (1974)

[Sha84] Y. Shapira and S. Foner, D. H. Ridgley, K. Dwight, and A. Wold, Phys. Rev. B 30, 4021 (1984)

[Sha86] Y. Shapira, S. Foner, P. Becla, and D.N. Domingues, M. J. Naughton and J. S. Brooks, Phys. Rev. B 33, 356 (1986)

[Shc04] More details can be found in the book: *Epitaxy of Nanostructures*, V.A. Shchukin, N.N. Ledentsov, D. Bimberg, Springer, 2004.

[Shi95a] A. J. Shileds, J. L. Osborn, M. Y. Simmons, M. Pepper, D. A. Ritchie, Phys. Rev. B 52, 5523 (1995)

[Shi95b] A. J. Shileds, M. Pepper, M. Y. Simmons, D. A. Ritchie, Phys. Rev. B 52, 7841 (1995)

[Sko93] M. S. Skolnick, D. J. Mowbray, and D.M. Whittaker, Phys. Rev. B 47, 6823 (1993)

[Sol07] A. Solga, Z. Cerman, B. F. Striffler, M. Spaeth, and W. Barthlott, Bioinsp. Biomim. 2, 126 (2007)

[Str39] I. Stranski and L. V. Krastanov, Akad. Wiss. Lett. Mainz Math. Natur K1 IIb146, 797 (1939)

[Str92] T. Strutz, A.M. Witowski, and P. Wyder, Phys. Rev. Let. 68, 3912 (1992)

[Tak98] S. Takeyama, H. Kunimatsu, K. Uchida, N. Miura, G. Karczewski, J. Jaroszynski, T. Wojtowicz, J. Kossut, Physica B 246, 200 (1998)

[Van01] L. M. K. Vandersypen, M. Steffen, G. Breyta, C. S. Yannoni, M. H. Sherwood, and I. L. Chuang, Nature 414, 883 (2001)

[War92] R. J. Warburton, J. G. Michels, R. J. Nicholas, J. J. Harris, and C. T. Foxon, Phys. Rev. B 46, 13394 (1992)

[Wet92] C. Wetzel, Al. L. Efros, A. Moll, B. K. Meyer, P. Omling, and P. Sobkowicz, Phys. Rev. B 45, 14052 (1992)

[Woj07] P. Wojnar, J. Suffczynski, K. Kowalik, A. Golnik, G. Karczewsiki, and J. Kossut, Phys. Rev. B 75, 155301 (2007)

[Yak95] D. R. Yakovlev, G. Mackh, B. Kuhn-Heinrich, W. Ossau, A. Waag, G. Landwehr, R. Hellmann, and E. O. Göbel, Phys. Rev. B 52, 12033 (1995)

[Yak97] D. R. Yakovlev, V. P. Kochereshko, R. A. Suris, H. Schenk, W. Ossau, A. Waag, G. Landwehr, P. C. M. Christianen and J. C. Maan, Phys. Rev. Lett. 79, 3974 (1997)

[Yak07] D. R. Yakovlev, Phys. Stat. Sol. (a) 204, 179 (2007)

[Yak08] D. R. Yakovlev, Summary of optical transitions and spin selection rules for trions in QWs, private communication (2008)

[Yu07] V. Yu. Ivanov, M. Godlewski, D. R. Yakovlev, S. Ryabchenko, G. Karczewski, and A. Waag, Phys. Stat. Sol. (a) 204, 174 (2007).

[Yug07] I. A. Yugova, A. Greilich, E. A. Zhukov, D. R. Yakovlev, M. Bayer, D. Reuter, and A. D. Wieck, Phys. Rev. B 75, 195325 (2007)

[Zib05] E.A. Zibik, L.R. Wilson, R.P. Green, G. Bastard, R. Ferreira, P.J. Phillips, D.A. Carder, J-P.R. Wells, M.S. Skolnick, J.W. Cockburn, M.J. Steer, and M. Hopkinson, Physica E 26, 408 (2005)

List of samples

Nonmagnetic samples

Nonmagnetic quantum wells					
Name	Material	Doping	Carrier density / $\frac{10^{10}}{cm^2}$	QW width / nm	Page
Ash250	GaAs/AlGaAs	n-type		25	48 59
040397C	CdTe/CdMnTe	undoped		8	56
090505AC	CdTe/CdMgTe	p-type		20	68 97
12216	GaAs/AlGaAs	p-type	0.15	15	63
11302	GaAs/AlGaAs	undoped		10	103
11309	GaAs/AlGaAs	n-type	97	10	92
32A21M7	AlGaAs/AlAs	n-type	3	20	61 101
zq1088	ZnSe/ZnMgSSe	n-type	15 - 20	8	105
zq1090	ZnSe/ZnMgSSe	undoped	0.5	8	105

Nonmagnetic quantum dots				
Name	Material	Doping	Annealing temp.	Page
11955-850°C	InGaAs/GaAs	n-type	850°C	114
11955-945°C	InGaAs/GaAs	n-type	945°C	109
11376-940°C	InGaAs/GaAs	undoped	940°C	117
Colloidal QDs	CdTe	undoped	—	123

Magnetic samples

Magnetic $Zn_{1-x}Mn_xSe$/ZnBeSe quantum wells				
Sample	Mn content, x	Electron concentration / 10^{10} cm^{-2}	QW width / Å	Page
CB1541	0.012	undoped	100	134 141
CB1542	0.004	undoped	100	136
CB1651	0.012	5	150	136
CB2422	0.02	undoped	100	132
CB2033	0.004	3	100	140
CB2034	0.004	32	100	138

Magnetic $Cd_{1-x}Mn_xTe$/ZnCdTe quantum dots			
Sample	Mn content, x	Doping	Page
032504A	0.03	undoped	144
602005B	0.0035	undoped	144
602005C	0.002	undoped	144
070306B	0	undoped	144

List of Figures

Index

Acknowledgements

I would like to thank all colleagues, friends, family and sponsors for supporting this work.

First of all, I would like to thank Prof. Dr. Manfred Bayer and Priv.-Doz. Dr. Dmitri R. Yakovlev, who supported me at any time and helped me a lot in my scientific research and beyond. A special thank goes also to Aleksey Dremin who introduced me to the experimental setup and ODR technique. I am grateful to Prof. Dr. Klaus Wille for appraising this thesis.

I would also like to thank Gregor Bartsch very much for a great time and excellent collaboration in the FIR lab, especially for his improvements of Origin.

Martin Kneip, Ingo Sänger and Matthias Schwab also helped me a lot at the initial stage of my research and with numerous technical problems. Thanks also to Thomas Auer, Hannes Kurtze, Alex Greilich and Ruth Oulton for many interesting discussions.

I appreciate the help of Prof. Dr. Fröhlich and Prof. Dr. Ulrike Woggon, the technical support of Klaus Wiegers and Thomas Stöhr and the support of Michaela Wäscher, as well as Najeeba Lenser.

I would like to thank all members of the Experimentelle Physik II group and their guests for the nice atmosphere, especially Ilja Akimov, Marcel Arlt, Marc Assmann, Dmitri Azamat, Ansgar Bauschulte, Thorsten Berstermann, Jan Brandt, Jordi Gomis Bresco, Jörg Debus, Sabine Dommers, Olga Dyatlova, Oleh Fedorych, Lucy Fokina, Tillmann Godde, Robert Heinle, Benjamin Kaminski, Björn Möller, Anindita Ray, Christian Sandfort, Oliver Schöps, Stefan Spatzek. Marcin Syperek, Vasily Temnov, Jean-Sebastian Tempel, and Markus Wiemann.

I am grateful to Gerhard Oeing-Hanhoff who sparked my interest in physics and always encouraged and supported me.

Finally, I would like to thank my parents Eva and Werner Gerbracht for their support, as well as my sister Daniela, my grandparents Rosemarie and Werner Gerbracht and Luzie Nowak. I also thank Jola and Ludger Gerbracht, Mechtild and Peter Lorig, and Magdalene and Ludger Gartmann.